Monte Carlo Studies of BFKL Physics

Thesis submitted for the degree of Doctor of Philosophy

Jeppe Rosenkrantz Andersen

September 2002

Institute for Particle Physics Phenomenology
Department of Physics
University of Durham

Acknowledgements

It is a great pleasure for me to have been supervised by Prof. James Stirling during the past three years. While guiding my research he has always been willing to listen to my ideas about how to solve problems at hand, and more importantly he has let me try them out, even though he might have seen a more direct solution to a specific problem. However, many of the results documented in this thesis would not have been found, were it not for the understanding of the many details that is developed through a students persistence, backed by the confidence of his or her supervisor that the problem will eventually be solved. And when I got stuck, James was always there to get the project back on track.

I have been very lucky that James also introduced me to a very motivating collaboration. I have enjoyed plenty discussions with especially Fabio Maltoni and Vittorio Del Duca, who together with Albert de Roeck have always been more than happy to keep me busy (often by simultaneous efforts).

The past three years have seen many adventures by Dr. Mike Leech and myself in the mountains of the Lake District, Scotland, and the Alps, all for which I am very grateful. I would like to also thank Mike and Lydia Heck for their huge effort in managing the ever growing complexity of the IPPP computer system, and especially for working so hard to minimise the downtime of the computer system when the institute got relocated to the new Ogden Centre just a week before the submission of this thesis.

Finally, I would like to thank students and post–docs of the past many years in Durham for creating, together with the staff members, such an inspiring and friendly atmosphere.

The Danish Research Agency is acknowledged for a studentship financing my studies in Durham, and the Nick Brown bursary is thanked for additional support to attend the small–x workshop in Lund 2002.

Abstract

We study the properties of the BFKL evolution of a t–channel gluon exchange in the high energy limit. In particular we formulate a solution to the BFKL evolution equation in terms of an explicit sum over emitted gluons, which allows for a Monte Carlo integration of the resulting rapidity ordered multi–gluon phase space. This formulation allows for an introduction of the running of the coupling to the BFKL evolution. More importantly, the Monte Carlo implementation of the solution to the BFKL evolution equation allows for studies of the exclusive final states resulting from the exchange.

The full control over the gluon radiation allows for energy and momentum conservation to be observed when calculating the hadronic cross sections. This is in contrast to the standard analytic approach to BFKL physics, which solves the BFKL equation by effectively summing over any number of gluons emitted and integrating over the full rapidity ordered allowed phase space. It is therefore impossible to reconstruct the parton momentum fractions exactly, and thus energy and longitudinal momentum conservation is violated. Although the effect is indeed formally subleading, we show that the numerical impact at present and planned collider energies is very significant. The reduction in parton flux due to the increased energy consumption by the BFKL evolution is sufficient to change the parton level result of an exponential rise of the dijet cross section as a function of the rapidity separation of the leading dijets to a situation much like the LO case. However, we identify the azimuthal correlation between the dijets as an observable sensitive to BFKL effects but more stable under the observation of energy and momentum conservation. We also apply the BFKL MC to a study of dijets at the Tevatron.

Finally we consider $W+2$–jet production, a process which in the limit of large rapidity separation between the two jets exhibit the same factorisation into two impact factors and a t–channel gluon exchange as dijet production. We identify observables in this setup, for which BFKL effects could be important.

Declaration

I declare that the research documented in this thesis has not previously been submitted for a degree at this or any other university.

Part of the research described in this thesis is the result of a collaboration between V. Del Duca, S. Frixione, F. Maltoni, C. R. Schmidt, W. J. Stirling and the author, and has been published in the following papers

- J. R. Andersen, V. Del Duca, S. Frixione, C. R. Schmidt and W. J. Stirling, "Mueller-Navelet jets at hadron colliders" JHEP **0102** (2001) 007 [arXiv:hep-ph/0101180].

- J. R. Andersen, V. Del Duca, F. Maltoni and W. J. Stirling, "W boson production with associated jets at large rapidities" JHEP **0105** (2001) 048 [arXiv:hep-ph/0105146].

Some of the results have been presented by the author at conferences and written up in the following reports

- J. R. Andersen *et al.*, "Multiparticle production in QCD jets" J. Phys. G **28** (2002) 2509 [arXiv:hep-ph/0205127].

- J. R. Andersen, "Forward jets and BFKL at hadron colliders" [arXiv:hep-ph/0207019].

Contents

Chapter 1

Introduction to Perturbative Quantum Chromodynamics

Quantum Chromodynamics (QCD) is one of the three gauge theories of the *Standard Model* of elementary particle physics. The Standard Model describes the interactions between leptons, quarks (the constituents of hadrons), and the gauge bosons mediating the interactions. So far, the Standard Model has been very successful in describing results from high energy experiments, in which perturbative methods can be applied. The *Electro-Weak* interactions are described by the direct product of the gauge-groups $SU(2) \times U(1)$ where the well-known QED interaction forms a $U(1)$ subgroup of the direct product. The electro-weak mixing described by the direct product generates the mass-difference between the gauge-bosons $W^{\pm}$ and Z^0 of the weak interaction, and leaves the photon massless. This is facilitated through the spontaneous symmetry breaking generated by the Higgs-mechanism. The *Strong interaction*, binding quarks into hadrons and ultimately also hadrons into nuclei, is described by the gauge group $SU(3)$ with the corresponding 8 gauge-bosons called *gluons*.

The success of perturbation theory applied to data from high energy experiments is explained by two facts. First of all, although the strength of the interactions described by the electro-weak part of the theory rises with energy, it is generally weak enough to allow for perturbative treatments at all accessible energies. The strength of the QED coupling α rises in this way from about $1/137$ at zero momentum transfers to about $1/127$ at energies of the mass of the Z^0 gauge boson. Contrary to this, the coupling strength of the QCD interactions α_s is generally larger but decreasing with increasing momentum transfers. In numbers we have $\alpha_s(M_Z^2) = 0.120$ and $\alpha_s(M_\tau^2) = 0.334$, where $M_Z = 91$ GeV and $M_\tau = 1.777$ GeV [1]. This will, it is hoped, allow QCD to explain both the non-perturbative effects like *confinement* of quarks into hadrons, and certainly the much celebrated *asymptotic freedom* of quarks at high energies, as two effects of the very same theory but with the coupling strength evaluated at two different energies. At reaction energies of a few GeV or more, the dynamics of the fundamental quarks can be read off from the observed hadrons in the final state due to quantum incoherence between the two effects. This is because the hard and soft interactions of QCD are caused by low- and high-energy interactions respectively and are happening with different typical time scales. The energy scale of change is somewhat sloppily taken to be Λ_{QCD}, the scale at which the coupling becomes "strong". The evolution of the coupling is predicted theoretically from perturbative calculations. However, as we will see, care has to be taken when interpreting quantities from perturbative calculations, since they in general depend on unphysical parameters introduced to the calculation. This includes the coupling constant, which so far has only been defined perturbatively, and Λ_{QCD} which is derived from the coupling. The successes of perturbative treatments of high-energy QCD experiments is due to the fact that the ambiguities introduced by the unphysical parameters scale with the coupling, and since the coupling of QCD decreases with energy, the predictions become more reliable at higher energies. Furthermore, if the coupling is small, fewer terms are needed in the perturbative expansion to get reliable results, just from the point of view of perturbative series in general.

It has to be stressed that confinement is one of the least well understood properties of the strong interactions, and has so far not been strictly derived from the basic field equations of QCD. This has to do with the fact that our understanding of realistic quantum field theories is based solely on perturbation theory, since the field equations are so complicated that we cannot solve the dynamics exactly. However, the confinement ensures that we only observe hadrons and not free quarks. Therefore, the non-perturbative parts of QCD play a key role in any experiment involving quarks, even at very high energies.

This chapter will give an overview of QCD and elaborate on some of the details mentioned above. We will, however, not give a general introduction to simple spinor algebra, gauge theories and quantum field theories. Such introductions can be found in excellent text books like Ref. [2, 3, 4].

1.1 The QCD Lagrangian

Quantum Chromodynamics is a quantum field theory based on the *gauge principle*. The theory is formulated on the basis of a Lagrangian containing the quark fields of the Standard Model. They come in six different *flavours* termed *up (u), charm (c), top (t)* and *down (d), strange (s), bottom (b)*. The *up-type* (u,c,t) quarks have electrical charge $-2/3e$ with e being the charge of the electron, whereas the *down-type* (d,s,b) quarks have electrical charge $1/3e$. Each flavour comes in three different charges with respect to QCD, called *colours*. Starting from the freely propagating quark fields we require the Lagrangian to be invariant when the fields transform as $\psi(x) \to \psi'(x) = U(x)\psi(x)$, which amounts to a redefinition of the charges and is called a *gauge transformation*. Specifically, we require the Lagrangian to be invariant when the quark fields transform according to $U(x)$ belonging to the group $SU(3)$. This will be elaborated upon in Section 1.1.1. As in QED we are then let to introduce gauge fields to make the derivatives of the quark fields transform in a gauge-invariant way. In QCD these gauge fields are called *gluons*, and eight gluons are needed to allow for a gauge transformation of the three charges of QCD. The demand of local $SU(3)$ invariance, and the addition of a kinetic part for the introduced gauge fields leads to the following classical Lagrangian

$$\mathcal{L}_{\text{classical}} = -\frac{1}{4} G^a_{\mu\nu} G^{\mu\nu}_a + \sum_{\text{flavours}}^{N_f} \bar{\psi}_i \left(i\gamma_\mu D^\mu_{ij} - m\delta_{ij} \right) \psi_j . \tag{1.1}$$

The $i, j = 1, 2, 3$ indices on the quark fields refer to the three entries in the "colour vector" ψ (one ψ for each quark flavour) of Dirac spinor fields. The $G^{\mu\nu}_a$ are field strength tensors for the a'th ($a = 1, \ldots, 8$) gluon field A^a_μ, and D is the covariant derivative. D ensures invariance under local gauge transformations of the quark and gluon fields and introduces the coupling between the quarks and gluons ($D^\mu_{ij} = \partial^\mu \delta_{ij} - igT^a_{ij} A^\mu_a$ with i, j being colour indices, g the coupling of QCD and T^a_{ij} *colour matrices* (see 1.1.1)). The coupling between the gluon fields are introduced in the field strength terms ($G^{\mu\nu}_a = \partial^\mu A^\nu_a - \partial^\nu A^\mu_a + g f_{abc} A^\mu_b A^\nu_c$ with f_{abc} the *structure constants* of the chosen representation of the gauge group). We will be concerned with the massless approximation, i.e. setting $m = 0$ in (1.1) (in the *Standard Model* the mass terms are generated by couplings to the Higgs field and do not enter directly as in (1.1). This is, though, irrelevant for our current purpose). The mass of the quarks determines the energy at which the respective flavour is included in the sum in (1.1).

Just as for QED, it is necessary to add a term to this classical Lagrangian to describe the gauge–fixing required to remove the unphysical degrees of freedom introduced to the gluons, both through the gauge–theory and the covariant formulation. We choose the Fadeev–Popov gauge–fixing method which is based on removing the zero-modes of the Gaussian operator for the gluon fields corresponding to the different gauge transformations of the physical field configurations. By choosing a specific gauge we get rid of this redundancy and can invert the quadratic operator to find the propagator and thereby start doing perturbation theory. The Fadeev–Popov gauge fixing will contribute to the final QCD Lagrangian with the following two terms:

$$\mathcal{L}_{\text{gauge-fixing}} = -\frac{1}{2\lambda}\left(\partial^\mu A_\mu^a\right)^2 \tag{1.2}$$

$$\mathcal{L}_{\text{ghost}} = \bar{\eta}^a\left(-\partial^2\delta^{ac} - g\partial^\mu f^{abc}A_\mu^b\right)\eta^c. \tag{1.3}$$

The first term is completely identical to the term introduced to fix the gauge in QED. And as for QED, the physical cross sections or decay rates calculated will be independent on the choice of gauge, even though the intermediate steps in the calculations can appear very different. This in general provides a non-trivial check of the validity of a calculation. In calculations we will often choose a specific value for the parameter λ, and it will turn out that for $\lambda = 1$ (the Feynman gauge) the propagator for the gluon is particularly simple (as for the photon in QED). Another popular choice is $\lambda \to 0$ (the Landau gauge).

As opposed to the case of QED, in QCD the integration measure in the Path Integral changes when performing the Fadeev-Popov gauge fixing. The ghost fields are introduced to describe the Jacobian resulting from the change of fields to integrate over in the functional integral. This addition to the classical Lagrangian takes away the unphysical degrees of freedom for the massless gluon fields introduced by making a Lorentz covariant theory (i.e. the effects of the introduced longitudinal polarisations for the massless gluons are removed). The *Fadeev-Popov* ghost fields η^a, $(a = 1, \ldots, 8)$, are *anti*-commuting spin-1 fields (bosons) and therefore clearly cannot represent physical particles. The final QCD Lagrangian is then given as the sum

$$\mathcal{L}_{\text{QCD}} = \mathcal{L}_{\text{classical}} + \mathcal{L}_{\text{gauge-fixing}} + \mathcal{L}_{\text{ghost}} \tag{1.4}$$

Of course the gauge fixing had to be done even if we could solve the theory exactly since the gauge transformation maps a field configuration to another field configuration corresponding to the same physical situation. In the Path Integral formulation of field theory we have to integrate only over different *physical* field configurations. We have chosen to use *covariant gauge fixing* which maintains the Lorentz covariance of the theory. It is also possible to do gauge fixing by other methods, e.g. Axial gauge fixing, which however breaks Lorentz covariance[1] but as a pay-off has no need for *ghosts*.

1.1.1 Colour $SU(N)$

In this subsection we will look a bit more into how the colour Lie group $SU(N)$ is implemented, having the choice $N = 3$ for QCD in mind. As already mentioned, the ψ's

[1]The Lorentz covariance is of course only broken in intermediate steps. The calculated S-matrix elements are still Lorentz covariant just as they are gauge invariant even though we break gauge invariance in our intermediate calculations.

in (1.1) are N-tuples where each entry is a Dirac spinor field (with 4 Dirac indices). The QCD Lagrangian is constructed to be invariant under *local gauge transformations*, i.e. rotations of the colour vector $\psi(x) \to \psi'(x) = U(x)\psi(x)$, where $U(x)$ belongs to the class of $N \times N$ unitary matrices ($U^\dagger U = 1 = UU^\dagger$ with unit determinant) generated by (N^2-1) $N \times N$-matrices $T^a : U(x) = e^{-igT^a A_a(x)}$. Formally, the T^a's belong to the *fundamental representation* of the Lie algebra, but in a sloppy language we say that the quarks "live" in the fundamental representation since they are acted on by matrices belonging to this representation. In the same manner of speaking we say that the gluon fields $A_a(x)$ "live" in the *adjoint representation*, since we can define an action on the T^a's whose elements in group theory language belong to the adjoint representation. The action of an element of the adjoint representation will (since the T^a's span the considered space of matrices) amount to a rotation of the gluon field $A(x) = T^a A_a(x)$. In the case of QCD the T^a's are known as *colour matrices*, and since $1 = \det(U) = \det\left(e^{-igT^a A_a(x)}\right) = e^{-ig\mathrm{Tr}(T^a)A_a(x)}$ it follows that the T^a's are traceless. We choose to normalise our coupling g so that the colour matrices obey

$$\mathrm{Tr}(T^a T^b) = T_F \delta^{ab} \quad \text{with} \quad T_F = \frac{1}{2} \tag{1.5}$$

With this convention the quadratic Casimir operators of the fundamental and adjoint representation become

$$T^a_{ij} T^a_{jk} \equiv C_F \delta_{ik} \quad \text{with} \quad C_F = \frac{N^2-1}{2N} \tag{1.6}$$

$$f^{acd} f^{bcd} \equiv C_A \delta_{ab} \quad \text{with} \quad C_A = N, \tag{1.7}$$

where the *structure constants* f^{abc} are defined through the relation $\left[T^a, T^b\right] = if^{abc}T^c$ and are therefore clearly basis dependent. The relations (1.6) and (1.7) are a result of the structure of $SU(N)$ only and are therefore independent of the number of quark flavours included in the theory.

1.2 Feynman Rules

The Lehmann, Symanzik and Zimmermann (LSZ) reduction formula relates the physical transition amplitudes to the amputated, one particle irreducible (1PI) Green's functions derived from the Lagrangian. Specifically, with the S-matrix describing the transition amplitude related to the scattering matrix T through $S = \mathbf{1} + iT$, the LSZ reduction formula relates T to the invariant matrix element $\mathcal{M}$ by

$$\left\langle p_1^f p_2^f \cdots \middle| iT \middle| p_1^i p_2^i \cdots \right\rangle = (2\pi)^4 \delta^{(4)}\Big(\sum_n p_n^i - \sum_m p_m^f\Big) i\mathcal{M}\left(p_n^i \to p_m^f\right) \tag{1.8}$$

for the scattering process with $p_1^i, p_2^i, \cdots$ incoming and $p_1^f, p_2^f, \cdots$ outgoing momenta. $\mathcal{M}$ is here the full 1PI $(n+m)$-point Green's function. For a $2 \to n$ scattering process the differential cross section becomes

$$\begin{aligned}
\mathrm{d}\sigma &= \frac{|\mathcal{M}\left(p_n^i \to p_m^f\right)|^2}{F}\mathrm{d}Q \\
F &= |\mathbf{v_A} - \mathbf{v_B}| 2E_A 2E_B = 4\sqrt{(p_A p_B)^2 - m_A^2 m_B^2} \qquad (1.9)\\
\mathrm{d}Q &= (2\pi)^4 \delta^{(4)}\left(p_A + p_B - \sum_m p_m^f\right) \prod_m \frac{\mathrm{d}p_m^f}{(2\pi)^3 2E_m^f}.
\end{aligned}$$

F describes the flux of the incoming particles while $\mathrm{d}Q$ is the phase space measure for the final state particles and $|\mathcal{M}|^2$ is the absolute square of the invariant matrix element for the scattering. For the decay rate of a particle with mass m_A one finds

$$\begin{aligned}
\mathrm{d}\Gamma &= \frac{|\mathcal{M}\left(m_A \to p_m^f\right)|^2}{F}\mathrm{d}Q \\
F &= 2m_A \qquad (1.10)\\
\mathrm{d}Q &= (2\pi)^4 \delta^{(4)}\left(p_A - \sum_m p_m^f\right) \prod_m \frac{\mathrm{d}p_m^f}{(2\pi)^3 2E_m^f}
\end{aligned}$$

in an obvious notation.

Having set up the Lagrangian of QCD we should therefore now discuss the solutions in terms of physical cross sections. Unfortunately, one cannot solve the functional integrals for $\mathcal{M}$ exactly, and so we need to apply perturbative methods. The *Feynman rules* provide a convenient tool of book-keeping in the calculation of the terms in this perturbative expansion of $\mathcal{M}$. They are based on the division of the Lagrangian into a "free" part consisting of the terms quadratic in the fields, and a "interacting" part consisting of the rest. The trick here is that the free part can be solved exactly and the interacting part is treated as a perturbative expansion in the coupling g. In this way, a contribution to a transition amplitude can be calculated as consisting of particles propagating freely in-between vertices of interaction. This gives rise to *Feynman diagrams* where freely propagating particles are pictured with lines and interactions as crossing of lines. Every type of propagating particle field has its own type of line assigned to it. In this way, propagating fermions are depicted with straight lines with an arrow (), gluons using curly lines () and finally ghosts using dashes (). The propagator lines have an arrow to indicate the flow of momentum if the corresponding field is anti-commuting. The contribution to a specific transition amplitude is then given as the sum of all topologically different diagrams with the specific initial and final state and a number of momentum conserving vertices in-between. The exact mathematical expression to substitute for each component of such diagrams can easily be derived from the Lagrangian. Combined with some simple additional rules they constitute the *Feynman rules* of QCD. Specifically, for a given diagram we would

1. Replace for each component of the Feynman-diagram the corresponding expression (see Table 1.1 p. 8). This should be done in a way as to preserve the correct order of the Dirac matrices. This is obtained by following the fermion lines "upstream" when converting the diagrams into formulas.
2. Multiply by (-1) for every anti-fermion line connecting the initial and the final state
3. Multiply by (-1) for every fermion or ghost loop
4. Impose momentum conservation at each vertex
5. Integrate over each undetermined momentum k: $\displaystyle\int \frac{\mathrm{d}^4 k}{(2\pi)^4 i}$
6. Multiply by the symmetry factor

The symmetry factor is needed to account for the correct counting of contributions from diagrams with identical particles, and can either be applied as a factor in the phase space or directly in the calculation of the matrix element. In Table 1.1 we have listed the Feynman rules in momentum space. There is a similar formulation in position space, which is simply obtained by a Fourier transformation of the rules listed. Furthermore, we have ignored the so-called "$+i\varepsilon$"–prescription to propagators, which is used to remind you that the integrals have to be *Wick-rotated* to Euclidean space before obtaining the final result. The $u(p), \bar{u}(p), v(p), \bar{v}(p)$ enlisted are the Dirac spinors parameterising the free-field solutions to the Dirac equation. We have listed the Feynman rules without the spin (and colour) indicies of the Dirac spinors and gluon polarisation vectors, since we will often be interested in cross section summed over spins (and colours) of the final states and averaged over spins (and colours) of the initial states. The Dirac spinors satisfy the following spin sums

$$\sum_s u^s(p)\bar{u}^s(p) = \not{p} + m, \qquad \sum_s v^s(p)\bar{v}^s(p) = \not{p} - m, \tag{1.11}$$

where we have used the standard notation $\gamma_\mu p^\mu = \not{p}$. For unpolarised cross sections one can in the Feynman gauge make the following substitution for sum over polarisations of the polarisation vector product for external gluons

$$\sum_\lambda \varepsilon_\mu^{\lambda,*}(p)\varepsilon_\nu^\lambda(p) \to -g_{\mu\nu}. \tag{1.12}$$

However, this substitution includes a sum over unphysical polarisations of the external gluons (indeed one sees from the above that 4 polarisations have been summed over).

Incoming particles

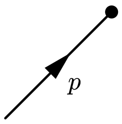

$u(p)$

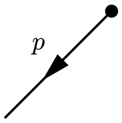

$\bar{v}(p)$

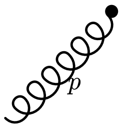

$\varepsilon_\mu(p)$

Outgoing particles

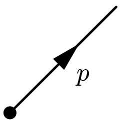

$\bar{u}(p)$

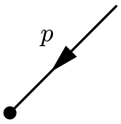

$v(p)$

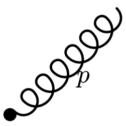

$\varepsilon_{\mu *}(p)$

Propagators

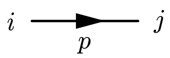

$$\frac{i\delta_{ij}(\not{p}+m)}{p^2-m^2}$$

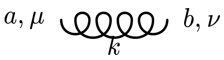

$$\frac{-i\delta_{ab}}{k^2}\left(g_{\mu\nu}-(1-\lambda)\frac{k_\mu k_\nu}{k^2}\right)$$

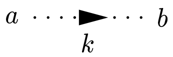

$$\frac{i\delta_{ab}}{k^2}$$

Vertices

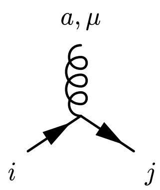

$$ig\gamma^\mu T^a_{ij}$$

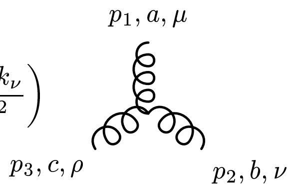

$$gf^{abc}\quad [(p_1-p_2)^\rho g^{\mu\nu} +(p_2-p_3)^\mu g^{\nu\rho} +(p_3-p_1)^\nu g^{\mu\rho}]$$

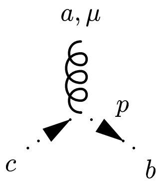

$$gf^{abc}p^\mu$$

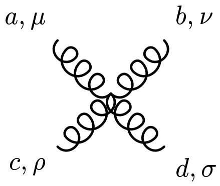

$$-ig^2[f^{abe}f^{cde}(g^{\mu\rho}g^{\nu\sigma}-g^{\mu\sigma}g^{\nu\rho}) +f^{ace}f^{bde}(g^{\mu\nu}g^{\rho\sigma}-g^{\mu\sigma}g^{\nu\rho}) +f^{ade}f^{bce}(g^{\mu\nu}g^{\nu\sigma}-g^{\mu\rho}g^{\nu\sigma})]$$

Table 1.1: The Feynman rules for $i\mathcal{M}$ of QCD in momentum space. Note that the momentum flow of anti-fermion lines is opposite to the direction of the arrow on the fermion propagator line. We have neglected the so-called "$+i\varepsilon$" prescription to propagators. Notice also that only the 3-gluon and the gluon-ghost vertex is momentum-dependent. The direction of all the momenta in the 3-gluon vertex is incoming. In other words $(p_1+p_2+p_3)=0$. For the incoming and outgoing antifermions, the momentum is understood to be opposite to the direction of the fermion arrow (charge flow).

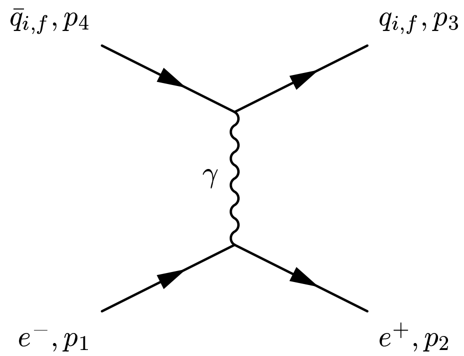

Figure 1.1: The leading order contribution to $e^+e^- \to$ hadrons at low energy: the electromagnetic production of a $q\bar{q}$–pair of flavour f and (anti-)colour i.

These degrees of freedom are removed by adding the contribution from external ghosts. While this is the preferred prescription for higher order calculations because of the more direct relation between the virtual and real corrections (and cancellation of the divergences mentioned in the next sections), for a tree–level calculation it often proves easier to instead explicitly sum over only the physical, transverse polarisations of the gluon by use of the following relation

$$\sum_\lambda \varepsilon_\mu^{\lambda,*}(p)\varepsilon_\nu^\lambda(p) \to -\left(g_{\mu\nu} - \frac{n_\mu p_\nu + n_\nu p_\mu}{n\cdot p} + \frac{n^2 p_\mu p_\nu}{(n\cdot p)^2}\right), \tag{1.13}$$

where n^μ is an arbitrary 4–vector.

1.3 Renormalisation

After setting up the Feynman rules, we can now start calculating perturbative quantities. There is, however, one complication. The Feynman rules derived from the Lagrangian will in many cases result in infinities arising in the calculation. We will first consider the generic example of the total cross section for hadron production in e^+e^- annihilation for massless QCD at an energy scale where the interference from weak physics can be ignored. We will see how all the divergences in the intermediate steps will either cancel or can be regularised.

The leading order contribution to the relevant matrix element for hadronic production is given by the Feynman Diagram in Fig. 1.1. At this level, gluon interactions do not enter, and all the vertices come from the QED (or rather electro–weak, but we are ignoring interference from Z^0's) part of the Standard Model Lagrangian with electrons and three colours of the quarks. Using the Feynman rules with a photon–quark vertex factor $(iQ_f e\gamma^\mu)$ with $(Q_f e)$ being the charge of the quark of flavour f one obtains, using the Feynman gauge and letting $q = (p_1 + p_2)$,

$$i\mathcal{M} = \frac{-iQ_f e^2}{q^2}\left(\bar{v}(p_2)\gamma^\mu u(p_1)\right)\left(\bar{u}(p_3)\gamma_\mu v(p_4)\right), \tag{1.14}$$

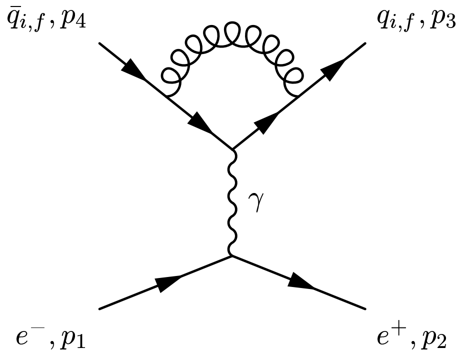

Figure 1.2: The one loop diagram contributing to $e^+e^- \to$ hadrons at NLO. By interference with the LO contribution, this diagram will give a correction proportional to g^2 to the LO cross section.

where we have left out the spin, flavour and colour indicies on the spinors. Using the properties in Eq. (1.11) and trace technology one finds for the unpolarised cross section summed over the three possible colours of the produced massless quarks

$$\sigma(\mathrm{e}^+\mathrm{e}^- \to \text{hadrons}) = \frac{4\pi\alpha^2}{3s} N \sum_{i=1}^{N_f} Q_i^2. \tag{1.15}$$

Here we implicitly use that the $q\bar{q}$–pair will produce hadrons at 100% probability. This result is the basis for the study of the so–called R-ratio

$$R = \frac{\sigma(\mathrm{e}^+\mathrm{e}^- \to \text{hadrons})}{\sigma(\mathrm{e}^+\mathrm{e}^- \to \mu^+\mu^-)} = N \sum_{i=1}^{N_f} Q_i^2 \tag{1.16}$$

at leading order.

Let us now study what happens at the next order in QCD perturbation theory (higher order QED corrections can be ignored, since the value of the QED coupling is much smaller than the value of the QCD coupling). This order will have contributions from the interference between the leading order amplitude and amplitudes with one gluon loop. For massless QCD, the only[2] loop diagram that contributes is depicted in Fig. 1.2.

Using the Feynman rules (for the Feynman gauge) we find

[2]This is true in the $\overline{\mathrm{MS}}$ renormalisation scheme. Also, in the massive case, external field renormalisation generates diagrams with loops on the external quark legs.

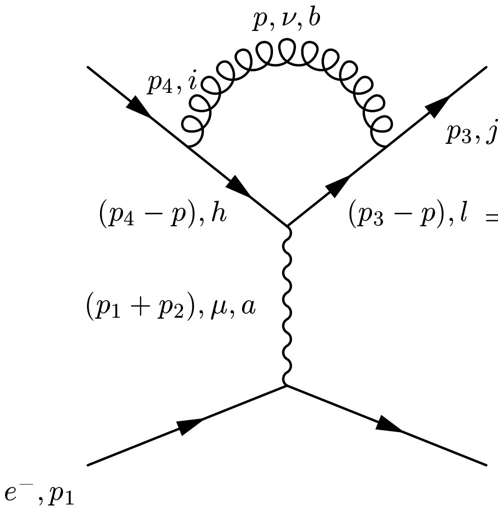

$$
\begin{aligned}
&= \bar{v}(p_2)(-ie\gamma_\mu)u(p_1)\frac{-i}{(p_1+p_2)^2}(iQ_f e)(ig)^2 \\
&\int \frac{\mathrm{d}^4 p}{(2\pi)^4 i} T^b_{ik}T^b_{kj}\frac{-i\bar{u}_j(p_3)\gamma^\nu(\not{p}_3 - \not{p})\gamma^\mu(-\not{p}_4 - \not{p})\gamma_\nu v_i(p_4)}{(p_3-p)^2(p_4+p)^2p^2}
\end{aligned}
\tag{1.17}
$$

Here, the minus in front of $\not{p}_4$ in the numerator is caused by the fact that the antifermion momentum (p_4) flows in the opposite direction of the fermion line. The interference with the leading order diagram in Fig. 1.1 will not introduce any new loop integrals, and by applying the rules in Eq. (1.9) we find that the contribution to the cross section from the virtual correction at NLO can be written in the form[3]

$$
\sigma_V(p_1, p_2) = \frac{1}{8s}\int\frac{\mathrm{d}^3 p_3}{(2\pi)^3 2E_3}\int\frac{\mathrm{d}^3 p_4}{(2\pi)^3 2E_4}(2\pi)^4\delta^{(4)}(p_1+p_2-p_3-p_4)F_V \tag{1.18}
$$

with

$$
F_V = \left(\sum_i Q_i^2\right)\frac{e^4}{q^4}\mathrm{Tr}[\not{p}_2\gamma^\mu\not{p}_1\gamma^\lambda]\mathrm{Tr}[\not{p}_3\Lambda_\mu\not{p}_4\gamma_\lambda] + \text{c.c.} \tag{1.19}
$$

where "c.c." denotes the complex conjugate and

$$
\Lambda_\mu = g^2 C_F\int\frac{\mathrm{d}^4 p}{(2\pi)^4 i}\frac{1}{p^2}\gamma_\nu\frac{\not{p}_3 - \not{p}}{(p_3-p)^2}\gamma_\mu\frac{\not{p}_4 + \not{p}}{(p_4+p)^2}\gamma^\nu \tag{1.20}
$$

describes the one loop QCD corrections to the $q\bar{q}\gamma$–vertex. The traces in Eq. (1.19) are over the implicit spinor indicies.

1.3.1 Regularisation

The integral in (1.20) is divergent in many regions of phase space. First of all it is divergent in the *soft and collinear* regions where $p^2 \to 0$ or p is (anti-)parallel to p_3 (p_4). We will term these divergences *infrared divergences*, and we will discuss them later in Sec. 1.4.1. For now, we will ignore them and concentrate on the so–called *ultra violet* divergence of the integral.

Eq. (1.20) is seen to be logarithmically divergent simply by counting the powers of p in the integrand: For large p the integrand has a p^{-4} behaviour, and by changing integration variables to spherical coordinates in 4 dimensions the integral takes the form

$$\int \frac{\mathrm{d}^4 k}{k^4} = \int_0^\infty \frac{k^3 \mathrm{d}k}{k^4} \int d\Omega = 2\pi^2 \int_0^\infty \frac{\mathrm{d}k}{k}, \tag{1.21}$$

which is logarithmically divergent in the $k \to \infty$ region. This feature is shared by all loop diagrams and, as we have seen, is a direct consequence of the Feynman rules derived from the QCD Lagrangian, which nonetheless describes the interaction we want to study. We therefore have to make meaning of the integrals, and the trick we use is very simple to state. We start by noting that if we reduce the number of space-time dimensions, the number of conjugate variables to integrate over in the momentum space integrals will also be reduced. Next we note that we can make the integral of (1.21) convergent by reducing the dimension of momentum space to $d = 4 - 2\epsilon, \epsilon > 0$. By then calculating all the integrals in the reduced number of dimensions, we will get an answer which depends on ϵ. The claim now is that the correct answer is obtained in the limit $\epsilon \to 0$.

However, it does not quite work this simply. First of all, the mass dimension of the Lagrangian (or more correctly the Lagrangian density) changes as we change the dimension of space-time, and since we want the particle and gauge fields to keep their mass dimensions and the coupling to remain dimensionless we have to introduce a dimension-full factor by hand. We enforce the right dimension on the Lagrangian by replacing g with $g\mu^\epsilon$, where μ is a quantity with the dimension of mass. The magnitude of μ is not constrained in a massless theory; if the masses were included, μ could be specified by the requirement that the pole of the propagator appears at the physical mass of the particle [5]. To calculate the integral in Eq. (1.20) we introduce the Feynman parametrisation for the propagator factors

$$\prod_{i=1}^{n} \frac{1}{A_i^{\alpha_i}} = \frac{\Gamma(\alpha)}{\prod_{l=1}^{n} \Gamma(\alpha_i)} \int_0^1 \left(\prod_{i=1}^{n} \mathrm{d}x_i x_i^{\alpha_i - 1} \right) \frac{\delta(1-x)}{\left(\sum_{i=1}^{n} x_i A_i \right)^{\alpha}}, \tag{1.22}$$

$$\alpha = \sum_{i=1}^{n} \alpha_i, \qquad x = \sum_{i=1}^{n} x_i.$$

Here, Γ is the standard Gamma–function. Although this introduces an extra integral, it proves very efficient in the calculation. The integral is then Wick rotated (for convenience) to go from the Minkowskian space time signature to a standard Euclidean one. This amounts to a change of coordinates for the time-like coordinate $p_0 \to iP_0$. Changing the space time dimension to $D = 4 - 2\epsilon$, the basic integral (for the slightly simpler case of diagrams of the self-energy type) becomes, expressed in terms of the Beta and Gamma functions[3, p.113]

$$\int \frac{\mathrm{d}^D K}{(2\pi)^D} \frac{1}{(K^2 + L^2)} = \frac{B(D/2, 2 - D/2)}{(4\pi)^{D/2} \Gamma(D/2)}. \tag{1.23}$$

The Beta function fulfills

$$B(p,q) = \frac{\Gamma(p)\Gamma(q)}{\Gamma(p+q)}, \tag{1.24}$$

and so the loop integrals can now be rewritten in terms of Γ-functions. These are then expanded in the limit $\epsilon \to 0$, and the result will at one loop always include the factor

$$\frac{\Gamma(1+\epsilon)}{\epsilon}(4\pi)^\epsilon = \frac{1}{\epsilon} + \ln(4\pi) - \gamma_E + O(\epsilon), \tag{1.25}$$

where γ_E is the Euler Constant and the divergence is now parameterised in terms of the $\frac{1}{\epsilon}$ term. It is now possible to render the Green's functions of the theory finite by adding *counter terms* to the Lagrangian, which effectively are new interactions introducing the same $1/\epsilon$–divergences, just with the opposite sign. These new interactions amount to a redefinition of the quantities in the old Lagrangian, which become divergent in the limit $\epsilon \to 0$ and are called *bare quantities.* Again we introduce some arbitrariness into the theory since it is not uniquely defined, how much of (1.25) to include in the counter term, as long as the final result for S-matrix elements is finite.

This way of regularising the divergent integrals is called *Dimensional Regularisation* and preserves the Lorentz structure and local gauge invariance of the Lagrangian. A *Renormalisation Scheme* (RS) consists of the choice of renormalisation scale μ and how many terms of (1.25) to include in the counter terms.

1.3.2 The Renormalisation Group

Dimensional Regularisation has the property that the unrenormalised or *bare* quantities of the Lagrangian can be written as a factor depending on ϵ times the renormalised quantity. For example the relation between the bare and renormalised wave functions is written

$$\psi_B = Z_\psi \psi, \quad A^a_{\mu B} = Z_{A^a} A^a_\mu, \quad \eta^a_{\mu B} = Z_{\eta^a}\eta^a_\mu, \tag{1.26}$$

(Some prefer to define these relations with $Z^{\frac{1}{2}}$ instead of just Z). This *Multiplicative Renormalisation* carries through to the 1 Particle Irreducible (1PI) Green's functions of the theory, so Green's functions in two different RS's (denoted by barred and unbarred quantities) would be related to the bare Green's functions Γ_B by

$$\Gamma = Z\Gamma_B, \quad \bar{\Gamma} = \bar{Z}\Gamma_B, \tag{1.27}$$

where $Z, \bar{Z}$ is a product of different wave function renormalisation factors, one for each external leg on the 1PI diagram corresponding to the Green's function. Clearly, the two renormalised Green's functions are related by

$$\bar{\Gamma} = z\Gamma, \quad z = \frac{\bar{Z}}{Z}, \tag{1.28}$$

where z is finite for $\epsilon \to 0$, since $Z, \bar{Z}$ have the same structure of divergences. The z relating different renormalisations of the bare Green's function would then be products of Z's, which gives rise to the term *Renormalisation Group*.

The independence of the bare Green's functions on the chosen renormalisation scale μ can now be exploited to calculate how the renormalised Green's functions scale with momentum. Consider a 1PI Green's function with n_A, n_F external gluon and quark legs with momenta g_i, q_i respectively. The relation between the bare and renormalised Green's function reads

$$Z_A^{n_A} Z_{\mathrm{q}}^{n_F} \Gamma_B^{n_A,n_F}(\mathrm{g}_i, \mathrm{q}_i, \lambda, g) = \Gamma^{n_A,n_F}(\mathrm{g}_i, \mathrm{q}_i, \lambda(\mu), g(\mu), \mu). \tag{1.29}$$

Applying $\mu\frac{d}{d\mu}$ to the right hand side of this equation we get

$$\begin{aligned} &\mu\frac{d}{d\mu}\Gamma^{n_A,n_F}(\mathrm{g}_i, \mathrm{q}_i, \lambda(\mu), g(\mu), \mu) = \\ &\left(\mu\frac{\partial}{\partial\mu} + \mu\frac{\partial g}{\partial\mu}\frac{\partial}{\partial g} + \mu\frac{\partial\lambda}{\partial\mu}\frac{\partial}{\partial\lambda}\right)\Gamma^{n_A,n_F}(\mathrm{g}_i, \mathrm{q}_i, \lambda(\mu), g(\mu), \mu) \end{aligned} \tag{1.30}$$

Noting that $Z_A^{n_A} = e^{n_A \ln Z_A}$ it is easy to use the μ–independence of Γ_B to get the following relation for the renormalised Green's function

$$\left(\mu\frac{\partial}{\partial\mu} + \beta(g)\frac{\partial}{\partial g} - n_A\gamma_A(g) - n_F\gamma_F(g) + \delta(g)\frac{\partial}{\partial\lambda}\right)\Gamma^{n_A,n_F}(\mathrm{g}_i, \mathrm{q}_i, \lambda(\mu), g(\mu), \mu) = 0, \tag{1.31}$$

with

$$\beta(g) = \mu\frac{\partial g}{\partial\mu}, \quad \gamma_A(g) = \mu\frac{\partial}{\partial\mu}Z_A, \quad \gamma_F(g) = \mu\frac{\partial}{\partial\mu}Z_{\mathrm{q}}, \quad \delta(g) = \mu\frac{\partial\lambda}{\partial\mu} \tag{1.32}$$

We will now use this equation to derive how Γ^{n_A,n_F} transforms under a scaling of momenta. If D is the mass dimension of the Green's function, it will satisfy the following relation

$$\Gamma^{n_A,n_F}(t\mathrm{g}_i, t\mathrm{q}_i, \lambda(\mu), g(\mu), t\mu) = t^D\Gamma^{n_A,n_F}(\mathrm{g}_i, \mathrm{q}_i, \lambda(\mu), g(\mu), \mu) \tag{1.33}$$

This means that $\Gamma^{n_A,n_F}(\mathrm{g}_i, \mathrm{q}_i, \lambda(\mu), g(\mu), \mu)$ satisfies the following relation

$$t\frac{d}{dt}\Gamma^{n_A,n_F}(t\mathrm{g}_i, t\mathrm{q}_i, \lambda(\mu), g(\mu), t\mu) = D\Gamma^{n_A,n_F}(t\mathrm{g}_i, t\mathrm{q}_i, \lambda(\mu), g(\mu), t\mu) \tag{1.34}$$

By expanding $\left(t\frac{d}{dt}\right)$ as $\left(t\frac{\partial}{\partial t} + \mu\frac{\partial}{\partial\mu}\right)$ we find that

$$\left(t\frac{\partial}{\partial t} + \mu\frac{\partial}{\partial\mu} + D\right)\Gamma^{n_A,n_F}(t\mathrm{g}_i, t\mathrm{q}_i, \lambda(\mu), g(\mu), \mu) = 0 \tag{1.35}$$

Using (1.31) to eliminate the derivative wrt. μ we find the following scaling relation

$$\begin{aligned} &\left(-t\frac{\partial}{\partial t} + \beta(g)\frac{\partial}{\partial g} - n_A\gamma_A(g) - n_F\gamma_F(g) + \delta(g)\frac{\partial}{\partial\lambda} + D\right) \\ &\cdot\Gamma^{n_A,n_F}(t\mathrm{g}_i, t\mathrm{q}_i, \lambda(\mu), g(\mu), \mu) = 0 \end{aligned} \tag{1.36}$$

The characteristic equations of this first order partial differential equation are given by:

$$t\frac{\partial \bar{g}}{\partial t} = \beta(\bar{g}(t)), \quad \bar{g}(t=1) = g, \tag{1.37}$$

$$t\frac{\partial \bar{\lambda}(t)}{\partial t} = \delta(\bar{\lambda}(t)), \quad \bar{\lambda}(t=1) = \lambda \tag{1.38}$$

and the solution to the differential equation (1.36) is

$$\begin{aligned}&\Gamma^{n_A,n_F}(t\mathrm{g}_i, t\mathrm{q}_i, \lambda(\mu), g(\mu), \mu)\\ &= t^D e^{-\int_{\bar{g}(0)}^{\bar{g}(1)} \mathrm{d}\tilde{g} \frac{n_A\gamma_A(\tilde{g})+n_F\gamma_F(\tilde{g})}{\beta(\tilde{g})}} \Gamma^{n_A,n_F}(\mathrm{g}_i, \mathrm{q}_i, \bar{\lambda}(t), \bar{g}(t), \mu).\end{aligned} \tag{1.39}$$

This gives the scaling of Γ with energy, and from (1.37) it follows that the energy (t) and μ dependence of the running coupling g are interchangeable.

1.3.3 The Running Coupling

Equation (1.39) expresses how we may find a Green's function at one energy scale by knowing it at another and just substituting the values of the gauge parameter and the coupling with the solutions to (1.37) and (1.38). In general, however, $\beta(\bar{g}), \gamma_F$ and γ_A can be calculated only perturbatively. Special attention is drawn to (1.37) since we may find the energy dependence of many dimensionless observables by just substituting the coupling with the solution to (1.37).

It has become customary to define a quantity α_s similar to the fine structure constant of QED

$$\alpha_s = \frac{g^2}{4\pi}, \tag{1.40}$$

and call this *the strong coupling constant* . The running of α_s is basically determined from the same β–function as that of g, since

$$gt\frac{\partial g}{\partial t} = \frac{1}{2}t\frac{\partial g^2}{\partial t} = 2\pi\frac{\partial \alpha_s}{\partial \ln t} = 2\pi\beta_{\alpha_s}(\alpha_s), \tag{1.41}$$

where $\beta_{\alpha_s}(\alpha_s)$ is traditionally called the *β–function of QCD*, which, as already mentioned, can only be calculated perturbatively. Unfortunately different conventions are used in defining the β–function. Often the notation

$$\beta(\alpha_s) = \frac{\partial \alpha_s}{\partial \ln t^2} = \frac{1}{2}\frac{\partial \alpha_s}{\partial \ln t} = \frac{1}{2}\beta_{\alpha_s}(\alpha_s) \tag{1.42}$$

is used, but as we see the β-functions differ only by a factor of 2. Different conventions for the definition of the β–function are used in different fields of study. To find $\beta(g), \gamma_A(g), \gamma_F(g)$ and $\delta(g)$ of (1.31) to a given order in α_s we would have to calculate all the Feynman diagrams that will contribute to the Green's function at the given order and apply (1.31) to each of the Green's functions. This will leave us with enough constraints to determine all the unknown functions.

However, perturbation theory suffers from a serious problem. The cancellation of the μ and generally RS dependence in the theory happens between different orders in the perturbative series, so when terminating the series at a certain order, we introduce a RS dependence to the theory. If we, as suggested above, demand that the Green's function of the theory to each order obey (1.31), the RS dependence will manifest itself as a dependence of e.g. $\beta_{\alpha_s}(\alpha_s)$ on the chosen RS.

It should come as no surprise that different renormalisation prescriptions will define different couplings, which can be related in perturbation theory. Consider for example the strong coupling constant in two different RS denoted by α_s and $\widetilde{\alpha}_s$:

$$\widetilde{\alpha}_s = \alpha_s \left(1 + \nu_1 \alpha_s + \nu_2 \alpha_s^2 + \cdots\right), \tag{1.43}$$

where ν_n can be calculated. Each coupling runs according to it's own β–function

$$\frac{\partial \alpha_s}{\partial \ln Q^2} = - \beta_0 \alpha_s^2 - \beta_1 \alpha_s^3 - \beta_2 \alpha_s^4 - \beta_3 \alpha_s^5 - \cdots \tag{1.44}$$

$$\frac{\partial \widetilde{\alpha}_s}{\partial \ln Q^2} = - \tilde{\beta}_0 \widetilde{\alpha}_s^2 - \tilde{\beta}_1 \widetilde{\alpha}_s^3 - \widetilde{\beta}_2 \widetilde{\alpha}_s{}^4 - \tilde{\beta}_3 \widetilde{\alpha}_s^5 - \cdots \tag{1.45}$$

It is not hard to show by inserting the expansion of (1.43) into (1.45) and comparing with (1.44) that *the first two β–function coefficients are universal*, and they are found to be

$$\beta_0 = \frac{1}{4\pi} \left(11 - 2/3 N_f\right), \quad \beta_1 = \frac{1}{16\pi^2} \left(102 - \frac{38}{3} N_f\right), \tag{1.46}$$

where N_f is the number of quark flavours included in the theory. β_2 and β_3 have been calculated in the $\overline{\mathrm{MS}}$-scheme and are given by [6] :

$$\begin{aligned}
\beta_2 =& \frac{1}{64\pi^3} \left(\frac{2857}{2} - \frac{5033}{18} N_f + \frac{325}{54} N_f^2 \right) \\
\beta_3 =& \frac{1}{256\pi^4} \left(\left(\frac{149753}{6} + 3564\zeta_3 \right) - \left(\frac{1078361}{162} + \frac{6508}{27}\zeta_3 \right) N_f \right. \\
&\left. + \left(\frac{50065}{162} + \frac{6472}{81}\zeta_3 \right) N_f^2 + \frac{1093}{729} N_f^3 \right)
\end{aligned} \tag{1.47}$$

where $\zeta_n = \zeta(n)$ is the Riemann ζ function.

1.4 Factorisation and Infrared Safety

It is now time for a discussion of the infrared divergences arising in the higher order corrections. We will start with a discussion of the infrared divergences of the NLO contribution to $e^+e^- \rightarrow$ hadrons and discuss how the divergences cancel once all the contributions to a physical observables are taken into account. Finally we will extend the discussion to divergences arising from radiation off QCD initial states, which are important for hadron collisions.

1.4.1 Infrared Singularities

As we saw in Section 1.4, the application of Feynman rules to higher orders corrections in the process $e^+e^- \to$ hadrons generates infrared divergences in the resulting integrals. These divergences can be studied by applying the same dimensional regularisation as used in the regularisation of the ultra violet divergences. However, for discussing the origin of these divergences, it proves more convenient to regularise them by introducing a small mass ν for the gluons[3] and m for the quarks. It then becomes clear that a class of divergences appear in the $\nu \to 0$ limit. This is the so-called *soft* divergences for $p^2 \to 0$ in Eq. (1.20). If the massless gauge field couples to itself or to another massless field like the quark it turns out that another class of divergences appear. This is called the *collinear* divergence because of the behaviour already pointed out in Section 1.3.1.

Although these infrared divergences arise in the loop integrals, it will turn out that they are canceled by other infrared divergences of opposite sign when the sum over all states contributing to a physical process is taken into account. If one considers the radiation of a real gluon (or photon) off the final state $q\bar{q}$ pair in the process $e^+e^- \to$ hadrons, then in the soft limit of vanishing energy of this gluon (or photon), the three particle final state is physically indistinguishable from the two particle $q\bar{q}$ final state. This real radiation is infrared divergent in the soft limit with a opposite sign and cancels the soft infrared divergence of the virtual vertex correction. For QED this is the so-called Bloch-Nordsieck theorem[7]. For QED with a non-vanishing electron mass, this guarantees the cancellation of all the infrared divergences when the sum over all relevant particle configurations is performed. One can even show that the cancellations occurs within classes of diagrams arising from considering different cuts to diagrams representing the square of the amplitude (see Ref.[3, p.344] for further details).

The situation for QCD is slightly more involved. This is because that even for non-vanishing quark masses, collinear divergences are generated from the gluon-splitting at higher orders (stemming from the triple and quartic gluon vertices). For $e^+e^- \to$ hadrons at NLO the structure of the infrared divergences is similar in QCD and QED final state radiation, since the triple and quartic gluon vertex does not yet enter. At higher orders though, even soft and collinear radiation of ghosts have to be taken into account when

[3] A simple Dirac mass term proportional to ν of the gauge field will break the gauge invariance of the QCD Lagrangian at the ν^2 level[3]. This is why the Higgs mechanism is necessary to give masses to the electro-weak gauge fields without breaking the gauge invariance.

considering which final states will contribute to a physical process. Despite all these complications, it has been possible to show that the total hadronic cross section in e^+e^- is infrared finite to all orders in perturbation theory in QCD[8, 9]. However, the more complicated structure of the infrared divergences results in a break down of the simpler Block-Nordsieck theorem (which applies only to soft divergences) for more complicated processes, for example at the NNLO order of quark-(anti-)quark scattering. Despite the complications of QCD infrared divergences, it is believed that the general Kinoshita-Lee-Naunberg theorem is valid for QCD perturbation theory – and to date no examples of a breakdown of the cancellation of all (soft and collinear) divergences have been found in QCD[3]. The Kinoshita-Lee-Naunberg theorem[10, 11] states that the transition rates of a massless theory are infrared finite when all soft and collinear degenerate final and initial states are summed over.

1.4.2 Infrared Safety

It should be apparent from the discussion in the previous section that care has to be taken when defining observables so that they are sufficiently inclusive to allow for the cancellation of infrared divergences between the virtual and real soft and collinear corrections at higher orders. This cancellation happens for total cross sections as mentioned in the previous section. If we consider e^+e^- collisions, most observables $\mathcal{I}$ can (within the perturbative framework) be written on the following form in terms of (fixed energy) $e^+e^- \to n$–particle parton cross sections σ_n and functions $\mathcal{S}_n$ (see Ref. [12])

$$\begin{aligned}
\mathcal{I} &= \frac{1}{2}\int \mathrm{d}\Omega_2 \frac{\mathrm{d}\sigma_2}{\mathrm{d}\Omega_2}\mathcal{S}_2(p_1^\mu, p_2^\nu) \\
&+ \frac{1}{3!}\int \mathrm{d}\Omega_2 \mathrm{d}E_3 \mathrm{d}\Omega_3 \frac{\mathrm{d}\sigma_3}{\mathrm{d}\Omega_2 \mathrm{d}E_3 \mathrm{d}\Omega_3}\mathcal{S}_3(p_1^\mu, p_2^\nu, p_3^\kappa) \\
&+ \frac{1}{4!}\int \mathrm{d}\Omega_2 \mathrm{d}E_3 \mathrm{d}\Omega_3 \mathrm{d}E_4 \mathrm{d}\Omega_4 \frac{\mathrm{d}\sigma_4}{\mathrm{d}\Omega_2 \mathrm{d}E_3 \mathrm{d}\Omega_3 \mathrm{d}E_4 \mathrm{d}\Omega_4}\mathcal{S}_4(p_1^\mu, p_2^\nu, p_3^\kappa, p_4^\lambda) \\
&+ \cdots
\end{aligned} \tag{1.48}$$

Examples of observables that can be written on this form is obviously the total hadronic cross section (with all the $\mathcal{S}_n = 1$), the n–jet cross sections and the thrust event–shape variable[12]. The cancellations of infrared divergences between the real and virtual corrections of the total hadronic cross section then implies that the observable $\mathcal{I}$ will be free of infrared divergences if (assuming that the functions $\mathcal{S}_n$ are symmetric under permutations of the arguments)

$$\mathcal{S}_n(p_1^\mu, \ldots, p_n^\nu) = \mathcal{S}_{n+1}(p_1^\mu, \ldots, (1-\lambda)p_n^\nu, \lambda p_n^\nu) \tag{1.49}$$

for $0 \leq \lambda \leq 1$. In words this means that the functions $\mathcal{S}_n$ should be insensitive to the emission of a soft or collinear particle and should not distinguish between the final state with two collinear particles and the state where these two are replaced by one carrying the total momentum of the two collinear ones. This is completely similar to the conditions under which the total cross sections are infrared finite.

Some observables, like the total dijet rate in hadronic collisions, even though infrared *finite* will still be *sensitive* to some infra red regulator, like the minimum transverse momentum of the dijet sample.

1.4.3 Factorisation and Parton Density Functions

The parton model first introduced to describe data on deep inelastic electron–proton scattering relies on one of the fundamental characteristics in the interplay between confinement and the perturbative regime of QCD called *factorisation.* This describes how the inelastic scattering can be described heuristically by a hard scattering between a constituent of the proton (called a parton) and an electron times the probability of finding this parton within the proton. This property is a consequence of the quantum mechanical incoherence between the long time–scale infrared properties of confinement and the short time–scale properties of a hard scattering. Using this formalism, all the infrared sensitivity involved in the (short term) "deconfinement" of a parton to take part in the hard scattering is factorised into process independent, hadron dependent *parton density functions* (pdfs), and all the process dependent pieces enter in the hard scattering matrix elements. The canonical example is the DIS structure function F_2 which is now calculable as[12]

$$F_2^{Vh}(x,Q^2) = \sum_{f,\bar{f},G} \int_0^1 \mathrm{d}\xi \; C_2^{Vi}\left(x/\xi, Q^2/\mu^2, \mu_f^2/\mu^2, \alpha_s(\mu^2)\right) \phi_{i/h}(\xi, \mu_f^2, \mu^2). \tag{1.50}$$

Here V describes which vector boson is exchanged (e.g. photon or W), and h denotes which hadron is being probed, while i is the parton index. C_2^{Vi} describes the perturbative hard scattering between the vector boson V and a parton of flavour i, and it is independent of the specific hadron involved. The function $\phi_{i/h}(\xi,\mu_f^2,\mu^2)$ is the process-independent parton density function which depends on the parton momentum fraction in the hadron ξ (also called the *Bjorken x-variable*), the renormalisation scale μ and the *factorisation scale* μ_f. μ_f discriminates between the soft physics of ϕ and the hard physics of the perturbative coefficient C. The observables should of course be independent of this arbitrary parameter (just as for the renormalisation scale μ), and this constraint allows the evolution of the parton density functions to be calculated perturbatively, even though they themselves cannot be calculated from first principles. One can think of this evolution in μ_f as the result of resolving the perturbative structure of partons with increasing μ_f. The gluon resolved at $\mu_{f,1}$ might have split into a quark–anti–quark pair at a $\mu_{f,2} \geq \mu_{f,1}$. The evolution of the pdfs is described by the famous DGLAP–equation and illustrated by the variation in shape with μ_f for selected parton distributions of the proton plotted in Figure 1.3. In these figures the gluon distribution has been divided by 10 to fit on the same plot.

The most remarkable property of the parton density functions measured in DIS is that not only are they universal within the class of observables in electron–proton collisions, but the very same pdfs are applicable also for the calculation of observables in hadron–hadron collisions. This relies on the fact that the soft confining colour field of the two protons do not interact on the time scale of the hard perturbative interaction. This means that e.g. the (leading–twist contribution to the) total cross section for a hard interaction in a proton–proton collision factorises into the following form[12] (setting $\mu_f = \mu$)

$$\sigma = \sum_{a,b} \int \cdots \int_0^1 \mathrm{d}\xi_a \int_0^1 \mathrm{d}\xi_b \, \phi_{a/P}(\xi_a, \mu^2) |\mathcal{M}_{ab}|^2 \left(x_a/\xi_a, x_b/\xi_b, \ldots, \mu/Q, \alpha_s(\mu)\right) \phi_{b/P}(\xi_b, \mu^2). \tag{1.51}$$

Here the dots symbolise the variables necessary to fully specify the four momenta of the particles of the process in question.

1.5 Dijet Production at Hadron Colliders

At hadron colliders, the production of two perturbative jets is the simplest exclusively QCD process to be studied. This process will in later chapters be utilised to study the properties of the gluon exchange in certain limits of the momentum transfer.

Since the two incoming partons (extracted from the colliding hadrons) in general will not have equal and opposite momenta, it proves convenient to use boost-invariant variables to describe the two-particle scattering. Neglecting any transverse momentum of the incoming partons[4], the two outgoing partons emerging from the scattering will be back to back in the azimuthal plane and have transverse momentum of equal size. Their momenta along the beam axis will depend on the momenta of the incoming partons, and so to describe the longitudinal motion we will use the variable *rapidity* (y) defined for a particle with energy E and longitudinal momentum p_z by

$$y = \frac{1}{2} \ln \left(\frac{E + p_z}{E - p_z} \right). \tag{1.52}$$

The rapidity variable is convenient since rapidity differences are invariant under boosts (along the z-axis). To describe a $2 \to 2$ particle scattering $(p_1, p_2) \to (p_3, p_4)$ it is conve-

[4]The transverse momenta of partons inside a proton is neglected in the normal sets of pdfs, but the transverse momentum distribution of especially gluons is currently being studied using so-called "unintegrated gluon distribution functions".

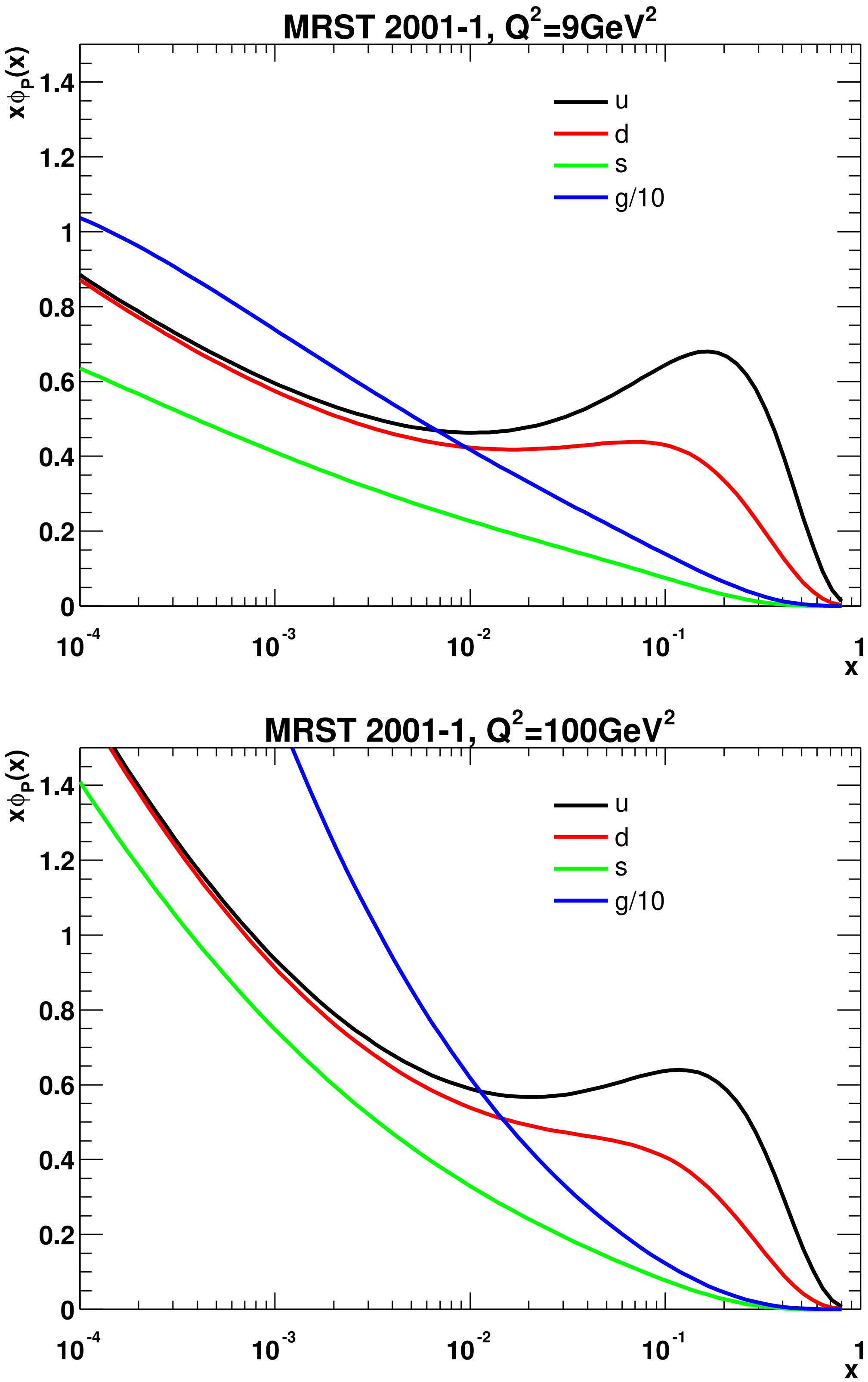

Figure 1.3: MRST pdfs of the proton at $\mu_f^2 = Q^2 = 9$ GeV^2 and $\mu_f^2 = Q^2 = 100$ GeV^2.

nient to use also the *Mandelstam variables* defined by

$$\begin{aligned}\hat{s} &\equiv (p_1+p_2)^2 \\ \hat{t} &\equiv (p_1-p_3)^2 = -\frac{1}{2}\hat{s}(1-\cos\theta) \\ \hat{u} &\equiv (p_2-p_3)^2 = -\frac{1}{2}\hat{s}(1+\cos\theta)\end{aligned} \tag{1.53}$$

where we have used the hat to signify that it is the parton–parton scattering rather than the hadron–hadron one that is being considered. Also given is the value of $\hat{t}$ and $\hat{u}$ for a scattering at the square of the energy $\hat{s}$ and a centre of mass scattering angle θ. Using Eq. (1.9) expressed in terms of the Mandelstam variables, we find for the $2 \to 2$ parton scattering

$$\frac{E_3 E_4 \mathrm{d}^6\sigma}{\mathrm{d}^3 p_3 \mathrm{d}^3 p_4} = \frac{1}{2\hat{s}}\frac{1}{16\pi^2}\overline{\sum}|\mathcal{M}|^2\delta^4(p_1+p_2-p_3-p_4), \tag{1.54}$$

where $\overline{\sum}$ symbolises the standard spin and colour average (sum) over the initial (final) state partons. All the different parton processes that contribute to dijet production at lowest order can be calculated from the diagrams in Fig. 1.4 by use of standard tricks like *crossing*, although the colour and spin sum and averaging complicates the relations between the diagrams slightly. By use of the factorisation theorem (Eq. (1.51)) the differential dijet cross section can be written as

$$\frac{\mathrm{d}^3\sigma}{\mathrm{d}y_3\mathrm{d}y_4\mathrm{d}p_\perp^2} = \frac{1}{16\pi s^2}\sum_{a,b,k,l=q,\bar{q},g}\frac{\phi_a(x_a,\mu^2)}{x_a}\frac{\phi_b(x_b,\mu^2)}{x_b}\overline{\sum}|\mathcal{M}_{ab\to kl}|^2\frac{1}{1+\delta_{kl}}, \tag{1.55}$$

where s is the hadronic center of mass energy, $\hat{s} = x_a x_b s$, and we have used the property

$$\frac{\mathrm{d}p_z}{\mathrm{d}y} = E. \tag{1.56}$$

The Kronecker delta δ_{kl} takes care of avoiding double counting of identical final state particles. The parton momentum fractions x_a, x_b are calculated through energy and momentum conservation to be

$$x_a = \frac{p_\perp}{\sqrt{s}}(\exp(y_3)+\exp(y_4)) \qquad x_b = \frac{p_\perp}{\sqrt{s}}(\exp(-y_3)+\exp(-y_4)). \tag{1.57}$$

The square of the colour and spin averaged and summed matrix element for the different processes contributing to dijet production (obtained by applying the Feynman rules to the diagrams in Fig. 1.4) is listed in Table 1.2 (taken from Ref.[2]), where q and q' denotes quarks of different flavour. Also listed is the value of the matrix element squared for a scattering angle of $\pi/2$. The gluon scattering sub-process dominates because of the bigger colour charge of the gluons compared to quarks.

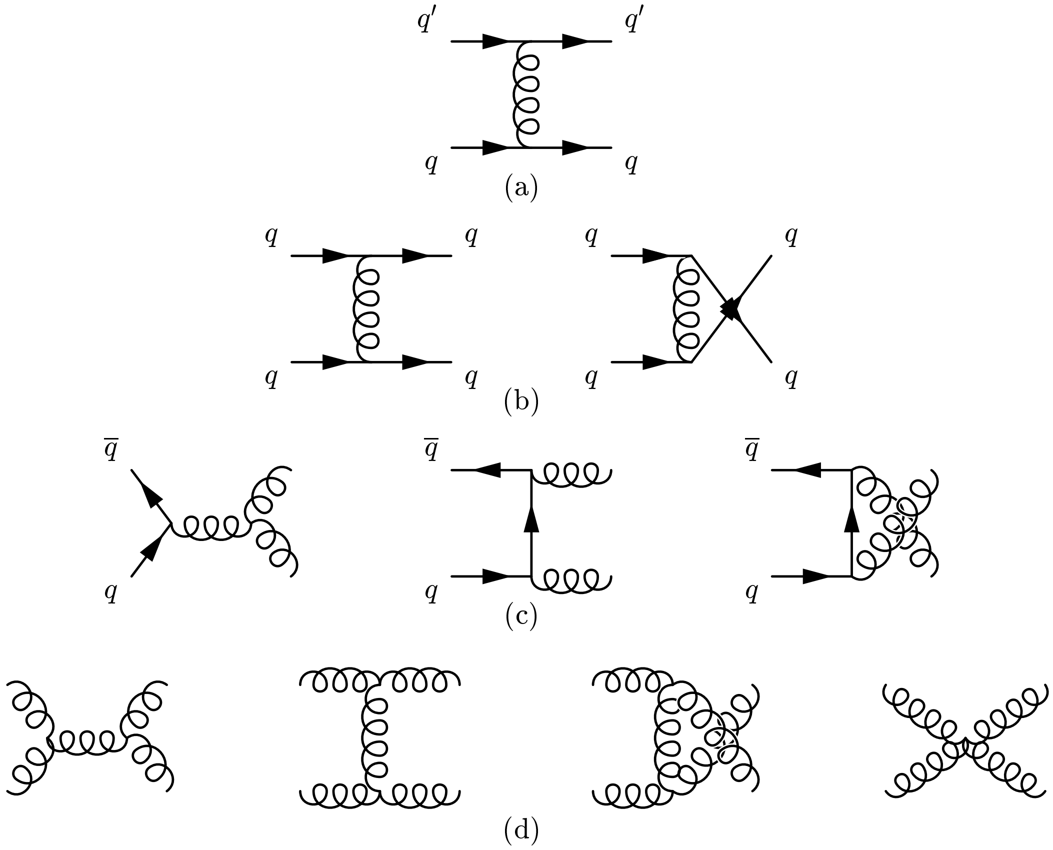

Figure 1.4: The diagrams needed for the calculation of the lowest order contribution to dijet production at hadron colliders.

1.5.1 Limiting Behaviour of the Partonic Cross Section

The dependence on the scattering angle of the different contributions to dijet production turn out to have a very interesting feature. The dominant subprocesses have a very similar dependence on the scattering angle. This is shown in Fig. 1.5, where the ratio of the quark–anti-quark and quark–gluon to the gluon–gluon scattering cross section is shown as a function of the absolute value of the cosine of the centre of mass scattering angle. When considering jets at the leading order level, the quark, anti–quark and gluon jets are indistinguishable, so when studying dijet cross sections, the scattering angle is only defined modulo $\pi/2$. This means that in the plot, the numerator is the sum of the contributions from $\cos(\theta)$ and $-\cos(\theta)$, whereas the denominator already has been symmetrised since the final states particles are identical. The observation that the ratios are almost constant (at the values $4/9$ and $(4/9)^2$, means that for every substitution of a gluon with a (anti-) quark, the partonic cross section is reduced by a factor $4/9 = C_F/C_A$, which is the relatively strength of the vertices) means that to a good approximation the total cross section can be obtained by rescaling just the gluon–gluon scattering cross section. This is called the *single effective subprocess approximation*[13], and within this approximation the total hadronic

Process	Number	Class	$\overline{\sum}\lvert\mathcal{M}\rvert^2/g^4$	$\theta=\pi/2$
$qq' \to qq'$	1	(a)	$\frac{4}{9}\frac{\hat{s}^2+\hat{u}^2}{\hat{t}^2}$	2.22
$q\overline{q'} \to q\overline{q'}$	2	(a)	$\frac{4}{9}\frac{\hat{s}^2+\hat{u}^2}{\hat{t}^2}$	2.22
$qq \to qq$	3	(b)	$\frac{4}{9}\left(\frac{\hat{s}^2+\hat{u}^2}{\hat{t}^2}+\frac{\hat{s}^2+\hat{t}^2}{\hat{u}^2}\right)-\frac{8}{27}\frac{\hat{s}^2}{\hat{t}\hat{u}}$	3.26
$q\overline{q} \to q'\overline{q'}$	4	(a)	$\frac{4}{9}\frac{\hat{t}^2+\hat{u}^2}{\hat{s}^2}$	0.22
$q\overline{q} \to q\overline{q}$	5	(b)	$\frac{4}{9}\left(\frac{\hat{s}^2+\hat{u}^2}{\hat{t}^2}+\frac{\hat{u}^2+\hat{t}^2}{\hat{s}^2}\right)-\frac{8}{27}\frac{\hat{u}^2}{\hat{t}\hat{s}}$	2.59
$q\overline{q} \to gg$	6	(c)	$\frac{32}{27}\frac{\hat{t}^2+\hat{u}^2}{\hat{t}\hat{u}}-\frac{8}{3}\frac{\hat{t}^2+\hat{u}^2}{\hat{s}^2}$	1.04
$gg \to q\overline{q}$	7	(c)	$\frac{1}{6}\frac{\hat{t}^2+\hat{u}^2}{\hat{t}\hat{u}}-\frac{3}{8}\frac{\hat{t}^2+\hat{u}^2}{\hat{s}^2}$	0.15
$gq \to gq$	8	(c)	$-\frac{4}{9}\frac{\hat{s}^2+\hat{u}^2}{\hat{s}\hat{u}}+\frac{\hat{u}^2+\hat{s}^2}{\hat{t}^2}$	6.11
$gg \to gg$	9	(d)	$\frac{9}{2}\left(3-\frac{\hat{t}\hat{u}}{\hat{s}^2}-\frac{\hat{s}\hat{u}}{\hat{t}^2}-\frac{\hat{s}\hat{t}}{\hat{u}^2}\right)$	30.4

Table 1.2: The square of the invariant matix element for the different processes contributing to dijet production. Also listed is the diagram class according to Fig. 1.4 that contribute to the specific cross section. Without spin and colour summation and averaging, the cross sections within one class would be obtained though simple crossing.

dijet cross section is obtained by convoluting the gluon–gluon scattering cross section with two copies of the *effective pdf* given by

$$S(x,\mu^2)=g(x,\mu^2)+\frac{4}{9}\sum_{f\in\text{flavours}}\left(q_f(x,\mu^2)+\overline{q}_f(x,\mu^2)\right). \tag{1.58}$$

where we have used $g(x,\mu^2)$ to denote $\phi_{g/P}(x,\mu^2)$ etc.

We would like to examine the behaviour of the cross sections in the limit of large rapidity difference between the two jets. In terms of the rapidity difference Δy between the two jets, the rapidity of the centre of mass (which is the mean rapidity since rapidity is additive) $\overline{y}$ and the transverse momentum square of the jets $k_\perp^2$, the Mandelstam variables

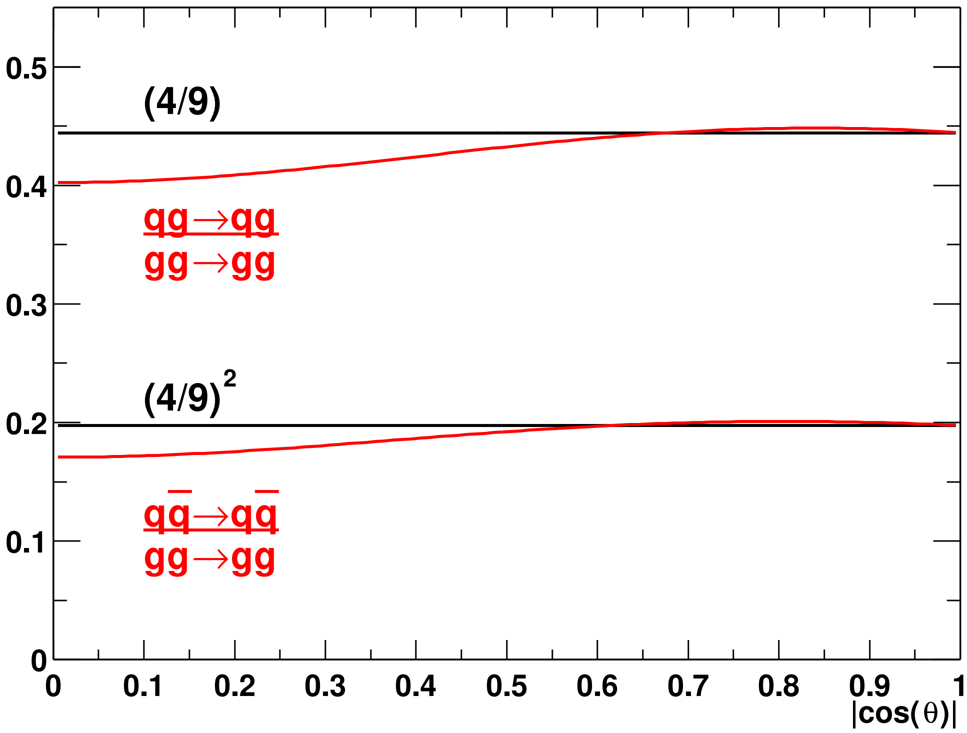

Figure 1.5: The quark–anti-quark and quark–gluon scattering normalised to the gluon–gluon matrix element squared as a function of the centre of mass scattering angle.

are given by

$$\begin{aligned} \hat{s} &= 4k_\perp^2 \cosh^2 \frac{\Delta y}{2} \\ \hat{t} &= -2k_\perp^2 \cosh \frac{\Delta y}{2} \exp\left(-\frac{\Delta y}{2}\right) \\ \hat{u} &= -2k_\perp^2 \cosh \frac{\Delta y}{2} \exp\left(\frac{\Delta y}{2}\right) \end{aligned} \tag{1.59}$$

where we see that the partonic subprocess is independent of $\overline{y}$, only the parton fluxes depend on this parameter through the parton momentum fractions x (1.57). In the large Δy limit, which will be the focus in much of the rest of the thesis, the Mandelstam variables become

$$\begin{aligned} \hat{s} &\approx -\hat{u} \approx k_\perp^2 \exp(\Delta y) \\ \hat{t} &\approx -k_\perp^2. \end{aligned} \tag{1.60}$$

We therefore find that in the large Δy limit

$$\Delta y \approx \ln\left(-\frac{\hat{s}}{\hat{t}}\right). \tag{1.61}$$

In fact, considering Eqs. (1.54) to (1.61) we see that the large Δy limit is equivalent to the high-energy (large $\hat{s}$) limit at fixed momentum transfer (fixed $\hat{t}$) (hereafter called *the HE limit*).

We can examine which processes contribute to dijet production in this limit by taking only the leading contribution in Δy according to Eq. (1.60) from the results of Tab. 1.2. For process number 9, the gluon–gluon scattering, we find

$$|\overline{\mathcal{M}}_{gg\to gg}|^2 \overset{\Delta y\to\infty}{=} \frac{9}{2} g^4 \frac{\hat{s}^2}{\hat{t}^2}. \tag{1.62}$$

One can trace back this behaviour to the diagrams of class (d) in Fig. 1.4 with a gluon exchange in the t channel, i.e. the second one. A calculation of this diagram retaining only terms to leading $\mathcal{O}(\hat{s}/\hat{t})$ and only physical polarisations of the external gluons, one obtains exactly the result of Eq. (1.62) (as we will see in Sec. 2.1) [14]. Whereas the contribution of specific diagrams to a cross section is obviously gauge dependent, Eq. (1.62) is the leading contribution to the full gluon–gluon scattering in the limit of large Δy. Examining the rest of the subprocess in Tab. 1.2 we find that the processes 4, 6, and 7 do not contribute with a leading term in $\hat{s}/\hat{t}$ to the total dijet cross section, whereas the result for the other processes is

$$\begin{aligned} |\mathcal{M}_{qq'\to qq'}|^2 &\overset{\Delta y\to\infty}{=} |\mathcal{M}_{qq\to qq}|^2 \overset{\Delta y\to\infty}{=} |\mathcal{M}_{q\bar{q}\to q\bar{q}}|^2 \overset{\Delta y\to\infty}{=} \frac{8}{9} g^4 \frac{\hat{s}^2}{\hat{t}^2} \\ |\mathcal{M}_{qg\to qg}|^2 &\overset{\Delta y\to\infty}{=} 2 g^4 \frac{\hat{s}^2}{\hat{t}^2}. \end{aligned} \tag{1.63}$$

These results are consistent with the observation that a gluon exchange in the t channel provides the leading contribution to scattering at large Δy. Of all the different subprocesses in dijet production, only those including a gluon exchange in the t channel have a term of dominant order in $\hat{s}/\hat{t}$.

Taking the ratios of the results in the large Δy limit in Eqs. (1.62) and (1.63) we regain the result of the single effective subprocess approximation

$$|\mathcal{M}_{gg\to gg}|^2 \overset{\Delta y\to\infty}{=} \frac{9}{4} |\mathcal{M}_{qg\to qg}|^2 \overset{\Delta y\to\infty}{=} \left(\frac{9}{4}\right)^2 |\mathcal{M}_{qq\to qq}|^2. \tag{1.64}$$

Chapter 2

Resummation of BFKL Logarithms

In this chapter (and in most of the rest of this thesis) we will consider certain higher order corrections to the gluon–gluon scattering which are logarithmically enhanced in the limit of large rapidity separation between the dijets studied in the previous chapter. The logarithmic enhancement of terms in the perturbative expansion is a general property of cross sections whenever more than one energy scale is involved in the process. A standard (massless) fixed–order perturbative calculation assumes that there is only one hard scale Q and that furthermore this is comparable to the hadron centre of mass energy $\sqrt{s} \approx Q$ (this last requirement is coming from the use of standard collinear factorisation). However, we saw in the last chapter that a large rapidity separation corresponds to the phase space region $\hat{s} \gg |\hat{t}|$ (see Eq. (1.61)). This is the so-called *semi–hard* region, where $\sqrt{s} \geq \sqrt{\hat{s}} \gg Q$, where Q is the scale of the momentum transfer. Of course Q still has to be big enough to accommodate a perturbative approach to the calculation. This means that the region of phase space where the resummation of the logarithmically enhanced terms is important is only accessible at the highest energy colliders at present (and even there only *maybe* so). Since $\hat{s} = x_a x_b s$ we can write

$$\ln \frac{s}{Q^2} = \ln \frac{1}{x_a} + \ln \frac{\hat{s}}{Q^2} + \ln \frac{1}{x_b} \tag{2.1}$$

This splitting up of the logarithm helps to illustrate that when $\sqrt{s} \gg Q$, large logarithms can arise from either the evolution of the pdfs ($\ln 1/x_a, \ln 1/x_b$) or from the hard scattering ($\ln \hat{s}/Q^2$). We will be concerned solely with logarithms of the last type, and for dijet production in the semi–hard region we can keep the parton momentum fractions relatively large to ensure that the normal pdfs are suitable to describe the processes. We will follow the presentation of Ref.[14] closely. A different introduction to the subject is available in

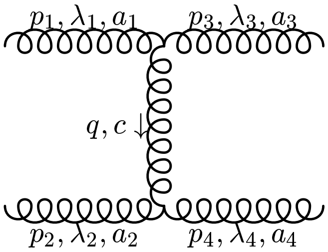

Figure 2.1: $gg \to gg$ scattering with a t–channel gluon exchange. The external gluons have been labeled with momentum, helicity and colour indicies.

Ref.[15] which also discusses the application of the resummation of the same logarithms to deep inelastic scattering.

2.1 A Further Look at Gluon Gluon Scattering

In this section we will explicitly calculate the $gg \to gg$ scattering in the limit of large rapidity separation and show that the result agrees with Eq. (1.62). Furthermore we will calculate the corrections at the next-to-leading order in this limit, consisting of $gg \to ggg$ real corrections and $gg \to gg$ with one loop. We will show that the higher order corrections are logarithmically enhanced and discuss how this generalises to all orders.

2.1.1 $gg \to gg$ at Leading Order

We will start by applying the Feynman rules using the notation from the diagram in Fig. 2.1. With p_1 ingoing and p_3, q outgoing, the upper triple–gluon vertex takes the form

$$g f^{a_1 a_3 c}((p_1+p_3)^\nu g^{\mu_1\mu_3} + (-p_3+q)^{\mu_1} g^{\mu_3\nu} + (-q-p_1)^{\mu_3} g^{\mu_1\nu}). \tag{2.2}$$

In the HE limit that we are considering, all the components of q are small compared to the components of p_1, p_3, so they can be dropped in sums. Furthermore, since the external gluons are on–shell, we can drop terms proportional to $p_1^{\mu_1}$ and $p_3^{\mu_3}$ since such terms contract with the polarisation vectors to give zero. Therefore, in the HE limit this upper vertex can be approximated by

$$2 g f^{a_1 a_3 c} g^{\mu_1\mu_3} p_1^\nu. \tag{2.3}$$

Using the equivalent form for the lower triple–gluon vertex and the relations

$$\frac{(p_1+p_3)^2}{2} = p_1 \cdot p_3 = \frac{\hat{s}}{2}, \quad \hat{t} = q^2, \tag{2.4}$$

one arrives at the following expressions for the matrix element

$$i\mathcal{M}^{a_1a_2a_3a_4}_{\lambda_1\lambda_2\lambda_3\lambda_4} = -2ig^2\frac{\hat{s}}{\hat{t}} f^{a_1a_3c} f^{a_2a_4c} g^{\mu_1\mu_3} g^{\mu_2\mu_4} \varepsilon^{\lambda_1}_{\mu_1}(p_1)\varepsilon^{*\lambda_3}_{\mu_3}(p_3)\varepsilon^{\lambda_2}_{\mu_2}(p_2)\varepsilon^{*\lambda_4}_{\mu_4}(p_4). \tag{2.5}$$

The square of the matrix element is now found by multiplying by the complex conjugate and using Eq. (1.7) repeatedly for the colour sums

$$f^{a_1a_3c}f^{a_1a_3c'}f^{a_2a_4c}f^{a_2a_4c'} = C_A^2\delta^{cc'}\delta^{cc'} = C_A^2(N_c^2-1). \tag{2.6}$$

To perform the sum over helicities we apply Eq. (1.13) where the vector n is chosen to be p_2 for the polarisation sum over p_1 and p_4 for the polarisation sum over p_3 etc. to always have an easy relation between the dot products and $\hat{s}$. Keeping only the leading term in $\hat{s}/\hat{t}$ and averaging over initial colour and helicity of the gluons we finally arrive at

$$|\overline{\mathcal{M}}_{gg\to gg}|^2 = \frac{9}{2}g^4\frac{\hat{s}^2}{\hat{t}^2} + \mathcal{O}(\hat{s}/\hat{t}), \tag{2.7}$$

in agreement with the result in Sec. 1.5.1, Eq. (1.62). The calculation here is obviously gauge-dependent, but only in sub-leading terms in $\hat{s}/\hat{t}$, as long as only physical polarisation of external gluons are considered (otherwise the diagrams with external ghosts would have to be included too), and as we have seen, including all the relevant diagrams to restore gauge invariance does not change the result in the HE limit.

We would now like to find a formula for the total cross section in the HE limit. Let us therefore first investigate the phase space in the large Δy limit. Using Eq. (1.9) and Eq. (1.56) we find for the 2–particle phase space

$$\mathrm{d}Q_2 = \int \frac{\mathrm{d}y_a \mathrm{d}^2\mathbf{k}_{a\perp}}{4\pi(2\pi)^2}\int \frac{\mathrm{d}y_b \mathrm{d}^2\mathbf{k}_{b\perp}}{4\pi(2\pi)^2}(2\pi)^4\delta^{(4)}\left(p_a+p_b-k_a-k_b\right), \tag{2.8}$$

where we have denoted the outgoing momenta of the gluon with the highest rapidity k_a and the lowest rapidity k_b.When studying the HE limit it is often beneficial to change coordinates to so-called *light-cone* coordinates given by

$$p^\pm = E \pm p_z, \tag{2.9}$$

and the transverse coordinates are left unchanged. The scalar product between two light-cone 4–vectors is $p\cdot q = (p^+q^- + p^-q^+)/2 - p_\perp\cdot q_\perp$. In this notation the only non-zero component of p_a is $p_a^+ = \sqrt{s}x_a$ and for p_b the only non-zero component is $p_b^- = \sqrt{s}x_b$, and the momenta for the outgoing particles are given by

$$k_i = (k_{i\perp}\exp(y_i), k_{i\perp}\exp(-y_i); \mathbf{k}_{i\perp}). \tag{2.10}$$

Using light-cone coordinates we can rewrite the integral over y_a, y_b and two of the δ-functionals of Eq. (2.8) as

$$\begin{aligned}&\int\frac{\mathrm{d}y_a}{4\pi}\int\frac{\mathrm{d}y_b}{4\pi}(2\pi)^2\delta(p_a^0+p_b^0-k_a^0-k_b^0)\delta(p_a^3+p_b^3-k_a^3-k_b^3)\\ =&2\int\frac{\mathrm{d}y_a}{4\pi}\int\frac{\mathrm{d}y_b}{4\pi}(2\pi)^2\delta(p_a^++p_b^+-k_a^+-k_b^+)\delta(p_a^-+p_b^--k_a^--k_b^-),\end{aligned} \tag{2.11}$$

where the factor two is coming from the Jacobian of the coordinate transformation. Using the HE approximation for the kinematics inside the δ–functionals we obtain

$$2\int\frac{\mathrm{d}y_a}{4\pi}\int\frac{\mathrm{d}y_b}{4\pi}(2\pi)^2\delta(p_a^+ + p_b^+ - k_a^+ - k_b^+)\delta(p_a^- + p_b^- - k_a^- - k_b^-)\approx\frac{1}{2\hat{s}}. \tag{2.12}$$

Using this in Eq. (2.8) we find

$$\begin{aligned}\mathrm{d}Q_2 &\approx \int\frac{\mathrm{d}^2\mathbf{k}_{a\perp}}{(2\pi)^2}\int\frac{\mathrm{d}^2\mathbf{k}_{b\perp}}{(2\pi)^2}\frac{1}{2\hat{s}}(2\pi)^2\delta^{(2)}\left(\mathbf{k}_{a\perp}+\mathbf{k}_{b\perp}\right)\\ &= \int\frac{\mathrm{d}^2\mathbf{k}_{a\perp}}{(2\pi)^2}\frac{1}{2\hat{s}} = \int\frac{\mathrm{d}k_{a\perp}^2}{4\pi}\frac{1}{2\hat{s}},\end{aligned} \tag{2.13}$$

where the last rewriting remains true, as long as the integrand is independent of the azimuthal angle. This is true for the HE limit of the $gg\to gg$ scattering, and therefore the differential $2\to 2$ gluon scattering cross section in the HE limit is given by

$$\frac{\mathrm{d}\hat{\sigma}_{gg\to gg}}{\mathrm{d}k_\perp^2}=\frac{|\overline{\mathcal{M}}_{gg\to gg}|^2}{16\pi\hat{s}^2}\approx\frac{9g^4}{32\pi\hat{t}^2}, \tag{2.14}$$

where we have used the flux factor $F=2\hat{s}$ as can easily be verified using Eq. (1.9). The total partonic cross section can be found by integrating Eq. (2.14) above some lower cut-off for the transverse momentum of the dijets.

2.1.2 $gg\to ggg$ in the Multi–Regge Limit

Before discussing the $2\to 3$ process in detail, we will introduce the variables we will use to describe a general $2\to n$ parton process and furthermore discuss the so–called *multi–Regge* kinematics. With the 4–momenta of the incoming particles given by

$$\begin{aligned}p_a &= (x_a\sqrt{s}/2, 0, 0, x_a\sqrt{s}/2)\\ p_b &= (x_b\sqrt{s}/2, 0, 0, -x_b\sqrt{s}/2)\end{aligned} \tag{2.15}$$

and the 4–momenta of the outgoing particles described in terms of their transverse momenta $\mathbf{k}_{i\perp}$ and rapidity y_i, we find using momenta conservation for the $2\to 2+n$ process

$$\begin{aligned}\mathbf{0} &= \sum_{i=0}^{n+1}\mathbf{k}_{i\perp}\\ x_a &= \sum_{i=0}^{n+1}\frac{k_{i\perp}}{\sqrt{s}}\exp(y_i)\\ x_b &= \sum_{i=0}^{n+1}\frac{k_{i\perp}}{\sqrt{s}}\exp(-y_i),\end{aligned} \tag{2.16}$$

where we have used $k_{i\perp}$ to denote the magnitude of the vector $\mathbf{k}_{i\perp}$. This is all just the straightforward generalisation of the situation for $2\to 2$ scattering in Eq. (1.57). We can furthermore define new Mandelstam variables $\hat{s}_{ij}$ by[14]

$$\begin{aligned}
\hat{s} &= x_a x_b s = \sum_{i,j=0}^{n+1} k_{i\perp} k_{j\perp} \exp(y_i - y_j) \\
\hat{s}_{ai} &= -2p_a \cdot k_i = -\sum_{j=0}^{n+1} k_{i\perp} k_{j\perp} \exp(y_j - y_i) \\
\hat{s}_{bi} &= -2p_b \cdot k_i = -\sum_{j=0}^{n+1} k_{j\perp} k_{i\perp} \exp(y_i - y_j) \\
\hat{s}_{ij} &= 2k_i \cdot k_j = 2k_{i\perp} k_{j\perp} \left(\cosh(y_i - y_j) - \cos(\phi_i - \phi_j)\right),
\end{aligned} \tag{2.17}$$

where ϕ_i is the azimuthal angle of the ith particle. We note that the Mandelstam variables only depend on differences between particle rapidities and therefore are boost invariants.

The *multi-Regge* region of phase space is where the rapidity of the outgoing particles are ordered and the transverse momenta are similar in size

$$y_0 \gg y_1 \gg y_2 \gg \cdots \gg y_{n+1} \qquad k_{i\perp} \approx k_\perp. \tag{2.18}$$

It is in this region that certain higher order corrections are logarithmically enhanced and can be resummed. Dropping all subleading contributions, the Mandelstam variables of Eq. (2.17) become in this limit

$$\hat{s} \approx k_{0\perp} k_{n+1\perp} \exp(y_0 - y_{n+1}) \tag{2.19}$$

$$\hat{s}_{ai} \approx -k_{0\perp} k_{i\perp} \exp(y_0 - y_i) \tag{2.20}$$

$$\hat{s}_{bi} \approx -k_{i\perp} k_{n+1\perp} \exp(y_i - y_{n+1}) \tag{2.21}$$

$$\hat{s}_{ij} \approx k_{i\perp} k_{j\perp} \exp(|y_i - y_j|). \tag{2.22}$$

The 5 diagrams contributing to the leading term in $\hat{s}/\hat{t}$ are the ones with a t–channel gluon[14] and are depicted in Fig. 2.2. The upper and lower vertices can still be approximated by the HE limit of the triple–gluon vertex (Eq. (2.3)), and omitting the helicity labels for the external gluons we find that the amplitude for the first diagram is given by

$$\begin{aligned}
i\mathcal{A}^{a_a a_b a_0 a_1 a_2}_{\mu_a \mu_b \mu_0 \mu_1 \mu_2} \approx & \left(2igf^{a_a a_0 c_1} \frac{1}{\hat{t}_1} p_{a\nu_1}\right) \\
& \cdot g f^{c_1 c_2 a_1} \left((q_1 + q_2)^{\mu_1} g^{\nu_1 \nu_2} + (-q_2 + k_1)^{\nu_1} g^{\nu_2 \mu_1} + (-k_1 - q_1)^{\nu_2} g^{\nu_1 \mu_1}\right) \\
& \cdot \left(2igf^{a_b a_2 c_2} \frac{1}{\hat{t}_2} p_{b\nu_2}\right),
\end{aligned} \tag{2.23}$$

where we have defined

$$\hat{t}_i = q_i^2 \approx -q_{i\perp}^2, \tag{2.24}$$

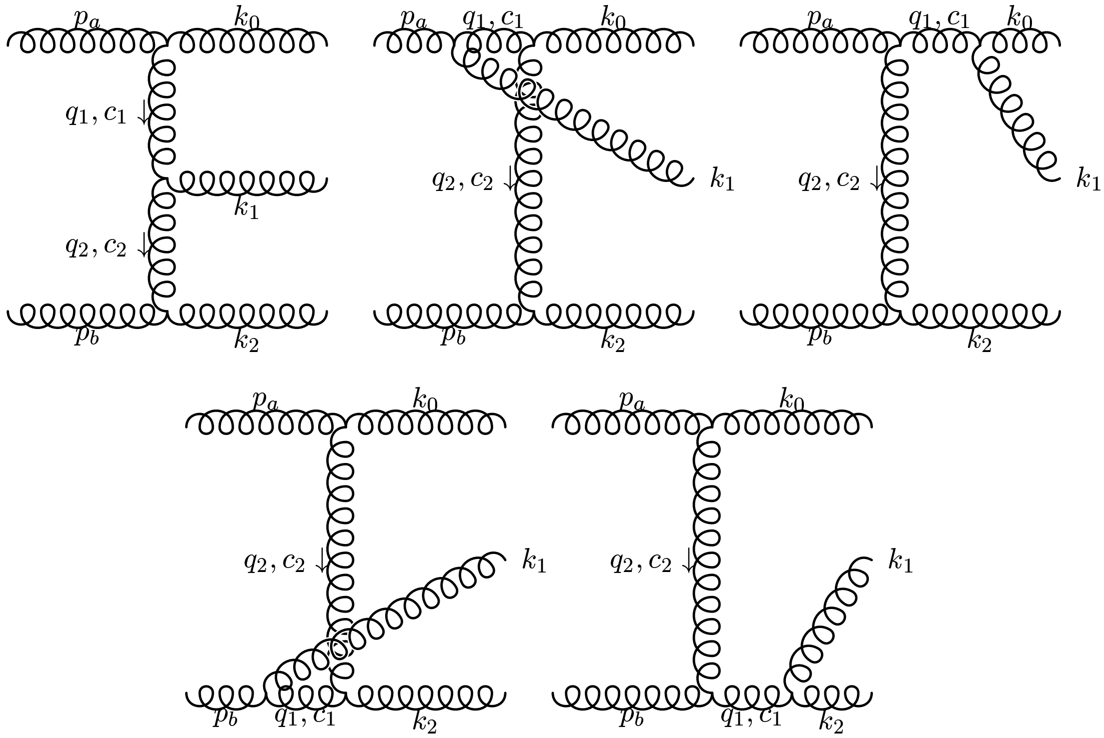

Figure 2.2: $gg \to ggg$ scattering through t–channel gluon exchange. The external gluons have been labeled only with momentum indicies, but colour and helicites will follow the same numbering.

where subleading terms have been dropped. This formula can be verified for e.q. q_1

$$q_1^2 = (p_a - k_0)^2 \approx q_{1\perp}^2, \tag{2.25}$$

which is obtained using Eq. (2.15). In Eq. (2.23) no approximation has yet been made to the $q_1 k_1 q_2$ three gluon vertex.

We now want to keep only the leading terms in $\hat{s}/\hat{t}$ of the contractions with the $q_1 k_1 q_2$–vertex. We first define

$$C_{\mathcal{A}}^{\mu_1} = \frac{2}{\hat{s}} p_{a\nu_1} \left((q_1 + q_2)^{\mu_1} g^{\nu_1\nu_2} + (-q_2 + k_1)^{\nu_1} g^{\nu_2\mu_1} + (-k_1 - q_1)^{\nu_2} g^{\nu_1\mu_1} \right) p_{b\nu_2}, \tag{2.26}$$

where apart from the contraction, we have also included one of the factors of two from Eq. (2.23) and divided by $\hat{s}$ (which of course will have to be multiplied into Eq. (2.23) when Eq. (2.26) is inserted). Rewriting Eq. (2.26) in terms of the Mandelstam invariants we find

$$C_{\mathcal{A}}^{\mu_1} = p_a^{\mu_1} \left(2\frac{\hat{s}_{b1}}{\hat{s}} + \frac{\hat{s}_{b2}}{\hat{s}} \right) - p_b^{\mu_1} \left(2\frac{\hat{s}_{a1}}{\hat{s}} + \frac{\hat{s}_{a0}}{\hat{s}} \right) + (q_1 + q_2)^{\mu_1}. \tag{2.27}$$

We now note that in the multi–Regge limit, $\hat{s}_{b1} \gg \hat{s}_{b2}$ and $\hat{s}_{a1} \gg \hat{s}_{a0}$, and the subleading terms will subsequently be dropped.

To proceed further we first decompose the metric tensor $g^{\mu\nu}$ as

$$g^{\mu\nu} = 2\frac{p_a^{\mu} p_b^{\nu} + p_a^{\nu} p_b^{\mu}}{\hat{s}} - \delta_{\perp}^{\mu\upsilon}, \tag{2.28}$$

where $\delta_\perp^{\mu v}$ is a Kronecker δ operating only on the "transverse" parts of a vector (i.e. it will form a dot-product of the x, y coordinates in the given frame with p_a, p_b along the z-axis). This decomposition can be derived using p_a, p_b in the form of Eq. (2.15) as a basis for polarisation vectors (see e.g. Ref. [14]). Using Eq. (2.28) we can rewrite $(q_1+q_2)^{\mu_1}$ as

$$(q_1+q_2)^{\mu_1} = (q_1+q_2)_\mu g^{\mu\mu_1} = p_b^{\mu_1}\left(\frac{\hat{s}_{a1}}{\hat{s}} + 2\frac{\hat{s}_{a0}}{\hat{s}}\right) - p_a^{\mu_1}\left(\frac{\hat{s}_{b1}}{\hat{s}} + 2\frac{\hat{s}_{b2}}{\hat{s}}\right) + (q_1+q_2)_\perp^{\mu_1}, \tag{2.29}$$

where $q_\perp^{\mu_1} = (0, \mathbf{q}_\perp, 0)$ such that $q_\perp^{\mu_1} q_{\perp\mu_1} = q_\perp \cdot q_\perp = -\mathbf{q}_\perp{}^2$. Dropping the subleading terms (actually, half of them cancel out) we find by substituting Eq. (2.29) into Eq. (2.27)

$$C_\mathcal{A}^{\mu_1} \approx p_a^{\mu_1}\frac{\hat{s}_{b1}}{\hat{s}} - p_b^{\mu_1}\frac{\hat{s}_{a1}}{\hat{s}} + (q_1+q_2)_\perp^{\mu_1}. \tag{2.30}$$

Putting it all into Eq. (2.23), we find that the contribution from the first diagram can be put in the form

$$\begin{aligned} i\mathcal{A}^{a_a a_b a_0 a_1 a_2}_{\mu_a\mu_b\mu_0\mu_1\mu_2} \approx 2i\hat{s}\left(igf^{a_a a_0 c_1} g_{\mu_a\mu_0}\right)&\frac{1}{\hat{t}_1} \\ \cdot\left(igf^{c_1c_2a_1} C_\mathcal{A}^{\mu_1}(q_1,q_2)\right)&\frac{1}{\hat{t}_2} \\ \cdot\left(igf^{a_b a_2 c_2} g_{\mu_b\mu_2}\right)&. \end{aligned} \tag{2.31}$$

This form resembles the form of the $gg \to gg$ matrix element of Eq. (2.23), with just the middle line added and the factors of $\hat{t}$ changed.

The calculation of the contribution to the matrix element for $gg \to ggg$ scattering in the HE limit from the rest of the diagrams in Fig. 2.2 follows along the same line. One finds (see e.g. Ref.[14]) that in the HE limit, the full $gg \to ggg$ amplitude can be written as

$$\begin{aligned} i\mathcal{M}^{a_a a_b a_0 a_1 a_2}_{\mu_a\mu_b\mu_0\mu_1\mu_2} \approx 2i\hat{s}\left(igf^{a_a a_0 c_1} g_{\mu_a\mu_0}\right)&\frac{1}{\hat{t}_1} \\ \cdot\left(igf^{c_1c_2a_1} C^{\mu_1}(q_1,q_2)\right)&\frac{1}{\hat{t}_2} \\ \cdot\left(igf^{a_b a_2 c_2} g_{\mu_b\mu_2}\right)&, \end{aligned} \tag{2.32}$$

where $C^{\mu_1}(q_1,q_2)$ is the so–called *Lipatov*–vertex, which sums up the contribution from an insertion of the third gluon either along the t–channel or as a bremsstrahlung gluon

$$C^{\mu_1}(q_1,q_2) = \left((q_1+q_2)_\perp^{\mu_1} + \left(\frac{\hat{s}_{b1}}{\hat{s}} + 2\frac{\hat{t}_1}{\hat{s}_{a1}}\right)p_a^{\mu_1} - \left(\frac{\hat{s}_{a1}}{\hat{s}} + 2\frac{\hat{t}_2}{\hat{s}_{b1}}\right)p_b^{\mu_1}\right). \tag{2.33}$$

The contribution proportional to $\hat{t}_1$ is from bremsstrahlung from the upper line, and $\hat{t}_2$ from the lower. The Lipatov vertex is non-local, but still gauge invariant (as can be verified by contracting it with Eq. $k_{1\mu_1}$).

By squaring the matrix element $\mathcal{M}$ of Eq. (2.32) and summing and averaging over helicities and colours (use FORM[16]) and noting that $\hat{s}_{a1}\hat{s}_{b1} = k_1^2\hat{s}$ when the approximate forms for the Mandelstam invariants (2.19)-(2.21) are used, we find

$$|\overline{\mathcal{M}}_{gg\to ggg}|^2 = \frac{16N_c^3g^6}{N_c^2-1}\frac{\hat{s}^2}{k_{0\perp}^2k_{1\perp}^2k_{2\perp}^2}. \tag{2.34}$$

This result can, not surprisingly, also be obtained by taking the HE limit of the full $gg \to ggg$ matrix element, just as for the $gg \to gg$ calculation. It is worth noting that the result has no collinear divergences. This is because that in the HE limit, all products of four–vectors of different particles are large.

We now want to show that the $gg \to ggg$ in the HE limit is logarithmically enhanced compared to the $gg \to gg$ cross section. In order to find the cross section for $gg \to ggg$ we need the three-particle phase space in the HE limit starting from the exact form

$$\mathrm{d}Q_3 = \int\frac{\mathrm{d}y_a\mathrm{d}^2\mathbf{k}_{a\perp}}{4\pi(2\pi)^2}\int\frac{\mathrm{d}y_b\mathrm{d}^2\mathbf{k}_{b\perp}}{4\pi(2\pi)^2}\int\frac{\mathrm{d}y_1\mathrm{d}^2\mathbf{k}_{1\perp}}{4\pi(2\pi)^2}(2\pi)^4\delta^{(4)}\left(p_a+p_b-k_a-k_1-k_b\right). \tag{2.35}$$

The arguments for the rewriting of the integrals over the phase space for particles a and b given in Sec. 2.1.1 still holds for the HE limit of the three particle phase space, and in the HE limit Eq. (2.35) can therefore be rewritten

$$\mathrm{d}Q_3 \approx \int\frac{\mathrm{d}^2\mathbf{k}_{a\perp}}{(2\pi)^2}\int\frac{\mathrm{d}^2\mathbf{k}_{b\perp}}{(2\pi)^2}\frac{1}{2\hat{s}}\int\frac{\mathrm{d}y_1\mathrm{d}^2\mathbf{k}_{1\perp}}{4\pi(2\pi)^2}(2\pi)^2\delta^{(2)}\left(\mathbf{k}_{a\perp}+\mathbf{k}_{1\perp}+\mathbf{k}_{b\perp}\right). \tag{2.36}$$

Using this and the flux factor $F = 2\hat{s}$ one readily finds[14]

$$\frac{\mathrm{d}\hat{\sigma}_{gg\to ggg}}{\mathrm{d}k_{a\perp}\mathrm{d}k_{b\perp}\mathrm{d}\phi} = \frac{N_c^3\alpha_s^3}{4\pi}\frac{\Delta y}{k_{a\perp}^2k_{b\perp}^2(k_{a\perp}^2+k_{b\perp}^2+2k_{a\perp}k_{b\perp}\cos\phi)}, \tag{2.37}$$

where ϕ is the azimuthal angle between the momenta of gluon a and b, and $\Delta y = y_a - y_b$ (the range for the integration of y_1). With $\Delta y \approx \ln(\hat{s}/|\hat{t}|)$ this shows that the $2 \to 3$ gluon scattering is logarithmically enhanced compared to the $2 \to 2$ process in the HE limit. Eq. (2.34) also shows that in this approximation the third gluon is emitted with equal probability in rapidity in the interval $y_b \le y_1 \le y_a$. Obviously, though, the multi-Regge kinematics is not a good approximation in all of this region.

2.1.3 $gg \to gg$ at NLO in the Multi-Regge limit

At the NLO of $gg \to gg$ scattering in the HE limit the virtual corrections are given by the diagrams in Fig. 2.3, corresponding to a t–channel gluon exchange in the physical s–region and u–region. One obtains for the sum of the two diagrams [14]

$$i\mathcal{M}^{aa_0ba_1}_{\mu_a\mu_b\mu_0\mu_1} \approx -2ig^2\frac{\hat{s}}{\hat{t}}f^{ada_0}f^{bda_1}g_{\mu_a\mu_0}g_{\mu_b\mu_1}\ln\frac{\hat{s}}{-\hat{t}}\alpha(\hat{t}). \tag{2.38}$$

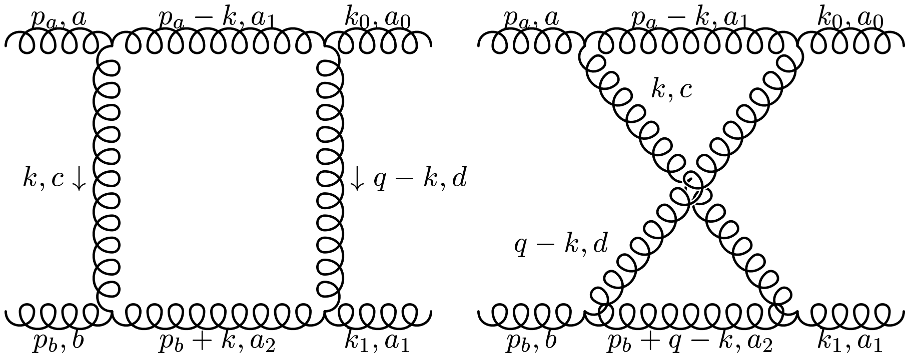

Figure 2.3: Diagrams contributing to virtual corrections to $gg \to gg$ at the NLO in the HE limit.

where

$$\begin{aligned}\alpha(\hat{t}) &= \alpha_s N_c \int \frac{\mathrm{d}^2\mathbf{k}_\perp}{(2\pi)^2} \frac{1}{k_\perp^2 (q-k)_\perp^2} \\ &\approx -\frac{\alpha_s N_c}{4\pi} \ln \frac{q_\perp^2}{\mu^2}\end{aligned} \tag{2.39}$$

and $\hat{t} = -q_\perp^2$. The remarkable feature of Eq. (2.38) is that only the colour octet piece of the interaction has a leading term in $\hat{s}/\hat{t}$, and the colour structure of the exchange is therefore the same as for the exchange of a single gluon calculated in Eq. (2.5). Among the diagrams giving a subleading contributions (and which have therefore been discarded) are the diagrams contributing to the gluon self–energy and the vertex–corrections that give rise to the running of the coupling. Therefore, in resuming only the leading contribution in $\hat{s}/\hat{t}$ we have kept the coupling fixed.

The integral in Eq. (2.39) is IR divergent and has been regularised by a simple cut–off μ^2. This IR divergence arises when the external gluons are taken on-shell, and can be rigorously regularised as was done in Ref. [17, 18]. It will turn out that the kernel of the integral equation describing the t–channel gluon exchange in the HE limit is IR safe and independent of the regularisation of Eq. (2.39).

2.2 The BFKL Equation

Comparing Eq. (2.38) and Eq. (2.5) we find that in the HE limit, the contribution from the virtual corrections included in Fig. 2.3 is logarithmically enhanced compared to the tree level contribution. In fact it turns out that the feature of the HE limit of the two–gluon exchange of the colour structure resembling that of a single gluon exchange carries through to all orders. This is the so–called *reggeisation* of the gluon. This furthermore implies that the sum of an infinite number of successive gluon exchanges in the t–channel can be obtained by simply replacing the $1/\hat{t}$ of the tree–level diagram with $1/\hat{t} \cdot (\alpha(\hat{t}) \ln \frac{\hat{s}}{|\hat{t}|})^n$

obtained from the exchange of $n+1$ gluons summed to all n, i.e.

$$\frac{1}{\hat{t}} \to \frac{1}{\hat{t}}\left(-\frac{\hat{s}}{\hat{t}}\right)^{\alpha(\hat{t})} \approx \frac{1}{\hat{t}} \exp\left(\alpha(\hat{t})\Delta y\right). \tag{2.40}$$

The tree–level amplitude in the HE limit for $2 \to n+2$ gluon scattering of Fig. 2.4 also generalises to the form already suggested by Eq. (2.32)

$$\begin{aligned} i\mathcal{M}^{a_a a_b a_0 a_1 \cdots a_{n+1}}_{\mu_a \mu_b \mu_0 \mu_1 \cdots \mu_{n+1}} \approx\ & 2i\hat{s}\left(igf^{a_a a_0 c_1} g_{\mu_a \mu_0}\right)\frac{1}{\hat{t}_1} \\ & \cdot \left(igf^{c_1 c_2 a_1} C^{\mu_1}(q_1,q_2)\right)\frac{1}{\hat{t}_2} \\ & \vdots \\ & \cdot \left(igf^{c_n c_{n+1} a_n} C^{\mu_n}(q_n,q_{n+1})\right)\frac{1}{\hat{t}_{n+1}} \\ & \cdot \left(igf^{a_b a_{n+1} c_{n+1}} g_{\mu_b \mu_{n+1}}\right), \end{aligned} \tag{2.41}$$

It is now conjectured that the reggeised gluon propagator taking into account the virtual corrections in the HE limit can be substituted into Eq. (2.41) by simply making the substitutions

$$\frac{1}{\hat{t}_i} \to \frac{1}{\hat{t}_i}\left(-\frac{\hat{s}_{i-1,i}}{\hat{t}_i}\right)^{\alpha(\hat{t}_i)} \approx \frac{1}{\hat{t}_i} \exp\left(\alpha(\hat{t})(y_{i-1}-y_i)\right)\right) \tag{2.42}$$

and thereby taking into account all the higher order contributions in the HE limit. The

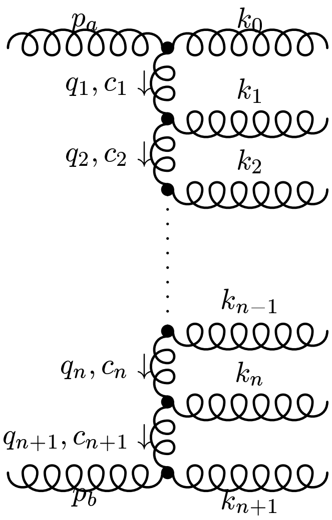

Figure 2.4: Multigluon emission amplitudes contributing to the HE limit. The dotted vertices denote the use of Lipatov effective vertices taking into account bremsstrahlung.

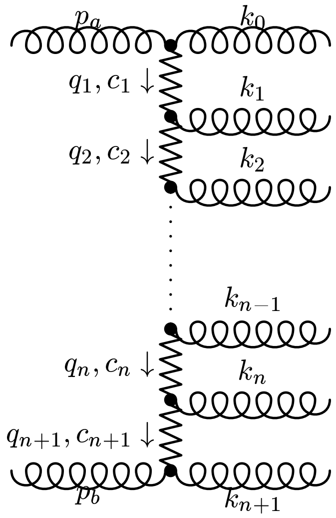

Figure 2.5: Multigluon emission amplitudes including the virtual corrections contributing to the HE limit. The dotted vertices denote the use of Lipatov effective vertices taking into account bremsstrahlung, and the zigzag lines denote the use of the reggeised gluons.

resulting amplitude is depicted in Fig. 2.5 and given by

$$\begin{aligned} i\mathcal{M}^{a_a a_b a_0 a_1 \cdots a_{n+1}}_{\mu_a \mu_b \mu_0 \mu_1 \cdots \mu_{n+1}} \approx\ & 2i\hat{s}\left(igf^{a_a a_0 c_1} g_{\mu_a \mu_0}\right) \frac{1}{\hat{t}_1} \exp\left(\alpha(\hat{t}_1)(y_0 - y_1)\right) \\ & \cdot \left(igf^{c_1 c_2 a_1} C^{\mu_1}(q_1, q_2)\right) \frac{1}{\hat{t}_2} \exp\left(\alpha(\hat{t}_2)(y_1 - y_2)\right) \\ & \vdots \\ & \cdot \left(igf^{c_n c_{n+1} a_n} C^{\mu_n}(q_n, q_{n+1})\right) \frac{1}{\hat{t}_{n+1}} \exp\left(\alpha(\hat{t}_{n+1})(y_n - y_{n+1})\right) \\ & \cdot \left(igf^{a_b a_{n+1} c_{n+1}} g_{\mu_b \mu_{n+1}}\right). \end{aligned} \tag{2.43}$$

This constitutes the resummation of the leading logarithms to the scattering amplitude for $2 \to (n+2)$ gluon scattering to all orders in α_s and its form was first proved in Ref.[18].

Looking at the form of Eq. (2.43) it should come as no surprise that the scattering cross section can be found as a solution to a recursive equation. In fact, in the HE limit the total cross section for $gg \to (n+2)g$ summed over $n \geq 0$ can be written in the form (from now on we use p_a, p_b to denote the momentum of the outgoing leading dijets)

$$\frac{\mathrm{d}\hat{\sigma}_{gg}(\Delta y)}{\mathrm{d}^2\mathbf{p}_{a\perp}\mathrm{d}^2\mathbf{p}_{b\perp}} \approx \left(\frac{C_A \alpha_s}{p^2_{a\perp}}\right) f(\mathbf{q}_{a\perp}, \mathbf{q}_{b\perp}, \Delta y) \left(\frac{C_A \alpha_s}{p^2_{b\perp}}\right), \tag{2.44}$$

where the terms in brackets are so–called *impact factors* and $f(\mathbf{q}_{a\perp}, \mathbf{q}_{b\perp}, \Delta y)$ is the solution to the *BFKL equation* to be discussed shortly, and $\mathbf{q}_{a\perp} = \mathbf{p}_{a\perp}, \mathbf{q}_{b\perp} = -\mathbf{p}_{b\perp}$. The impact factors are simply the square of the first and last terms in brackets in Eq. (2.43) including a factor of their respective $1/\hat{t}_i$. The leading order result for the asymptotic cross section is obtained by substituting a transverse momentum conserving delta functional for f, thereby requiring the dijets to be back to back.

The recursive relation for f can be found in the Laplace transformed variable for Δy (a trick performed to disentangle the nested integrations over the rapidities of the intermediate gluons),

$$\tilde{f}(\mathbf{q}_{a\perp}, \mathbf{q}_{b\perp}, \omega) = \int_0^\infty \mathrm{d}\Delta y \, e^{-\omega \Delta y} f(\mathbf{q}_{a\perp}, \mathbf{q}_{b\perp}, \Delta y) \tag{2.45}$$

and is given by

$$\omega \, \tilde{f}(\mathbf{q}_{a\perp}, \mathbf{q}_{b\perp}, \omega) = \frac{1}{2} \, \delta^{(2)}(\mathbf{q}_{a\perp} - \mathbf{q}_{b\perp}) + \frac{\overline{\alpha}_s}{\pi} \int \frac{\mathrm{d}^2 \mathbf{k}_\perp}{\mathbf{k}_\perp^2} K(\mathbf{q}_{a\perp}, \mathbf{q}_{b\perp}, \mathbf{k}_\perp), \tag{2.46}$$

with

$$\overline{\alpha}_s = \frac{\alpha_s C_A}{\pi} \tag{2.47}$$

and where the kernel $K(\mathbf{q}_{a\perp}, \mathbf{q}_{b\perp}, \mathbf{k}_\perp)$ is given by

$$K(\mathbf{q}_{a\perp}, \mathbf{q}_{b\perp}, \mathbf{k}_\perp) = \tilde{f}(\mathbf{q}_{a\perp} + \mathbf{k}_\perp, \mathbf{q}_{b\perp}, \omega) - \frac{q_{a\perp}^2}{\mathbf{k}_\perp^2 + (\mathbf{q}_{a\perp} + \mathbf{k}_\perp)^2} \tilde{f}(\mathbf{q}_{a\perp}, \mathbf{q}_{b\perp}, \omega). \tag{2.48}$$

The virtual corrections enter through the factor ω on the left hand side of the recursive relation Eq. (2.46) and in the second term of the BFKL kernel. The first term of the BFKL kernel accounts for the real radiation. One notices that the BFKL equation is independent of the scale μ^2 used to regularise the divergent integral arising from the virtual corrections (Eq. (2.39)). The μ–dependence cancels in the construction of the BFKL equation, since μ–independent terms of the form $\alpha(\hat{t}_1) - \alpha(\hat{t}_i)$ arise in the iterative solutions, ultimately resulting in the ω–factor on the left hand side of the BFKL equation. Also, it is worth nothing that the BFKL equation is infrared finite in the sense that the kernel (Eq. (2.48)) vanishes as $\mathbf{k}_\perp \to \mathbf{0}$ i.e. the soft real and virtual corrections cancel.

It is possible to solve the BFKL equation analytically by writing $\tilde{f}(\mathbf{q}_{a\perp}, \mathbf{q}_{b\perp}, \omega)$ as a Fourier transform with respect to the azimuthal angle between $\mathbf{q}_{a\perp}$ and $\mathbf{q}_{b\perp}$ and the variable $\log(q_{a\perp}^2/q_{b\perp}^2)$, (see e.g. Ref.[19, 20]). Specifically, we rewrite

$$\tilde{f}(\mathbf{q}_{a\perp}, \mathbf{q}_{b\perp}, \omega) = \frac{1}{2\pi} \sum_n \exp(in\Delta\phi) \frac{1}{2\pi} \int_{-\infty}^{\infty} \mathrm{d}z \exp\left(-iz \log(q_{a\perp}^2/q_{b\perp}^2)\right) \tilde{f}_n(z, \omega). \tag{2.49}$$

By substituting this into the BFKL equation one finds [19, 21]

$$\omega \tilde{f}_n(z, \omega) = \frac{1}{\sqrt{q_{a\perp}^2 q_{b\perp}^2}} + \omega_0(n, z) \tilde{f}_n(z, \omega), \tag{2.50}$$

where

$$\omega_0(n, z) = \left(\frac{\alpha_s C_A}{\pi}\right) 2\chi_n(z), \tag{2.51}$$

are the eigenvalues of the BFKL equation with (obtained through some rewritings[14])

$$\chi_n(z) = \mathrm{Re}\left[\psi(1) - \psi\left(\frac{1+|n|}{2} + iz\right)\right]. \tag{2.52}$$

ψ is the logarithmic derivative of the gamma function. The inverse Laplace transform is given by

$$f(\mathbf{q}_{a\perp}, \mathbf{q}_{b\perp}, \Delta y) = \frac{1}{2\pi i}\int_{c-i\infty}^{c+i\infty} \mathrm{d}\omega e^{\omega \Delta y} \tilde{f}(\mathbf{q}_{a\perp}, \mathbf{q}_{b\perp}, \omega) \tag{2.53}$$

with c chosen so that all the singularities of $\tilde{f}(\mathbf{q}_{a\perp}, \mathbf{q}_{b\perp}, \omega)$ have a real part less than the real part of c. Applying this to Eq. (2.50) we find the solution to the BFKL equation

$$f(\mathbf{q}_{a\perp}, \mathbf{q}_{b\perp}, \Delta y) = \frac{1}{(2\pi)^2\sqrt{q_{a\perp}^2 q_{b\perp}^2}} \sum_{n=-\infty}^{\infty} e^{in\phi} \int_{-\infty}^{\infty} \mathrm{d}z \left(\frac{q_{b\perp}^2}{q_{a\perp}^2}\right)^{iz} e^{\omega_0(n,z)\Delta y}. \tag{2.54}$$

It is worth noticing that this way of solving the BFKL equation effectively has summed over the radiation of any numbers of gluons (the exponential is a power series in α_s) and integrated over the phase space of any radiated gluon. Also, one observes that the solution of Eq. (2.54) is symmetric under exchange of $\mathbf{q}_{a\perp}$ and $\mathbf{q}_{b\perp}$ as expected from physical principles. f is the Green's function for the evolution of a t–channel BFKL gluon exchange evolving the transverse momentum from $\mathbf{q}_{a\perp}$ to $\mathbf{q}_{b\perp}$. Described like this, it should be symmetric under the exchange of the two transverse momenta.

2.3 Dijet Production and BFKL

It is possible to push the analytic solution even further to find a closed expression for the full partonic dijet production of Eq. (2.44) including the full effects of the BFKL radiation. By inserting Eq. (2.54) into Eq. (2.44) and integrating $\mathbf{p}_{a\perp}$ and $\mathbf{p}_{b\perp}$ above some cut-off $p_{\perp\mathrm{min}}$ one finds[19]

$$\hat{\sigma}_{gg} = \frac{\alpha_s^2 C_A^2 \pi}{2p_{\perp\mathrm{min}}^2} \int_{-\pi}^{\pi} \mathrm{d}\phi \frac{1}{2\pi} \sum_{n=-\infty}^{\infty} e^{in\phi} \frac{1}{2\pi} \int_{-\infty}^{\infty} \mathrm{d}z \frac{1}{z^2+\frac{1}{4}} \exp\left(2\bar{\alpha}_s \chi_n(z) \Delta y\right). \tag{2.55}$$

Performing the integral over the azimuthal angle, only the contribution from $n = 0$ survives, and we find

$$\hat{\sigma}_{gg} = \frac{\alpha_s^2 C_A^2}{4p_{\perp\mathrm{min}}^2} \int_{-\infty}^{\infty} \mathrm{d}z \frac{1}{z^2+\frac{1}{4}} \exp\left(2\bar{\alpha}_s \chi_0(z) \Delta y\right). \tag{2.56}$$

This result for the dijet BFKL cross section as a function of the rapidity separation Δy is compared to the prediction in the HE limit of pure dijet production (2.14) in Fig. 2.6. Expanding $\chi_0(z)$ around the saddle point at $z = 0$ we find

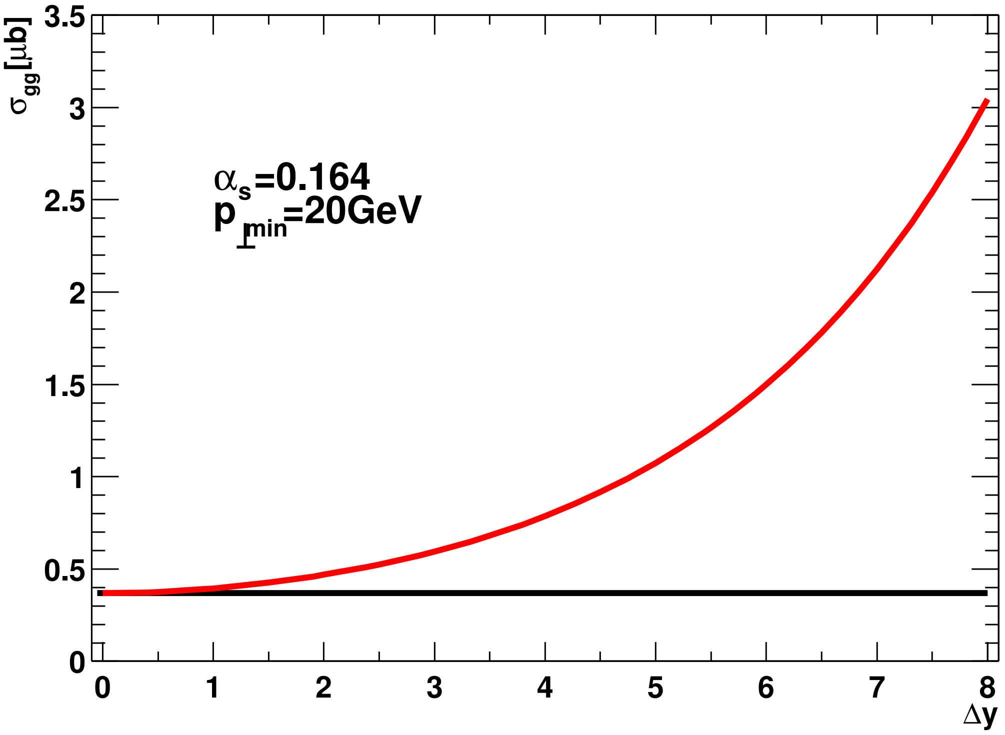

Figure 2.6: Partonic dijet cross section at fixed α_s for the HE limit of dijet production (2.14) (black) and for dijet production supplemented with BFKL evolution of the gluon exchanged in the t–channel (2.56) (red).

$$\chi_0(z) = 2\ln 2 - 7\zeta_3 z^2 + \cdots . \tag{2.57}$$

We can find the large Δy behaviour of the solution by approximating the exponential with the expansion around $z = 0$ and performing the integral to find

$$\hat{\sigma}_{gg} \overset{\Delta y \to \infty}{\to} \frac{4C_A^2 \alpha_s^2}{2p_{\perp \min}} \frac{\exp\left(4\ln 2\bar{\alpha}_s \Delta y\right)}{\sqrt{7\zeta_3 \pi \bar{\alpha}_s \Delta y/2}}. \tag{2.58}$$

Eq. (2.58) shows that asymptotically, at very large Δy, the cross section grows exponentially with Δy. Using the approximate forms of the Mandelstam variables (Eq. (2.19)) we find that this corresponds to a power–like growth with $\hat{s}$, which violates the Froissart unitarity bound (for two to two particle processes[22]) limiting the growth of the asymptotic total cross section to the square of the logarithm of $\hat{s}$. The parameter $\lambda = 4\ln 2\bar{\alpha}_s$ in the asymptotic exponential growth like $\exp(\lambda\Delta y)$ is often called the *BFKL intercept.*

2.4 Problems of the BFKL Solution

The exponential rise in the partonic cross section is one of the most dramatic predictions derived from the BFKL equation. However, as we will discuss in this section, it is not obvious that this seemingly bulletproof signature of BFKL is a precision observable, since an additional dependence on the rapidity separation is introduced into the hadronic cross section by including the parton density functions. Traditionally, when calculating BFKL predictions, the pdfs are estimated by their values at the leading approximations of the parton momentum fractions implicit in Eq. (2.19), and at a Q^2 similar to the lower bound on the transverse momentum of the dijets. The hadronic cross section for dijet production is therefore often written as (see e.g. Ref. [20])

$$\frac{\mathrm{d}\sigma}{\mathrm{d}^2\mathbf{p}_{a\perp}\mathrm{d}^2\mathbf{p}_{b\perp}\mathrm{d}y_a\mathrm{d}y_b} = x_a^0 S(x_a^0, p_{\perp\min}^2) x_b^0 S(x_b^0, p_{\perp\min}^2) \frac{\mathrm{d}\hat{\sigma}_{gg}(\Delta y)}{\mathrm{d}^2\mathbf{p}_{a\perp}\mathrm{d}^2\mathbf{p}_{b\perp}}, \tag{2.59}$$

with

$$x_a^0 = \frac{p_{a\perp}}{\sqrt{s}} e^{y_a}, \quad x_b^0 = \frac{p_{b\perp}}{\sqrt{s}} e^{-y_b}, \tag{2.60}$$

and $S(x, \mu^2)$ the effective pdf given by Eq. (1.58). While the leading logarithmic approximation might be valid for the hard scattering matrix element, it will only be valid for the pdfs as well if they are slowly varying in the relevant region of x. This is certainly not the case for BFKL searches in dijet production at present colliders, where medium to large values of x $(0.01 \leq x \leq 0.6)$ of the dominating gluon distribution are being probed (at large x, the gluon pdf is falling off approximately as $(1-x)^7$).

Recognising the problem of the pdf dependence, other observables have been suggested in the search for BFKL signatures. Among these is the average azimuthal angle between the two leading jets [19, 23]. It is the hope that most of the pdf dependence cancels in forming the average. With $C_n(t)$ given by by the last integral of Eq. (2.55)

$$C_n(t) = \frac{1}{2\pi} \int_{-\infty}^{\infty} \frac{\mathrm{d}z}{z^2 + \frac{1}{4}} \exp\left(2\bar{\alpha}_s \chi_n(z) \Delta y\right), \tag{2.61}$$

it is found[19, 24] that the average dijet azimuthal angle $\Delta\phi = |\phi_1 - \phi_2| - \pi$ is given by

$$\langle \cos \Delta\phi \rangle (\Delta y) = \frac{C_1(t)}{C_0(t)} \tag{2.62}$$

with $t = \bar{\alpha}_s \Delta y$. Based on this prediction it is seen that as $\Delta y \to \infty$ the dijets become completely uncorrelated in azimuthal angle, because of all the extra BFKL gluons being emitted. However, even if the pdf dependence would cancel to a large extend in forming this ratio, it is clear that as the edge of available phase space is approached when $\Delta y \to \infty$ (or rather $\Delta y \to 11$ for the LHC with a minimum transverse momentum of the dijets of

20 GeV), the amount of BFKL radiation will decrease (due to lack of phase space) and therefore the dijets should return to the LO back to back configuration. This feature will be completely missed if the Bjorken xs are evaluated using only the kinematics of the dijets and not including the full contribution from all the BFKL gluons. However, it is also clear that by the very nature of the fully inclusive solution of the partonic BFKL equation (2.54), the information on the number of BFKL gluons emitted and their respective momenta is lost. Therefore, with the analytic solution to the BFKL equation it is not possible to take into account the energy consumed by the BFKL gluons when it comes to evaluating the total centre of mass energy of the collision. In other words, using the analytic solution to the BFKL equation, the BFKL gluons are emitted at no cost in energy. Although the terms neglected are formally subleading, their numerical impact might be considerable at present day colliders.

2.5 Reformulation of the BFKL Solution

Summing up the discussion of the last few sections we remind the reader of the following facts of the analytic LL BFKL approach

1. The LL BFKL resummation is performed at fixed coupling constant, and thus any variation in the scale at which α_s is evaluated appears in the next-to-leading-logarithmic (NLL) terms.

2. Because of the strong rapidity ordering, any two-parton invariant mass is large. Thus there are no collinear divergences in the LL BFKL resummation; jets are determined only at LO and accordingly have a trivial structure.

3. Energy and longitudinal momentum are not conserved, and since the momentum fractions x of the incoming partons are reconstructed from the kinematic variables of the outgoing partons, the BFKL theory can severely and systematically underestimate the exact value of the x's, and thus grossly overestimate the parton luminosities.

In fact, if $n+2$ partons are produced, energy-momentum conservation gives

$$\begin{aligned} x_a =& \frac{p_{a\perp}}{\sqrt{s}} e^{y_a} + \frac{p_{b\perp}}{\sqrt{s}} e^{y_b} + \sum_{i=1}^{n} \frac{k_{i\perp}}{\sqrt{s}} e^{y_i} \\ x_b =& \frac{p_{a\perp}}{\sqrt{s}} e^{-y_a} + \frac{p_{b\perp}}{\sqrt{s}} e^{-y_b} + \sum_{i=1}^{n} \frac{k_{i\perp}}{\sqrt{s}} e^{-y_i} \end{aligned} \tag{2.63}$$

The momentum fractions in the high-energy limit (2.60) are recovered by imposing the strong rapidity ordering (2.18). However, the requirement $x_a, x_b \leq 1$ effectively imposes an upper limit on the transverse momentum integrals of the BFKL gluons, which has been neglected in the analytic solution of the BFKL equation.

In an attempt to go beyond the analytic leading-logarithm BFKL results, a Monte Carlo approach has been adopted [24, 25, 26]. The basic idea of the Monte Carlo BFKL model is to solve the BFKL equation while maintaining kinematic information on each radiated gluon. This is done by unfolding the integration over the rapidity-ordered BFKL gluon phase space and introducing a resolution scale μ to discriminate between resolved and unresolved radiation. The latter combines with virtual corrections to form an IR safe integral. Thus the solution to the BFKL equation is recast in terms of phase space integrals for resolved gluon emissions, with form factors representing the net effect of unresolved and virtual emissions. Besides addressing the first and last of points mentioned in the list above, the BFKL MC therefore also allows for the details of the final state to be investigated.

2.5.1 Solution for Fixed Coupling

By solving the BFKL equation (2.46) by iteration, which amounts to unfolding the summation over the intermediate radiated gluons and making their contributions explicit, it is possible to include the effects of both the running coupling and the overall kinematic constraints. It is also straightforward to implement the resulting iterated solution in an event generator.

The first step in this procedure is to separate the $\mathbf{k}_\perp$ integral in (2.46) into 'resolved' and 'unresolved' contributions, according to whether they lie above or below a small transverse energy scale μ. The scale μ is assumed to be small compared to the other relevant scales in the problem (the minimum transverse momentum $p_{\perp\min}$ for example). The virtual and unresolved contributions are then combined into a single, finite integral. The BFKL equation becomes

$$\begin{aligned}\omega\,\tilde{f}(\mathbf{q}_{a\perp},\mathbf{q}_{b\perp},\omega) &= \frac{1}{2}\,\delta^{(2)}(\mathbf{q}_{a\perp}-\mathbf{q}_{b\perp}) + \frac{\bar{\alpha}_s}{\pi}\int_{k_\perp^2>\mu^2}\frac{\mathrm{d}^2\mathbf{k}_\perp}{k_\perp^2}\,\tilde{f}(\mathbf{q}_{a\perp}+\mathbf{k}_\perp,\mathbf{q}_{b\perp},\omega)\\ &\quad + \frac{\bar{\alpha}_s}{\pi}\int\frac{\mathrm{d}^2\mathbf{k}_\perp}{k_\perp^2}\left[\tilde{f}(\mathbf{q}_{a\perp}+\mathbf{k}_\perp,\mathbf{q}_{b\perp},\omega)\,\theta(\mu^2-k_\perp^2) - \frac{q_{a\perp}^2\,\tilde{f}(\mathbf{q}_{a\perp},\mathbf{q}_{b\perp},\omega)}{k_\perp^2+(\mathbf{q}_{a\perp}+\mathbf{k}_\perp)^2}\right].\end{aligned} \tag{2.64}$$

This is just a rewriting of the integrals and is μ–independent. The combined unresolved/virtual integral can now be simplified by noting that since for the unresolved contribution $k_\perp^2 \ll q_{a\perp}^2, q_{b\perp}^2$ by construction, the $\mathbf{k}_\perp$ term in the argument of $\tilde{f}$ can be neglected, giving

$$
\begin{aligned}
&(\omega-\omega_0(\mathbf{q}_{a\perp}))\,\tilde{f}(\mathbf{q}_{a\perp},\mathbf{q}_{b\perp},\omega)\\
&=\frac{1}{2}\,\delta^{(2)}(\mathbf{q}_{a\perp}-\mathbf{q}_{b\perp})\;+\;\frac{\bar{\alpha}_s}{\pi}\int_{k_\perp^2>\mu^2}\frac{\mathrm{d}^2\mathbf{k}_\perp}{k_\perp^2}\,\tilde{f}(\mathbf{q}_{a\perp}+\mathbf{k}_\perp,\mathbf{q}_{b\perp},\omega)
\end{aligned}
\tag{2.65}
$$

where (see Appendix A).

$$
\omega_0(\mathbf{q}_{a\perp})=\frac{\bar{\alpha}_s}{\pi}\int\frac{\mathrm{d}^2\mathbf{k}_\perp}{k_\perp^2}\left[\theta(\mu^2-k_\perp^2)\;-\;\frac{q_{a\perp}^2}{\mathbf{k}_\perp^2+(\mathbf{q}_{a\perp}+\mathbf{k}_\perp)^2}\right]=\bar{\alpha}_s\,\ln\left(\frac{\mu^2}{q_{a\perp}^2}\right). \tag{2.66}
$$

Neglecting the $k_\perp$–dependence in the unresolved integral obviously introduces some μ–dependence into the solution. This, however, turns out to be very weak for reasonable choices of μ, and the μ–dependence of the final result can be checked by simply varying μ. The virtual and unresolved contributions are now contained in ω_0 and we are left with an integral over resolved real gluons. We can now solve (2.65) iteratively. Since f depends only on the rapidity separation, let us for simplicity assume that $y_a=\Delta y, y_b=0$. The solution for the general case can be obtained by simply shifting the rapidities after f has been calculated. By iterating (remembering that ω_0 depends on the first argument of f relevant in each step of the iteration) and performing the inverse transform we quickly find

$$
f(\mathbf{q}_{a\perp},\mathbf{q}_{b\perp},\Delta y)\;=\;\sum_{n=0}^{\infty}f^{(n)}(\mathbf{q}_{a\perp},\mathbf{q}_{b\perp},\Delta y)\,. \tag{2.67}
$$

where

$$
\begin{aligned}
f^{(0)}(\mathbf{q}_{a\perp},\mathbf{q}_{b\perp},\Delta y)&=\left[\frac{\mu^2}{q_{a\perp}^2}\right]^{\bar{\alpha}_s\Delta y}\;\frac{1}{2}\,\delta^{(2)}(\mathbf{q}_{a\perp}-\mathbf{q}_{b\perp})\,,\\
f^{(n\geq1)}(\mathbf{q}_{a\perp},\mathbf{q}_{b\perp},\Delta y)&=\left[\frac{\mu^2}{q_{a\perp}^2}\right]^{\bar{\alpha}_s\Delta y}\;\left\{\prod_{i=1}^{n}\int\mathrm{d}^2\mathbf{k}_{i\perp}\,\mathrm{d}y_i\,\mathcal{F}_i\right\}\;\frac{1}{2}\,\delta^{(2)}(\mathbf{q}_{a\perp}-\mathbf{q}_{b\perp}-\sum_{i=1}^{n}\mathbf{k}_{i\perp})\,,\\
\mathcal{F}_i&=\frac{\bar{\alpha}_s}{\pi k_{i\perp}^2}\,\theta(k_{i\perp}^2-\mu^2)\,\theta(y_{i-1}-y_i)\;\left[\frac{(\mathbf{q}_{a\perp}+\sum_{j=1}^{i-1}\mathbf{k}_{j\perp})^2}{(\mathbf{q}_{a\perp}+\sum_{j=1}^{i}\mathbf{k}_{j\perp})^2}\right]^{\bar{\alpha}_s y_i}.
\end{aligned}
\tag{2.68}
$$

The form of $f^{(n)}$ is found by performing the inverse transform of the m'th ($m>n$) iterative solution to Eq. (2.65) and picking out the n'th term. For example we find $f^{(0)}$ as

$$
\begin{aligned}
f^{(0)}(\mathbf{q}_{a\perp},\mathbf{q}_{b\perp},\Delta y)&=\frac{1}{2\pi i}\int_{c-i\infty}^{c+i\infty}\mathrm{d}\omega\,\exp(\omega\Delta y)\,\tilde{f}^{(0)}(\mathbf{q}_{a\perp},\mathbf{q}_{b\perp},\omega)\\
&=\frac{1}{2}\delta^{(2)}(\mathbf{q}_{a\perp}-\mathbf{q}_{b\perp})\mathrm{Res}\left(\frac{\exp(\omega\Delta y)}{\omega-\omega_0},\omega_0\right)\\
&=\frac{1}{2}\delta^{(2)}(\mathbf{q}_{a\perp}-\mathbf{q}_{b\perp})\left[\frac{\mu^2}{q_{a\perp}^2}\right]^{\alpha_s C_A\Delta y/\pi},
\end{aligned}
\tag{2.69}
$$

where $\mathrm{Re}(c) < \omega_0$, and $\mathrm{Res}(f(x), x_0)$ is the residue of f at x_0. Thus the solution to the BFKL equation is recast in terms of phase space integrals for resolved gluon emissions, with form factors representing the net effect of unresolved and virtual emissions. In this way, each $f^{(n)}$ depends on the resolution parameter μ, whereas the full sum f does not. Changing μ simply shifts parts of the cross section from one $f^{(n)}$ to another. We will present the result of the numerical evaluation of the integrals in Chapter 4. Here we will just mention that for a choice of $p_{\perp\mathrm{min}} = 20$ GeV, choosing $\mu = 1$ GeV will guarantee the result to be close to the $\mu \to 0$ GeV limit, and at the same time the number of resolved gluons to integrate over is kept manageable. Lowering μ will obviously increase the number of resolved gluons in the sum (2.67). The strong ordering of the rapidities for the gluons emitted along the BFKL chain is made explicit in Eq. (2.68) by the $\theta(y_{i-1}-y_i)$–functionals.

It is interesting to note that the leading order in α_s result of the HE limit with $f(\mathbf{q}_{a\perp}, \mathbf{q}_{b\perp}, \Delta y) = \frac{1}{2}\delta^{(2)}(\mathbf{q}_{a\perp} - \mathbf{q}_{b\perp})$ has been modified by a form factor

$$\left[\frac{\mu^2}{q_{a\perp}^2}\right]^{\bar{\alpha}_s \Delta y} \leq 1. \tag{2.70}$$

This is underlining the fact that the enhancement of the cross section found by including BFKL evolution of the t–channel gluon exchange requires gluons to be radiated and fill the rapidity interval separating the two leading dijets. Compared to the case of LO dijet production, the BFKL cross section with the extra requirement that no gluons are radiated between the dijets is reduced by the form factor of Eq. (2.70). This, as well as the corresponding form factors arising in the terms of multi–gluon emissions

$$\left[\frac{(\mathbf{q}_{a\perp} + \sum_{j=1}^{i-1} \mathbf{k}_{j\perp})^2}{(\mathbf{q}_{a\perp} + \sum_{j=1}^{i} \mathbf{k}_{j\perp})^2}\right]^{\bar{\alpha}_s y_i}, \tag{2.71}$$

is a consequence of the summation of unresolved gluon radiation in the relevant rapidity intervals. With the solution in the form of Eq. (2.68) it is easy to see that when $\Delta y \to 0$, the LO configuration is obtained with the jets back to back and the correct normalisation. But as soon as $\Delta y > 0$, the rapidity interval is filled with BFKL radiation, gradually reducing the azimuthal correlation between the leading dijets.

It is also worth noting that the symmetry between $\mathbf{q}_{a\perp}$ and $\mathbf{q}_{b\perp}$ apparently is broken in this new solution to the BFKL equation. However, this asymmetry is only apparent, and it can be tested by explicit numerical calculations that the final result is indeed symmetric in $\mathbf{q}_{a\perp}$ and $\mathbf{q}_{b\perp}$.

2.5.2 Solution for Running Coupling

The treatment in the last section is valid when the coupling α_s is kept fixed, as required by the LL formulation of BFKL. The running of the coupling enters in the NLL piece of the BFKL kernel, an area of active research over the past 10 years. It is found that the NLL contribution to the BFKL kernel can be split into a part from the running of the coupling, and a part from "genuine" NLL corrections. The effects of the running of the coupling are expected to be sizeable and possibly even dominate in the region of phase space relevant for dijet production. We can estimate the effects of introducing the running of the coupling into the BFKL kernel simply by moving the factors of α_s in the modified BFKL equation (2.64) inside the momentum integrals. Potentially this could lead to problems with the divergence of the coupling in the infrared region, and we will therefore have to regulate this behaviour. We will however later see that the dependence on the infrared behaviour of the coupling is very weak, as long as suitable cuts are placed on $\mathbf{q}_{a\perp}, \mathbf{q}_{b\perp}$. We will choose to introduce the lowest order running of the coupling since this is what will be introduced by the NLL terms of the BFKL equation. Therefore, the coupling evaluated at the scale $q_\perp^2$ is given by

$$\alpha_s(q_\perp^2) = \frac{1}{b\ln(q_\perp^2/\Lambda^2)}, \tag{2.72}$$

with $b = \beta_0$ of Eq. (1.46) ($N_f = 4$, and we will choose $\Lambda = 200\text{MeV}$). We will simply regulate the behaviour at $q_\perp^2 \to 0$ by freezing the value of α_s at some scale $Q_0 > \Lambda$

$$\alpha_s(q_\perp^2) = \begin{cases} \alpha_0 \equiv \alpha_s(Q_0^2) & \text{for} \quad q_\perp^2 \leq Q_0^2 \\ \alpha_s(q_\perp^2) & \text{for} \quad q_\perp^2 > Q_0^2 \end{cases} \tag{2.73}$$

In practice, we will often choose to freeze the evolution of the coupling below scales resulting in $\alpha_s(q_\perp^2) > 1$, so $\alpha_0 = 1$, but as already mentioned we will see that the results are insensitive to any reasonable choice.

Including the running of the coupling and splitting the integration region into a resolved and unresolved phase space, the BFKL equation becomes

$$\begin{aligned} \omega\,\tilde{f}(\mathbf{q}_{a\perp},\mathbf{q}_{b\perp},\omega) &= \frac{1}{2}\,\delta^{(2)}(\mathbf{q}_{a\perp}-\mathbf{q}_{b\perp}) + \int_{k_\perp^2>\mu^2} \frac{\mathrm{d}^2\mathbf{k}_\perp}{k_\perp^2}\,\frac{\alpha_s(k_\perp^2)C_A}{\pi^2}\tilde{f}(\mathbf{q}_{a\perp}+\mathbf{k}_\perp,\mathbf{q}_{b\perp},\omega) \\ &+ \int \frac{\mathrm{d}^2\mathbf{k}_\perp}{k_\perp^2}\,\frac{\alpha_s(k_\perp^2)C_A}{\pi^2}\left[\tilde{f}(\mathbf{q}_{a\perp}+\mathbf{k}_\perp,\mathbf{q}_{b\perp},\omega)\,\theta(\mu^2-k_\perp^2) - \frac{q_{a\perp}^2\,\tilde{f}(\mathbf{q}_{a\perp},\mathbf{q}_{b\perp},\omega)}{k_\perp^2+(\mathbf{q}_{a\perp}+\mathbf{k}_\perp)^2}\right]. \end{aligned} \tag{2.74}$$

Approximating again $f(\mathbf{q}_{a\perp}+\mathbf{k}_\perp,\mathbf{q}_{b\perp},\omega)$ by $f(\mathbf{q}_{a\perp},\mathbf{q}_{b\perp},\omega)$ in the last integral over the unresolved phase space we rewrite Eq. (2.74) as

$$\begin{aligned} (\omega-\omega_0(\mathbf{q}_{a\perp}))\,\tilde{f}(\mathbf{q}_{a\perp},\mathbf{q}_{b\perp},\omega) &= \frac{1}{2}\,\delta^{(2)}(\mathbf{q}_{a\perp}-\mathbf{q}_{b\perp}) \\ &+ \int_{k_\perp^2>\mu^2} \frac{\mathrm{d}^2\mathbf{k}_\perp}{k_\perp^2}\,\frac{\alpha_s(k_\perp^2)C_A}{\pi^2}\tilde{f}(\mathbf{q}_{a\perp}+\mathbf{k}_\perp,\mathbf{q}_{b\perp},\omega), \end{aligned} \tag{2.75}$$

where we have assumed $Q_0^2 < \mu^2$, and

$$\begin{aligned}\omega_0(\mathbf{q}_{a\perp}) &= \int \frac{\mathrm{d}^2\mathbf{k}_\perp}{k_\perp^2}\,\frac{\alpha_s(k_\perp^2)C_A}{\pi^2}\left[\theta(\mu^2-k_\perp^2)\; - \;\frac{q_{a\perp}^2}{\mathbf{k}_\perp^2+(\mathbf{q}_{a\perp}+\mathbf{k}_\perp)^2}\right]\\ &= \frac{C_A}{\pi b}\ln\left(\frac{\widetilde{\alpha}_s(\mathbf{q}_{a\perp}^2)}{\widetilde{\alpha}_s(\mu^2)}\right)\end{aligned} \tag{2.76}$$

with

$$\widetilde{\alpha}_s(\mathbf{q}_\perp^2) = \begin{cases} \alpha_0\left(\frac{Q_0^2}{q_\perp^2}\right)^{\alpha_0 b} & \text{for}\quad q_\perp^2 \le Q_0^2 \\ \alpha_s(q_\perp^2) & \text{for}\quad q_\perp^2 > Q_0^2 \end{cases}. \tag{2.77}$$

The problem is put in exactly the same form as in the previous case with a constant coupling, with just a different $\omega_0(\mathbf{q}_{a\perp})$ and therefore different form factors. Following the same path for finding the solution as for the constant coupling, we write the solution for f in the form

$$f(\mathbf{q}_{a\perp},\mathbf{q}_{b\perp},\Delta y) \;=\; \sum_{n=0}^{\infty} f^{(n)}(\mathbf{q}_{a\perp},\mathbf{q}_{b\perp},\Delta y)\;. \tag{2.78}$$

where now

$$f^{(0)}(\mathbf{q}_{a\perp},\mathbf{q}_{b\perp},\Delta y) = \left[\frac{\widetilde{\alpha}_s(q_{a\perp}^2)}{\widetilde{\alpha}_s(\mu^2)}\right]^{C_A\Delta y/(\pi b)}\frac{1}{2}\delta^{(2)}(\mathbf{q}_{a\perp}-\mathbf{q}_{b\perp}) \tag{2.79}$$

and

$$\begin{aligned}f^{(n\geq 1)}(\mathbf{q}_{a\perp},\mathbf{q}_{b\perp},\Delta y) &= \left[\frac{\widetilde{\alpha}_s(q_{a\perp}^2)}{\widetilde{\alpha}_s(\mu^2)}\right]^{C_A\Delta y/(\pi b)}\left\{\prod_{i=1}^{n}\int \mathrm{d}^2\mathbf{k}_{i\perp}\mathrm{d}y_i\mathcal{F}_i\right\}\\ &\quad\cdot\frac{1}{2}\delta^{(2)}(\mathbf{q}_{a\perp}-\mathbf{q}_{b\perp}-\sum_{i=1}^{n}\mathbf{k}_{i\perp})\\ \mathcal{F}_i &= \frac{\alpha_s(k_{i\perp}^2)C_A}{k_{i\perp}^2\pi^2}\theta(k_{i\perp}^2-\mu^2)\theta(y_{i-1}-y_i)\left[\frac{\widetilde{\alpha}_s((\mathbf{q}_{a\perp}+\sum_{j=1}^{i}\mathbf{k}_{j\perp})^2)}{\widetilde{\alpha}_s((\mathbf{q}_{a\perp}+\sum_{j=1}^{i-1}\mathbf{k}_{j\perp})^2)}\right]^{C_A y_i/(\pi b)}\end{aligned} \tag{2.80}$$

A consistent use of the running of the coupling would require the coupling also to run in the impact factors at either end of the chain. Without BFKL evolution of the t–channel gluon, running coupling effects in the impact factors would result in a LO HE prediction (for similar cuts) lying below the black line of Fig. 2.6, since α_s there has been evaluated at $p_{\perp\min}$. There is no immediate analytic result available in the literature to compare with the numerical solution of Eqs. (2.79)-(2.80), although some research into the introduction of a running coupling to the LL BFKL evolution has been undertaken (see e.g. Ref. [27, 28]).

Chapter 3

Monte Carlo Techniques

In this chapter we will discuss techniques for an efficient numerical evaluation of the integrals Eq. (2.67)-(2.68) and Eq. (2.79)-(2.80) arising from the rewriting of the BFKL equation by the introduction of a resolution scale. We will take a slightly sloppy definition of the term *efficient* to mean *fast* and *stable*. By *fast* we will generally mean that the numerical integration will require few evaluations of the integrand, while *stable* implies that the estimated numerical value of the integral converges to the correct result, and the estimated uncertainty of the numerical integral is reliable during the process of convergence.

We will start the discussion by a short review of integration of one–dimensional functions, which will serve as a background to the solution of the problem at hand, namely the numerical integration of multi–dimensional functions. Finding the solution for the BFKL evolution will typically require integration over a function depending on 24 to 60 variables (three for every BFKL gluon emitted in addition to what is needed for the LO process). It will turn out that many of the neat tricks for numerical integration of one–dimensional functions will not work in multiple dimensions, and we will therefore apply the technique of Monte Carlo integration, which, just as most other numerical integration algorithms, relies on the fact that the average value of a function is given by the integral over a domain divided by its area (or generally volume). The Monte Carlo procedure makes extensive use of the generation of (pseudo-) random numbers. Finally we will discuss how the numerical evaluation of multi–dimensional integrals can be parallelised to run on multiple computers simultaneously, thereby reducing the real time necessary to obtain a reliable estimate of an integral.

3.1 Numerical Integration in One Dimension

We will start the discussion of numerical integration by briefly reviewing some standard solutions to the problem of obtaining a numerical evaluation of the integral

$$I = \int_a^b \mathrm{d}x\, f(x). \tag{3.1}$$

Many of these are related in one way or another to the relation between the integral in Eq. (3.1) and the average value $\langle f(x)\rangle$ of f on the interval $[a,b]$

$$\langle f(x)\rangle_{x\in[a,b]} = \frac{\int_a^b \mathrm{d}x\, f(x)}{b-a}. \tag{3.2}$$

The first few standard methods for the numerical evaluation use equally spaced points for the evaluation of the integrand given by

$$x_n = a + (n-1)h, \quad n = 1,2,\ldots,N, \quad h = \frac{b-a}{N-1}, \tag{3.3}$$

We will also make use of the notation

$$f_n \equiv f(x_n). \tag{3.4}$$

Using all of this, the *Trapezoidal rule* for estimating the integral (3.1) reads (see e.g. Ref. [29])

$$I = h\left(\frac{1}{2}f_1 + \frac{1}{2}f_2\right) + \mathcal{O}(h^3 f''), \tag{3.5}$$

where f'' denotes the second derivate of f evaluated somewhere in the interval. As indicated by the behaviour of the remainder, this formula will integrate any first order polynomial (a straight line) exactly. Furthermore, this formula clearly displays the relation of Eq. (3.2). The equally well known *Simpson's rule*, evaluating f at three points in the interval, states

$$I = h\left(\frac{1}{3}f_1 + \frac{4}{3}f_2 + \frac{1}{3}f_3\right) + \mathcal{O}\left(h^5 f^{(4)}\right). \tag{3.6}$$

We see here that the three evaluation of the function are given different weights in the calculation of the average of the function. Simpson's rule will integrate any third order polynomial exactly.

Both the trapezoidal and Simpson's rule can be applied iteratively to subdivide the interval $[a,b]$. The result for the *composite trapezoidal rule* is

$$I = h\left(\frac{1}{2}f_1 + f_2 + f_3 + \cdots + f_{N-1} + \frac{1}{2}f_N\right) + \mathcal{O}\left(\frac{(b-a)^3 f''}{N^2}\right), \tag{3.7}$$

displaying explicitly the dependence of the error estimate on the number evaluations of the function. The *composite Simpsons rule* reads

$$I = h\left(\frac{1}{3}f_1 + \frac{4}{3}f_2 + \frac{2}{3}f_3 + \frac{4}{3}f_4 + \cdots + \frac{2}{3}f_{N-2} + \frac{4}{3}f_{N-1} + \frac{1}{3}f_N\right) + \mathcal{O}\left(N^{-4}\right), \tag{3.8}$$

where we have indicated the dependence of the error on N only. N here has to be a multiple of $6 = 3 \cdot 2$ since Eq. (3.8) is derived by applying Eq. (3.6) to non-overlapping pairs of subintervals of the interval $[a, b]$.

Much more sophisticated methods of numerical integrations exists; among other the *Gaussian quadratures* which will integrate exactly polynomials of remarkably high order for a given number of functional evaluations. In fact, the Gaussian quadratures can, for a given number of abscissas N, be tailored to integrate exactly any function consisting of the product of polynomials of order $2N-1$ and a function $W(x)$, which has to fulfill certain analyticity requirements. This very high degree of polynomials integrated exactly is obtained by a clever choice of the position of the abscissas and weights, based on finding the roots of a orthonormal set of polynomials with respect to the inner product

$$\langle f|g\rangle = \int_a^b \mathrm{d}x\, W(x) f(x) g(x). \tag{3.9}$$

For a given N, the integral is then estimated by

$$\int_a^b \mathrm{d}x\, W(x) f(x) \approx \sum_{j=1}^{N} w_j f(x_j), \tag{3.10}$$

where the error is a function of the $2N$'th derivative evaluated somewhere in the integration interval.

The last method we would like to introduce for evaluating integrals numerically may seem very crude compared to the methods already presented, but it will nevertheless prove superior in higher dimensions. The method is based on the simple formula Eq. (3.2) relating the average of the function in an interval $[a, b]$ to the integral over the same interval, and is called the *Monte Carlo* method. It simply consists of evaluating the function f at random points in the interval. As long as the distribution of random numbers in the interval is flat, the central limit theorem guarantees that the integral estimated in this way will converge to the right value

$$\int_a^b \mathrm{d}x\, f \approx l\langle f\rangle \pm l\sqrt{\frac{\langle f^2\rangle - \langle f\rangle^2}{N}} \tag{3.11}$$

with l the length of the interval, $l = (b-a)$, and

$$\langle f\rangle = \frac{1}{N}\sum_{i=1}^{N} f(x_i), \quad \langle f^2\rangle = \frac{1}{N}\sum_{i=1}^{N} f^2(x_i). \tag{3.12}$$

It is seen that the error *estimate* behaves like $N^{-1/2}$ and therefore the method generally converges far slower than any of the other methods mentioned so far. Also, there is no guarantee that the error is distributed as a Gaussian, and the estimate should therefore only be taken for what it is: an estimate of the error. If the estimates obtained were distributed according to a Gaussian, then the error estimate would correspond to the one standard deviation.

3.2 Numerical Integration in $n \geq 2$ Dimensions

Numerical integration in multiple dimensions is significantly harder than its one–dimensional counterpart. First of all, the required number of function evaluations to reach a certain accuracy grows with the power of the dimension D for any of the methods based on abscissas placed along the coordinate axes. Therefore, in D dimensions the generalised trapezoidal rule will have an error estimate behaving like $\mathcal{O}\left(N^{-2/D}\right)$ while Simpson's rule converges slightly faster as $\mathcal{O}\left(N^{-4/D}\right)$, with N the total number of evaluations of the integrand. Secondly, the integration domain can be arbitrarily complicated and is in general no longer described by just the endpoints of intervals. This problem significantly complicates the use of any of the methods that work so well for one–dimensional integrals.

The Monte Carlo method generalised to n dimensions still converges according to the Central Limit theorem, i.e. with an error estimate decreasing as $N^{-\frac{1}{2}}$. This means that for sufficiently high number of dimensions of the integral, the Monte Carlo method will convergence faster than any of the other methods. For multiple dimensions the straightforward generalisation of the Monte Carlo estimate of the integral is given by

$$\int_V \mathrm{d}\Omega\, f \approx V\langle f\rangle \pm V\sqrt{\frac{\langle f^2\rangle - \langle f\rangle^2}{N}}, \tag{3.13}$$

$$\langle f\rangle = \frac{1}{N}\sum_{i=1}^{N} f(x_i), \quad \langle f^2\rangle = \frac{1}{N}\sum_{i=1}^{N} f^2(x_i). \tag{3.14}$$

where V is the volume to integrate over. Apart from the faster convergence in higher dimensions, the Monte Carlo methods benefit from the ease of implementing complicated integration domains. As long as there is a way of testing whether a given point lies within the boundaries, the random points can be generated in a domain fully containing the integration domain, and the value of the function is then set to zero if the sampled point happens to lie outside the integration domain. This simply corresponds to the rewriting of the integral

$$\int_V \mathrm{d}\Omega\, f = \int_W \mathrm{d}\Omega\, f|_V, \tag{3.15}$$

with $V \subseteq W$. The reason that this does not work for other integration routines is that simply constraining f to have non-zero values in V spoils some of the analyticity properties on W assumed in the derivation of the methods ($f|_V$ will generally not be smooth on W). W should obviously be chosen to be not too much bigger than V. This is because the domain $W \setminus V$ will increase the error estimate in Eq. (3.11) (now with W substituted for V). Sample points in this region will not reduce the variance, but the volume has been increased.

So far we have not been concerned about the generator of the random numbers used in the Monte Carlo algorithm. It is however apparent that the higher the dimensionality of the problem, the more requirements the random number generator has to fulfil for the algorithm to work well. Consider for example a one–dimensional problem on the interval $[0,1]$. If the random numbers are taken from the string $(x_1, 1-x_1, x_2, 1-x_2, \ldots)$ with $x_1, x_2, \ldots$ random, then the Monte Carlo estimate of the integral will still converge to the central value, since all which is required of the random numbers in the one dimensional problem is that they are generated at equal probability in any sub–interval of the integration interval. However, if the same series is used in the two–dimensional problem on $[0,1] \times [0,1]$ to generate the sample points (x, y), then the function $f(x, y)$ will only be sampled along the line $y = 1 - x$, which obviously will not generally result in a good estimate of the average on the square. For multi–dimensional problems, it is therefore necessary to worry about possible correlations between elements in the series of "random" numbers.

3.3 Importance Sampling

In Eq. (3.13) the Monte Carlo error estimate is written in the form

$$E_{\mathrm{MC}} = \frac{\sigma_{\mathrm{MC}}}{\sqrt{N}}, \tag{3.16}$$

where σ_{MC} is a Monte Carlo estimate of the standard deviation on the integration volume of the integrand

$$\sigma^2 = V \int_V \mathrm{d}\Omega\, f^2 - \left(\int_V \mathrm{d}\Omega\, f \right)^2, \tag{3.17}$$

where V denotes both the domain and the measure (size or volume) of the domain (in a hopefully obvious notation). It is therefore possible to improve the convergence of the Monte Carlo method by reducing the variance of the function. This can be done by clever coordinate transformations, and is often called *importance sampling* since the coordinate transformations which will improve the convergence will turn out to correspond to simply sampling the integrand where it contributes the most to the integral.

To be specific we will consider just a one–dimensional integral, we can think of picking one of the many in the integral over V. The specific integral can then be rewritten

$$\int_a^b \mathrm{d}x f(x) = \int_a^b \mathrm{d}x\, g(x) \left(\frac{f(x)}{g(x)}\right) = \int_a^b \mathrm{d}x\, g(x)h(x), \tag{3.18}$$

where to begin with the trick is to find a $h(x) = f(x)/g(x)$ that is more slowly varying than f (so that the variance is decreased). Obviously, just applying Eq. (3.18) as it stands will not lead to any improvements. The trick is to make a change of variables and rewrite the integral

$$\int_a^b \mathrm{d}x\, g(x)h(x) = \int_{G(a)}^{G(b)} \mathrm{d}y\, h\left(G^{(-1)}(y)\right), \tag{3.19}$$

where $\mathrm{d}G(x)/\mathrm{d}x = g(x)$ (the boundary condition is unimportant since any constant added to G will just have to be subtracted from the inverse function $G^{(-1)}$). $g(x)$ can be normalised so that

$$\int_a^b \mathrm{d}x\, g(x) = 1, \tag{3.20}$$

and the fundamental theorem for Monte Carlo integration then states that

$$\int_a^b \mathrm{d}x\, f(x) = \int_a^b \mathrm{d}x\, g(x)\frac{f(x)}{g(x)} \approx \left\langle \frac{f(x)}{g(x)} \right\rangle \pm \sqrt{\frac{\langle f^2(x)/g^2(x)\rangle - \langle f(x)/g(x)\rangle^2}{N}}. \tag{3.21}$$

Choosing $g(x) = 1/l$ we recover Eq. (3.11). It can now be shown (see e.g. Ref.[30]) that an optimal choice for $g(x)$, i.e. one that reduces the variance the most, is one that is proportional to $|f(x)|$. The method of importance sampling is however only useful, if the following requirements are met

1. $g(x)$ is non–negative in the region of integration
2. The function $G(x)$, $\mathrm{d}G(x)/\mathrm{d}x = g(x)$ must be known analytically. If the integral of $g(x)$ is normalised to 1, then $G(x)$ can be chosen to vary between 0 and 1 ($G(a) = 0, G(b) = 1$), and $G(x)$ will describe the probability of picking a x_i with $x_i \leq x$.
3. $G(x)$ must be invertible (to be used in Eq. (3.19)), or it must be possible to generate random numbers distributed as $g(x)$.

Obviously, the function $f(x)/g(x)$ has also to vary less than $f(x)$ for the procedure to improve the convergence properties of the numerical integration. These requirements severely limits the applicability of importance sampling. First of all a detailed understanding of the behaviour of the function $f(x)$ on the interval of integration is necessary to choose $g(x)$. Secondly, this choice is constrained by the requirement that $g(x)$ be integrable analytically and that the integral has an analytic inverse. The problem becomes even clearer when one remembers that we have set out to integrate $f(x)$ numerically in the first place, presumably since it is too complicated to integrate analytically. The optimal choice of $g(x)$ proportional to $f(x)$ in this method would require us to be able to integrate $f(x)$ analytically in the first place. However, this paradox is not as bad as it might seem at first, which we will illustrate by an example, which will also help to illustrate the method in general.

Consider the integral

$$\begin{aligned} f(x) &= \frac{1+\exp(x)}{x^2} \\ \int_{0.1}^{1.0} \mathrm{d}x\, f(x) &= \left[-\frac{\exp(x)}{x} + \mathrm{Ei}(x)\right]_{0.1}^{1.0} \approx 20.8514, \end{aligned} \tag{3.22}$$

where $\mathrm{Ei}(x)$ is the exponential integral function

$$\mathrm{Ei}(x) = -\int_x^\infty \mathrm{d}x\, \frac{\exp(x)}{x} = \ln x + \frac{x}{1\cdot 1!} + \frac{x^2}{2\cdot 2!} + \frac{x^3}{3\cdot 3!} + \cdots . \tag{3.23}$$

We have chosen a function which can actually be integrated (semi-)analytically, but in real life physics examples this would generally not be the case. $f(x)$ is plotted for the relevant interval on Fig. 3.1. On the interval of integration, the most important behaviour is the $1/x^2$ suppression, which can be integrated analytically with an analytic inverse. We will therefore perform a change of variables according to the following choice (see Eq. (3.18))

$$g(x) = \frac{1}{9}x^{-2}, \quad y = G(x) = -\frac{1}{9x}, \quad G^{(-1)}(y) = -\frac{1}{9y}, \tag{3.24}$$

where we have normalised $g(x)$ according to Eq. (3.20). The integral of Eq. (3.22) is therefore rewritten

$$\int_{0.1}^{1.0} \mathrm{d}x\, f(x) = \int_{0.1}^{1.0} \mathrm{d}x\, x^{-2}\, (1+\exp(x)) = 9\int_{-10/9}^{-1/9} \mathrm{d}y\, \left(1+\exp\left(-\frac{1}{9y}\right)\right) \tag{3.25}$$

The new integrand (including the factor of 9) is plotted in Fig. 3.2. Comparing with $f(x)$ in Fig. 3.1 we see that the variance is significantly reduced. In fact, the variance can be calculated analytically by Eq. (3.17) applied to one dimension

$$\sigma^2 \equiv l\int_a^b \mathrm{d}x\, [f(x)]^2 - \left[\int_a^b \mathrm{d}x\, f(x)\right]^2 . \tag{3.26}$$

Using this we find that $\sigma_f \approx 31.16$ while $\sigma_h \approx 2.63$. Since the Monte Carlo algorithm converges with an error estimate of $\sigma/\sqrt{N}$ this means that the required accuracy will be reached by a factor 140 fewer function evaluations by integrating h instead of f. This is illustrated in Fig. 3.3, where we compare the Monte Carlo estimates for the integral of Eq. (3.22) and Eq. (3.25) versus the number N of evaluations of the integrand. The error estimates turn out maintain an almost constant factor of proportionality given by the ratio of the analytically calculated standard deviations of the integrands. This example was particularly simple since we chose to generate the random numbers according to a distribution which was already part of the integrand (the x^{-2} part). However, we hope it serves to illustrate that considerable progress can be made in reducing the variance without actually performing the integral analytically, which otherwise is the suggestion made in the analysis of the optimal choice for $g(x)$ mentioned earlier. It is interesting to note that if the integration interval had been different, the exponential behaviour of the numerator could have been more important than the x^2 suppression, and the applied substitution would have been much less efficient in reducing the variance. Also, it should be clear that tremendous progress can be made in multi–dimensional integrals if variance reduction is applied in more than one of the dimensions.

The hunt is therefore on for functions resembling the behaviour of the integrand for all the variables. We would like to elaborate slightly on the connection between the coordinate transformation and choosing a non–uniform sampling of the interval of integration, since we believe it will be instructive. Consider again the integral of $f(x)$ between a and b. We

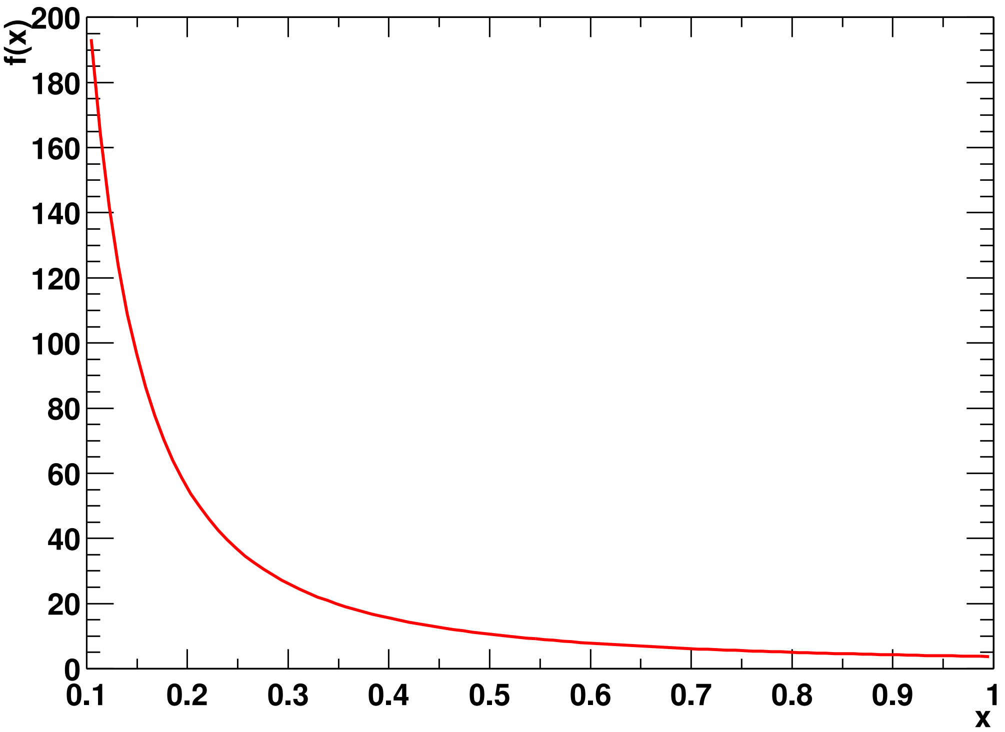

Figure 3.1: $f(x)$

can now make a change of variables to a random number r in the interval $[0,1]$

$$\int_a^b \mathrm{d}x\, f(x) = \int_0^1 \mathrm{d}r\, \frac{\mathrm{d}x}{\mathrm{d}r} f\left(x(r)\right), \tag{3.27}$$

where, following the idea of importance sampling, we would now like $x(r)$ to be peaked at values of x that maximises $|f(x)|$. The question is, how do we go about constructing such a $x(r)$. We will work through an example that will turn out to be useful in the construction of the Monte Carlo integration routine for the BFKL integrals. Consider the function

$$g(x) = \left(\left(\frac{x-d}{e}\right)^2 + 1\right)^{-1}, \tag{3.28}$$

where we have left in the parameters d, e. For suitable choices of d, e, $g(x)$ will describe closely the dependence of the integrand for the total cross section (think of $f(x)$) on the transverse momenta of some of the particles (e.g. the two leading dijets). We will call the normalised integral of $g(x)$ $G(y)$,

$$r = G(y) = \int_a^y \mathrm{d}x\, g(x) \Big/ \int_a^b \mathrm{d}x\, g(x)\ . \tag{3.29}$$

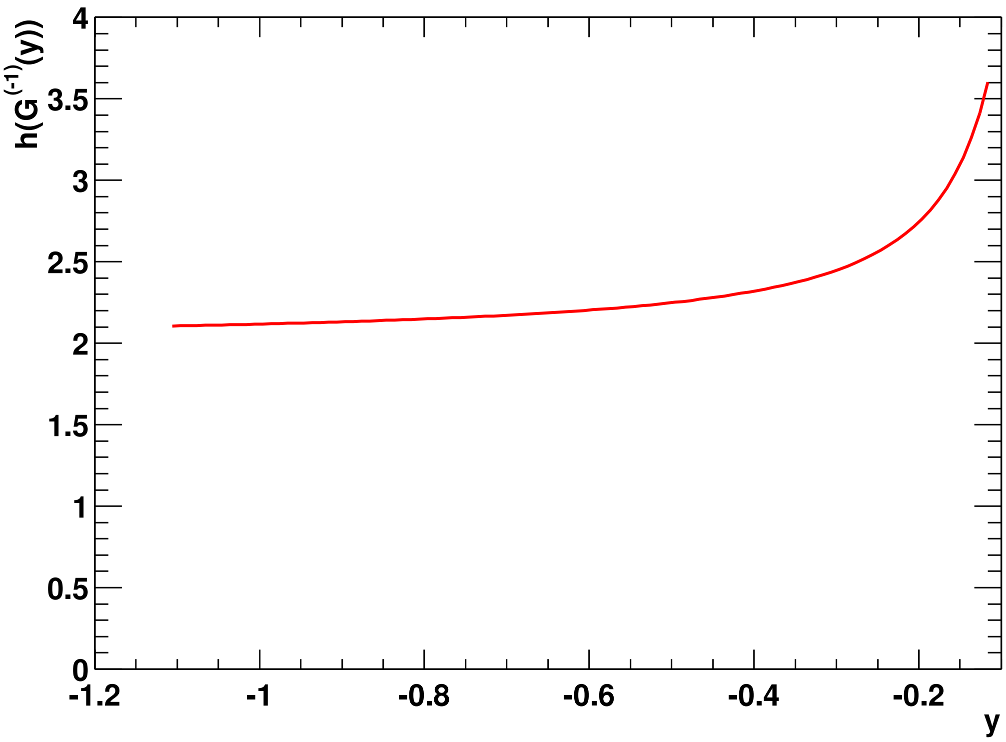

Figure 3.2: $h(x)$ according to Eq. (3.19) and Eq. (3.25), including the prefactor 9.

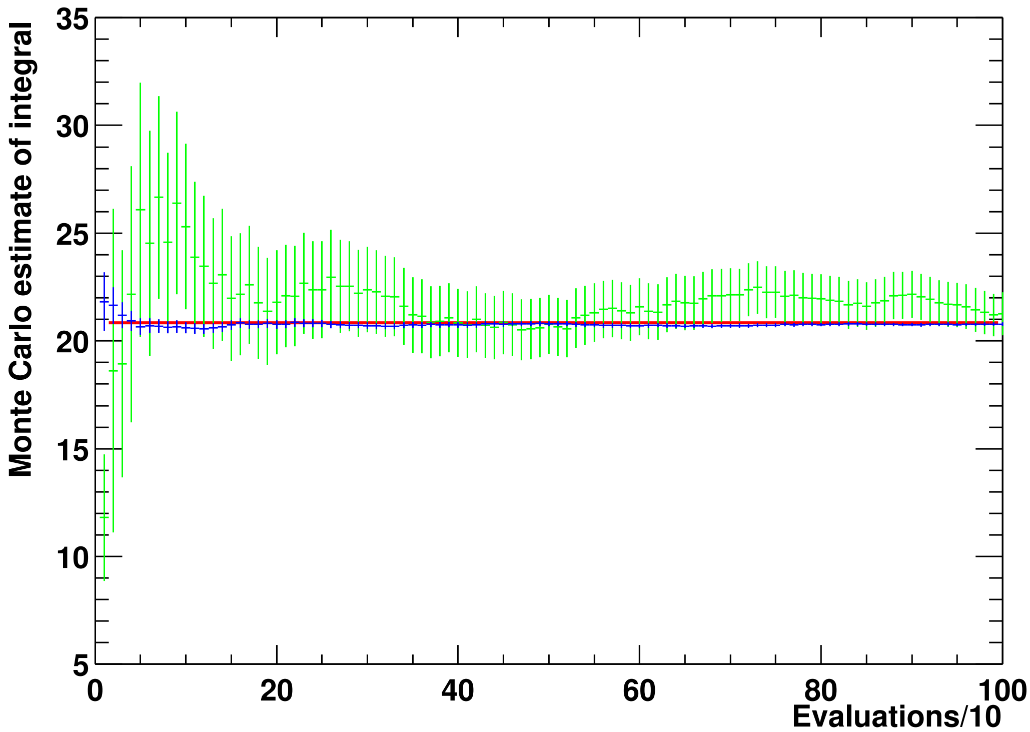

Figure 3.3: Monte Carlo integration of the integral in Eq. (3.22) compared to the integration of Eq. (3.25) versus the number of evaluations of the function. The red line is the correct value of the integral, and the blue crosses indicate the value found by applying the Monte Carlo procedure to Eq. (3.25). The green crosses are the result of a Monte Carlo approximation to the integral in Eq. (3.22).

$G(y)$ increases monotonously from 0 to 1 for $a \leq y \leq b$, describing how the random number r (to be picked at random) should be distributed as a function of y. The inverse function $G^{(-1)}(r)$ is given by

$$G^{(-1)}(r) = d + e \tan\left(\arctan\left(\frac{a-d}{e}\right) - r \arctan\left(\frac{a-d}{e}\right) + r \arctan\left(\frac{b-d}{e}\right)\right), \quad (3.30)$$

and the derivate is given by

$$\begin{aligned}\frac{\mathrm{d}x}{\mathrm{d}r} = \frac{\mathrm{d}G^{(-1)}(r)}{\mathrm{d}r} &= e\left(-\arctan\left(\frac{a-d}{e}\right) + \arctan\left(\frac{b-d}{e}\right)\right) \\ &\cdot \left(\sec\left(\arctan\left(\frac{a-d}{e}\right) - r\ \arctan\left(\frac{a-d}{e}\right) + r\ \arctan\left(\frac{b-d}{e}\right)\right)\right)^2 .\end{aligned} \quad (3.31)$$

Armed with these formula we are ready to tackle the integral of Eq. (3.27) with a reduced variance, if the function $g(x)$ describes well the behaviour of $f(x)$. We hope that this example has also helped to highlight the connection between the change of variables in the example of variance reduction of Eq. (3.19) and the concept of importance sampling of Eq. (3.27). Importance sampling is simply a special case of variance reduction with a coordinate transformation to the interval $[0, 1]$.

Finally we should mention that there are other strategies for improving on the convergence of the naïve Monte Carlo like *stratified sampling*, and furthermore there are standard programs like `VEGAS`[31] that applies adaptive Monte Carlo techniques to multi–dimensional integrals. This is done by seeking out intervals of each variable contributing most to the integral, and sample these areas more often (just like in importance sampling). However, these algorithm converge very slowly for problems of higher dimensions (say, more than 10 dimensions), since they have to first "learn" about the behaviour of the integrand by sampling randomly, before they adapt the sampling grid. Certainly, `VEGAS` proved completely inadequate for the problem at hand of evaluating numerically the integrals arising in the BFKL solution.

3.4 Random Number Generators

The series of random numbers generated by the computer during a Monte Carlo integration is often strictly speaking not random, but rather a deterministic series of numbers, which mimic many of the properties of a truly random series. Such series are called *pseudo–random*, and while it might at first seem strange to consciously choose not to use truly random numbers gathered from e.g. radioactive decay experiments or electronic noise, it does have its merits. It allows for the properties of the algorithm for the pseudo–random number generator to be studied, and the same sequence of pseudo–random numbers can be used for calculations over and over again, which can help in debugging. More importantly, though, is the fact that it is possible to make sure that different random numbers are being used if the calculation is split up to run on different computers, with the final result being combined from each individual computer. We will discuss how to do this in the next section.

The most basic *multiplicative linear congruential* pseudo–random number generators constructs a series s_i of integers in the interval $[0, m-1]$, where m is some (big) integer, e.g. the biggest which can be represented by the computer. The float $x_i = s_i/m$ will then belong to the interval $[0, 1[$ (it is customary not to generate 1 in the series). Starting from a seed s_i, the next number in the pseudo–random series is then generated according to the formula

$$s_{i+1} = (as_i + c) \mod m, \tag{3.32}$$

with a, c integers. This formula highlights a potential problem of all deterministic random[1] number generators running on a computer. The generator only has a finite number of internal states (specified by s_i), and so the series of numbers generated will repeat itself after a given time (called the period). This is though a well understood problem, and far from the worst faced by the linear congruential random number generators. While such generators will indeed give a flat distribution of random numbers in the interval $[0,1[$ with only a small and negligible correlation between two consecutive points in the series, it was realised that in higher dimensions the points sampled by these algorithms cluster together in planes, thus sampling the n dimensions unevenly — much like the example of the series $(x_1,(1-x_1),\ldots)$ of Sec. 3.2.

We will therefore in our Monte Carlo routines choose a better random number generator called `RANLUX` [32, 33], which is based on the dynamics of a classical chaotic systems. The properties of more advanced random number generators are generally less well understood than those of multiplicative linear congruential ones, but recent progress in the understanding of `RANLUX` has been made. It has a very long period, and passes the by now standard `DIEHARD` set of tests for a random number generator (which many linear congruential generators fail). It is of course difficult to set up rigorous finite tests of random number generators (since per definition you will only have tested a finite part of the series), so instead of making sure to use a random number generator with no correlations between elements, you have to just make sure *not* to use a random number generator that is *known* to fail the tests. Another good random number generator is `RAN2` of Ref.[29], which we used at the beginning of our project. The `CLHEP` project[34] has implemented many of the commonly used (and good!) random number generators, and using this framework it is very easy to change from one generator to another, thus testing whether a result is just a "statistical fluctuation" or real physics.

3.5 Parallelising Monte Carlo Calculations

There are several added benefits of the Monte Carlo method not mentioned previously. Firstly, the estimate of the accuracy of the numerical integration can be calculated after each evaluation of the function. This means that one can continue the numerical integration until a target accuracy has been met. While this is in principle also possible for say the Gaussian Quadratures, all the previous evaluations of a function are thrown away if it is decided that a higher accuracy is needed. This is because the positions of the abscissas depend on the number of function evaluations and therefore on the accuracy requested (in

[1] In the context of pseudo–random number generators, we will use the word *random* to mean *psedu–random*.

fact, the position of the abscissas for a $m+1$ point Gaussian quadrature lies in-between the points for the m point evaluation method).

Secondly, and this is particularly important for applications in particle physics, once a Monte Carlo integration of the cross section has been constructed, it is very easy to calculate the differential distribution of any quantity derived from the event configuration. If we let $\mathrm{d}\sigma/\mathrm{d}\Omega$ describe the differential cross section for a process and x_i being the four–momenta of the participating particles, then we could imagine wanting to know how the average total energy depended on the maximum rapidity separation between particles in the ensemble. The total energy of the process is calculable from the four–momenta, and the average is then given by

$$\langle s\rangle = \int \mathrm{d}\Omega s(x_i)\mathrm{d}\sigma/\mathrm{d}\Omega \Bigg/ \int \mathrm{d}\Omega \mathrm{d}\sigma/\mathrm{d}\Omega. \tag{3.33}$$

So far this would apply equally well to other approaches than Monte Carlo. However, the Monte Carlo method excels when we come to ask for the differential distribution of $\langle s\rangle$ as a function of the maximum rapidity separation y, which leads us to the concept of *binning*. $\mathrm{d}\langle s\rangle/\mathrm{d}y$ can be found by simply calculating y for each of the phase space points sampled in the Monte Carlo evaluation of the two integrals in Eq. (3.33) and then form the ratio bin by bin. The differential quantity is then found in the limit of the bin width going to zero. This is completely identical to the correspondence between differentials and derivatives. For the Gaussian quadrature method, one would have to find the intervals contributing to each bin for each and every integration variable and then tailor the integration routine to them.

The binning process can be viewed as running the calculation for the integrated cross section with different cuts for each bin. The contribution to bin n will come from a phase space slice V_n, and the Monte Carlo estimates are given by

$$\begin{aligned} I_n &= \int_{V_n} \mathrm{d}\Omega\, f = \int_V \mathrm{d}\Omega\, f|_{V_n} \\ &\approx V\langle f|_{V_n}\rangle_V \pm V\sqrt{\frac{\langle f^2|_{V_n}\rangle_V - \langle f|_{V_n}\rangle_V^2}{N}} \\ &= \langle Vf|_{V_n}\rangle_V \pm \sqrt{\frac{\langle (Vf)^2|_{V_n}\rangle_V - \langle Vf|_{V_n}\rangle_V^2}{N}}, \end{aligned} \tag{3.34}$$

where we have found the last trivial rewriting particularly useful in constructing and analysing the Monte Carlo algorithms.

Each generation of a set of momenta required to evaluate the differential cross section at a certain point in phase space will use a certain number of random numbers, and the generation of the phase space point is completely independent of the generation of the previous and next phase space point. As long as a different set of random numbers is used on each computer, the Monte Carlo estimate can therefore be formed from evaluations of the integrand made on different computers. This is where it becomes useful that the random number generators produce a series of numbers, and that the internal state of the generator can be described by a few parameters. This means that we can start the Monte Carlo calculation with different seeds to the random number generator and so run several independent calculations simultaneously, and just make sure that the calculations stop before the set of random numbers used in the calculations start to overlap. Practically this is ensured by running once the random number generator and saving the status of it for every say, $2 \cdot 10^9$ random numbers generated, and then making sure that each individual calculation does not use more. The `CLHEP` framework proved to be very useful in programming this solution.

If each of the distributed calculations perform the same number of evaluations, then the central value (for any bin) for the combined result will be given by the average of the Monte Carlo estimates (of the central value for any bin). We can also find the estimated error on the combined calculation. Let us first rewrite the square of the error estimate for a single calculation with N evaluations

$$\begin{aligned} E^2 &= \frac{\langle V^2 f^2|_{V_n}\rangle_V - \langle V f|_{V_n}\rangle_V^2}{N} \\ &= \sum_{i\in\mathcal{N}} \left(\frac{V}{N} f|_{V_n}(\mathbf{x}_i)\right)^2 - \frac{1}{N}\left(\sum_{i\in\mathcal{N}} \frac{V}{N} f|_{V_n}(\mathbf{x}_i)\right)^2 , \end{aligned} \tag{3.35}$$

where $\mathcal{N}$ is the set of configurations i of the random number generator contributing to the Monte Carlo estimate (for the simple random number generators, i is an integer and $\mathcal{N}$ is a set of such), and $\mathbf{x}_i$ is the set of four–momenta corresponding to a specific choice of random numbers. N is the number of different configurations in $\mathcal{N}$, i.e. the number of "events" generated. Now, if we add together two independent calculations each consisting of the same number N of evaluations we find with $N_t = 2N$ being the total number of function evaluations

$$\begin{aligned} E^2 = &\sum_{i\in\mathcal{N}_1} \left(\frac{V}{N_t} f|_{V_n}(\mathbf{x}_i)\right)^2 + \sum_{i\in\mathcal{N}_2} \left(\frac{V}{N_t} f|_{V_n}(\mathbf{x}_i)\right)^2 \\ &- \frac{1}{N_t}\left(\sum_{i\in\mathcal{N}_1} \frac{V}{N_t} f|_{V_n}(\mathbf{x}_i) + \sum_{i\in\mathcal{N}_2} \frac{V}{N_t} f|_{V_n}(\mathbf{x}_i)\right)^2 \end{aligned} \tag{3.36}$$

$$\begin{aligned} &= \left(\frac{1}{2}\right)^2 \left(\sum_{i\in\mathcal{N}_1} \left(\frac{V}{N} f|_{V_n}(\mathbf{x}_i)\right)^2 + \sum_{i\in\mathcal{N}_2} \left(\frac{V}{N} f|_{V_n}(\mathbf{x}_i)\right)^2\right) \\ &- \left(\frac{1}{2}\right)^3 \frac{1}{N}\left(\sum_{i\in\mathcal{N}_1} \frac{V}{N} f|_{V_n}(\mathbf{x}_i) + \sum_{i\in\mathcal{N}_2} \frac{V}{N} f|_{V_n}(\mathbf{x}_i)\right)^2 . \end{aligned} \tag{3.37}$$

These formula are easily generalised to the case of combining more than two calculations. Since the sums depend on N, the number of events generated in each calculation, this formula shows how it is not necessary to decide how many independent calculations have to be performed when they are started. If after say 10 independent calculations each of 10^9 events the error is still not sufficiently small, one can start the next ten calculations and add the result in the end. It is seen from Eq. (3.36) that the leading contribution to the error is the sum of the squares, and that the term consisting of the square of the sum is suppressed by the number of evaluations. Therefore this last term is often dropped in the estimation of the error (which anyway assumes a Gaussian distribution of the errors), but we have left it in for completion.

Chapter 4

Dijet Production and BFKL

In the previous chapters we have developed the formalism and techniques necessary for implementing a Monte Carlo for the BFKL evolution of a t–channel gluon exchange. In this chapter we will present some results for dijet production obtained using this approach. The BFKL Monte Carlo will allow for energy and momentum conservation to be incorporated, which was the main motivation for constructing it. It will, as we will see, also help answer questions about the event topology, and help shed light on the question of the relevant scale for α_s for the fixed coupling BFKL exchange. We will start by studying the characteristics of partonic cross section and then study the impact of the energy conservation on the hadronic dijet cross section at the LHC and the Tevatron. Finally, we present a study on Mueller–Navelet dijet ratios at the Tevatron published in Ref.[35].

4.1 Characteristics of the Partonic Cross Section

The first valid question to ask is if the BFKL Monte Carlo approach with fixed coupling reproduces the known solution of Eq. (2.56) to the BFKL equation for partonic dijet production. In Fig. 4.1 we compare the predictions of the analytic BFKL solution plotted in Fig. 2.6 with that obtained from the Monte Carlo reformulation with a $\mu = 1$ GeV and extending the sum over resolved gluons n to 20 (we will later see that these are sensible choices). The red crosses are obtained using the Monte Carlo approach on the fixed order solution of Eqs. (2.67)–(2.68) (with the same value of α_s as in Fig. 2.6) whereas the green circles are obtained using a running coupling in the BFKL chain with a value of $\Lambda = 200$ GeV, $N_f = 4$ and freezing the running at a scale corresponding to $\alpha_s(Q_0^2) = 1$. In the last case, the running coupling is also applied to the impact factors, which is why the green circles do not line up with the black lines in the $\Delta y \to 0$ limit. This is the limit where the BFKL effects vanish (since there is no rapidity–ordered phase space for

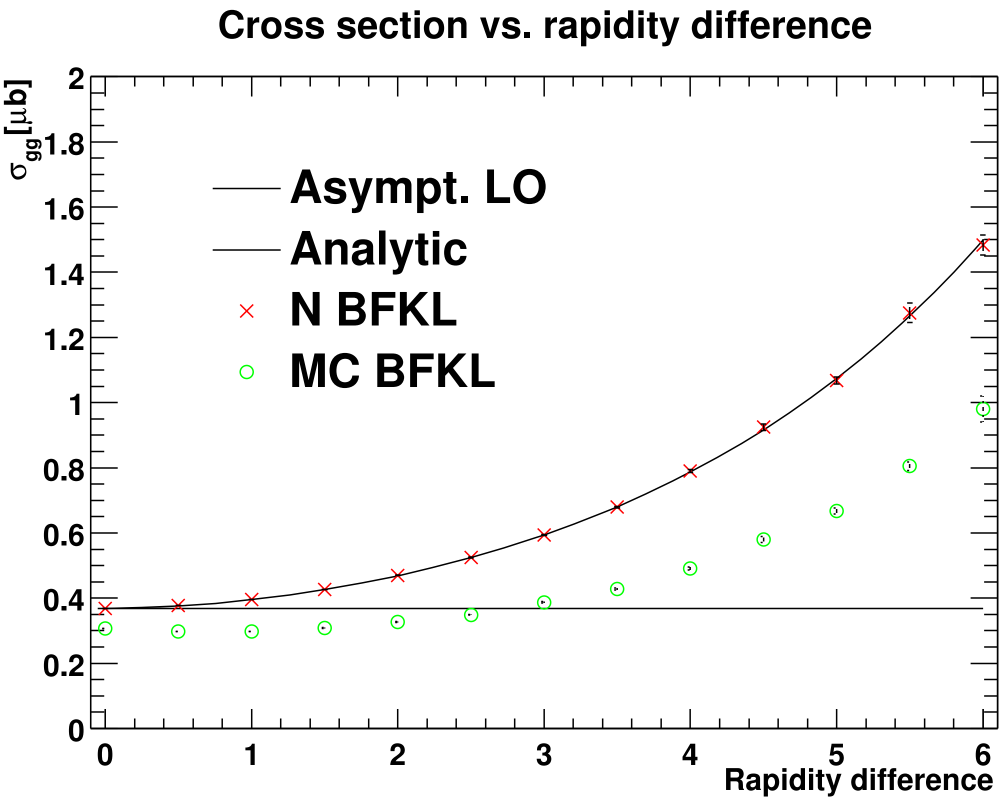

Figure 4.1: The cross section for partonic dijet production including the prediction from the analytic solution to the BFKL equation (black rising line), the Monte Carlo fixed (red crosses) and running (green circles) coupling solution. $\alpha_s = 0.164$.

gluon emission) and the LO result is regained. We see that the iterative solution to the BFKL equation and the subsequent Monte Carlo implementation agrees very well with the analytic result. In fact the two results are indistinguishable. Unfortunately there is no analytic prediction available in the literature for dijet production in the case of LL BFKL supplemented by a running coupling (although it may be possible to obtain such a result from the work in Ref.[27]). Both Monte Carlo results are obtained within a reasonable running time corresponding to about 5-10 CPUminutes for every point. Understanding the behaviour of the nested integrals of rapidities proved to be the key in constructing a efficient importance sampling routine that allows a fast integration over the rapidity ordered multi–gluon phase space (see Appendix B).

In Fig. 4.2 we have fixed the rapidity separation between the leading dijets at $\Delta y = 3$ and also zoomed in on values of the differential dijet cross section between $0.55\mu b$ and $0.65\mu b$. The cross section is seen to be only weakly dependent on the choice of μ, in fact varying μ between 0.2 GeV and 7 GeV only leads to a variation in the predicted cross section of 12% for this particular choice of the coupling, rapidity difference and minimal

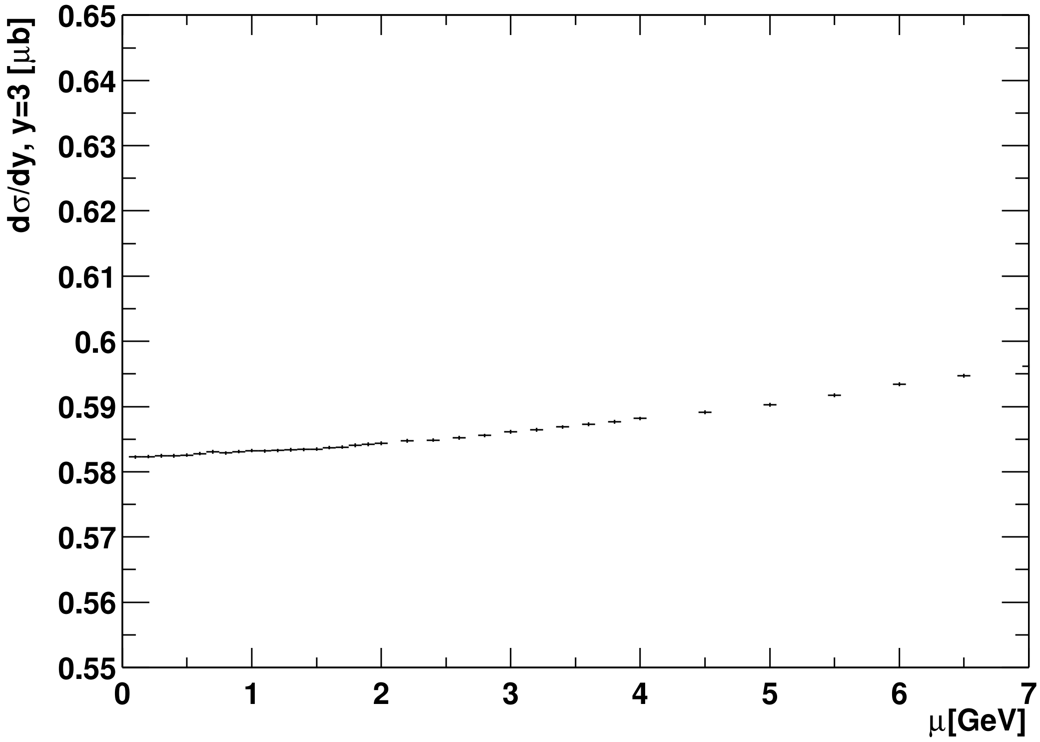

Figure 4.2: The μ–dependence of the Monte Carlo prediction for the partonic dijet cross section including BFKL evolution at $\Delta y = 3$.

transverse momenta of the leading dijets (20 GeV). All the results presented in this chapter are calculated with a choice of $\mu = 1$ GeV, and from Figs. 4.1–4.2 we see that this is indeed a good choice. In fact one could have chosen μ slightly bigger and still have obtained a valid result. The benefits thereby would be that the average dimension of the resolved gluon phase space would be reduced (fewer BFKL gluons passing the higher cut on transverse momenta are emitted), but since the running time of the numerical integration routine is not a problem we will just choose $\mu = 1$ GeV.

4.1.1 Radiation from the BFKL chain

Having justified that the reformulation of the solution to the BFKL equation does reproduce the known analytic solution, we can now begin to ask more detailed questions, where the answer is not known beforehand. Let us first study how the solution to the Monte Carlo BFKL is distributed on the different number of resolved gluons. This is plotted in Fig. 4.3 for the standard choice of the resolution scale $\mu = 1$ GeV and for different choices of the rapidity separation between the leading dijets. Each curve integrates to give the cross section at the specific choice of rapidity separation. This figure shows that

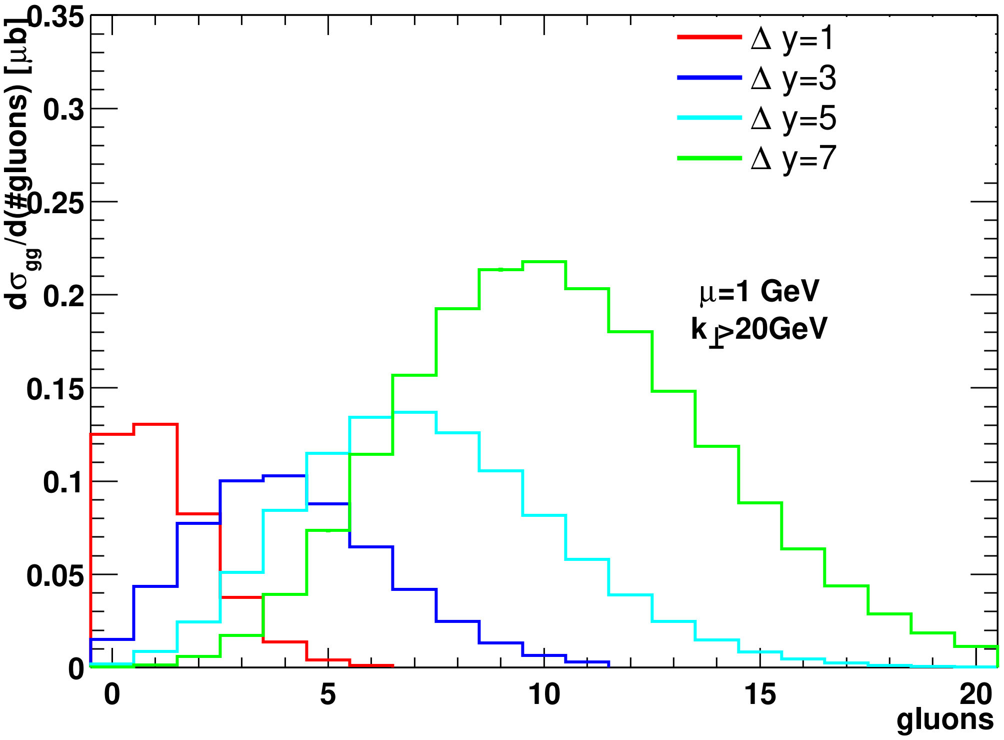

Figure 4.3: The contribution to the partonic cross section for choices of the rapidity separation from different numbers of resolved gluons. $p_{\perp\min} = 20$ GeV for the leading dijets.

the solution to the BFKL equation f gets contribution from 2-3 extra resolved gluons for every added unit of rapidity span of the BFKL chain. We will later see that the average number of gluons per unit of rapidity is roughly constant along the chain.

The number of jets in a BFKL event will be different from the numbers suggested by this plot, since important effects like showering, recombination and hadronisation are not taken into account, and the cut of 1 GeV on the transverse momenta of the BFKL gluons is very low. We can, however, study the average number of harder gluons in a BFKL event by asking how many of the "resolved" gluons in Fig. 4.3 would pass a cut of say 20 GeV on the transverse momentum. This is shown on Fig. 4.4, where also the lines of Fig. 4.3 are included for comparison. The integral over the dashed and full lines of every colour is the same. In the Monte Carlo model with a resolution scale $\mu_1 = 1$ GeV, the contribution from zero hard gluons with a cut–off of $p_{\perp 1} = 20$ GeV should be roughly the same as the contribution from zero resolved gluons in a Monte Carlo model with a resolution scale $\mu_2 = 20$ GeV, up to corrections of order $(p_{\perp 1}/\mu_1)^2$, which is in fact related to the $(\mu/p_\perp)^2$ behaviour seen on the choice of μ in Fig. 4.2. It has been checked that the predictions for hard versus resolved gluons for different choices of the hard and resolution scale do

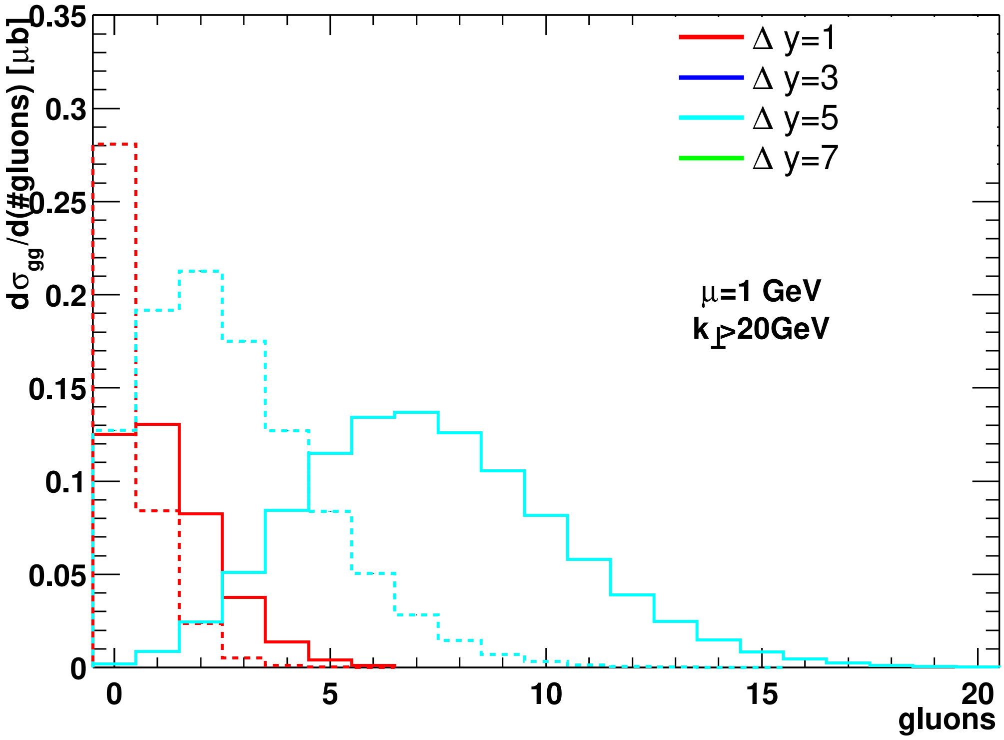

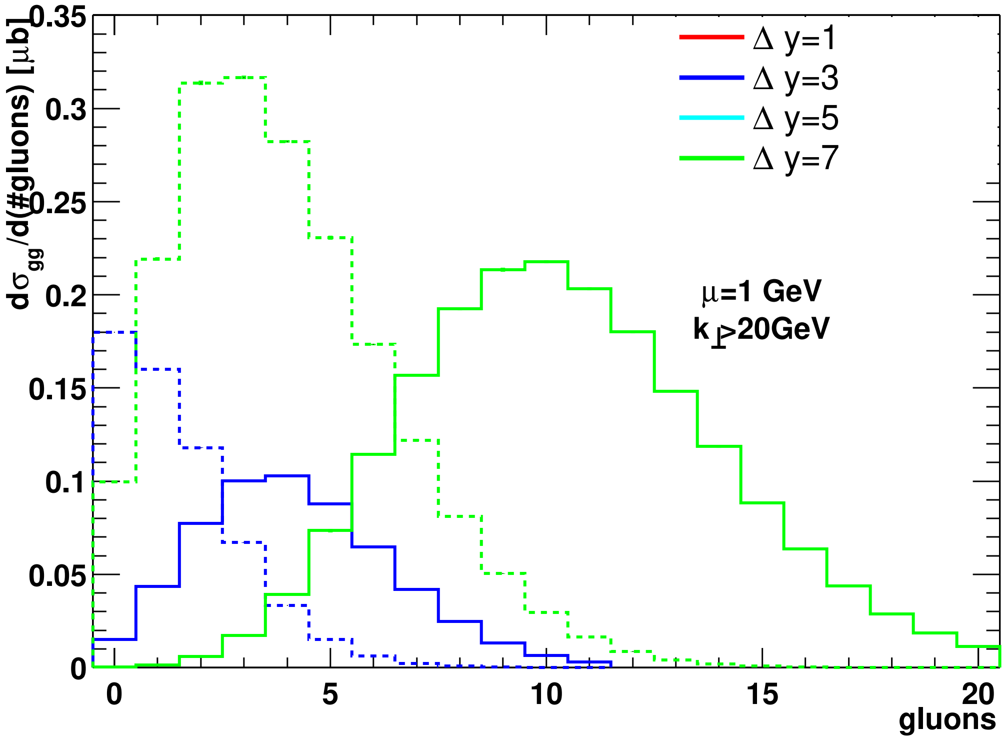

Figure 4.4: The contribution to the partonic cross section for choices of the rapidity span of the BFKL chain from different numbers of resolved (full) and "hard" (dashed) gluons emitted from the BFKL chain.

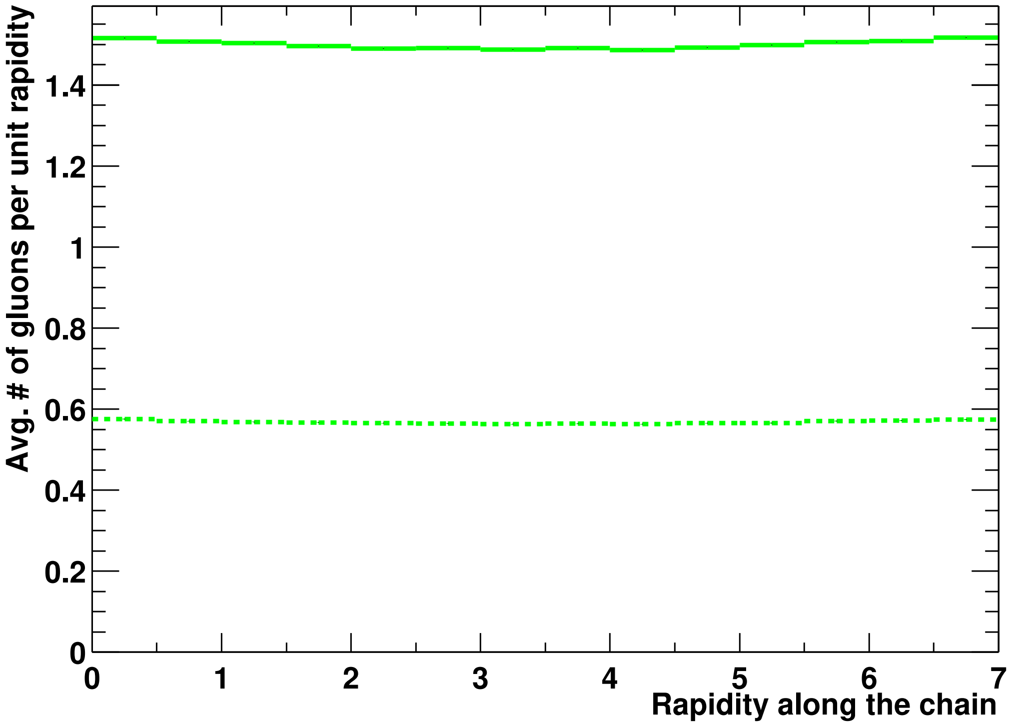

Figure 4.5: The average density of emitted gluons along the BFKL chain

indeed observe this behaviour. This serves as a consistency check of the understanding of the physics described by the Monte Carlo formulation of the BFKL gluon exchange.

The conclusion to be drawn from Fig. 4.4 is that about one gluon per two units of rapidity interval is emitted from the BFKL chain with a relatively hard transverse momentum. Some hard gluons are expected in the multi–Regge kinematics, where all transverse momenta are assumed to be of the same order of magnitude as that of the two leading dijets. On Fig. 4.5 we plot the average density of emitted gluons along a BFKL chain spanning 7 units of rapidity. The integral of this quantity will equal the average number of emitted gluons for the same span in rapidity. The upper line is the density of resolved gluons, whereas the lower density is that of harder ($k_\perp$ >20 GeV) BFKL gluons. This figure confirms that the BFKL gluons are emitted with equal probability per rapidity interval along the chain. Analytic results have been obtained for the jet multiplicity from the BFKL exchange (applied to deep inelastic scattering but the results can be modified to apply to dijet production too) by C. Ewerz and B.R. Webber [36, 37], but unfortunately these results apply to the Laplace transformed $\tilde{f}$ and are wildly oscillating in ω. A calculation of the jet multiplicity for a given rapidity span Δy would require an integral over ω. Failing to do this analytically, it would be interesting to compare our

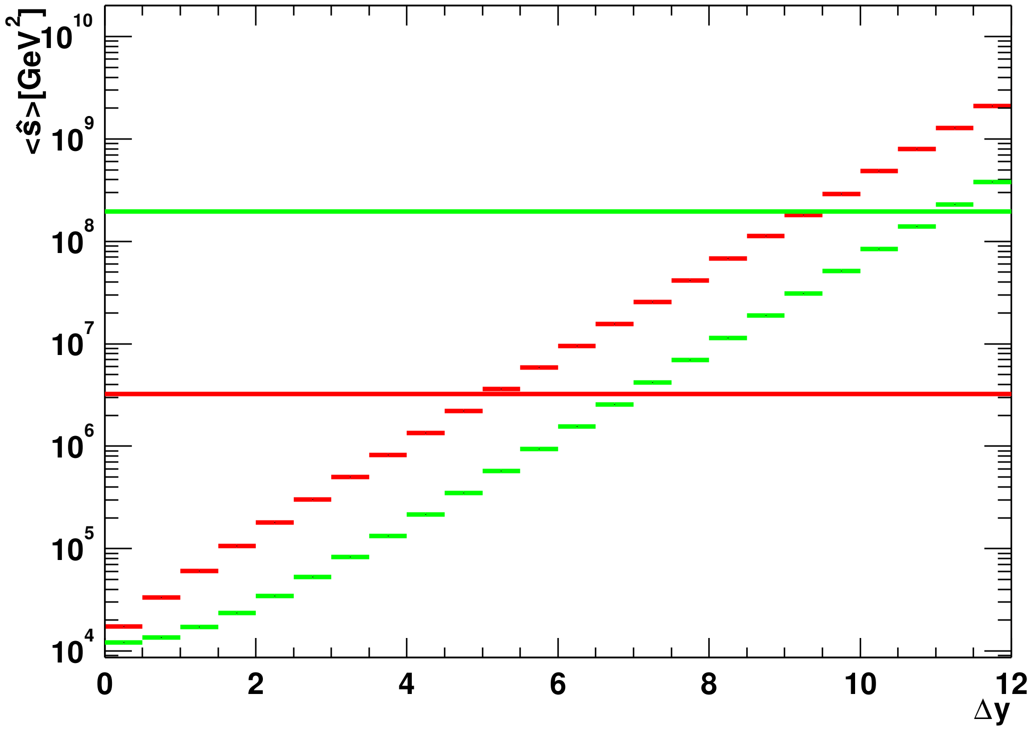

Figure 4.6: The average centre of mass energy in $gg \rightarrow gg$ scattering with (red) and without (green) BFKL evolution of the t channel gluon, with $p_{\perp\min} = 20$ GeV for the di-jets. Also plotted is the hadronic centre of mass energy squared for the Tevatron ($(1.8\text{TeV})^2$) and the LHC.

result with a numerical integration of the results obtained by C. Ewerz and B.R. Webber.

4.1.2 Energy Consumption of the BFKL Evolution

We can now answer one of the questions motivating the construction of the Monte Carlo model: How much energy goes into creating the LL BFKL radiation? In Fig. 4.6 we have plotted the average centre of mass energy squared for normal dijet production (in which case $\langle s^2 \rangle$ is given analytically by Eq. (1.59)) and for dijet production in the high energy limit with BFKL evolution of the t–channel gluon exchange. The prediction for pure dijet production coincides with the standard prediction for BFKL evolution, when the BFKL equation is solved analytically and the contribution from the BFKL gluons to the centre of mass energy is neglected. Therefore, while the BFKL Monte Carlo so far has answered questions about the radiation from the LL BFKL chain, Fig. 4.6 is in some way a first measure of the impact of including the contribution from the BFKL radiation to the centre of mass energy.

The contribution from the BFKL radiation to the centre of mass energy is formally subleading compared to the contribution from the leading dijets. Indeed we see in Fig. 4.6 that asymptotically (which is reached fast), the two curves have the same slope, even though they are offset by about 1.5 units of rapidity. This means that the kinematic limit of dijet production with BFKL evolution at hadron colliders is reached 1.5 units of rapidity before an estimate based on only the energy of the leading dijets. The rapid decrease of the pdfs as the kinematic limit is approached means that the horizontal lines of interest for a given hadron collider lie considerably lower than the lines indicated on the figure. Therefore, the effect of including the contribution from the BFKL radiation in the energy and momentum conservation is bigger than it may seem at first glance. When considering the implications on the cross section it must also be remembered that the BFKL evolution predicts an exponential rise with the rapidity span Δy. Therefore, effectively reducing the available rapidity span has a big impact on the prediction for the cross section.

We can see explicitly why the two curves in Fig. 4.6 have the same asymptotic behaviour. We have already seen that the radiation from the BFKL chain is distributed evenly in rapidity along the chain. We can approximate the Bjorken x's given by Eq. (2.16) by assuming that all the $k_{\perp i}$ are equal to k and that the gluons are distributed evenly spaced over the rapidity span Δy, separated by Δy_i. The Bjorken x's for the $2 \to n$ scattering then become (with $y = e^{-\Delta y_i}$ and assuming that $y_0 + y_n = 0$. The centre of mass energy is independent of this last assumption)

$$x_a = x_b = \frac{k}{\sqrt{s}} e^{\Delta y/2}(1 + y + y^2 + \cdots + y^n) = \frac{k}{\sqrt{s}} e^{\Delta y/2} \frac{1 - y^{n+1}}{1 - y}. \tag{4.1}$$

In the large Δy limit, $n \to \infty$ when the radiation is evenly spaced. Therefore we find in the large Δy limit

$$\hat{s} \propto k^2 e^{\Delta y} \frac{1}{(1 - e^{-\Delta y_i})^2}, \tag{4.2}$$

which has to be compared with the pure dijet prediction $\hat{s} \propto k^2 e^{\Delta y}$ with the same dependence on Δy. It is radiation from the region of the chain close to the endpoints that contribute the most to $\hat{s}$, since the middle part of the chain will give exponentially suppressed contributions to the energy (this is just a refinement of the asymptotic argument for dropping the contribution from the chain all together). This is why asymptotically there is only a difference in the normalisation and not the shape of the two curves in Fig. 4.6. From Eq. (4.2) we see that the smaller Δy_i, the bigger the difference in normalisation. A small Δy_i can be achieved by increasing α_s, thereby increasing the amount of radiation in the region close to the endpoints of the chain.

The observation that there is insufficient energy available at present day colliders for all the BFKL radiation resummed in the analytic approach has led some to introduce reduced effective rapidity separations [38] to be used when making phenomenological predictions of BFKL signatures for comparison with data. The idea behind this is simply to somehow emulate the reduction of phase space for BFKL radiation dictated by energy and momentum conservation by reducing the rapidity span Δy that is fed into the solution to the BFKL equation. It should be clear that the available BFKL Monte Carlo takes such effects into account exactly (the reduction in effective rapidity separations were estimated using the BFKL Monte Carlo approach of Ref.[25]).

4.1.3 The Running Coupling Case

In this section we will compare the results obtained in the Monte Carlo formalism incorporating the running of the coupling to that of the fixed coupling case of the previous section. The introduction of the running of the coupling leads to a significant overall increase in the number of gluons being emitted for a given rapidity span of the chain compared to the fixed coupling scenario, see Fig. 4.7–4.8. This, of course, is partly due to the choice of scale for the coupling in the constant coupling case. A lower renormalisation scale would have led to more radiation. Fig. 4.8 is very interesting in that it shows that the LL prediction of a uniform distribution of the BFKL radiation along the chain is changed in the running coupling case. There is increased activity at the ends of the chain before a plateau of activity is reached about 1.5 units of rapidity from the ends (at least for the $\Delta y = 7$ case). We also see that most of the additional radiation is soft, and so the number density of "harder" BFKL gluons emitted at the plateau is not much different from the fixed coupling case, although again the endpoints show increased radiation also of harder gluons. This effect is still being investigated. In Fig. 4.10 we see that $\langle \hat{s} \rangle$ for the running coupling case grows faster than for the constant coupling case. This is a consequence of the bigger number of gluons radiated (and therefore the slower growth of $\langle \hat{s} \rangle$ for the constant coupling case is a consequence of the chosen lower value of the coupling). However, we also see that asymptotically, the two subleading effects (first of all the effects of the running of the coupling, and secondly the effects of the gluon radiation on the centre of mass energy) are less pronounced, and the slope of the running coupling curve becomes similar to the slope of the leading dijet curve. The reason for the running coupling curve to start lower than the leading order fixed coupling one is that the transverse momentum spectrum is softer in the running coupling case.

4.1.4 The Relevant Scale of α_s in the BFKL Chain

In this section we will investigate which choices of scale for evaluating the coupling can be considered sensible in the constant coupling BFKL formalism. Since the Monte Carlo

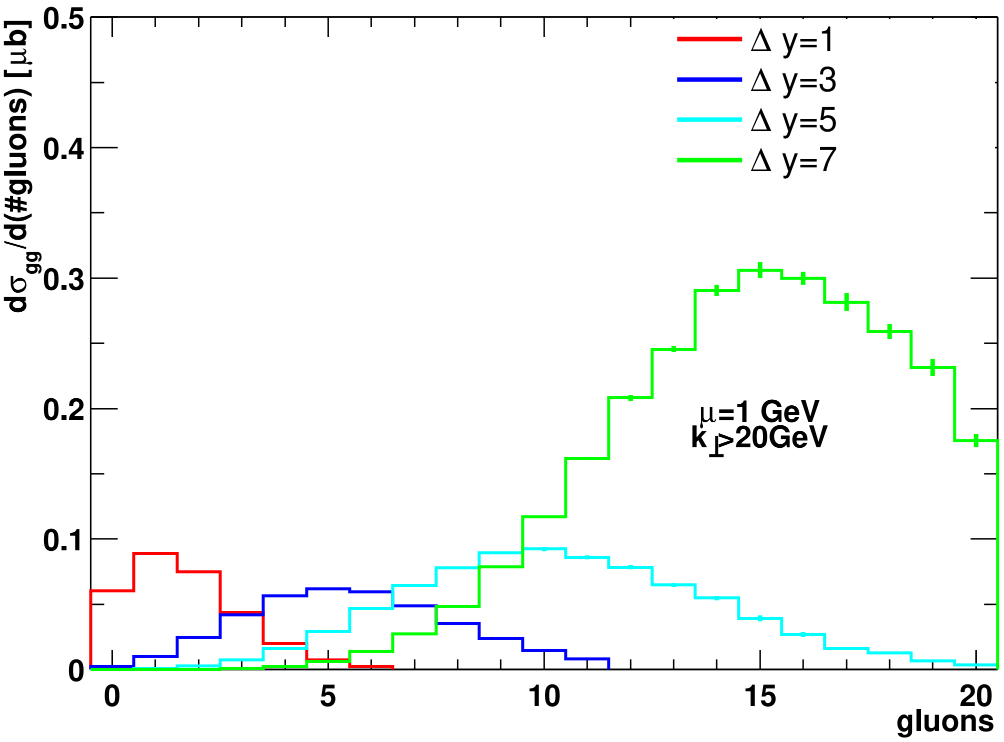

Figure 4.7: The contribution to the partonic cross section for choices of the rapidity separation from different number of resolved gluons for the running coupling scenario. $p_{\perp\min} =$ 20 GeV for the leading dijets.

approach offers complete control over all the momenta in the calculation, we can study how the vector sum

$$\mathbf{q}_{a\perp} + \sum_{j=1}^{i} \mathbf{k}_{j\perp} \tag{4.3}$$

evolves along the chain. The square of this is the scale relevant for evaluating the coupling (as seen in the running coupling formalism). Since each of the emissions $\mathbf{k}_{j\perp}$ is approximately random and independent of any other radiation, the vector sum of Eq. (4.3) will perform a random walk in the transverse vector plane. This is the argument behind *Bartel's Cigar*, the suggestion that this vector sum takes the shape of a cigar. The end points will obviously be fixed to the value of the leading dijets, but the sum is free to evolve randomly along the chain. In Fig. 4.11 we plot the evolution of this vector sum along the chain in the case of constant coupling for a chain of fixed length of 6 units of rapidity and the transverse momenta of the leading dijets fixed between 20 GeV and 30 GeV. Also, we have removed the very ends of the chain, since the plot is very peaked at these points. The units along the z–axis are arbitrary but for a given point along the BFKL chain the

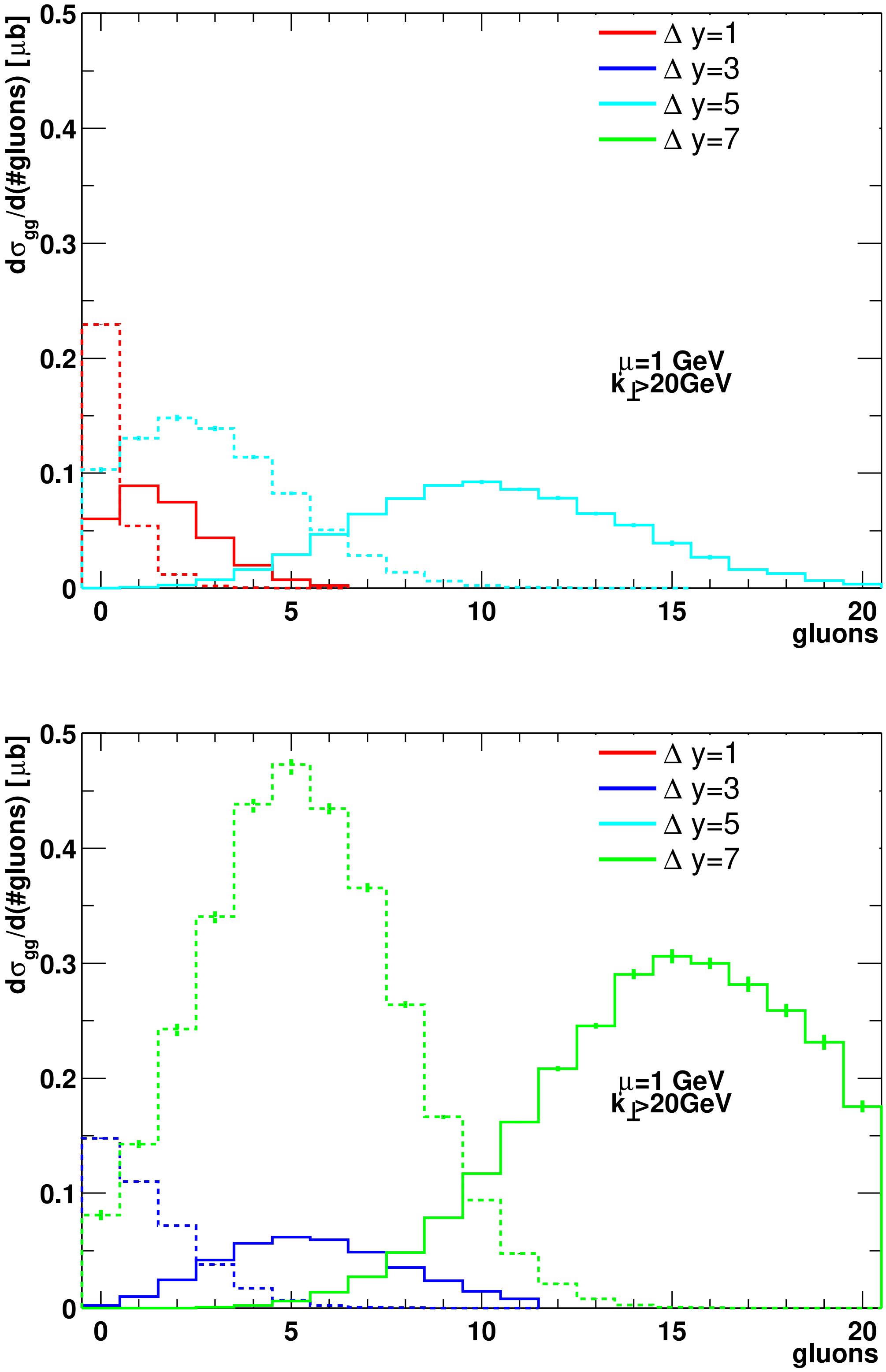

Figure 4.8: The contribution to the partonic cross section for choices of the rapidity span of the BFKL chain from different number of resolved (full) and "hard" (dashed) gluons emitted from the running coupling BFKL chain. MC errors only.

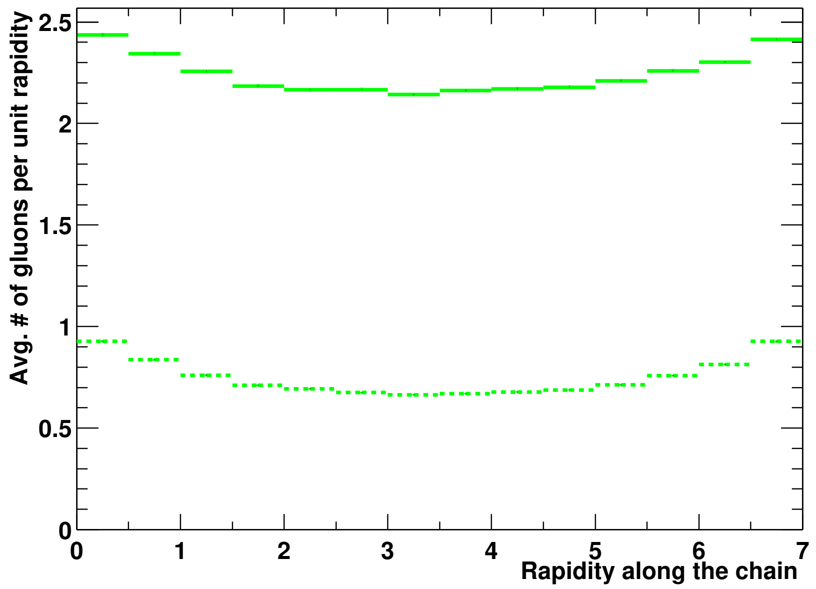

Figure 4.9: The average density of emitted gluons along the BFKL chain for the running coupling formalism.

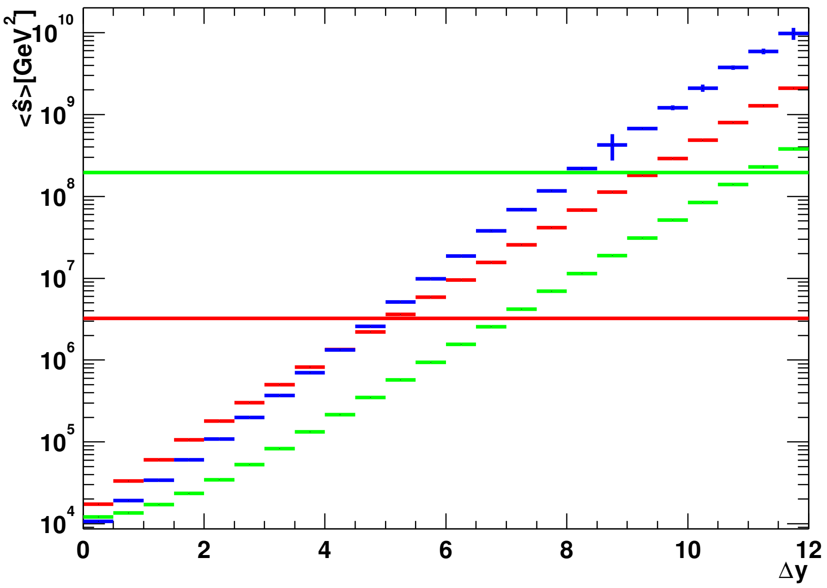

Figure 4.10: The average centre of mass energy in $gg \to gg$ scattering with constant coupling (red) and running coupling (blue) BFKL evolution of the t channel gluon, and the pure dijet case (green). $p_{\perp\min} = 20$ GeV for the leading dijets. Also plotted is the hadronic centre of mass energy squared for the Tevatron ($(1.8\text{TeV})^2$) and the LHC.

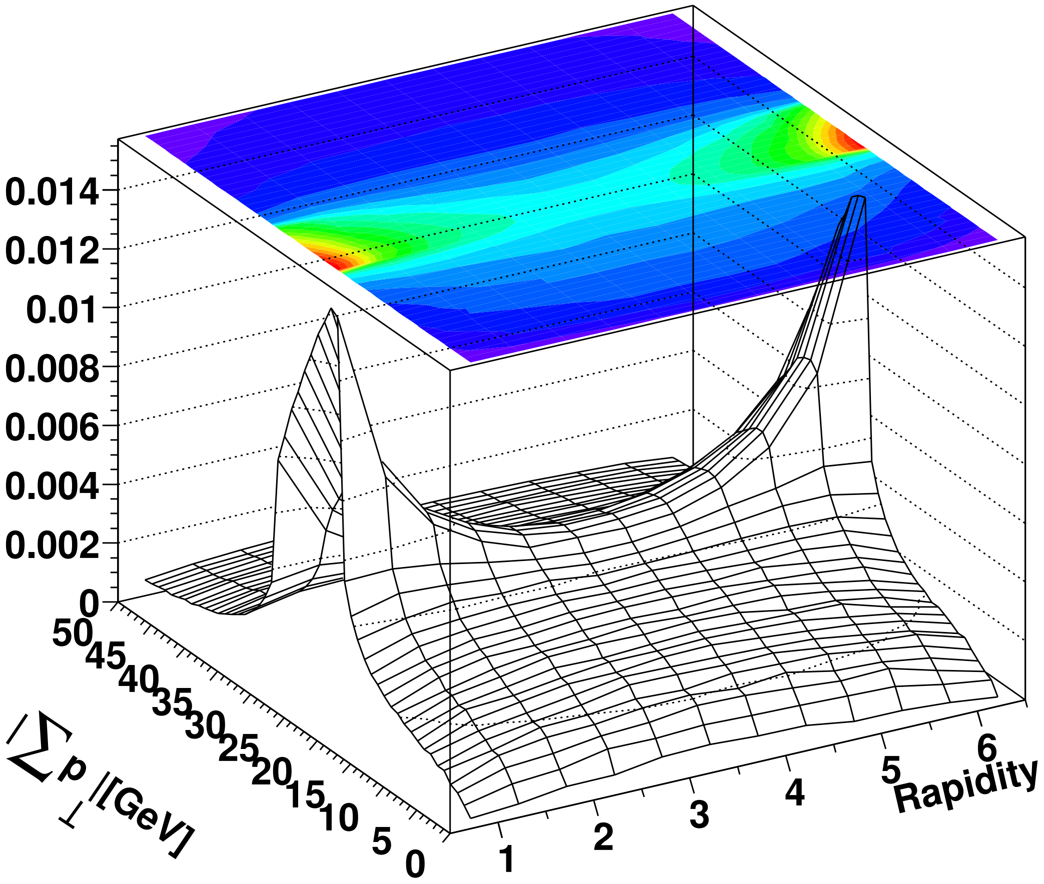

Figure 4.11: Bartel's cigar in the fixed coupling scenario. Please see the text for further details.

figure describes the frequency of appearance of the absolute value of the transverse vector sum. An event with e.g. 8 gluons will contribute to the plot in 9 bins, so that the absolute value of the transverse vector connecting two Lipatov vertices in the chain will be plotted at the average rapidity of the two emitted gluons. The integral of the plot is therefore the differential cross section at 6 units of rapidity times the average number of resolved gluons plus one. We see that the much feared diffusion into the infrared regime of the coupling is apparently not a problem, at least there is no suggestion of such a problem from the fixed coupling calculation. It would be interesting to make connection to the work of Ref.[44] suggesting a dramatic transition to the infrared regime for less modest values of the rapidity span. The slightly strange appearance of Fig. 4.11 could be due to the fact that an event with an extreme amount of gluon radiation will contribute to the plot in many bins, even if the contribution to the cross section from this specific configuration is very low.

Therefore, perhaps the contributions to the plot should be weighted, so that each event configuration only contributes according to its contribution to the cross section, instead of the contribution to the cross section times the number of BFKL gluons (+1) in the event. This could perhaps also help to make a more direct relation between the shape of the figure and the amount of radiation. For example, we know from Fig. 4.9 that the density of emitted gluons is constant along the chain, which is not at all apparent from Fig. 4.11.

4.2 The Hadronic Cross Section

Until now we have been concerned solely with the partonic cross section. It is now time to consider the impact of taking into account the energy taken up by the BFKL radiation. We assume factorisation and the differential hadronic cross section is then given by

$$\mathrm{d}\sigma = x_a f(x_a,\mu_F^2)\, x_b f(x_b,\mu_F^2)\, \mathrm{d}\hat{\sigma}, \tag{4.4}$$

with x_a, x_b given by Eq. (2.63). We will choose a factorisation scale of $\mu_F = (p_{a\perp}+p_{b\perp})/2$. The cross sections in Eq. (4.4) are differentials with respect to the phase space of all involved particles. In the standard analytic approach to BFKL, the partonic cross section has already been integrated over the BFKL radiation, so the factorisation formula of Eq. (4.4) for dijet production is often approximated by [19, 20, 23]

$$\frac{\mathrm{d}\sigma}{\mathrm{d}^2\mathbf{p}_{a\perp}\mathrm{d}^2\mathbf{p}_{b\perp}\mathrm{d}y_a\mathrm{d}y_b} = x_a^0 S(x_a^0, p^2_{\perp\mathrm{min}}) x_b^0 S(x_b^0, p^2_{\perp\mathrm{min}}) \frac{\mathrm{d}\hat{\sigma}_{gg}(\Delta y)}{\mathrm{d}^2\mathbf{p}_{a\perp}\mathrm{d}^2\mathbf{p}_{b\perp}}, \tag{4.5}$$

where $Sg(x,\mu_F)$ is the effective pdf of Eq. (1.58), and

$$x_a^0 = \frac{p_{a\perp}}{\sqrt{s}} e^{y_a}\,, \qquad x_b^0 = \frac{p_{b\perp}}{\sqrt{s}} e^{-y_b}\,. \tag{4.6}$$

are the Bjorken parton momentum fractions in the high-energy limit. a and b label the forward and backward outgoing jet, respectively (except in the Bjorken momentum fractions, where a, b label the incoming gluons). The reason for choosing the minimum transverse momentum for the leading dijets as the factorisation scale is that the partonic cross section will be dominated by this region of phase space. Sometimes the Bjorken x's are approximated by the exact $2 \to 2$ scattering form of Eq. (1.57). Whichever of these last two approximations are chosen, the BFKL gluons are emitted at no cost in energy or longitudinal momentum of the incoming partons. This is because in the high-energy limit, the scattering cross section with BFKL evolution when written on the following form has already been integrated over the BFKL gluon phase space

$$\frac{\mathrm{d}\hat{\sigma}_{gg}(\Delta y)}{\mathrm{d}^2\mathbf{p}_{a\perp}\mathrm{d}^2\mathbf{p}_{b\perp}} = \left[\frac{C_A\alpha_s}{p^2_{a\perp}}\right] f(\mathbf{q}_{a\perp}, \mathbf{q}_{b_\perp}, \Delta y) \left[\frac{C_A\alpha_s}{p^2_{b\perp}}\right]. \tag{4.7}$$

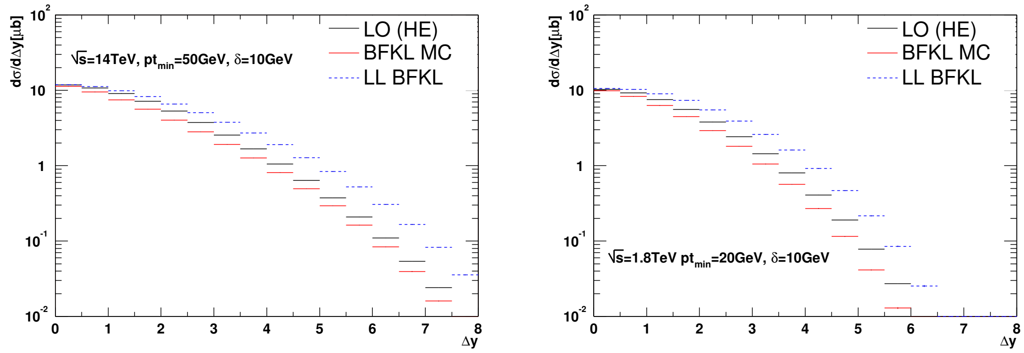

Figure 4.12: The hadronic dijet cross section. Besides the cut on the minimum transverse momentum of the leading dijets, there has been introduced a cut on the scalar sum of the transverse momenta (see text for further details). The value of α_s in the BFKL chain is chosen to be the same for the two plots.

The exponential rise of the partonic cross section with BFKL evolution is driven by the emission of BFKL gluons. At the same time, the approximation of the Bjorken x's in Eq. (4.6) systematically underestimates the correct value of the parton momentum fractions and thereby (in the region of relatively high parton momentum fractions) systematically overestimates the parton flux. By applying the approximations of Eq. (4.6), the BFKL radiation driving the exponential rise in the partonic cross section is emitted at no consequence for the decreasing pdfs. In the rest of this chapter we will investigate the impact of conserving energy and longitudinal momenta on the predictions for BFKL effects in hadronic dijet production. We will use the fit to the pdfs of Ref. [39].

In Fig. 4.12 we have plotted the prediction for the hadronic dijet cross section at the Tevatron and the LHC for the high energy limit of QCD with and without BFKL evolution of the t–channel gluon. We have included the prediction for the BFKL evolution both using the parton momentum fractions in Eq. (4.6) and the exact version of Eq. (2.59). The same quantities are plotted in Fig. 4.13 in the case of the introduction of the running coupling, both at the impact factors and in the BFKL evolution.

The numbers obtained using the truly asymptotic version of the parton momentum fractions obviously still show the same exponential growth over the high energy limit of LO QCD. However, the perhaps surprising and important conclusion to be drawn from these figures is that the reduction in parton flux as a result of adding energy and longitudinal momentum conservation is (at LHC energies) to lower the parton flux in such a way as to approximately cancel the rise in the subprocess cross section with increasing dijet rapidity separation ($\hat{\sigma}_{jj} \sim \exp(\lambda\Delta y)$) predicted from the standard BFKL approach. This strong pdf suppression is due to the dijet production being driven by the gluon pdf, which is very steeply falling in x for the region in x of interest. This means that even the slightest

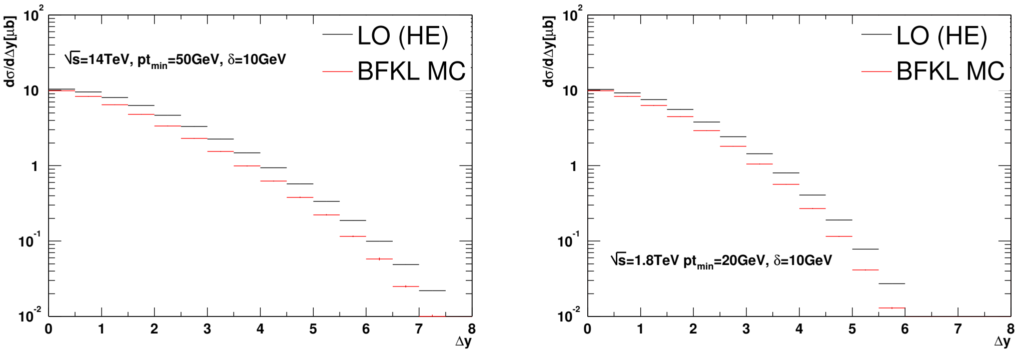

Figure 4.13: The hadronic dijet cross section. The cuts are the same as those used in Fig. 4.12. The predictions using only the leading contribution to the parton momentum fractions has been left out, since the running coupling is only implemented in the BFKL MC, and therefore there is no analytic calculation to compare with.

change in x has a dramatic impact on the parton flux. The leading-order QCD prediction for the hadronic dijet cross section is therefore only slightly modified when including BFKL evolution of the t-channel gluon to an almost no-change situation at the LHC. Note that the overall normalisation of the LL BFKL cross section is questionable, since first of all the relevant scale for evaluating the coupling might well be different from the chosen scale of the transverse momentum of the leading dijets. Secondly, we have not at all discussed the (related) variation of the results with varying renormalisation scale. Therefore, the relevant question to ask is not if the BFKL predictions lie slightly above or below the LO predictions, but whether a different shape in the distributions is predicted.

It turns out that dijet production with a simple cut on the minimum transverse momentum of the jets is extremely infra–red sensitive due to incomplete cancellations of higher order virtual and real corrections on the region of phase space where both jets are close to the lower limit [40]. This problem will be discussed further in Sec. 4.3.4. Here we will just note that the curves in Fig. 4.12– 4.13 have been produced with a lower cut on the transverse momenta of the dijets *and* a lower cut on the sum of the size of the transverse momenta. While at leading order this effectively amounts to just one single cut on the transverse momenta, it has a different effect for higher order corrections and for the BFKL prediction.

With the expected fingerprint of BFKL, the exponential rise of the cross section with increasing rapidity separation between the leading dijets, completely annihilated by the pdf suppression one might fear that the BFKL resummation is completely irrelevant at present collider energies. This would certainly be the case if the result of imposing the energy and momentum conserving constraint was that there would be no energy left to emit any of the higher order BFKL gluons, or if their number would be significantly

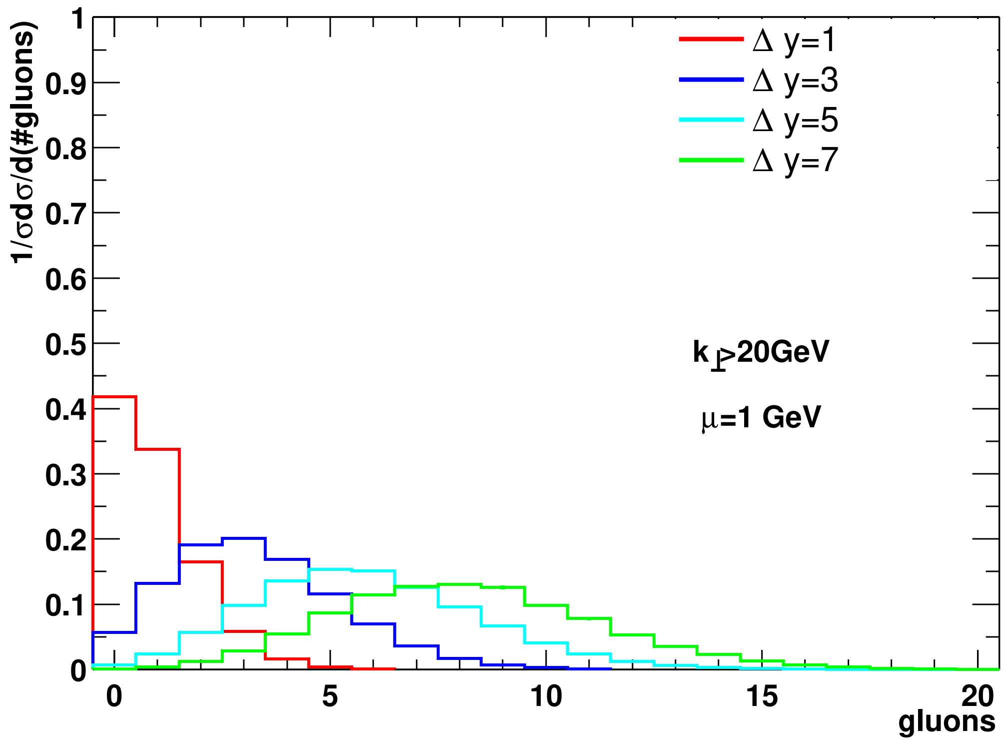

Figure 4.14: The contribution to the hadronic cross section from different number of resolved gluons (constant coupling case). This figure is to be compared with Fig. 4.3 in the partonic case. Since the hadronic cross section falls off rapidly with increasing rapidity span, the cross section for each rapidity span has been normalised to 1.

reduced. This (luckily) turns out not to be the case. In Fig. 4.14 we have plotted the equivalent of Fig. 4.3 for the hadronic cross section. By comparing with Fig. 4.3 we see that the energy and momentum conserving constraint has decreased the number of resolved gluons compared to a calculation of the hadronic dijet production with BFKL based on the asymptotic values of the parton momentum fractions (such a calculation would have identical BFKL signatures to that of the partonic calculations). In Fig. 4.15 we plot the equivalent of Fig. 4.4 for the partonic case. We see again, that the introduction of the pdf constraint has reduced the number of gluons emitted from the BFKL chain. In particular, the amount of harder radiation is significantly reduced for the larger rapidity spans.

In Fig. 4.18 we investigate how this decrease of emission is distributed along the BFKL chain. We have plotted the equivalent of Fig. 4.5 for hadronic dijet production, i.e. after the inclusion of the pdfs evaluated at the relevant energy for the LHC. The figure has many curves, but is not as complicated as it might appear at first sight. The four upper lines describe the number density of resolved gluons, and the lower four lines describe the

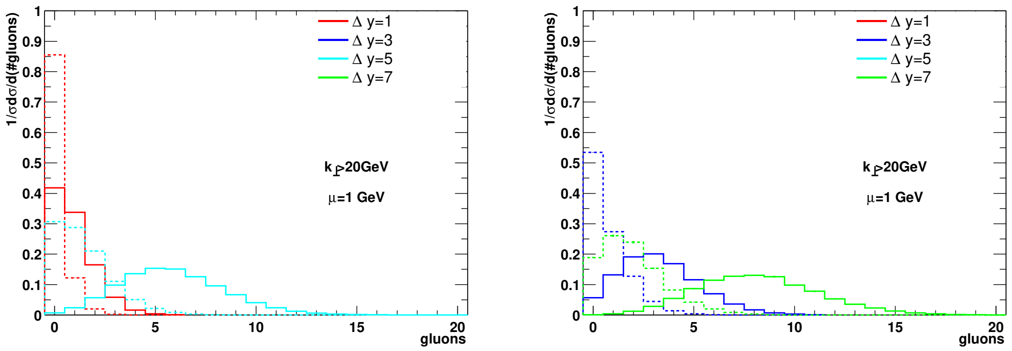

Figure 4.15: The contribution to the hadronic cross section from different number of resolved gluons and harder gluons (constant coupling case). This figure is to be compared with Fig. 4.4 in the partonic case. Since the hadronic cross section falls off rapidly with increasing rapidity span, the contribution for each rapidity span has been normalised to 1.

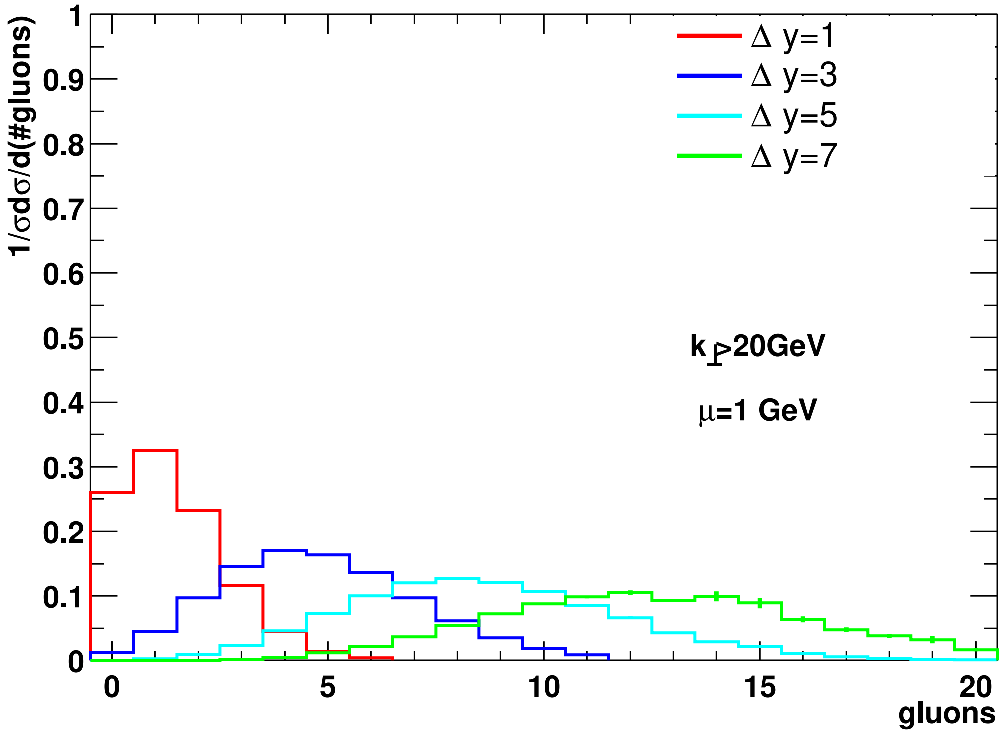

Figure 4.16: The contribution to the hadronic cross section from different number of resolved gluons (running coupling case). This figure is to be compared with Fig. 4.7 in the partonic case. Since the hadronic cross section falls off rapidly with increasing rapidity span, the cross section for each rapidity span has been normalised to 1.

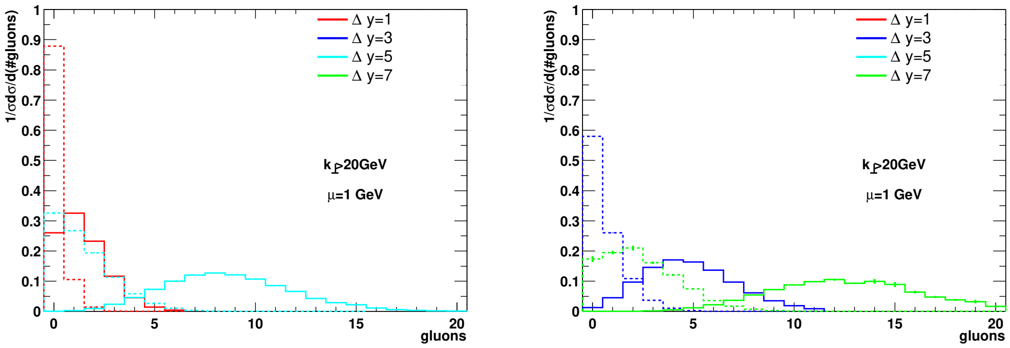

Figure 4.17: The contribution to the hadronic cross section from different number of resolved gluons and harder gluons (running coupling case). This figure is to be compared with Fig. 4.4 in the partonic case. Since the hadronic cross section falls off rapidly with increasing rapidity span, the contribution for each rapidity span has been normalised to 1.

same for harder ($p_\perp > 20$ GeV) gluons. The black lines are obtained by ignoring the contribution of the BFKL radiation to the parton momentum fractions. We see that in this case the prediction from the partonic calculation of a flat distribution of the emission along the chain is unchanged, as expected. The red lines are obtained by evaluating the pdfs at the values of the exact parton momentum fractions of Eq. (2.16), and correspond to the predictions of the BFKL curve in Fig. 4.12. We see that the amount of gluon emission is reduced, just as expected from a comparison between Fig. 4.3 and Fig. 4.14. Fig. 4.18 clearly shows the suppression of radiation close to the endpoints of the BFKL chain. This is caused by the fact that radiation in these regions contributes the most to the increase in the parton momentum fractions. Therefore, radiation in the endpoint regions lead to a relatively bigger pdf suppression than similar radiation in the middle of the chain. The amount of radiation in the central region of the chain is about 92% overall and 75% for the harder radiation compared to the partonic case. At the endpoints the radiation drops significantly lower, but just how much depends on the span of the chain. These numbers depend on the specific shape of the (gluon) pdf, and to access this dependence we have also included the result of performing a similar calculation with toy pdfs that are constant at the value 1 for values of the parton momentum fractions (pmf) between 0 and 1. Such a calculation results in the blue and green line for the leading and full contribution to the pmf respectively. The suppression of radiation at the end points is still visible, but far less dramatic than in the physical case, since the addition contribution from the BFKL radiation to the pmf only has an effect if the pmf thereby increases beyond 1. In the physical case, the pdfs fall off roughly as $(1-x)^7$, and therefore any increase in x has significant consequences.

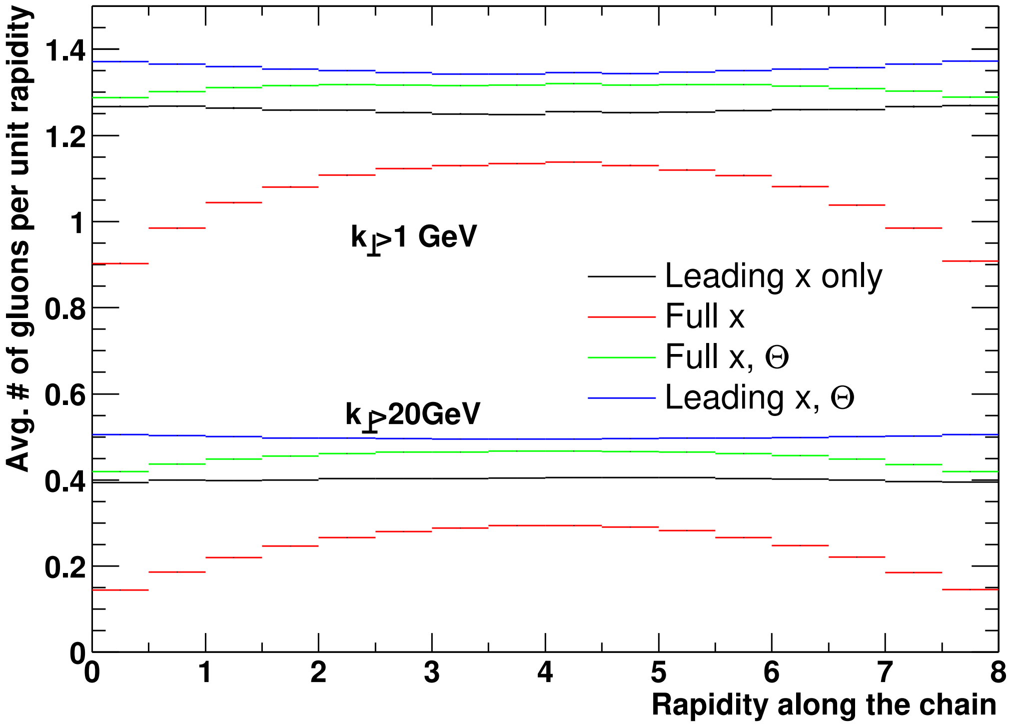

Figure 4.18: The average density of emitted gluons along the BFKL chain for the constant coupling formalism in the case hadronic dijet production. Please see text for further details.

One might at first be surprised to find that there is any difference between the results of the calculations resulting in the blue and the black curves on Fig. 4.18. This difference is presumably generated since in the case of the unphysical flat pdfs the leading dijets are on average much harder than in the physical case. This feeds back into the BFKL equation to give an overall harder event.

The important conclusion to be drawn from Fig. 4.18 is that the suppression of the BFKL evolution is not as dramatic as suggested by the cancellation of the BFKL rise in the dijet cross section by the pdf suppression. Fig. 4.18 might also support the idea of introducing an effective reduced rapidity span of the BFKL chain in analytic calculations. The BFKL evolution is obviously most important in a reduced rapidity span, where the BFKL emission is only slightly reduced compared to the partonic prediction. In the next section we will discuss an observable less sensitive to the steepness of the gluon pdf.

4.2.1 Angular Decorrelation

The leading dijets will at leading order be back–to–back. However, the distribution of the azimuthal angle between the jets is smeared by gluon radiation and by hadronisation. Part of the gluon radiation originates from the mechanism responsible for BFKL effects, namely from gluon radiation in the rapidity interval between the jets. Accordingly, the transverse momentum imbalance [23, 41] and the azimuthal angle decorrelation [19, 23, 24, 38, 42] have been proposed as observables sensitive to BFKL effects, even when the pdf suppression is taken into account. This is because that the pdf dependence to some extent will cancel in forming the ratio when calculating the average azimuthal angle of the leading dijets, and therefore the result will be closer to what is expected from the partonic calculation.

To be specific, we will study the average azimuthal angle between the dijets as a function of the rapidity difference between them. The partonic prediction can be calculated analytically by use of the closed form Eq. (2.54) of the solution to the BFKL equation. Although the pdfs will cancel to some extent for the full hadronic prediction, there is still some residual dependence on the energy of the event. As the kinematic limit of dijet production is neared, the event configuration must go back to the pure dijet case of only two partons produced. This means that the leading dijets go back to the back–to–back LO configuration. This feature will be completely missed in the analytic approach, where the energy–consumption of the BFKL radiation is not taken into account. This will potentially pose a big problem for the analytic approach, since it will first of all predict a too big decorrelation between the dijets with increasing rapidity span of the BFKL chain, and secondly it will predict this to continue to the kinematic limit. It is not clear a priori in which region of rapidities the analytic prediction will be valid, since first "asymptotic values" of the rapidity span has to be reached for the formalism to be valid, but these "asymptotic values" cannot be too big in order not to be in conflict with the total energy available at the collider. In essence, examining this problem is what the construction of the Monte Carlo approach is all about.

It is clear that the LO prediction of the back–to–back dijets is very sensitive to higher order corrections. It is also very sensitive to any cut in phase space that might spoil the cancellation between virtual and real higher order corrections. Therefore, in Fig. 4.19 we have plotted the average azimuthal angle between the leading dijets as a function of the rapidity separation between them with the same cut on the sum of the transverse momenta of the leading dijets mentioned earlier. We have plotted the numbers for both the case of the asymptotic versions of the pmf and that of the exact form. A striking feature of the plot is the apparent linear decrease of the cosine of the average azimuthal angle with

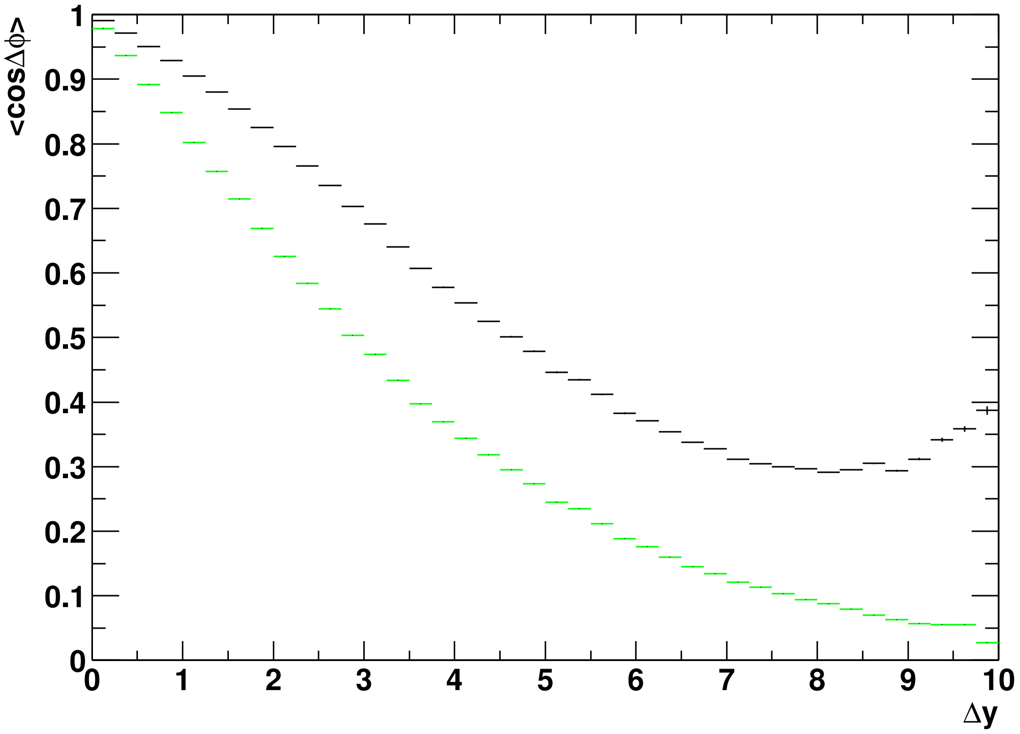

Figure 4.19: The average azimuthal angle of the leading dijets as a function of the rapidity separation between them. The black points is obtained using the exact form of the parton momentum fractions, whereas the green points are those obtained using the asymptotic version. The MC errors are underestimated on this plot, since the same random numbers were used in forming the numerator and denominator of the of relevant fraction, and therefore the respective errors are correlated. This was not taken into account in calculating the MC errors of the figure.

increasing rapidity separation in the region of rapidity separation between roughly 2 and 6. This linear behaviour is expected if every extra unit of rapidity span is filled with the same amount of radiation, which is exactly what the conclusion from the equivalent of Fig. 4.18 for a short rapidity span, where the plateau of radiation is reached closer to the ends of the chain. Therefore, one might argue that the BFKL evolution is relevant at the LHC only for rapidity separations between say 2 (before *Asymptotia* is reached) and say 6-7 (where the effects of the finite energy available sets in). The exact numbers obviously depends on the specific cuts applied. But the idea remains the same. When conserving energy and momentum, there is both a lower and an upper limit on the rapidity span for the validity for the BFKL approach.

An earlier study [24] of the dijet angular correlation showed reasonable agreement between the Monte Carlo BFKL approach and data from the Tevatron. A NLO QCD calculation gives too little decorrelation between the leading dijets, but both this and the BFKL prediction should be taken as only preliminary results in a comparison with data, since any parton level prediction has to be supplemented with parton showering and hadronisation before comparison with the hadron level data is made. In this way, the LO prediction of back–to–back jets is changed to describe data to the same degree of satisfaction when showering and hadronisation is applied according to the event generator HERWIG[43]. However, this particular study was carried out with equal and opposite cuts on the leading dijets leading to a very high sensitivity to Sudakov logarithms due to the incomplete cancellations between higher order virtual and real corrections. This means that the BFKL logarithms get "polluted" with other logarithms, and it is not clear which leads to the biggest effect. It would therefore be interesting to repeat the experimental study with the choice of a more suitable set of cuts to minimise the Sudakov logarithms.

4.3 Dijet Production at the Tevatron

In this section we will describe a study where we have applied the Monte Carlo approach to BFKL to a study of dijet production at the Tevatron run 1. The study was published in Ref.[35] and contains work from other authors. Specifically, the NLO QCD calculations were performed by Stefano Frixione, and the analytic BFKL calculations are the original work of Vittorio Del Duca and Carl Schmidt. However, for completion we will describe the full work in this thesis.

Long ago Mueller and Navelet suggested [20] to look for evidence of BFKL evolution by measuring dijet cross section at hadron colliders as a function of the hadronic centre-of-mass energy $\sqrt{s}$, at fixed momentum fractions $x_{a,b}$ of the incoming partons. This is equivalent to measuring the rates as a function of the rapidity interval $\Delta y = |y_a - y_b|$ between the jets. In fact, at large enough rapidities we have seen that the rapidity interval is well approximated by the expression $\Delta y \simeq \ln(\hat{s}/|\hat{t}|)$, where $\hat{s} = x_a x_b s$ and $|\hat{t}| \simeq p_{\perp a} p_{\perp b}$, with $p_{\perp a,b}$ being the moduli of the transverse momenta (i.e., the transverse energies) of the two jets. Thus, since the cross section tends to peak at the smallest available transverse energies, Δy grows as $\ln s$ at fixed $x_{a,b}$.

It is clear that the measurement proposed by Mueller and Navelet is not feasible at a collider run at a fixed energy; on the other hand, to look for the BFKL-driven rise of the parton cross section directly in the dijet production rate $d\sigma/\Delta y$ as a function of Δy is difficult due to the steep fall-off of the parton densities, as explained in the previous sections. However, as we have seen, the emission of BFKL gluons in the rapidity span between the leading dijets will lead to some degree of decorrelation in the azimuthal angle. The azimuthal angle decorrelation has indeed been studied by the D0 Collaboration at the Tevatron Collider [45]. As expected, a NLO partonic Monte Carlo generator, JETRAD [46, 47], predicts too little decorrelation. However, the analytic BFKL formalism predicts a much stronger decorrelation than that observed in the data. In fact, the data are well described by the HERWIG Monte Carlo generator [43], which dresses the basic $2 \to 2$ parton scattering with parton showers and hadronisation. This hints at a description of the azimuthal angle decorrelation in terms of a standard Sudakov resummation [48]. It therefore appears that, in the presence of Sudakov logarithms, it is quite difficult to cleanly extract the presence of BFKL logarithms from this observable, not least because the latter are expected to be smaller than the former in the energy range explored at present. It thus comes as no surprise that D0 Collaboration [45] find no strong evidence of BFKL effects in their data.

Recently, the D0 Collaboration [49] has revisited the original Mueller-Navelet proposal, and has measured the ratio

$$R = \frac{\sigma(\sqrt{s_A})}{\sigma(\sqrt{s_B})} \tag{4.8}$$

of dijet cross sections obtained at two different centre-of-mass energies, $\sqrt{s_A} = 1800$ GeV and $\sqrt{s_B} = 630$ GeV. The dijet events have been selected by tagging the most forward/backward jets in the event, and the cross section is measured as a function of the momentum transfer, defined as $Q^2 = p_{a\perp} p_{b\perp}$, and of the quantities

$$x_1 = \frac{2p_{a\perp}}{\sqrt{s}} e^{\bar{y}} \cosh(\Delta y/2)\,, \qquad x_2 = \frac{2p_{b\perp}}{\sqrt{s}} e^{-\bar{y}} \cosh(\Delta y/2)\,, \tag{4.9}$$

with $\bar{y} = (y_a + y_b)/2$, $\Delta y = y_a - y_b \geq 0$, and y_a (y_b) are the rapidities of the most forward (backward) jet. The dimensionless quantities x_1 and x_2 are reconstructed from the tagged jets using Eq. 4.9, irrespective of the number of additional jets in the final state. In leading-order kinematics, for which only two (back-to-back) jets are present in the final state, we have $x_1 = x_a$ and $x_2 = x_b$, the momentum fractions of the incoming partons. Higher-order corrections will spoil this relation; however, if one assumes that $x_1 = x_a$ and $x_2 = x_b$ are still reasonable approximation, this implies that when the ratio in Eq. (4.8) is computed at fixed x_1 and x_2, the contributions due to the parton densities cancel to a large extent, thus giving the possibility of studying BFKL effects without any contamination from long-distance phenomena.

In the analysis performed by D0 [49], jets have been selected by requiring $k_{a,b\perp} >$ 20 GeV, $|y_{a,b}| < 3$, and $\Delta y > 2$. The cross section was measured for ten (x_1, x_2) bins, of which we list in 4.1 the six with the upper bound of the range in x_1 smaller than or equal to the upper bound of the range in x_2 (the others may be obtained by interchanging $x_1 \leftrightarrow x_2$). Finally, a cut on the momentum transfer, $400 < Q^2 < 1000$ GeV^2, has been imposed. With larger statistics, a binning in Q^2 would also be possible. These cuts

	x_1 range	x_2 range
bin 1	0.06-0.10	0.18-0.22
bin 2	0.10-0.14	0.14-0.18
bin 3	0.10-0.14	0.18-0.22
bin 4	0.14-0.18	0.14-0.18
bin 5	0.14-0.18	0.18-0.22
bin 6	0.18-0.22	0.18-0.22

Table 4.1: (x_1, x_2) bins, with the upper bound of range in x_1 not larger than the upper bound of the range in x_2.

select dijet events at large rapidity intervals. To have a crude estimate of the typical Δy values involved, we observe that, in a given (x_1, x_2) bin, the data accumulate at the minimum x_1 and x_2 in order to maximise the parton luminosity, and at minimum $k_\perp$ in order to maximise the partonic cross section. We can then use the LO kinematics (4.9) to obtain the effective rapidity interval. For instance, in bin 5 we find $\Delta y_{_A} \simeq 5.3$ at $\sqrt{s_{_A}}$=1800 GeV, and $\Delta y_{_B} \simeq 3.1$ at $\sqrt{s_{_B}} = 630$ GeV. In addition, we see that in the large–Δy limit, $\Delta y_{_A} \to \Delta y_{_B} + \ln(s_{_A}/s_{_B})$.

The data collected by D0 are compared to BFKL predictions as given by Mueller and Navelet, and an effective 'BFKL intercept' is then extracted (see Eq. (4.21) below). However, we argue in this analysis that the different reconstruction of the x's used by D0 as compared to the original Mueller-Navelet analysis (see Eqs. (4.9) and (4.16)), and some of the acceptance cuts imposed in the experimental analysis, like the introduction of an upper bound on the momentum transfer Q^2, actually spoil the correctness of this procedure, and require modifications of the Mueller-Navelet formulae. These modifications are subleading from the standpoint of the BFKL theory, however they have an impact on the extraction of the BFKL intercept at subasymptotic energies. Furthermore, the fact that dijet events are selected by means of transverse momentum cuts which are the *same* for the two tagged jets poses additional problems: large logarithms of (non-BFKL) perturbative origin enter the cross section, and thus the ratio of Eq. (4.8) is affected by the same kind of problems as the azimuthal decorrelation.

In this study we address the quantitative importance of these issues on the D0 analysis using a combination of analytic and numerical techniques and several different theoretical approximations for dijet production.

4.3.1 The Standard Mueller-Navelet Analysis

By integrating out the azimuthal angles in the solution of the BFKL equation Eq. (2.54), one finds the azimuthally averaged solution

$$\bar{f}(q_{a\perp}, q_{b\perp}, \Delta y) \;=\; \frac{1}{4\sqrt{q_{a\perp}^2 q_{b\perp}^2}} \int_{-\infty}^{\infty} d\nu \, e^{\omega(\nu)\Delta y} \left(\frac{q_{a\perp}^2}{q_{b\perp}^2}\right)^{i\nu}, \tag{4.10}$$

where

$$\omega(\nu) = -2\bar{\alpha}_s \left[\mathrm{Re}\,\psi\left(1/2 + i\nu\right) - \psi(1)\right] \tag{4.11}$$

$$= A - B\nu^2 + \mathcal{O}(\nu^4)\,, \tag{4.12}$$

with ψ the digamma function, and

$$\bar{\alpha}_s \;=\; \alpha_s N_c/\pi, \quad A \;=\; 4\bar{\alpha}_s \ln 2, \quad B \;=\; 14\zeta(3)\,\bar{\alpha}_s, \tag{4.13}$$

Furthermore, with the pmf given by the asymptotic values of Eq. (2.60) we can write the hadronic cross section in the approximation of Eq. (4.5) as [20]

$$\frac{d\sigma}{dx_a^0 dx_b^0} \;=\; \int dp_{a\perp}^2 dp_{b\perp}^2 S(x_a^0, \mu_F)\, S(x_b^0, \mu_F)\, \frac{d\hat{\sigma}_{gg}}{dp_{a\perp}^2 dp_{b\perp}^2}\,, \tag{4.14}$$

In order to elucidate how the D0 Collaboration [49] evaluates the effective BFKL intercept, we follow the original Mueller-Navelet approach [20], i.e. we substitute Eq. (2.44) and Eq. (4.10) into Eq. (4.14) and integrate it over the size of the transverse momenta $p_{a\perp}$ and $p_{b\perp}$ above a threshold $E_\perp$, at fixed coupling α_s and fixed x_a^0, x_b^0. The rapidity interval $\Delta y = |y_a - y_b|$ in Eq. 4.10 is determined from the x's (Eq.2.60),

$$\Delta y = \ln \frac{x_a^0 x_b^0 s}{p_{a\perp} p_{b\perp}} \tag{4.15}$$

and since it depends on $p_{a\perp} p_{b\perp}$, it is not a constant within the integral. However, the dominant, i.e. the leading logarithmic, contribution to Eq. 4.10 comes from the largest value of Δy, which is attained at the transverse momentum threshold, thus in Ref. [20] Δy is fixed at its maximum by reconstructing the x's at the kinematic threshold for jet production and setting them in a one-to-one correspondence with the jet rapidities

$$x_a^{\mathrm{MN}} = \frac{E_\perp}{\sqrt{s}} e^{y_a} \qquad\qquad x_b^{\mathrm{MN}} = \frac{E_\perp}{\sqrt{s}} e^{-y_b}\,. \tag{4.16}$$

Then the factorisation formula (4.14) is evaluated at fixed $x_a^{\mathrm{MN}}, x_b^{\mathrm{MN}}$. Having fixed the rapidity interval (4.15) to

$$\Delta y = \ln \frac{x_a^{\mathrm{MN}} x_b^{\mathrm{MN}} s}{E_\perp^2}\,, \tag{4.17}$$

the integration over $p_{a\perp}$ and $p_{b\perp}$ can be straightforwardly performed[1], and the gluon-gluon cross section Eq. (2.44) becomes

$$\hat{\sigma}_{gg}(p_{a\perp}>E_{\perp}, p_{b\perp}>E_{\perp}) = \frac{\pi C_A^2 \alpha_s^2}{2E_{\perp}^2} \mathcal{F}(\Delta y, 1)\,, \tag{4.18}$$

with

$$\mathcal{F}(z,t) = \frac{1}{2\pi} \int_{-\infty}^{\infty} d\nu\, \frac{e^{\omega(\nu) z}}{\nu^2 + 1/4} \cos(2\nu \ln t)\,. \tag{4.19}$$

For $\bar{\alpha}_s \Delta y \ll 1$, we can expand Eq.(4.19) and obtain [20]

$$\hat{\sigma}_{gg}(\mathbf{p}_{a\perp}>E_{\perp}, \mathbf{p}_{b\perp}>E_{\perp}) = \frac{\pi C_A^2 \alpha_s^2}{2E_{\perp}^2} \left[1 + \mathcal{O}\left((\bar{\alpha}_s \Delta y)^2\right)\right]\,. \tag{4.20}$$

On the other hand, for $\Delta y \gg 1$ we can perform a saddle-point evaluation of Eq. (4.19), and using the small-ν expansion (4.12), we obtain the asymptotic behaviour of the gluon-gluon cross section [18, 50]

$$\hat{\sigma}_{gg}^{(\Delta y \gg 1)}(p_{a\perp}>E_{\perp}, p_{b\perp}>E_{\perp}) = \frac{\pi C_A^2 \alpha_s^2}{2E_{\perp}^2} \frac{e^{A\Delta y}}{\sqrt{\pi B \Delta y/4}}\,. \tag{4.21}$$

At very large rapidities the resummed gluon-gluon cross section grows exponentially with Δy, in contrast to the LO ($\mathcal{O}(\alpha_s^2)$) cross section (4.20), which is constant at large Δy. From the asymptotic formula (4.21) the effective BFKL intercept $\alpha_{\text{BFKL}} \equiv A + 1$ can be derived. In the experiment of Ref. [49] the BFKL intercept is measured by considering the ratio of hadronic cross sections, Eq. (4.14), obtained at different centre-of-mass energies and at fixed $x_{1,2}$ and scale. This, it is hoped, allows the dependence on the parton densities to cancel, and the ratio of hadronic cross sections is therefore approximately equal to that of partonic cross sections evaluated at the relevant Δy values.

In Eq. (4.18) and Eq.(4.21) we have summarised the standard Mueller-Navelet analysis in which it is assumed that the x's are reconstructed through Eq. (4.16), and that the jet transverse momenta are unbounded from above. However, this is not the case for the D0 analysis, since

a) D0 collect data with an upper bound on $Q^2 = p_{a\perp} p_{b\perp}$, which is of the same order of magnitude as the square of the lower cut on the jet transverse momenta, and thus cannot be ignored in the integration over the transverse momenta.

b) D0 reconstruct the x's through Eq. (4.9), which is well approximated by Eq. (2.60), but not by Eq. (4.16). As we have seen, any BFKL radiation will introduce further corrections in the form of Eq. (2.63), which can have a significant impact on the value of the pdfs.

[1] In order to do the integrals analytically, it is necessary to fix the factorisation scale μ_F in Eq. (4.14), e.g. $\mu_F = E_{\perp}$.

We examine these two issues, and the modifications they entail on Eq.(4.18) and Eq.(4.21), in turn.

4.3.2 Dijet Production with an Upper Bound on Q^2

In the Mueller-Navelet analysis the integration over the transverse momenta is taken up to infinity on the grounds that a finite and large upper bound on the transverse momenta would entail a contribution which is power suppressed in the ratio of the jet threshold to the upper bound. However, D0 collect data with an upper bound on $Q^2 = p_{a\perp}p_{b\perp}$, namely $Q^2_{\mathrm{max}} = 1000$ GeV^2, while $Q^2_{\mathrm{min}} = E^2_\perp = 400$ GeV^2. When $Q^2_{\mathrm{min}} \sim Q^2_{\mathrm{max}}$, the upper bound cannot be ignored in the integration over the transverse momenta.

In order to assess what the modification on Eq. (4.18) and Eq. (4.21) is, we integrate the gluon-gluon cross section of Eq. (4.7) over the transverse momenta $p_{a\perp}$ and $p_{b\perp}$ above a threshold $E_\perp$ with the upper cut $Q^2 < Q^2_{\mathrm{max}}$ imposed. We obtain

$$\hat\sigma_{gg}(p_{a\perp}\!>E_\perp, p_{b\perp}\!>E_\perp, p_{a\perp}p_{b\perp}\!< Q^2_{\mathrm{max}}) = \frac{\pi C_A^2\alpha_s^2}{2E_\perp^2}\left[\mathcal{F}(\Delta y,1) - \frac{E_\perp^2}{Q^2_{\mathrm{max}}}\mathcal{G}\left(\Delta y, \frac{E^2_\perp}{Q^2_{\mathrm{max}}}\right)\right], \tag{4.22}$$

with rapidity interval Δy defined in Eq. (4.17), $\mathcal{F}$ defined in Eq. (4.19), and

$$\mathcal{G}(z,t) = \mathcal{F}(z,t) - \frac{1}{2\pi}\int_{-\infty}^{\infty} d\nu\,\frac{e^{\omega(\nu)z}}{\nu^2+1/4}\,\frac{\sin(2\nu\ln t)}{2\nu}\,. \tag{4.23}$$

The analytic form of Eq. (4.22) depends on the particular definition of the upper cutoff Q^2_{max} that D0 uses, and changes substantially the shape of the gluon-gluon cross section (see Fig. 4.20) and in particular its subasymptotic dependence on Δy. At $\bar\alpha_s\Delta y \ll 1$, we expand the exponentials in Eq. (4.22) and obtain

$$\hat\sigma_{gg}(p_{a\perp}\!>E_\perp, p_{b\perp}\!>E_\perp, p_{a\perp}p_{b\perp}\!< Q^2_{\mathrm{max}}) = \frac{\pi C_A^2\alpha_s^2}{2E_\perp^2}\left[1 - \frac{E_\perp^2}{Q^2_{\mathrm{max}}} + \mathcal{O}\left(\bar\alpha_s\Delta y\right)\right]. \tag{4.24}$$

Thus for the D0 cuts, $Q^2_{\mathrm{max}} = 1000$ GeV^2, Eq. (4.24) lowers the LO cross section (4.20) by 40%. At $\Delta y \gg 1$ a saddle-point evaluation of Eq. (4.22) yields

$$\begin{aligned}\hat\sigma_{gg}^{(\Delta y\gg 1)}(p_{a\perp}\!>E_\perp, p_{b\perp}\!>E_\perp, p_{a\perp}p_{b\perp}\!< Q^2_{\mathrm{max}}) &= \frac{\pi C_A^2\alpha_s^2}{2E_\perp^2}\, e^{A\Delta y} \qquad (4.25)\\ \times\left\{e^{B\Delta y/4}\left[\Phi\left(\frac{\ln(Q^2_{\mathrm{max}}/E^2_\perp)+B\Delta y/2}{\sqrt{B\Delta y}}\right) - \Phi\left(\frac{\sqrt{B\Delta y}}{2}\right)\right] - \frac{E^2_\perp}{Q^2_{\mathrm{max}}}\Phi\left(\frac{\ln(Q^2_{\mathrm{max}}/E^2_\perp)}{\sqrt{B\Delta y}}\right)\right\}&,\end{aligned}$$

with the error function

$$\Phi(x) = \frac{2}{\sqrt\pi}\int_0^x dt e^{-t^2}\,. \tag{4.26}$$

Using the asymptotic expansion of the error function at $x \gg 1$, for very large rapidities $\sqrt{B\Delta y} \gg 1$ and at fixed $Q^2_{\max}/E^2_\perp$ we obtain

$$\hat{\sigma}_{gg}^{(\Delta y \gg 1)}(p_{a\perp}, p_{b\perp} > E_\perp, p_{a\perp}p_{b\perp} < Q^2_{\max}) = \frac{\pi C_A^2 \alpha_s^2}{2E_\perp^2} \frac{e^{A\Delta y}}{\sqrt{\pi B \Delta y/4}} \left[1 - \frac{E_\perp^2}{Q^2_{\max}} \left(1 + \ln \frac{Q^2_{\max}}{E^2_\perp}\right)\right], \tag{4.27}$$

which is simply the asymptotic cross section of Eq. (4.21) reduced by a constant factor. For the D0 values of $E_\perp^2$ and $Q^2_{\max}$, this corresponds to a reduction by a factor of about 4.3 in the standard asymptotic formula (4.21).

Although it might appear from Eq. (4.27) that the only effect of the $Q^2_{\max}$ cut is to change the normalisation relative to Eq. (4.21), which would drop out of the ratio of cross sections, one has to keep in mind that both equations are derived (from Eqs. (4.22) and (4.18) respectively) in the asymptotic limit $\Delta y \gg 1$. In Fig. 4.20 we plot both the integral formulae and their asymptotic solutions. We see that the differences $\hat{\sigma}_{gg} - \hat{\sigma}_{gg}^{(\Delta y \gg 1)}$ are roughly constant with respect to Δy, and thus the relative differences get smaller with increasing Δy. However, at the Δy values relevant to D0 analysis, it appears that non-negligible subleading corrections to the asymptotic formulae should be taken into account when determining the effective BFKL intercept. As can be inferred from Fig. 4.20, these effects are more important when a Q^2 cut is imposed, since in this case it takes longer for the exponential rise with Δy to set in.

In conclusion, the effect of an upper bound on the product of the jet transverse momenta can have a significant effect on both the normalisation and Δy dependence of the gluon-gluon cross section. For the D0 values, the increase of the cross section from small to large Δy is weakened by a factor of approximately 2, as shown in Fig. 4.20. Care must therefore be taken in attributing any observed cross section increase exclusively to the $e^{A\Delta y}$ 'BFKL' factor.

4.3.3 Dijet Production at x's Fixed as in the D0 Set-up

In the analysis performed by D0, the x's are reconstructed through Eq. (4.9). Since the jets are selected by requiring that $\Delta y > 2$, Eq. (4.6) is a good approximation to Eq. (4.9). Conversely, the x's (4.16) used in the Mueller-Navelet analysis are by definition a good approximation to the D0 x's (4.9) only at the kinematic threshold for jet production. Therefore in this section we shall examine the modifications induced on Eq. (4.18) and Eq. (4.21) by defining the x's as in Eq. (4.6). First, we note that in this case the jet rapidities are not fixed, rather in a given (x_a^0, x_b^0) bin all the transverse momenta and rapidities contribute which fulfil Eq. (4.6). Thus the rapidity interval between the jets cannot be used as an independent, fixed observable. For convenience, we rewrite the

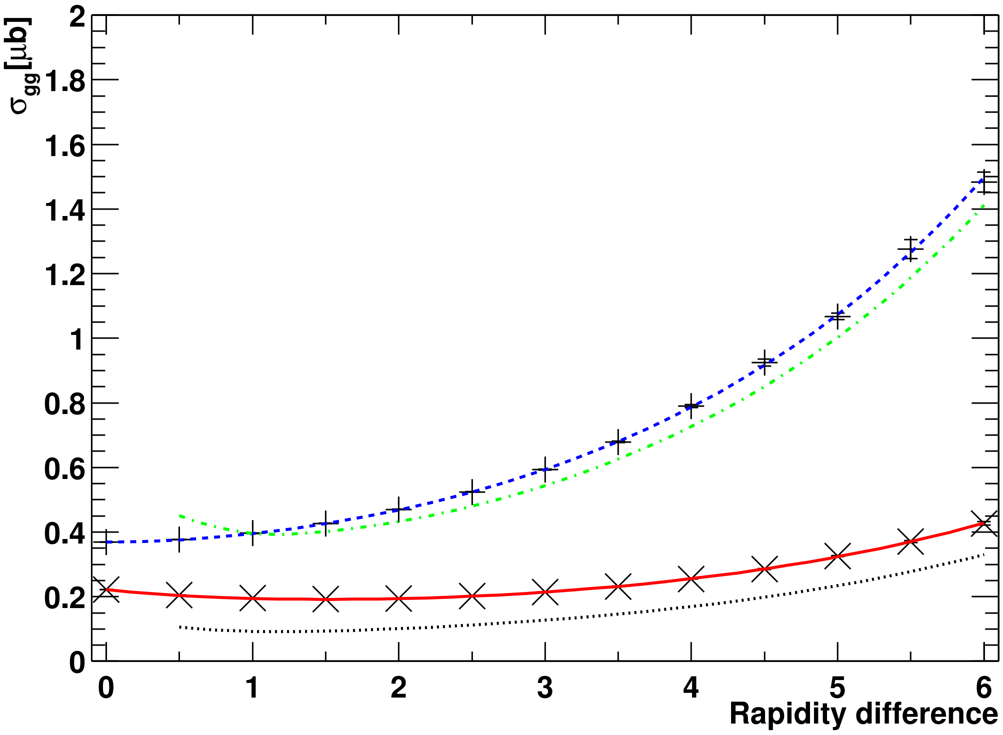

Figure 4.20: The dependence of the LL BFKL gluon-gluon subprocess cross section on the dijet rapidity separation Δy, without (Eq. (4.18), upper dashed line) and with (Eq. (4.22), lower solid line) the $Q^2_{\rm max}$ cut. The 'data points' are the same quantities calculated using the BFKL Monte Carlo, with α_s fixed and no additional kinematic cuts. Also shown are the asymptotic $\Delta y \gg 1$ approximations, Eqs. (4.21) and (4.27). The parameter values are $\alpha_s = 0.164$, $E_\perp = 20$ GeV, $Q^2_{\rm max} = 1000$ GeV^2.

rapidity interval in Eq. (4.15) as

$$\Delta y = Y + \ln \frac{E_\perp^2}{p_{a\perp} p_{b\perp}} \,, \tag{4.28}$$

with[2]

$$Y = \ln \frac{x_a^0 x_b^0 S}{E_\perp^2} \,. \tag{4.29}$$

The requirement that the rapidity interval be positive, $\Delta y \geq 0$, imposes an effective upper bound on Q^2,

$$Q^2_{\rm max} = E_\perp^2 e^Y \,. \tag{4.30}$$

[2]The constant Y resembles the rapidity interval of Eq. (4.17) used in the Mueller-Navelet analysis, however it is not the same since Eq. (4.28) implies that $\Delta y \leq Y$, while Eq. (4.15) and Eq. (4.17) are just two different ways of defining the same rapidity interval.

Integrating then the gluon-gluon cross section (4.7) over $p_{a\perp}$ and $p_{b\perp}$ above $E_\perp$, at fixed x_a^0, x_b^0 and fixed coupling α_s, we obtain

$$\hat{\sigma}_{gg}(p_{a\perp}\!>\!E_\perp, p_{b\perp}\!>\!E_\perp, p_{a\perp}p_{b\perp}\!<Q^2_{\rm max}) = \frac{\pi C_A^2 \alpha_s^2}{2E_\perp^2}\left[\widetilde{\mathcal{F}}(Y,1) - \frac{E_\perp^2}{Q^2_{\rm max}}\widetilde{\mathcal{G}}\left(Y, \frac{E_\perp^2}{Q^2_{\rm max}}\right)\right], \tag{4.31}$$

with

$$\widetilde{\mathcal{F}}(z,t) = \frac{1}{2\pi}\int_{-\infty}^{\infty} d\nu \, \frac{e^{\omega(\nu)z}}{\nu^2 + \dfrac{[1+\omega(\nu)]^2}{4}}\, t^{\omega(\nu)}\, \cos(2\nu \ln t)\,, \tag{4.32}$$

$$\widetilde{\mathcal{G}}(z,t) = \widetilde{\mathcal{F}}(z,t) - \frac{1}{2\pi}\int_{-\infty}^{\infty} d\nu \, \frac{e^{\omega(\nu)z}}{\nu^2 + \dfrac{[1+\omega(\nu)]^2}{4}}\, t^{\omega(\nu)}(1+\omega(\nu))\frac{\sin(2\nu\ln t)}{2\nu}\,, \tag{4.33}$$

and $\omega(\nu)$ as in Eq. (4.11). Note that as $Y \to 0$ in Eq. (4.30), the upper bound on Q^2 goes to the kinematic threshold, $Q^2_{\rm max} \to E_\perp^2$, and accordingly the cross section (4.31) vanishes. Note also that the tilde functions $\widetilde{\mathcal{F}}$ (4.32) and $\widetilde{\mathcal{G}}$ (4.33) reduce to the functions $\mathcal{F}$ (4.19) and $\mathcal{G}$ (4.23) for $\alpha_s \ll 1$ but $\alpha_s Y \approx 1$. This is understandable because the limit $\alpha_s \ll 1$ is equivalent to neglecting subleading corrections, since $(\alpha_s)^2\Delta y \ll \alpha_s \Delta y$, and therefore to neglecting differences in the definition of the rapidity interval, $\Delta y \approx Y$. For $Y \gg 1$ we perform a saddle-point evaluation of Eq. (4.31), and obtain the asymptotic behaviour

$$\begin{aligned} &\hat{\sigma}_{gg}^{(Y\gg 1)}(p_{a\perp}\!>\!E_\perp, p_{b\perp}\!>\!E_\perp, p_{a\perp}p_{b\perp}\!<Q^2_{\rm max}) \\ &= \frac{\pi C_A^2\alpha_s^2}{2E_\perp^2}\frac{e^{AY}}{\sqrt{\pi B Y/4}}\frac{1}{(1+A)^2}\left[1 - \left(\frac{E_\perp^2}{Q^2_{\rm max}}\right)^{1+A}\left(1 + (1+A)\ln\frac{Q^2_{\rm max}}{E_\perp^2}\right)\right]. \end{aligned} \tag{4.34}$$

We can also use the above analysis to include the D0 experimental cuts of $Q^2 < 1000$ GeV^2 and $\Delta y > 2$. In this case the analysis holds unchanged except that the upper bound on Q^2 is given by

$$Q^2_{\rm max} = \min(1000\,{\rm GeV}^2,\, E_\perp^2 e^{(Y-2)})\,, \tag{4.35}$$

where we have used the fact that $\Delta y > 2$ imposes the second effective upper bound on Q^2. The shape of the cross section as a function of Y depends crucially on whether the upper bound on Q^2 is given by Eq. (4.30) or (4.35) (see Fig. 4.21). This is more clearly apparent in the asymptotic region, $Y \gg 1$, since for the upper bound (4.30) we can safely take $Q^2_{\rm max} \to \infty$, with only the first term in the square brackets of Eq. (4.34) contributing; conversely, when the upper bound is given by Eq. (4.35), the sharp cutoff $Q^2_{\rm max} = 1000$ GeV^2 is much more restrictive than the bound (4.30) and depletes the cross section, which is given by the whole Eq. (4.34).

Using Fig. 4.21, we can get some idea of the expected effect of the $\Delta y > 2$ cut on the cross section ratio measured by D0. From Eq. (4.35) we see that this cut is inconsequential when

$$Y > 2 + \ln(1000\ \mathrm{GeV}^2/\mathrm{E}_\perp^2) \simeq 2.92\,, \tag{4.36}$$

where we have used $E_\perp = 20$ GeV. Conversely, this cut removes the entire cross section for $Y \leq 2$. For $\sqrt{s} = 1800$ GeV we find $Y > 2.92$ for all bins, so the cut has no effect. However, for $\sqrt{s} = 630$ GeV we find $Y = 2.37$ in bin 1, $Y = 2.63$ in bin 2, and $Y = 2.88$ in bin 3, where we have used the minimum x_1 and x_2 in each bin to evaluate Y. Thus, bins 1 and 2 (and to some extent bin 3) get depleted at 630 GeV, simply due to the $\Delta y > 2$ cut. In section 4 we will see that this leads to a large cross section ratio in these bins, independent of the BFKL dynamics.

Finally, we note that the asymptotic cross section Eq. (4.34) has the same shape in Y as Eq. (4.21) in Δy but different normalisation: at $\alpha_s(Q^2 = 400\ \mathrm{GeV}^2) = 0.164$, the normalisation of Eq. (4.34) with upper bound (4.30) is a factor 2.1 smaller than the one of the standard asymptotic formula (4.21), which becomes a factor 5.4 smaller than the one of Eq. (4.21) if the upper bound (4.35) is used. However, as Fig. 4.21 shows, for the values of rapidity interval relevant to the D0 analysis we are far from the asymptotic region, and thus all the caveats made at the end of Sec. 4.3.2 on the extraction of the BFKL intercept from the D0 data apply in this case as well.

4.3.4 Equal Transverse Momentum Cuts: a Dangerous Choice

We now take a closer look at the set-up specific to the D0 analysis of Ref. [49]. As a preliminary observation, we might say that the values Δy probed are quite far from the asymptotic region where Eq. (4.21) is expected to hold, particularly at $\sqrt{s} = 630$ GeV, where Δy is of the order of 2 to 3; unfortunately, here the only solution is to wait for the LHC to come into operation. A more serious, but solvable, problem is the following: dijet rates are quite sensitive to the emission of soft and collinear gluons, in the case in which they are defined by imposing equal cuts on the transverse energies of the two tagged jets. In this sense, a dijet total rate is completely analogous to the azimuthal correlation mentioned above. A detailed discussion on this point is given in Ref. [40], and will not be repeated here. In the current study, we will limit ourselves to illustrating the discussion of Ref. [40] by means of examples relevant to dijet production at the Tevatron. We will do this in two steps. First, in Subsection 4.3.5, we will report on a study on this issue using a fixed-order perturbative computation, showing that dijet cross sections defined with unequal transverse momentum cuts do not have the same problems as those defined with

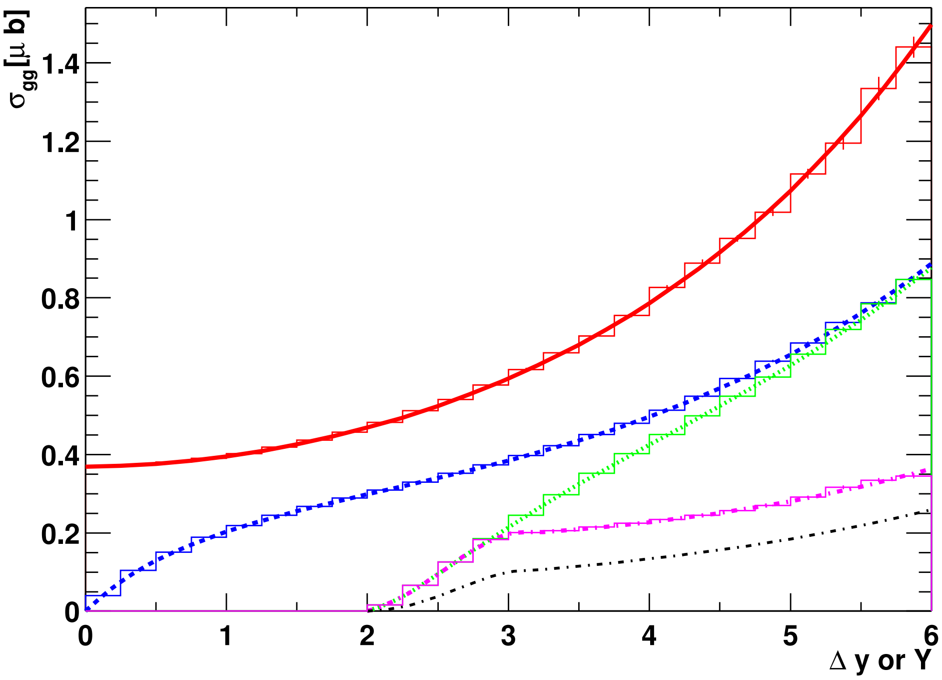

Figure 4.21: The dependence of the LL BFKL gluon-gluon cross section on Δy in the standard Mueller-Navelet calculation (Eq. (4.18)) (upper solid line) and on Y for the D0 setup (Eq. (4.31)). Four curves are shown for the definition of x's applied in the D0 analysis: Dashed line for the requirement $\Delta y > 0$, dotted line for $\Delta y > 2$, dash-dotted for $Q^2_{\rm max}$ of Eq. (4.35) and finally the lower, fat dash-dotted line for the asymptotic behaviour (Eq. (4.34)) using $Q^2_{\rm max}$ of Eq. (4.35). The histograms are filled using the MC.

equal cuts. Then, in Subsection 4.3.6, we will repeat the standard BFKL dijet analysis in the more general case of unequal transverse momentum cuts.

4.3.5 Dijet Cross Sections at Fixed Perturbative Order

In this subsection[3], we consider jet production at fixed perturbative order in QCD. In particular, we use the partonic event generator of Ref. [51], which is accurate to NLO for any one- or two-jet observables. Similarly to what has been done previously for the gluon-gluon cross section, we define a total dijet cross section as follows:

$$\sigma(\mathcal{D},\mathcal{C}) = \sigma(p_{a\perp}\!>\!E_\perp, p_{b\perp}\!>\!E_\perp+\mathcal{D},\mathcal{C}), \tag{4.37}$$

[3]In the fixed order pQCD analysis we set $\mu_F = (p_{a\perp}+p_{b\perp})/2$.

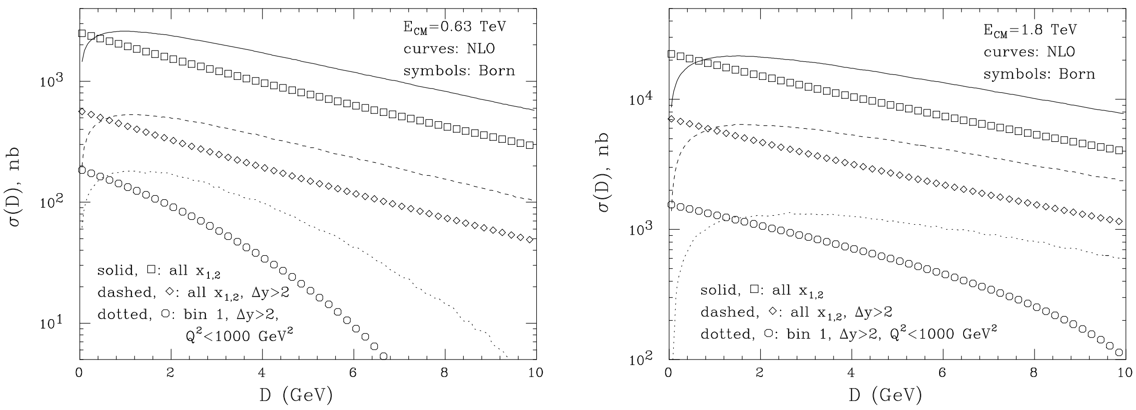

Figure 4.22: Dijet rates, as defined in Eq. (4.37), for various cuts $\mathcal{C}$. The cases of $\sqrt{s} = 630$ GeV (left) and of $\sqrt{s} = 1800$ GeV (right) are both considered. Dotted curves and circles have been rescaled by factor of 10 (left) and 50 (right). See the text for details.

where $\mathcal{C}$ generically indicates a set of cuts to be added to transverse-momentum cuts. As already mentioned, D0 have

$$\mathcal{C}: \qquad |y_i| < 3, \;\; \Delta y > 2, \;\; Q^2 < 1000 \text{ GeV}^2 \tag{4.38}$$

$(i = a, b)$, together with some additional cuts on x_1 and x_2; furthermore, $E_\perp = 20$ GeV.

The rates defined in Eq. (4.37) are shown in Fig. 4.22, the left (right) panel presenting the case of $\sqrt{s} = 630$ GeV ($\sqrt{s} = 1800$ GeV). Each plot consists of three sets of results, corresponding to different choices of $\mathcal{C}$; for each of these choices, both the NLO results (displayed by the solid, dashed, and dotted curves) and the LO results (displayed by the boxes, diamonds and circles) are given. The solid curves and the boxes are obtained by imposing only the pseudorapidity cuts $|y_i| < 3$. The dashed curves and the diamonds correspond to the previous cuts on y_i plus the cut $\Delta y > 2$. Finally, the dotted curves and the circles are relevant to the cuts given in Eq. (4.38), plus those that define bin number 1 (see Table 4.1). Notice that the results relevant to bin 1 have been multiplied by a factor of 10 and 50 at $\sqrt{s} = 630$ GeV and $\sqrt{s} = 1800$ GeV respectively, so that they can be shown together with the other results on the same plot.

From the cross section definition in Eq. (4.37), it is clear that the smaller $\mathcal{D}$, the larger the phase space available; thus, one naively expects that the smaller $\mathcal{D}$, the larger the cross section. This is indeed what happens at the LO level, regardless of the cuts $\mathcal{C}$. On the other hand, the NLO cross section increases when $\mathcal{D}$ decreases *only if $\mathcal{D}$ is not too close to zero*; when $\mathcal{D}$ approaches zero, $\sigma(\mathcal{D})$ has a local maximum, and then turns over, eventually dropping below the LO result. As discussed in Ref. [40], at $\mathcal{D} = 0$ the NLO result is finite (i.e., does not diverge), but the slope $d\sigma/d\mathcal{D}$ is infinite. Fig. 4.22 thus clearly shows that at $\mathcal{D} = 0$ (which corresponds to the definition adopted in the experimental analysis) the

	NLO			Born		
	$\mathcal{D}=0$	$\mathcal{D}=2$	$\mathcal{D}=4$	$\mathcal{D}=0$	$\mathcal{D}=2$	$\mathcal{D}=4$
bin 1	-0.12(6)	1.55(4)	2.62(7)	1.681(3)	2.340(7)	4.16(3)
bin 2	-0.16(4)	1.14(3)	1.46(4)	1.265(3)	1.417(4)	1.739(8)
bin 3	-0.16(5)	0.92(3)	1.13(4)	1.074(3)	1.098(5)	1.138(6)
bin 4	-0.19(6)	0.92(4)	1.15(5)	1.036(4)	1.045(6)	1.068(8)
bin 5	-0.35(5)	0.82(3)	1.01(4)	1.026(4)	1.027(6)	1.020(7)
bin 6	-0.45(9)	0.82(7)	1.08(9)	1.015(9)	1.01(1)	1.00(1)

Table 4.2: Fixed-order predictions for the ratio defined in Eq. (4.8). Numbers in parentheses give the statistical error, which affect the last digit of the results shown. The values of $\mathcal{D}$ are given in GeV.

cross section is affected by large logarithms, that can spoil the analysis performed in terms of BFKL dynamics, exactly as in the case of the azimuthal decorrelation.

Fig. 4.22 already suggests a possible solution to this problem: simply define a dijet rate by considering *different* transverse momentum cuts on the two jets (that is, $\mathcal{D} > 0$). From the plots, we can expect that the potentially dangerous logarithms affecting the region $\mathcal{D} = 0$ are not large starting from $\mathcal{D}$ of the order of 3 or 4 GeV. The figure might also at first sight seem to imply that a similar problem arises in the large $\mathcal{D}$ region in the case in which the (physically relevant) cuts on x_1 and x_2 are imposed (dotted curves and circles). However, it is easy to understand that in such a case the large difference between the NLO and LO results is simply due to phase space: in fact, at LO $\mathcal{D} \geq 0$ effectively forces *both* jets to have $k_\perp > E_\perp + \mathcal{D}$; at NLO, this is no longer true.

Let us therefore consider again the ratio of Eq. (4.8), now rewritten to indicate explicitly the cuts adopted:

$$R(\mathcal{D},\mathcal{C}) = \sigma(\mathcal{D},\mathcal{C};\sqrt{s}=1800\text{ GeV})/\sigma(\mathcal{D},\mathcal{C};\sqrt{s}=630\text{ GeV})\,, \tag{4.39}$$

with $\mathcal{C}$ given in Eq. (4.38), and additional (binning) cuts on x_1 and x_2. Our predictions for R, both at NLO and LO, are presented in Table 4.2, where we show the results for all of the bins of Table 4.1. The entries relevant to $\mathcal{D} = 0$ display a pathological (negative) behaviour at NLO. However, even if they were positive, they could not be considered reliable, since any fixed-order QCD computation (beyond LO) is unable to give a sound prediction in this case. On the other hand, we see that for larger values of $\mathcal{D}$ the situation improves, in the sense that it reproduces our naive expectation: the ratio should converge towards one, for increasing Δy (i.e., larger bin numbers); while for $\mathcal{D} = 2$ GeV the NLO results are still sizeably different from the LO results, in the case of $\mathcal{D} = 4$ GeV the NLO

	$\sqrt{s} = 1.8$ TeV			$\sqrt{s} = 0.63$ TeV		
	$\mathcal{D} = 0$	$\mathcal{D} = 2$	$\mathcal{D} = 4$	$\mathcal{D} = 0$	$\mathcal{D} = 2$	$\mathcal{D} = 4$
bin 1	31.01(3)	21.24(3)	14.19(2)	18.46(3)	9.080(2)	3.399(1)
bin 2	22.66(2)	15.52(2)	10.36(2)	17.91(2)	10.98(2)	5.969(2)
bin 3	13.50(2)	9.22(2)	6.16(2)	12.57(2)	8.39(2)	5.41(2)
bin 4	12.11(3)	8.29(2)	5.54(2)	11.69(3)	7.20(2)	5.19(2)
bin 5	7.19(1)	4.90(1)	3.26(1)	7.10(1)	4.78(2)	3.19(1)
bin 6	4.25(2)	2.89(2)	1.92(1)	4.19(2)	2.85(2)	1.92(1)

Table 4.3: Cross sections in nanobarns as given in Eq. (4.37), at the LO and for two different centre-of-mass energies. Statistical errors are given in parentheses.

and LO results are statistically compatible (within one standard deviation) for bins 3–6, and they are both approaching one.

Inspection of Fig. 4.22 and Table 4.2 tells us that, in order to avoid the presence of large logarithms of non-BFKL nature in the cross section, a value of $\mathcal{D} = 4$ GeV is probably a better choice than $\mathcal{D} = 2$ GeV. Of course, the larger $\mathcal{D}$, the smaller the cross section, and therefore the fewer the events. In order to give an estimate of the loss of events that one faces when going from $\mathcal{D} = 0$ to larger values, we present in Table 4.3 our LO predictions for the rate defined in Eq. (4.37), with the cuts of Eq. (4.38) and our six bins. Of course, it is well known that NLO corrections are mandatory in jet physics to get good agreement with data. However, here we just want to have a rough idea of the number of events lost when increasing one of the transverse energy cuts; this number is sensibly predicted by the ratio $\sigma(\mathcal{D})/\sigma(\mathcal{D} = 0)$, even if σ is only computed at LO. From the table, we see that at $\mathcal{D} = 4$ GeV the number of events decreases, compared to the case $\mathcal{D} = 0$, by a factor slightly larger than two; this factor gets much larger only for the first two bins at $\sqrt{s} = 630$ GeV, which are however less relevant from the point of view of BFKL dynamics.

4.3.6 Dijet Production in the BFKL Theory with an Asymmetric Cut

We now turn again to the BFKL equation, and study the dependence on the offset $\mathcal{D}$ introduced in the previous subsection. We start by integrating the gluon-gluon cross section (4.7) over $p_{a\perp} > E_\perp$ and $p_{b\perp} > E_\perp + \mathcal{D}$ with the upper cut $Q^2 = p_{a\perp} p_{b\perp} < 1000$ GeV^2, and with the x's defined as in the Mueller-Navelet analysis, Eq. (4.16),

$$\hat{\sigma}_{gg}(p_{a\perp} > E_\perp, p_{b\perp} > E_\perp + \mathcal{D}, p_{a\perp}p_{b\perp} < Q^2_{\max}) = \frac{\pi C_A^2 \alpha_s^2}{2E_\perp(E_\perp + \mathcal{D})} \tag{4.40}$$
$$\times \left\{ \mathcal{F}\left(\Delta y, \frac{E_\perp}{E_\perp + \mathcal{D}}\right) - \frac{E_\perp(E_\perp + \mathcal{D})}{2Q^2_{\max}} \left[\mathcal{G}\left(\Delta y, \frac{E_\perp^2}{Q^2_{\max}}\right) + \mathcal{G}\left(\Delta y, \frac{(E_\perp + \mathcal{D})^2}{Q^2_{\max}}\right)\right]\right\},$$

with $\mathcal{F}$ and $\mathcal{G}$ defined in Eq. (4.19) and Eq. (4.23). Repeating the calculation as in Sec. 4.3.3, with the x's defined as in Eq. (4.6), yields a cross section of the same form as Eq. (4.40) up to replacing the rapidity interval (4.17) with the constant (4.29), the upper bound $Q^2_{\max}$ above with Eq. (4.35) and the function $\mathcal{F}$ ($\mathcal{G}$) with $\widetilde{\mathcal{F}}$ ($\widetilde{\mathcal{G}}$), Eq. (4.32) Eq. (4.33). At $\mathcal{D} = 0$ we recover Eq. (4.22) and Eq. (4.31) respectively. However, near $\mathcal{D} = 0$ Eq. (4.40) and its analogous one with the tilda functions display the same qualitative behaviour when expanded to NLO as the exact NLO cross section [40]. In order to see this, we take Eq. (4.40) in the limit $Q^2_{\max} \to \infty$, such that only the first term on the right hand side of Eq. (4.40) survives. We analyse its NLO term by expanding its exponential to $\mathcal{O}(\alpha_s)$,

$$\hat{\sigma}_{gg}(p_{a\perp} > E_\perp, p_{b\perp} > E_\perp + \mathcal{D})$$
$$= \frac{C_A^2 \alpha_s^2}{4E_\perp(E_\perp + \mathcal{D})} \int_{-\infty}^{\infty} d\nu \, \frac{1 - 2\bar{\alpha}_s \Delta y \left[\mathrm{Re}\, \psi\left(1/2 + i\nu\right) - \psi(1)\right]}{\nu^2 + 1/4} \left(\frac{E_\perp}{E_\perp + \mathcal{D}}\right)^{2i\nu} \tag{4.41}$$
$$+ \mathcal{O}\left((\bar{\alpha}_s \Delta y)^2\right).$$

The denominator has poles at $\nu = \pm i/2$. For the LO term, the integration over ν is straightforward. For the NLO term, we use the integral representation of the digamma function,

$$\psi(z) - \psi(1) = \int_0^1 dx \, \frac{1 - x^{z-1}}{1 - x} \tag{4.42}$$

and after performing the integrals over ν and x, we find

$$\hat{\sigma}_{gg}(p_{a\perp} > E_\perp, p_{b\perp} > E_\perp + \mathcal{D})$$
$$= \frac{\pi C_A^2 \alpha_s^2}{2} \left\{ \frac{1}{E_\perp^2} \left[1 - \bar{\alpha}_s \Delta y \left(\frac{-2E_\perp \mathcal{D} - \mathcal{D}^2}{(E_\perp + \mathcal{D})^2} \ln \frac{-2E_\perp \mathcal{D} - \mathcal{D}^2}{E_\perp^2} + 2 \ln \frac{E_\perp + \mathcal{D}}{E_\perp} \right) \right] \theta(-\mathcal{D}) \right.$$
$$\left. + \frac{1}{(E_\perp + \mathcal{D})^2} \left[1 - \bar{\alpha}_s \Delta y \left(\frac{2E_\perp \mathcal{D} + \mathcal{D}^2}{E_\perp^2} \ln \frac{2E_\perp \mathcal{D} + \mathcal{D}^2}{(E_\perp + \mathcal{D})^2} + 2 \ln \frac{E_\perp}{E_\perp + \mathcal{D}} \right) \right] \theta(\mathcal{D}) \right\}$$
$$+ \mathcal{O}\left((\bar{\alpha}_s \Delta y)^2\right). \tag{4.43}$$

At LO, transverse-momentum conservation forces the cross section to behave like $1/E_\perp^2$ for $\mathcal{D} < 0$ and like $1/(E_\perp + \mathcal{D})^2$ for $\mathcal{D} > 0$, even though the cuts over the transverse momenta are asymmetric, see Fig. 4.23. For $\mathcal{D}=0$, Eq. (4.43) reduces to Eq. (4.20). For $|\mathcal{D}| \ll E_\perp$, Eq. (4.43) becomes

$$\hat{\sigma}_{gg}(p_{a\perp}>E_\perp, p_{b\perp}>E_\perp+\mathcal{D}) = \frac{\pi C_A^2 \alpha_s^2}{2E_\perp^2}\left[1 - \bar{\alpha}_s \Delta y \, \frac{2|\mathcal{D}|}{E_\perp} \ln \frac{2|\mathcal{D}|}{E_\perp} + \mathcal{O}(\mathcal{D})\right] + \mathcal{O}\left((\bar{\alpha}_s \Delta y)^2\right) . \tag{4.44}$$

The slope of Eq. (4.43) with respect to $\mathcal{D}$ is negative (positive) for $\mathcal{D} < 0\,(> 0)$, and infinite at $\mathcal{D}=0$, in agreement with Ref. [40]. In addition, by using Eq. (4.44) to evaluate the ratio (4.8) and remembering that asymptotically $\Delta y_{A} \to \Delta y_{B} + 2\ln(1800/630)$, we find that the NLO BFKL ratio also goes to 1 as Δy grows, in agreement with Table 4.2.

In the BFKL Monte Carlo approach, the implementation of asymmetric cuts on the jets is straightforward. For fixed α_s and no additional cuts or parton densities, the analytic result of Eq. (4.40) is reproduced, see Fig. 4.23.

Finally, we can use the BFKL Monte Carlo to calculate the 'D0' cross section ratios defined in Eq. (4.8), in the various bins. Table 4.4 gives the predictions using the Monte Carlo run in two modes:

Naive: fixed α_s, no kinematic constraints, parton densities evaluated at Bjorken x's given in Eq. (4.6).

Full: running α_s, energy–momentum conservation applied, parton densities evaluated at x_a, x_b values given in Eq. (2.63).

Evidently neither the naive BFKL nor the BFKL MC calculation shows the 'pathological' behaviour of the exact NLO calculation at $\mathcal{D}=0$ (this is already apparent from Fig. 4.23). Instead the numbers are quite stable against variations in $\mathcal{D}$. For all $\mathcal{D}$ the naive BFKL calculation shows an initial decrease in the cross section ratios, before reaching a minimum around bin 4 where the expected rise due to BFKL dynamics sets in. The initial decrease is simply the subasymptotic effect of the $\Delta y > 2$ cut on the cross section at $\sqrt{s} = 630$ GeV, as discussed in Section 4.3.3, and consistent with the qualitative behaviour of the Born cross section ratios in Table 4.2. On the other hand, if the effects from the parton densities did factorise out completely, one would expect an asymptotic (in bin number) ratio of $R = (S_A/S_B)^\lambda$ with $\lambda = \frac{\alpha_s C_A}{\pi} 4\ln 2 \approx 0.45$ [26]. This gives $R \approx 2.6$ for the D0 values. However, we have already argued that such a rise is *not* expected in the D0 analysis, mainly because of the rather stringent Q^2 cut (see Fig. 4.20 and Fig. 4.21). Furthermore, the expected rise is also slightly decreased by the cut in $x_a, x_b \le 1$, and hence on $p_{a\perp}$ and $p_{b\perp}$, introduced by the parton densities. The full BFKL MC calculation ratios also show an initial decrease to a minimum around bin 4. However now the ratio is *below* 1 already from bin 3 onwards. Such an effect was already reported and explained in Ref. [26]. It

	Naive BFKL			BFKL MC		
	$\mathcal{D}=0$	$\mathcal{D}=2$	$\mathcal{D}=4$	$\mathcal{D}=0$	$\mathcal{D}=2$	$\mathcal{D}=4$
bin 1	2.16(4)	2.56(5)	3.61(8)	1.615(3)	2.013(5)	2.922(8)
bin 2	1.47(4)	1.53(4)	1.73(4)	1.048(2)	1.114(2)	1.289(3)
bin 3	1.22(4)	1.16(4)	1.10(3)	0.866(2)	0.851(2)	0.872(2)
bin 4	1.18(4)	1.12(4)	1.14(4)	0.806(4)	0.783(2)	0.787(2)
bin 5	1.26(6)	1.14(5)	1.11(5)	0.847(2)	0.824(2)	0.820(3)
bin 6	1.31(8)	1.28(7)	1.20(6)	0.863(3)	0.841(3)	0.838(3)

Table 4.4: BFKL predictions for the ratio defined in Eq. (4.8). Numbers in parentheses give the statistical error, which affect the last digit of the results shown. The values of $\mathcal{D}$ are given in GeV.

is a kinematic effect due to an effective upper limit on the transverse momentum allowed for each emitted gluon. As the rapidity separation between the dijets is increased towards its maximum allowed value, the BFKL gluon phase space is squeezed from above and the 'naive' cross section is heavily suppressed. The higher the collision energy the more dramatic the effect, and hence the ratio R falls below 1.

4.4 Conclusions

In this chapter we started by analysing the characteristics of the BFKL evolution using the BFKL MC approach developed in earlier chapters. We started by observing that the BFKL MC does indeed reproduce the partonic cross section obtained in the analytic approach, and it is stable under variations of the resolution scale. We then analysed in detail some characteristic radiation patterns from the BFKL chain to back the analysis of the energy consumption by the BFKL evolution. Here we found that the contribution to the centre of mass energy results in a given energy being reached about 1.5 units of rapidity before an estimate based solely on the leading dijets. This in turn implies that the contribution from the BFKL evolution to the parton momentum fractions significantly reduces the parton fluxes at present (Tevatron) and future (LHC) collider energies. This implies that the parton level prediction of a BFKL rise of cross section over the leading order result does not carry through to the hadronic level at the given collider energies. We therefore studied the azimuthal angle correlation and found that it is possible to get a prediction for this observable that is much more stable under the observation of energy and momentum conservation. However, the angular correlation is very sensitive to other logarithms when too simplistic cuts are placed on the dijet transverse momenta. However,

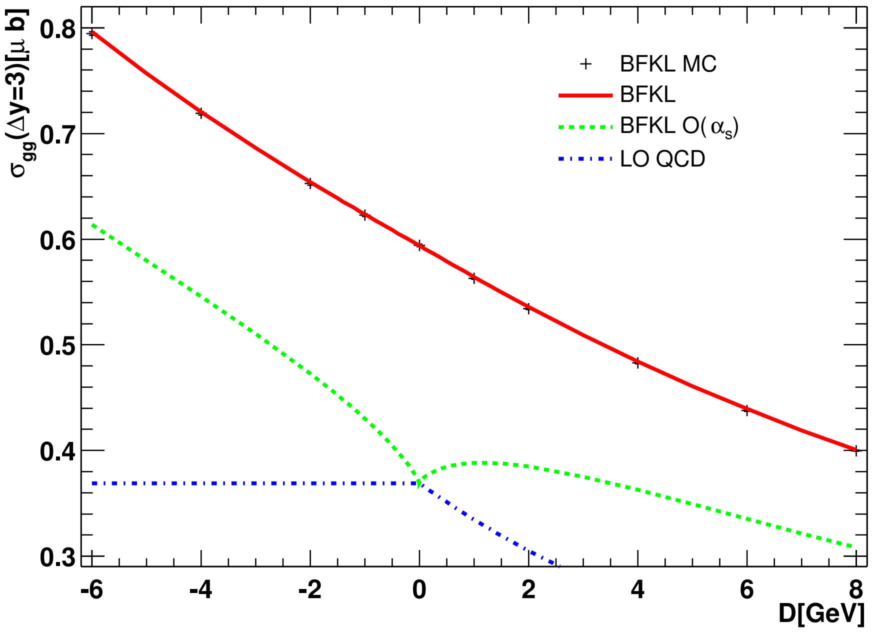

Figure 4.23: The dependence of the gluon-gluon subprocess cross section on the offset $\mathcal{D}$, for fixed separation $\Delta y = 3$. The resummed prediction Eq. (4.40) is shown as a solid line, with the results of the corresponding BFKL Monte Carlo calculation superimposed. The dash-dotted line is the LO contribution, and the dashed line is the $\mathcal{O}(\alpha_s)$ contribution of Eq. (4.43). The parameter values are $\alpha_s = 0.164$, $E_\perp = 20$ GeV, $Q^2_{\max} = \infty$.

it is hoped that future studies will be able to clarify whether there is any hope of getting a good BFKL observable in dijet production.

Finally, we have reconsidered the suggestion by Mueller and Navelet of studying dijet cross sections at large rapidity intervals and for different hadronic centre-of-mass energies, in order to find evidence of BFKL physics. We were motivated by a recent paper by the D0 Collaboration [49], where dijet data have been used to measure the effective BFKL intercept by comparison with the standard analytic asymptotic formulae given by Mueller and Navelet. We have argued that the definition of the momentum fractions used by D0 and some of the acceptance cuts imposed by D0 spoil the correctness of this procedure, and require a more careful theoretical investigation.

In particular, we are concerned by a difference between D0 and the standard Mueller-Navelet analysis in the reconstruction of the momentum fraction x of the incoming partons, by the presence of an upper bound on the momentum transfer Q^2, and by the requirement that the two tagged jets have the same minimum transverse energy.

The Q^2 cut allows, at the experimental level, and together with the binning cuts on

$x_{1,2}$, a reduction of the systematic errors, since in the ratio of the cross sections measured at different centre-of-mass energies the dependence on the parton densities cancels to a significant extent. We have shown that, at the level of partonic cross sections, the upper bound on Q^2 and the x's used in the D0 analysis reduce the Mueller-Navelet cross section by a factor of more than 5. On the other hand, the dependence on such a cut, as well as the dependence on the precise definition of the x's, cancel out when considering the ratio of cross sections obtained at different energies. However, this is only true when the *asymptotic* forms of the cross sections are considered. Unfortunately, at the energies and rapidity intervals probed at the Tevatron, it appears that the asymptotic expansions do not reproduce accurately enough the exact analytic results; in particular, the quality of the approximations are worse in the case in which an upper cut on Q^2 is imposed. We are therefore led to conclude that, regardless of the use of cross sections or of rates of cross sections to study BFKL physics, the effect of an upper bound on Q^2 cannot be ignored.

As far as the cuts on the transverse momenta of the trigger jets are concerned, we have pointed out that in the case in which such cuts are chosen to be equal, even the cross sections (and not just the azimuthal angle correlation) are plagued with large logarithms of perturbative, non-BFKL origin. In this sense, the total dijet rates are therefore on the same footing as the azimuthal decorrelations. We therefore believe that a much safer choice is to have different cuts on the transverse momenta of the two jets.

Chapter 5

W Production with Associated Jets

In this chapter we will discuss another application of the BFKL Monte Carlo to a process in the limit of $\hat{s} \gg \hat{t}$. A motivation for the analysis of processes in the limit $\hat{s} \gg \hat{t}$, and in particular for dijet production in hadron collisions at large rapidity intervals, inclusive or with a rapidity gap, is to use it as a test ground for the production of a Higgs boson in association with jets at the LHC. A Higgs boson is mainly produced via gluon fusion, $g\,g \to H$, mediated by a top-quark loop. If the Higgs-boson mass is above the threshold for vector-boson production, the Higgs boson decays mostly into a pair of W or Z bosons. The signal, though, is likely to be swamped by the $W\,W$, QCD and $t\,\bar{t}$ backgrounds. A Higgs boson of such a mass is also produced in $q\,q \to q\,q\,H$ via electroweak boson fusion, $W\,W$ and $Z\,Z \to H$, though at a smaller rate [52]. However, this would have a distinctive radiation pattern with a large gap in parton production in the central rapidity region, because the outgoing quarks give rise to forward jets in opposite directions [53, 54], with no colour exchanged between the parent quarks that emit the weak bosons [55, 56]. Accordingly, the topology of the final state has been used to reduce the overwhelming $W\,W + 2$-jet background [57]. In fact, requiring two forward jets in opposite directions in $W\,W + 2$-jet production, which implies a large dijet invariant mass, will mean that the parton sub-processes become dominated by gluon exchange in the crossed channel, with the W's produced forward in rapidity.

In this chapter, we analyse forward W production in association with jets as a natural extension of dijet production at hadron colliders, and as a process that for large dijet invariant masses shares the same dynamical features (i.e., gluon exchange in the crossed channel) as $W\,W + 2$-jet production with forward jets, but is considerably simpler to analyse. There are additional reasons to consider this process: firstly, it could be experimentally easier to pick up forward W bosons that decay leptonically than forward jets; once a forward lepton has triggered the event, one observes the jets that are associated to it, with no limitations on their transverse energy. Conversely, in a pure jet sample one usually triggers the event on a jet of relatively high transverse energy, thus the triggering jet cannot be too forward. Secondly, W production in association with jets lends itself naturally to extensions to the high-energy limit, since it favours configurations with a forward W boson, as we shall see in Sec. 5.1.2.

This study has been published in Ref.[58] and contains work by other authors. We will here concentrate on the work performed with the BFKL Monte Carlo but include other parts of the analysis where this helps in putting this into context.

5.1 Kinematics of $W+1$-jet and $W+2$-jet Production

In this section we analyse in detail the kinematics of W production in association with one or two jets, and we show that in $p\,p$ colliders asymmetric configurations with a forward W boson are naturally favoured.[1] The results presented here have been obtained using tree-level matrix elements generated by MADGRAPH [59] and analysed by F. Maltoni, V. Del Duca and W.J. Stirling.

5.1.1 $W+1$-jet Production

We consider the hadroproduction of a W boson with an associated jet. At leading order (LO), the parton subprocesses are $q\,\bar{q} \to W\,g$ and $q\,g \to W\,q$. The momentum fractions of the incoming partons are given through energy-momentum conservation by

$$\begin{aligned} x_a &= \frac{|p_{j_\perp}|}{\sqrt{s}} e^{y_j} + \frac{m_\perp}{\sqrt{s}} e^{y_W} , \\ x_b &= \frac{|p_{j_\perp}|}{\sqrt{s}} e^{-y_j} + \frac{m_\perp}{\sqrt{s}} e^{-y_W} , \end{aligned} \tag{5.1}$$

with $p_{j_\perp}$ the jet (and the W) transverse momentum and $m_\perp = \sqrt{m_W^2 + |p_{j_\perp}|^2}$ the W transverse mass.

We would like to study the typical distributions in y_j and in y_W. At proton-antiproton colliders, the subprocess $q\,\bar{q} \to W\,g$ is leading; since the incoming quark and antiquark are valence quarks and the up and the down quark distribution functions have different shapes, this impose an asymmetry in the rapidity distribution of W^+ versus W^- bosons, both in fully inclusive (Drell-Yan) W boson production [2] and in $W+1$-jet production, and accordingly a large plateau for the rapidity distribution of the W boson as a whole.

[1]Unless stated otherwise, we always understand W to include both W^+ and W^- production.

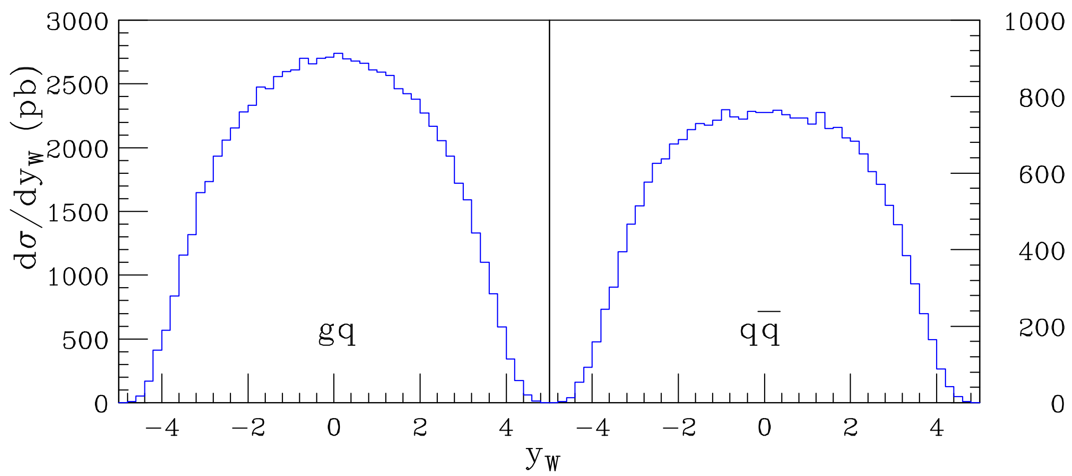

Figure 5.1: Rapidity distributions of the W boson for the subprocesses (a) $q\,g \to W\,q$ and (b) $q\,\bar{q} \to W\,g$ at the LHC centre-of-mass energy $\sqrt{s} = 14$ TeV and with $p_{j_\perp \min} = 30$ GeV.

Also at proton-proton colliders, the W boson may be produced abundantly in the forward rapidity region. As in the $W^\pm$ rapidity asymmetry, the physical mechanism is the difference in the shape of the pdfs of the incoming partons. In fact, to be definite let us consider the subprocess $q\,g \to W\,q$, which at proton-proton colliders is dominant, and suppose that the incoming gluon enters from the negative-rapidity direction while the quark enters from the positive-rapidity direction, so we can identify x_a as the gluon and x_b as the quark momentum fractions. The gluon distribution function is very steep, so it pays off to have x_a as small as possible, which can be achieved by taking y_W negative. That increases considerably the value of x_b, but, because of the shape of the valence-quark distribution function, it can be achieved without paying a high price. In Fig.5.1, we consider the rapidity distribution of the W boson in $W+1$-jet production, broken up into its parton components. The renormalisation and factorisation scales, μ_R and μ_F, are taken to be equal to $(|p_{j_\perp}| + m_\perp)/2$. In Fig.5.1 and Fig.5.6 we have taken the W mass to be $m_W = 80.44$ GeV, we have used the pdfs of the package MRST99cg and evolved α_s accordingly [60]. Applying the argument above to both the gluon incoming directions for $q\,g \to W\,q$, yields a broad rapidity distribution of the W boson, Fig.5.1a. The picture above applies to the subprocess $q\,\bar{q} \to W\,g$ too, Fig.5.1b, since the antiquark is in this case a sea quark.

In case the W boson is produced forward in rapidity, with which rapidity is the jet typically produced? If the jet is produced in the opposite hemisphere with respect to the W boson, the rapidity interval $|y_W - y_j|$ is large, however we know that in this case $W+1$-jet production is strongly suppressed (at LO), since its parton subprocesses can only have

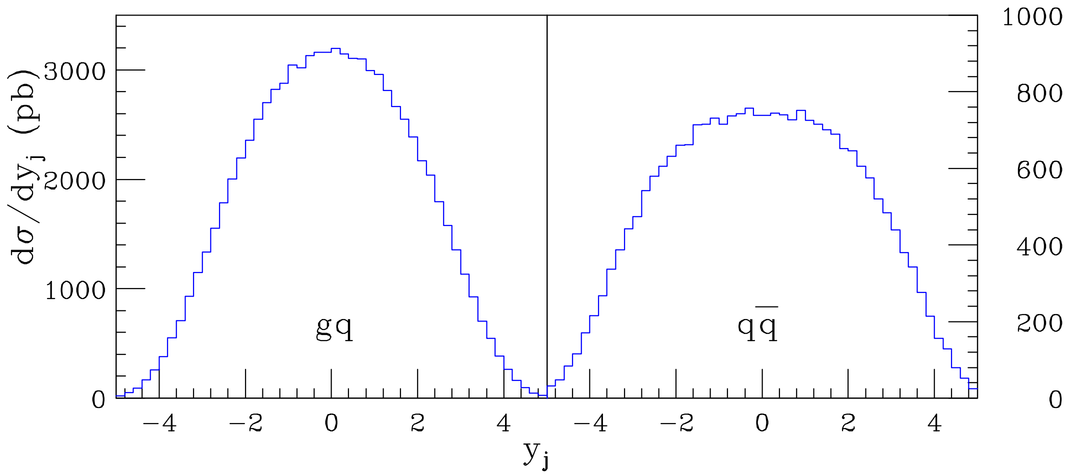

Figure 5.2: Rapidity distributions of the jet for the subprocesses (a) $q\,g \to W\,q$ and (b) $q\,\bar{q} \to W\,g$ at the LHC centre-of-mass energy $\sqrt{s} = 14$ TeV and with $p_{j_\perp \min} = 30$ GeV.

quark exchange in the crossed channel, and thus the related production rate falls off with the parton centre-of-mass energy $\hat{s}$. Thus this configuration is dynamically disfavoured. On the other hand, jet production in the same hemisphere as the W boson or centrally in rapidity keeps x_a small without substantially increasing x_b. However, whether the jet is produced in the central region or in the same hemisphere as the W boson depends on the detailed shape of the pdfs, namely on how large we can afford to make x_b while keeping x_a small. In Fig.5.2 we plot the rapidity distributions of the jet at LHC energies.

5.1.2 $W + 2$-jet Production

Let us consider the hadroproduction of a W boson with two associated jets. At LO the parton subprocesses are

$$\begin{aligned}
&(a) \quad g\,g \to W\,q\,\bar{q}\,, \\
&(b) \quad q\,\bar{q} \to W\,g\,g, W\,q\,\bar{q}\,, \\
&(c) \quad q\,q \to W\,q\,q\,, \\
&(d) \quad q\,g \to W\,q\,g\,.
\end{aligned} \tag{5.2}$$

The momentum fractions of the incoming partons are given through energy-momentum conservation by

$$\begin{aligned}
x_a &= \frac{|p_{j_1\perp}|}{\sqrt{s}} e^{y_{j_1}} + \frac{|p_{j_2\perp}|}{\sqrt{s}} e^{y_{j_2}} + \frac{m_\perp}{\sqrt{s}} e^{y_W}\,, \\
x_b &= \frac{|p_{j_1\perp}|}{\sqrt{s}} e^{-y_{j_1}} + \frac{|p_{j_2\perp}|}{\sqrt{s}} e^{-y_{j_2}} + \frac{m_\perp}{\sqrt{s}} e^{-y_W}\,,
\end{aligned} \tag{5.3}$$

subprocesses	$\sigma(W^+)$	$\sigma(W^-)$
$g\,g \to W\,q\,\bar{q}$	170	170
$q\bar{q} \to W\,g\,g + W\,q\,\bar{q}$	580	400
$q\,q \to W\,q\,q$	400	300
$q\,g \to W\,q\,g$	3300	2200

Table 5.1: Total cross sections (pb) for the production of $W^\pm$ boson in association with two jets with transverse momentum $p_{j_{1,2}\perp} \geq 30$ GeV and interjet distance $R(j_1, j_2) = \sqrt{(y_{j_1} - y_{j_2})^2 + (\phi_{j_1} - \phi_{j_2})^2} \geq 0.4$ on the rapidity-azimuthal angle plane.

with $p_{j_{1,2}\perp}$ the jet transverse momenta and $m_\perp = \sqrt{m_W^2 + |\mathbf{p}_{j_1\perp} + \mathbf{p}_{j_2\perp}|^2}$ the W transverse mass. For the four subprocesses of Eq. (5.2), the total cross section for the production of a W boson in association with two jets is given in Tab.5.1.

Next, we would like to study the rapidity distributions of the W boson and the two jets. In Fig.5.3 and Fig.5.6 we plot the rapidity distributions of the W and of the two jets in $W + 2$-jet production. The renormalisation and factorisation scales, μ_R and μ_F, are taken to be equal to $(|p_{j_1\perp}| + |p_{j_2\perp}| + m_\perp)/2$. The subprocess $g\,g \to W\,q\,\bar{q}$ is perfectly symmetric, thus the W boson and the two jets are produced mostly in the central rapidity region. However, in the other subprocesses this is not the case: looking at the distributions in y_W (Fig.5.3) we see that as we move from (a) to (d) the W boson tends to be produced more and more forward in rapidity. Examining the distributions in y_{j_2} (Fig.5.4), where j_2 is the jet that is closest to the W, we see that this jet tends to follow the W in rapidity. From the distributions in $y_{j_1} - y_{j_2}$ (Fig.5.5), we see that in (a) and (b) jet 1 tends to be produced more centrally; in (d) it follows the W boson and jet 2, thus emphasizing the kinematical features already noted in $W + 1$-jet production (the twin peaks observed in Fig.5.5 in (a), (b) and (d) are due to requiring two jets with interjet distance $R(j_1, j_2) \geq 0.4$); finally in (c) it tends to be produced far in rapidity from the W boson and jet 2.

To understand how these configurations come about, we consider $q\,g \to W\,q\,g$ and follow the analysis of Sec.5.1.1, i.e. we identify x_a as the gluon and x_b as the quark momentum fractions. To make x_a as small as possible at the price of increasing x_b, the W boson is produced forward (Fig.5.3). Note that with respect to Sec.5.1.1 this is made easier by the presence of two jets, which let the W boson have a transverse momentum as small as kinematically possible: ultimately, when the jets are balanced in transverse momentum, the W transverse mass reduces to the mass, $m_\perp \to m_W$. In addition, one jet, say j_2, is always linked to the W boson via a quark propagator as in $W + 1$-jet production, so it tends to follow the W in rapidity, as in Fig.5.4, however the position of the other jet is a dynamical feature peculiar of $W + 2$-jet production: thanks to the gluon exchanged

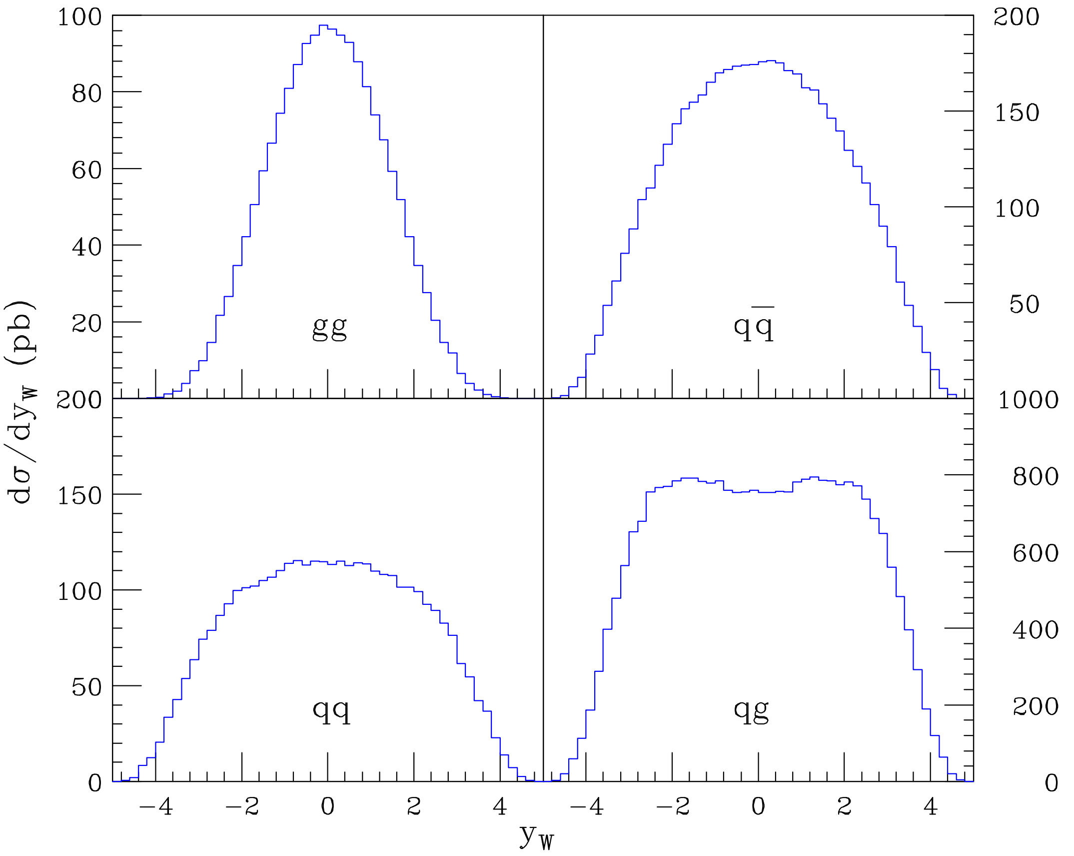

Figure 5.3: Distributions in y_W for the subprocesses of Eq. (5.2) at the LHC centre-of-mass energy $\sqrt{s} = 14$ TeV and with $p_{j_\perp \mathrm{min}} = 30$ GeV.

in the crossed channel, that jet can be easily separated in rapidity from the W boson. In $q\bar{q} \to W\,g\,g, W\,q\,\bar{q}$, the kinematical mechanism is the same as in $q\,g \to W\,q\,g$ since the antiquark has a sea quark pdf, however only $q\bar{q} \to W\,q\,\bar{q}$ can have a gluon exchanged in the crossed channel. For $g\,g \to W\,q\,\bar{q}$, which has equal pdfs for the incoming particles and no gluon exchanged in the crossed channel, we obtain a central distribution, as expected. Note, however, that in Fig.5.3 and following the contribution of $g\,g \to W\,q\,\bar{q}$ to $W + 2$-jet production is quite small. The $q\,q \to W\,q\,q$ channel is peculiar, since the largest contribution comes from valence-quark distributions, which tend to have rather large x's. In addition, at the dynamical level it features only diagrams with gluon exchange in the crossed channel. Thus to make one x large, it tends to have the W boson and a jet slightly forward in rapidity, while to make the other x large, it has the second jet well forward (and opposite) in rapidity.

Next, we require that the two jets are produced with a sizeable rapidity interval, $|y_{j_1} - y_{j_2}| \geq 2$, and look at the rapidity distribution of the W boson with respect to the jet average, $y_W - (y_{j_1} + y_{j_2})/2$ (Fig.5.6). Now the requirement that the rapidity interval

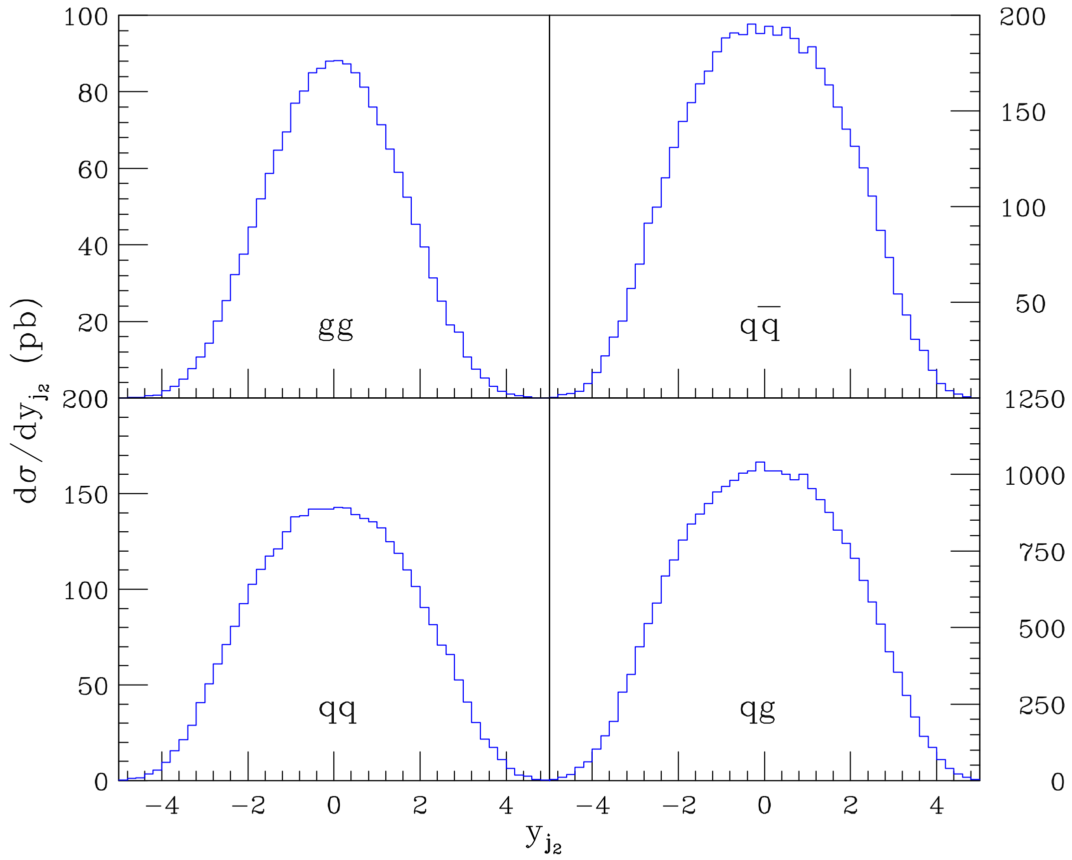

Figure 5.4: Distributions in y_{j_2}, where j_2 is the jet that is closest to the W, for the subprocesses of Eq. (5.2) at the LHC centre-of-mass energy $\sqrt{s} = 14$ TeV and with $p_{j_\perp \min} = 30$ GeV.

between the jets is large makes the subprocesses with gluon exchange in the crossed channel stand out even more, and the W boson, which is linked to one of the jets by quark exchange in the crossed channel, to follow that jet in rapidity. This is stressed by the double peaks in (b), (c) and (d). Note that the dip between the peaks is maximal for $q\,q \to W\,q\,q$, which features only diagrams with gluon exchange in the crossed channel. Conversely $g\,g \to W\,q\,\bar{q}$ yields the W boson in the central rapidity region and approximately equidistant from the two jets, however it is strongly suppressed since it can only have quark exchange in the crossed channel.

The plots of Fig.5.6 are characterised by the dominance of the subprocesses featuring gluon exchange in the crossed channel. The same feature is exhibited by events where we select the jet, say j_1, that in rapidity is furthest away from the W, require that $|y_W - y_{j_1}| \geq 2$, and examine the distribution in $y_W - y_{j_2}$. Since in this case j_2 is always linked to the W boson by quark exchange, the distributions are all centered about zero. The leading subprocesses factorise then naturally into two scattering centres: an impact factor for

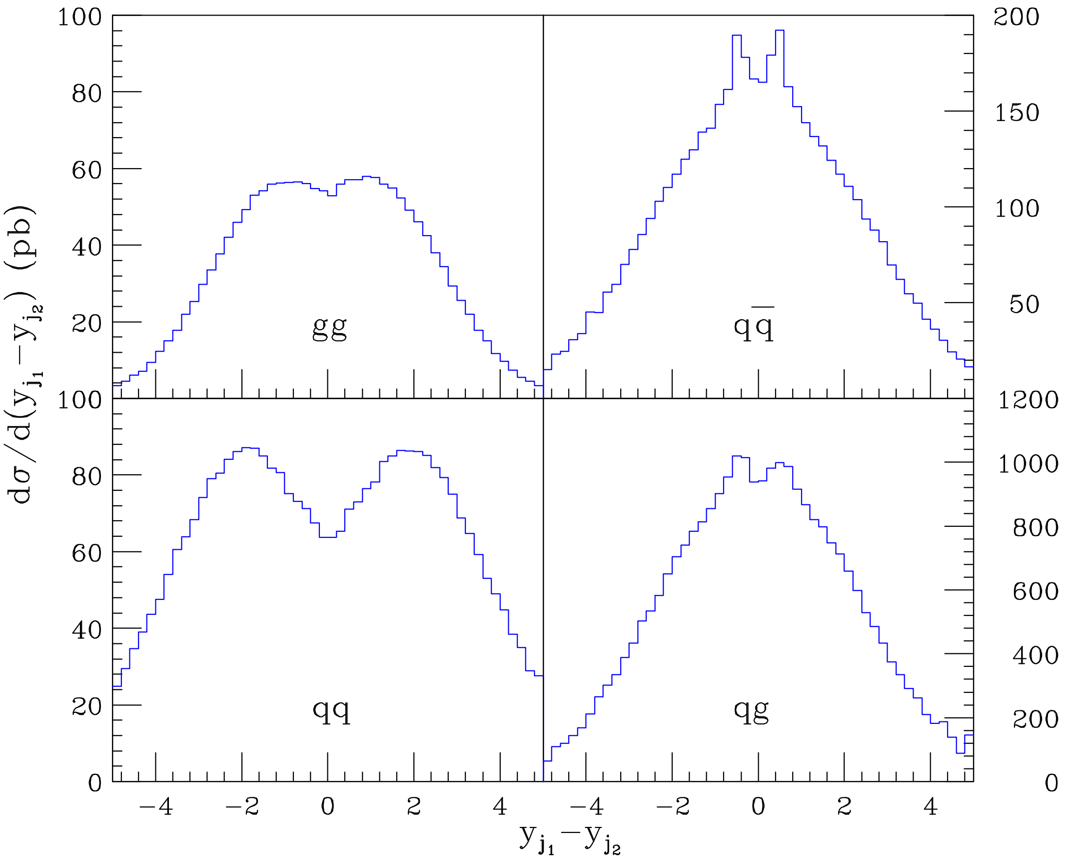

Figure 5.5: Distributions in $y_{j_1} - y_{j_2}$ for the subprocesses of Eq. (5.2) at the LHC centre-of-mass energy $\sqrt{s} = 14$ TeV and with $p_{j_\perp \mathrm{min}} = 30$ GeV.

$W + 1$-jet production, and an impact factor for jet production. The two impact factors are connected by the gluon exchanged in the crossed channel. Accordingly, the dashed lines of Fig. 5.6 have been obtained by taking the high-energy limit of the amplitudes featuring crossed-channel gluon exchange (see Eq. (5.13). On these amplitudes we can then insert the universal leading-logarithmic corrections of $\mathcal{O}(\alpha_s^n \ln^n(\hat{s}/|\hat{t}|))$, and resum them through the BFKL equation.

5.2 The Production Rate for $W + 2$ Jets

In the collision of two hadrons A and B, the differential production rate of a W boson with two associated jets is given in terms of the rapidities and transverse momenta by

$$\frac{d\sigma}{d^2p_{j_1\perp} d^2p_{j_2\perp} d^2p_{W_\perp} dy_{j_1} dy_{j_2} dy_W} = \sum_{ij} x_a f_{i/A}(x_a, \mu_F^2)\, x_b f_{j/B}(x_b, \mu_F^2)\, \frac{|\mathcal{M}_{ij}|^2}{256\pi^5 \hat{s}^2}\, \delta^2\left(p_{W_\perp} + p_{j_{1\perp}} + p_{j_{2\perp}}\right) , \tag{5.4}$$

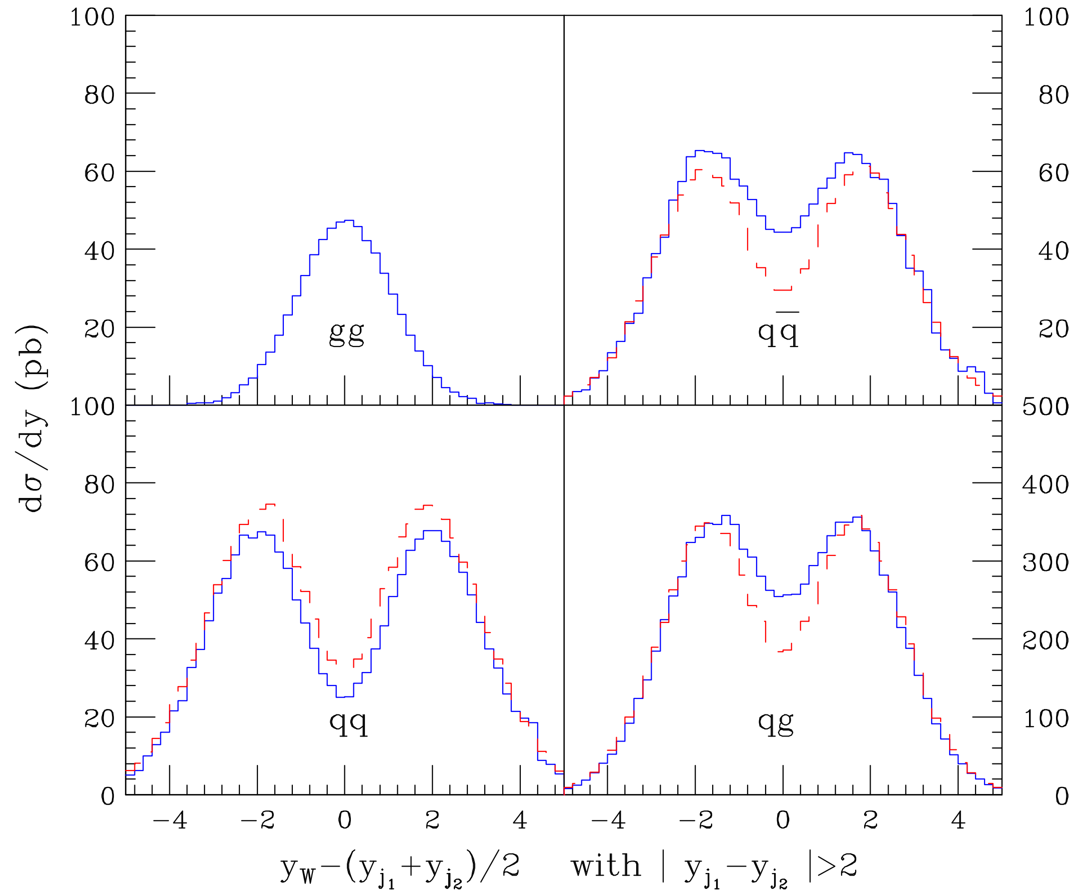

Figure 5.6: Distributions of the rapidity of W boson with respect to the jet average, $y_W - (y_{j_1} + y_{j_2})/2$ at $|y_{j_1} - y_{j_2}| \geq 2$ for the subprocesses of Eq. (5.2) at the LHC centre-of-mass energy $\sqrt{s} = 14$ TeV and with $p_{j\perp\min} = 30$ GeV. The dashed line has been generated by taking the amplitudes in the high-energy limit, as explained after Eq. (5.13).

with parton momentum fractions (5.3). In Eq. (5.4) the dynamics of the scattering is fully contained in the squared amplitude.

In W + 2-jet production in the limit $|y_{j_1} - y_{j_2}| \gg 1$ (see Sec.5.1.2), the parton subprocesses $q\,q \to W\,q\,q$ and $q\,g \to W\,q\,g$ and $q\,\bar{q} \to W\,q\,\bar{q}$ all feature gluon exchange in the crossed channel. Thus the functional form of the corresponding QCD amplitudes is the same, just as for the simpler case of dijet production. They differ only by the colour strength in the impact factor for jet production, separated from the impact factor for W boson and the other jet by the gluon in the crossed channel. The impact factor for W+jet production can now be calculated using spinor techniques and neglect subamplitudes with like–helicity gluons, since these will be subleading in the high–energy limit. An alternative approach is to calculate the squared amplitude for $qg \to qgW$ scattering, and then take the high–energy limit defined in this case as

$$y_W \simeq y_q \gg y_g \,, \qquad\qquad |p_{W_\perp}| \simeq |p_{q_\perp}| \simeq |p_{g_\perp}| \,. \tag{5.5}$$

This is the approach chosen in Ref.[58]. In the high energy limit, the squared matrix element factorises into two impact factors connected with a t–channel gluon exchange, just as in the dijet case. We can then identify an outgoing parton with a (anti)quark, while the other, which we will call b', we can take to be a gluon according to the effective subprocess approximation. The squared amplitude summed (averaged) over final (initial) colours and helicities, reduces to

$$|\overline{\mathcal{M}}_{q\,g\to W\,q\,g}|^2 = \frac{4\hat{s}^2}{\hat{t}^2} I^{qW}(p_a, p_q, p_W, q) I^g(p_b, p_{b'}) \,, \tag{5.6}$$

with

$$I^{qW}(p_a, p_q, p_W, q) = -\frac{\delta^{cc'}}{2N_c t_{abb'} t_{a'bb'}} g^2 \frac{g_W^2}{2} \left[m_W^2 \frac{t_{abb'}}{t_{a'bb'}} \left(z + \frac{t_{a'bb'}}{t_{abb'}} \right)^2 - \hat{t}\left(1+z^2\right) \right] \,, \tag{5.7}$$

where we have defined the light–cone momentum fraction

$$z = \frac{p_q^+}{p_q^+ + p_W^+} \,, \tag{5.8}$$

and Lorentz invariants

$$\begin{aligned} t_{a'bb'} &= (p_a + p_W)^2 \approx -p_q^+ p_W^- - |p_{W_\perp}|^2, \\ t_{abb'} &= (p_q + p_W)^2 \end{aligned} \tag{5.9}$$

In Eq. (5.7), q describes the momentum flow into the impact factor from the crossed channel. In this formulation, the Kronecker delta $\delta^{cc'}$ combines with a similar $\delta^{cc'}$ from the one–jet gluon impact factor

$$I^g(p_j, p_{j'}) = g^2 \,\frac{C_A}{N_c^2 - 1}\, \delta^{cc'} \,. \tag{5.10}$$

We see that this gluon impact factor indeed does lead to the same result as in Eq. (2.44), if the matrix element squared for dijet production is written on the same factorised form as Eq. (5.6). This is in fact how the $W + 1$jet impact factor can be found starting from the $W + 2$jet matrix element squared. By assuming HE factorisation in the high energy limit of Eq. (5.5), one can divide the known matrix element squared by the known one–jet impact factor and keep only the leading terms in $\hat{s}/\hat{t}$. This will then be the $W + 1$jet impact factor.

Assuming an asymptotic form of factorisation, the differential hadronic cross section for $W + 2$–jet production is then given by

$$\begin{aligned} &\frac{d\sigma}{d^2p_{q_\perp} d^2p_{b'_\perp} d^2p_{W_\perp} dy_q dy_{b'} dy_W} \\ =& \qquad \sum_i x_a^0 Q_i(x_a^0, \mu_F^2)\, x_b^0 S(x_b^0, \mu_F^2) \frac{I^{qW} I^g}{32\pi^5 |q_{a_\perp}|^2 |q_{b_\perp}|^2} \frac{\delta^2(q_{a_\perp} - q_{b_\perp})}{2} \,, \end{aligned} \tag{5.11}$$

where $q_{a\perp} = -p_{q\perp} - p_{W\perp}$ and $q_{b\perp} = p_{b'_\perp}$, and where we have substituted $\hat{t}^2$ with $|q_{a\perp}|^2|q_{b\perp}|^2$. In the first pdf the sum is over (anti)quark flavours, and the impact factors are given in Eqs. (5.10) and (5.7). The last term is the LO term of the BFKL resummation. Thus, to obtain the BFKL-resummed cross section we just need to replace $\delta^{(2)}(\mathbf{q}_{a\perp} - \mathbf{q}_{b\perp})/2$ with $f(\mathbf{q}_{a\perp}, \mathbf{q}_{b\perp}, \Delta y)$ given in Eq. (2.54). The asymptotic parton momentum fractions are given by

$$
\begin{aligned}
x_a^0 &= \frac{1}{\sqrt{s}} \left(p_{q\perp} e^{y_q} + m_\perp e^{y_W} \right) \\
x_b^0 &= \frac{1}{\sqrt{s}} p_{b'\perp} e^{y_{b'}}
\end{aligned}
\tag{5.12}
$$

However, in Eq. (5.11) energy and longitudinal momentum are not conserved. The parton momentum fractions in the high-energy limit, x_a^0 and x_b^0, given in Eq. (5.12) underestimate the exact ones (5.3) and accordingly the pdfs can be grossly overestimated. Thus for numerical applications and for a comparison with experimental data, it can be convenient to perform the high-energy limit only on the dynamical part of Eq. (5.4), by writing the squared amplitude in the factorised form (5.6), while leaving the kinematics untouched. This leads to

$$
\begin{aligned}
&\frac{d\sigma}{d^2p_{q\perp} d^2p_{b'_\perp} d^2p_{W\perp} dy_q dy_{b'} dy_W} \\
&= \sum_i x_a Q_i(x_a, \mu_F^2)\, x_b S(x_b, \mu_F^2) \frac{1}{32\pi^5} \left[\frac{I^{qW} I^g}{\hat{t}^2} \right] \frac{\delta^2(q_{a\perp} - q_{b\perp})}{2} .
\end{aligned}
\tag{5.13}
$$

For the invariants $\hat{t}$ and $t_{a'bb'}$, implicit in the square brackets, two options are possible:[2]

(a) they are taken to be exact, namely $\hat{t} = 2p_b \cdot p_{b'}$ and $t_{a'bb'} = (p_{a'} + p_W)^2$. For instance, the dashed lines of Fig. 5.6 have been obtained from Eq. (5.13) with option (a);

(b) $\hat{t}$ and $t_{a'bb'}$ are in the high-energy limit, as defined in Eq. (5.9) and by $\hat{t} \approx -|q_{b'\perp}^2|$.

Note that Eq. (5.13), with the two approximations for the dynamics above, and Eq. (5.11) have the same theoretical validity, however their numerics may be rather different. In order to examine this in detail, in Fig.5.7 we consider $W + 2$-jet production as a function of the rapidity interval between the jets $\Delta y = |y_{j_1} - y_{j_2}|$. For the renormalisation and the factorisation scales we keep the same choice as in Sec.5.1.2. The solid curve is the exact production rate (5.4); the dot-dashed curve is the production rate in the high-energy limit (5.11); the two dashed curves are given by the production rate (5.13), with the two approximations listed above: (b) is the upper dashed curve, and (a) is the lower one. Note that the exact production rate is contained between curves (a) and (b), with (b)

[2]The invariant $t_{abb'}$ is the same in the exact and high-energy kinematics.

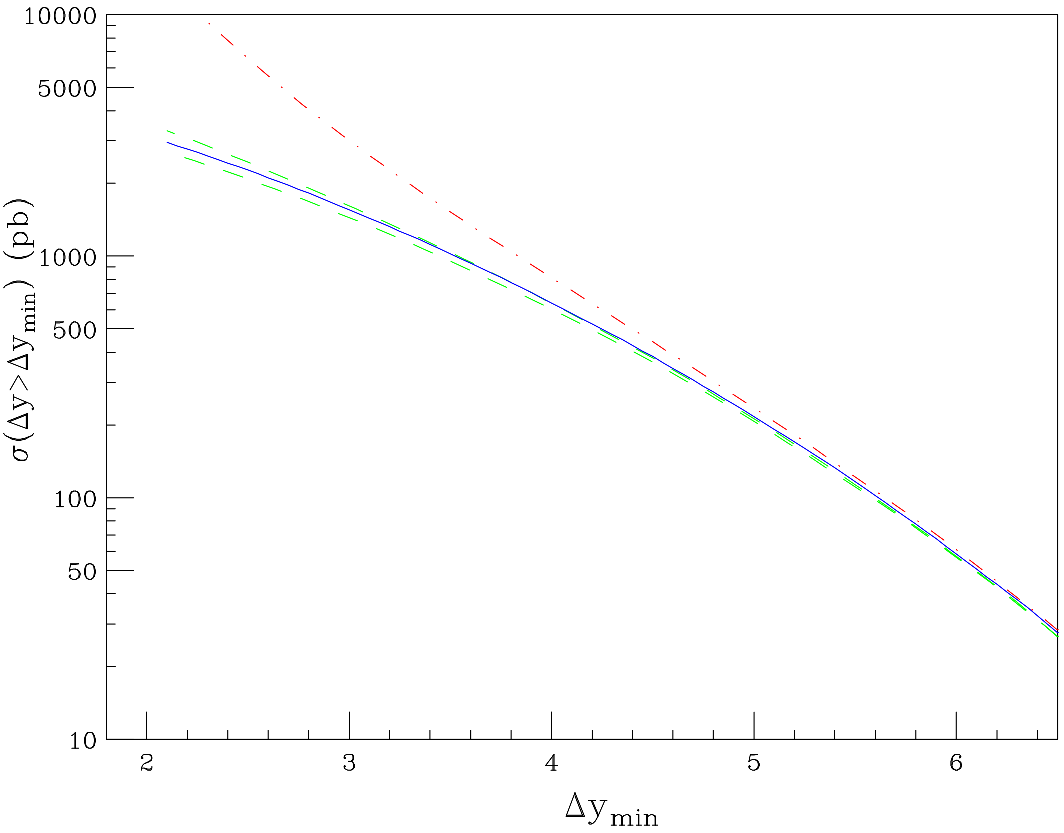

Figure 5.7: The $W+2$-jet production rate as a function of the rapidity interval between the jets $\Delta y = |y_{j_1} - y_{j_2}|$. The solid curve is the exact production rate (5.4); the dot-dashed curve is the production rate in the high-energy limit (5.11); the two dashed curves are given by the production rate (5.13), with the two approximations for the dynamics mentioned in the text.

yielding the best numerical approximation to the exact curve, while the high-energy limit on the LO kinematics and dynamics (the dot-dashed curve) is rather distant from the exact production rate, unless Δy is quite large. The range between curves (a) and (b) may be viewed as a band of uncertainty on the high-energy limit at LO.

5.3 BFKL Observables

After having considered several approximations to the high-energy limit and introduced the BFKL Monte Carlo as the tool that we shall use to analyse the BFKL gluon radiation, we turn now to the analysis of the effects of the BFKL radiation on some observables in $W+2$–jet production.

When including BFKL evolution of the t–channel gluon exchange by substituting $f(\mathbf{q}_{a\perp}, \mathbf{q}_{b\perp}, \Delta y)$ for the δ–functional in Eq. (5.13), the parton momentum fractions should be evaluated as

$$
\begin{aligned}
x_a &= \frac{p_{j_1\perp}}{\sqrt{s}} e^{y_{j_1}} + \frac{p_{j_2\perp}}{\sqrt{s}} e^{y_{j_2}} + \frac{m_\perp}{\sqrt{s}} e^{y_W} + \sum_{i=1}^{n} \frac{k_{i\perp}}{\sqrt{s}} e^{y_i} \,, \\
x_b &= \frac{p_{j_1\perp}}{\sqrt{s}} e^{-y_{j_1}} + \frac{p_{j_2\perp}}{\sqrt{s}} e^{-y_{j_2}} + \frac{m_\perp}{\sqrt{s}} e^{-y_W} + \sum_{i=1}^{n} \frac{k_{i\perp}}{\sqrt{s}} e^{-y_i} \,,
\end{aligned}
\tag{5.14}
$$

where the sum is over the gluons emitted from the BFKL evolution. Using the parton momentum fractions of Eq. (5.14) will observe energy and momentum conservation, but similar to the dijet case, it would only be possible to use the asymptotic versions of Eq. (5.12) in an analytic approach.

From Eq. (4.10) we see that in order to detect evidence of a BFKL-type behaviour in a scattering process, we need to obtain Δy as large as possible. In the context of dijet production this can be done by minimizing the jet transverse energy, and maximizing the parton centre-of-mass energy $\hat{s}$. Since $\hat{s} = x_a x_b s$, in a fixed-energy collider this is achieved by increasing the parton momentum fractions $x_{a,b}$, and then measuring the dijet production rate $d\sigma/d\Delta y$. However, in dijet production the following three effects hinder the characteristic growth of the BFKL ladder (4.10) with respect to LO production, as we have seen in the previous chapter:

as the x's grow the parton luminosities fall off, making it difficult to disentangle the eventual BFKL-driven rise of the parton cross section from the pdfs fall off [23, 19] (see the results of the previous chapter);

the implementation of the exact x's Eq. (5.14) in the BFKL Monte Carlo [26], rather than using $x^0_{a,b}$ (Eq. (5.12)) as prescribed by the high–energy limit, shifts the pdfs toward smaller values, and thus further suppresses the production rate. This effect is already present at $\mathcal{O}(\alpha_s^3)$ [38];

in dijet production both the tagged jets have typically the same minimum transverse energy; at NLO, the dijet cross section as a function of the difference $\mathcal{D}$ between the minimum transverse energies of the two jets turns out to have a slope $d\sigma/d\mathcal{D}$ which is infinite at $\mathcal{D} = 0$ [40, 35]. This hints to the presence of large logarithms of Sudakov type, which can conceal the logarithms of type $\ln(\hat{s}/\hat{t})$ characteristic of the BFKL dynamics.[3]

In Fig.5.8 we consider $W + 2$-jet production as a function of Δy, and with acceptance cuts y_W, $y_{j_2} \geq 1$ and $y_{j_1} \leq -1$, or y_W, $y_{j_2} \leq -1$ and $y_{j_1} \geq 1$. For all of the curves of Fig.5.8 and Fig.5.13, we choose $\mu_{R1} = p_{j_{1\perp}}$ and $\mu_{R2} = (p_{j_{2\perp}} + m_\perp)/2$ as renormalisation

[3]Logarithms of Sudakov type are contained in the BFKL solution (4.10), however they lack the running of α_s and they are not consistently resummed.

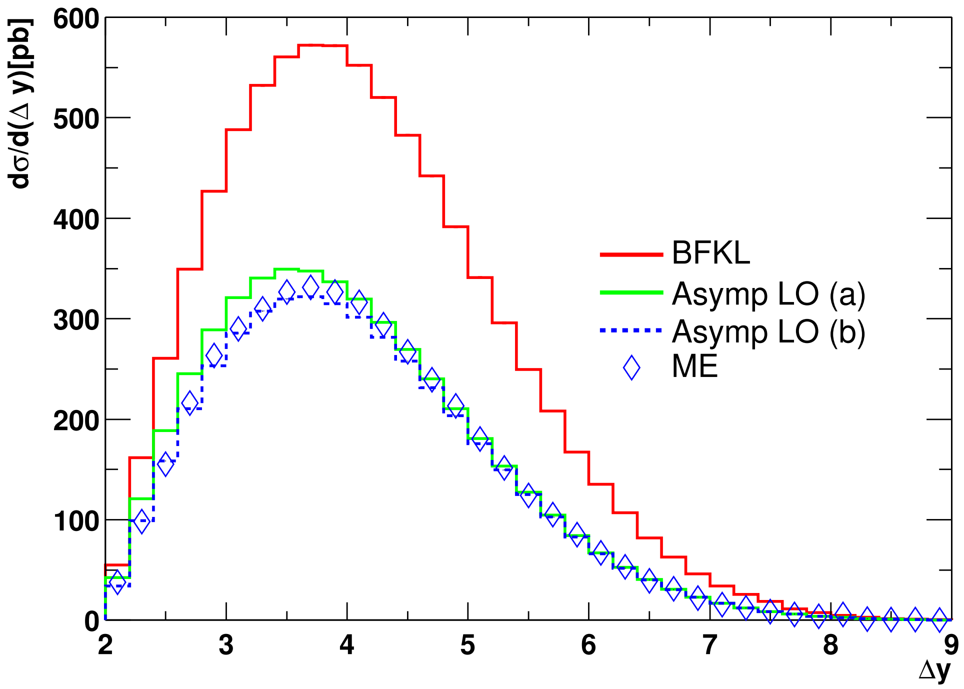

Figure 5.8: The $W+2$-jet production rate as a function of the rapidity interval between the jets $\Delta y = |y_{j_1} - y_{j_2}|$, with acceptance cuts $y_W, y_{j_2} \geq 1$ and $y_{j_1} \leq -1$, or $y_W, y_{j_2} \leq -1$ and $y_{j_1} \geq 1$. The diamonds are the exact production rate (5.4); the dashed curve is the production rate in the high-energy limit (5.13) with option (a); the dotted curve is the same with option (b); the solid curve includes the BFKL corrections.

scales, and $\mu_{F1} = \mu_{F2} = (|p_{j_{1\perp}}| + |p_{j_{2\perp}}| + m_\perp)/2$ as factorisation scales. We justify the peculiar scale choices above as follows: we note that our calculations are at LO (from the renormalisation point of view), thus the scale choice is completely arbitrary, as long as it is physically unambiguous. However, a uniform choice for all of the curves in the same figure is required for a consistent comparison between different approximations. In addition, in the high–energy limit the impact factors for $W+1$-jet production on one side and for jet production on the other can be viewed as two almost independent scattering centres linked by a gluon exchanged in the crossed channel, thus it makes sense to run α_s according to the scale set by each impact factor. Accordingly, in the LO calculation α_s^2 must be understood as $\alpha_s(p_{j_{1\perp}}^2)\,\alpha_s\left((p_{j_{2\perp}} + m_\perp)^2/4\right)$. In the high–energy limit it is possible (and would make sense) to choose the factorisation scales equal to the renormalisation scales, however for the exact production rate this choice would not be physically sensible since no high–energy factorisation is present, thus for the factorisation scales we keep the same choice as in the previous figures.

In Fig.5.8 the diamonds represent the exact production rate (5.4); the dashed curve is the production rate in the high–energy limit (5.13) with option (a); the dotted curve is the same with option (b); the solid curve includes the BFKL corrections. In Fig.5.8 and Fig.5.13 we have computed the BFKL corrections using Eq. (5.13) with option (b). However, the particular option we choose is immaterial since the uncertainty related to the choice of option in Eq. (5.13) is much smaller than the uncertainties intrinsic to the BFKL resummation, the latter being due to the leading-log approximation, the choice of scale of α_s and the approximation on the incoming parton momentum fractions. Note that the curve of Fig.5.8 is both qualitatively and quantitatively different from $d\sigma/d\Delta y$ in dijet production: the peak in Fig.5.8 is a striking confirmation of the dominance of the configurations asymmetric in rapidity, discussed in Sec.5.1.2. In fact the symmetric acceptance cut strongly penalises the asymmetric configurations when Δy approaches its minimum value; since the asymmetric configurations dominate the $W + 2$-jet production rate, the effect is a strong depletion of the latter. In addition, the BFKL ladder (solid curve), which includes energy–momentum conservation (Eq. (5.14)), shows a substantial increase of the cross section with respect to the LO analysis (dotted and dashed curves), as opposed to a decrease in the dijet case.

To understand how this comes about, we note that the presence of at least three particles in the final state makes the threshold configurations, and thus the logarithms of Sudakov type, much less compelling than in the dijet case. Secondly, the implementation of the kinematic constraint (5.14) in the BFKL Monte Carlo, rather than using $x^0_{a,b}$ (Eq. (5.12)) in the high-energy limit, has a much lesser impact than in the dijet case. This is due to the fact that the valence quark distribution in $q\,g \to q\,g\,W$ is much less sensitive to x variations than the gluon distribution in $g\,g \to g\,g$. To analyse this more precisely, we consider in Fig.5.9 the ratio $f(x^0, \mu_F^2)/f(x, \mu_F^2)$ of the pdf as a function of the x^0's (Eq. (5.12)) in the high-energy limit versus the pdf as a function of the exact x (Eq. (5.14)). The ratio is calculated for each event in the Monte Carlo as the ratio of the pdf evaluated at x^0 compared to an evaluation at x, weighted with the contribution of this event to the cross section according to (5.13) with option (b) and the BFKL ladder added. Finally, this distribution is binned in Δy. To be definite, since the high-energy factorisation implies that each impact factor is associated to one of the two incoming partons, we can term the ratio $f(x_a^0, \mu_F^2)/f(x_a, \mu_F^2)$ as the one associated to the impact factor for $W + 1$-jet production, and the ratio $S(x_b^0, \mu_F^2)/S(x_b, \mu_F^2)$ as the one associated to the impact factor for jet production. As we see from Fig.5.9, the solid curve is much further away from 1 than the dashed-dotted curve. Since the effective pdf is dominated by the gluon distribution, this implies that the ratio $S(x_b^0, \mu_F^2)/S(x_b, \mu_F^2)$ is much more sensitive to variations of the x's than the ratio $f(x_a^0, \mu_F^2)/f(x_a, \mu_F^2)$, which is made by va-

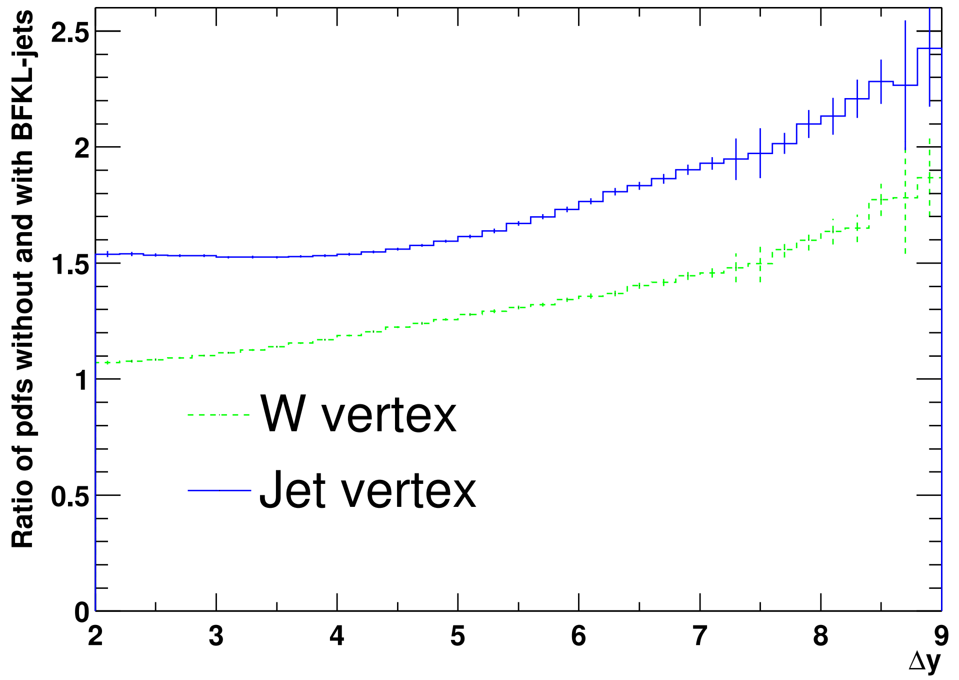

Figure 5.9: The ratio $f(x^0, \mu_F^2)/f(x, \mu_F^2)$ of the pdf as a function of the x^0's (5.12) in the high-energy limit versus the pdf as a function of the exact x (5.14); the dashed-dotted curve is the ratio $f(x_a^0, \mu_F^2)/f(x_a, \mu_F^2)$, and the solid curve is the ratio $S(x_b^0, \mu_F^2)/S(x_b, \mu_F^2)$.

lence quark distributions. Accordingly, we obtain a smaller depletion of the BFKL Monte Carlo prediction in $W + 2$-jet production as compared to dijet production. In addition, both the curves in Fig.5.9 rise as Δy grows. This implies that the BFKL radiation, which enters the determination of the x's in the denominator, yields as expected a contribution which is growing with Δy.

In Fig. 5.10 we have plotted the differential cross section as a function of the different contributions to the parton momentum fractions from x_1 (the quark part of Eq. (5.14)), x_2 (the gluon part of the contribution to x_b in Eq. (5.14)), x_W (the W part of Eq. (5.14)) and finally x_{BFKL} (the BFKL part of Eq. (5.14)). The average values of the contribution to the parton momentum fractions are given in Tab. 5.2. We see that the contribution from the W dominates x_a and ensures that the pdf is probed in the region relative flat region of the quark. Also, we see that the contribution from the BFKL radiation is indeed less than the contribution from any of the other sources.

A variable that has been extensively studied as possibly sensitive to BFKL effects is the azimuthal angle decorrelation $\Delta\phi = |\phi_{j_1} - \phi_{j_2}| - \pi$ between the most forward and backward jets in inclusive dijet samples. At LO the jets are supposed to be back to back,

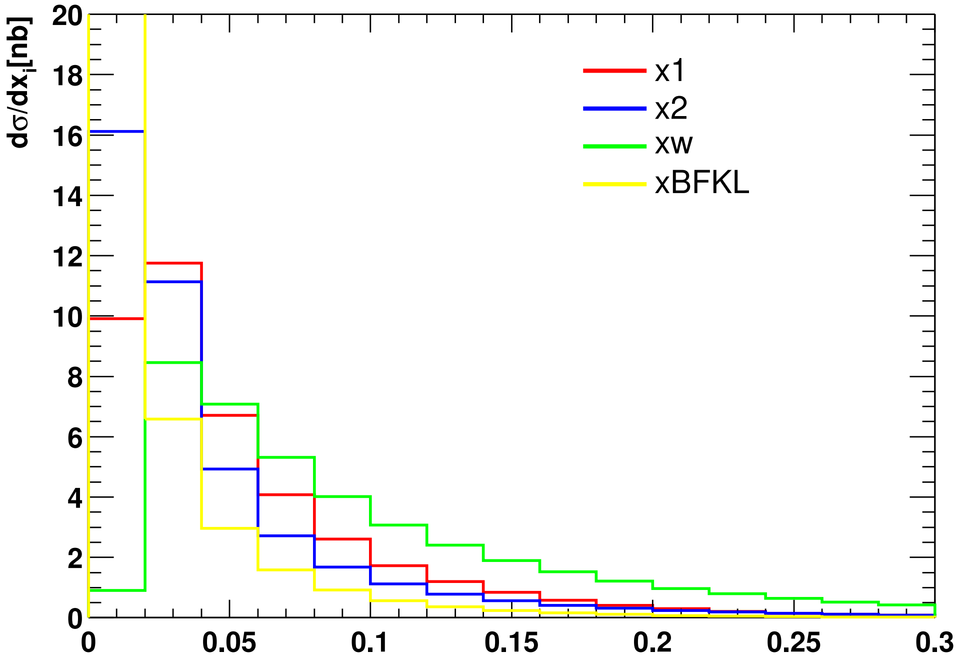

Figure 5.10: The differential cross section on different contributions to the parton momentum fractions.

with a correlation which is smeared by gluon radiation induced by parton showers and hadronization. However, if we look at the correlation also as a function of Δy, we expect the gluon radiation between the jets to further blur the information on the mutual position in transverse momentum space, and thus the decorrelation to grow with Δy. In $W + 2$-jet production we expect the logarithms of Sudakov type to play a much less significant role than in dijet production. Thus, in analogy with dijet production, in Fig.5.11 we consider the average azimuthal angle $\langle \cos \Delta\phi \rangle$ as a function of the rapidity interval between the jets Δy. The acceptance cuts are the same as for Fig.5.8. The diamonds are the exact

	Avg. value
x_1	0.0746
x_2	0.0648
x_W	0.1231
x_{BFKL}	0.0460

Table 5.2: The average contribution to the parton momentum fractions distributed on different sources.

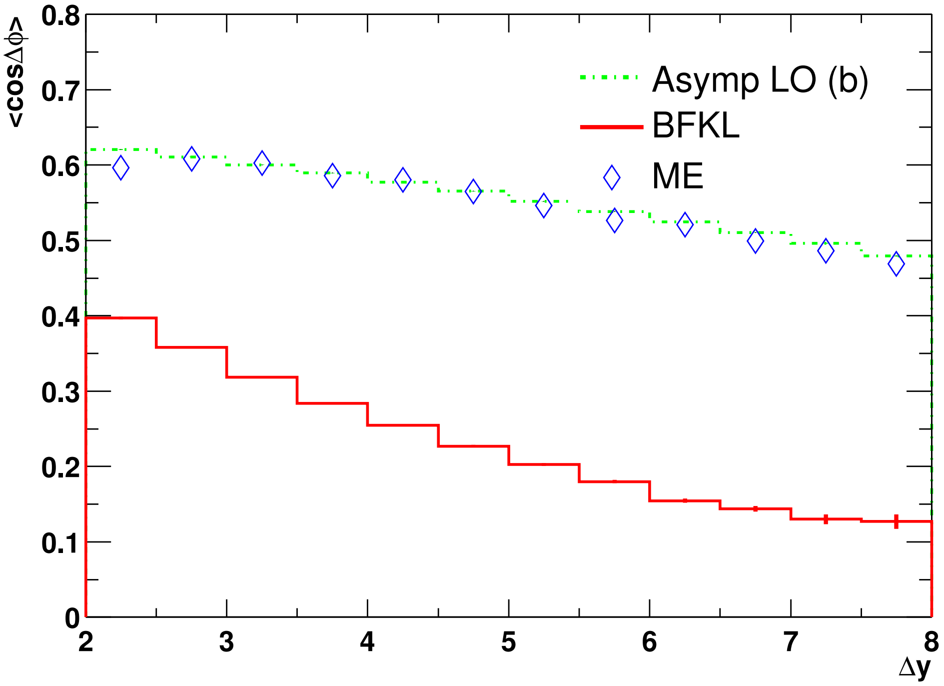

Figure 5.11: The average azimuthal angle $\langle \cos \Delta\phi \rangle$, where $\Delta\phi = |\phi_{j_1} - \phi_{j_2}| - \pi$, as a function of the rapidity interval between the jets $\Delta y = |y_{j_1} - y_{j_2}|$, with acceptance cuts $y_W, y_{j_2} \geq 1$ and $y_{j_1} \leq -1$, or $y_W, y_{j_2} \leq -1$ and $y_{j_1} \geq 1$. The diamonds are the exact production rate (5.4); the dashed-dotted curve is the production rate in the high-energy limit (5.13) with option (b); the solid curve includes the BFKL corrections.

production rate (5.4); the dashed-dotted curve is the production rate in the high-energy limit (5.13) with option (b); the solid curve includes the BFKL corrections. The average azimuthal angle being defined as a ratio of production rates is much less sensitive to scale variations than the curves of Fig.5.8.

In Fig.5.12 we plot the BFKL prediction for the mean number of jets $\langle n \rangle$ with $p_\perp > p_{j\perp\min} = 30$ GeV, emitted by the BFKL ladder as a function of the rapidity interval between the jets Δy, and the BFKL prediction for the same variable in the rapidity range $-1 < y_j < 1$. We see that the mean number of jets rises approximately linearly with Δy, and accordingly that the mean number of jets in the rapidity range $-1 < y_j < 1$ stays constant. We can crudely understand this, by noting that for a very large Δy the cross section obtained from substituting the BFKL solution of Eq. (4.10) into Eq. (5.11)

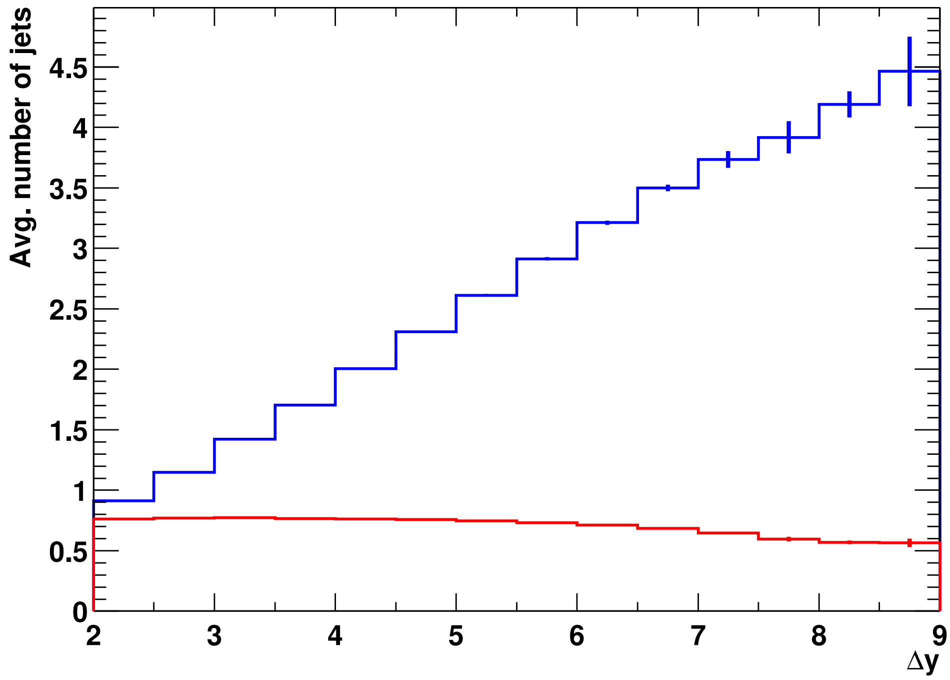

Figure 5.12: Solid: the BFKL prediction for the mean number of jets $\langle n \rangle$ with $p_\perp > p_{j\perp\min} =$ 30 GeV as a function of the rapidity interval between the jets $\Delta y = |y_{j_1} - y_{j_2}|$. Dotted: the same in the rapidity range $-1 < y_j < 1$.

behaves like

$$\sigma|_{\Delta y} \sim e^{\omega(0,0)\Delta y} = \sum_{n=0}^{\infty} \frac{(\omega(0,0)\Delta y)^n}{n!}\,, \tag{5.15}$$

with $\omega(0,0) = 4\ln 2 C_A \alpha_s/\pi$, and a power of α_s for each real correction to, and therefore for each emitted gluon from, the BFKL ladder. Up to corrections of type $\ln(p_\perp/p_{j\perp\min})$ [25], the mean number of jets emitted by the BFKL ladder is then

$$\langle n \rangle = \frac{(n\sigma)|_{\Delta y}}{\sigma|_{\Delta y}} \simeq \omega(0,0)\Delta y\,. \tag{5.16}$$

For $\alpha_s(p^2_{j\perp\min})$ with $p_{j\perp\min} = 30$ GeV, this yields typically a jet each second unit of rapidity, which is in rough agreement with Fig.5.12.

Finally, in Fig.5.13 we consider $W + 2$-jet production as a function of the transverse momentum $q_{a_\perp} = -(p_{q_\perp} + p_{W_\perp})$ exiting from the impact factor I^{qW} for $W + 1$-jet production. At LO, $q_{a_\perp} = q_{b_\perp} = p_{b'_\perp}$, thus $q_{a_\perp}$ is bound to be equal to the transverse momentum of the jet opposite to the impact factor I^{qW} (and thus to be always larger than 30 GeV). In presence of the gluon radiation of the BFKL ladder, this is not longer true, and $q_{a_\perp}$ is

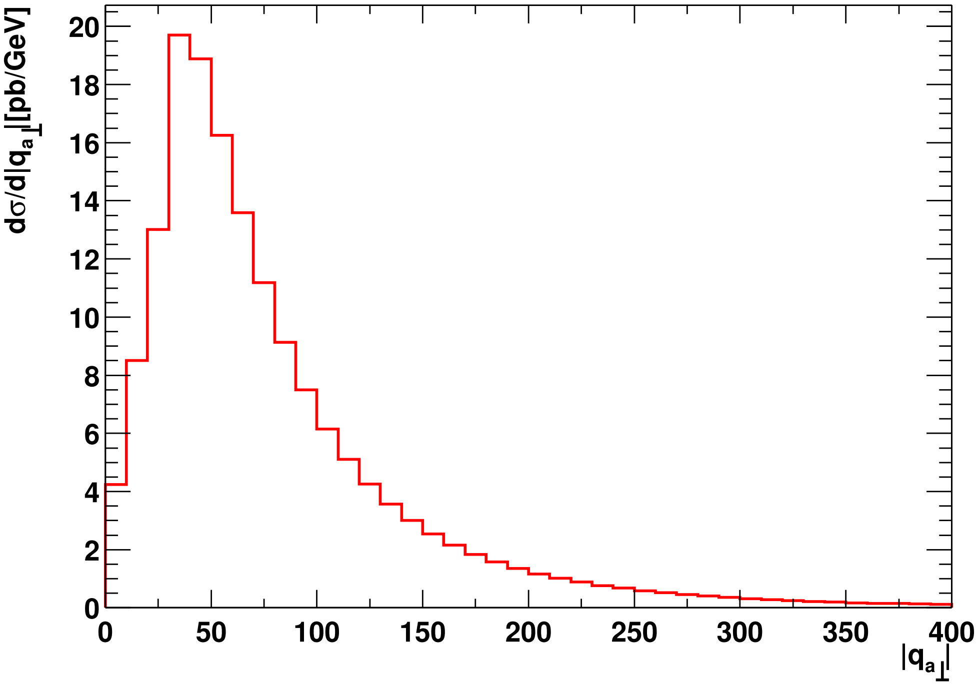

Figure 5.13: The $W + 2$-jet production rate, including BFKL corrections, as a function of the transverse momentum $q_{a_\perp}$, with $q_{a_\perp} = -(p_{q_\perp} + p_{W_\perp})$.

allowed to go to zero. However, a simple power-counting argument shows that the production rate is finite as $q_{a_\perp} \to 0$. In fact from Eq. (5.7) we know that $I^{qW} \sim \mathcal{O}(|q_{a_\perp}|^2)$. Substituting it, and the ladder (4.10) which goes like $\mathcal{O}(1/|q_{a_\perp}|)$, in Eq. (5.11), we see that as far as the behaviour in $q_{a_\perp}$ is concerned,

$$\frac{d\sigma}{dq_{a_\perp}^2} \sim \frac{q_{a_\perp}^2}{q_{a_\perp}^3} \delta^2(q_{a_\perp} + p_{q_\perp} + p_{W_\perp}) \,, \tag{5.17}$$

and therefore the distribution $\mathrm{d}\sigma/\mathrm{d}q_{a_\perp}$ is finite as $q_{a_\perp} \to 0$, in agreement with Fig.5.13.

5.4 Conclusions

In this chapter we have discussed the characteristics of a process that in the high energy limit provides a natural extension of the dijet production studied in the previous chapter.

In Sec. 5.1 we have examined the exact LO inclusive rapidity distribution for $W+1$-jet and $W + 2$-jet production; as for the latter, we have seen that the dominant parton subprocess $q\,g \to q\,g\,W$ produces a great deal of W bosons forward in rapidity. This is due to the different shape of the pdfs of the incoming quark and gluon, and to gluon exchange in the crossed channel which loosens the bound between the W boson and a jet on one (rapidity) side, and the other jet on the other side.

In Sec. 5.2 we have compared several high-energy approximations at LO to the exact production rate. The range between the most extreme high-energy approximations may be considered as the theoretical uncertainty on the high-energy limit at LO.

In Sec. 5.3 we have considered some BFKL footprints, most notably the rate $\mathrm{d}\sigma/\mathrm{d}\Delta y$ and the azimuthal angle decorrelation $\mathrm{d}\sigma/\mathrm{d}\Delta\phi$ as functions of the rapidity interval Δy between two tagged jets. These observables had already been considered in inclusive dijet production, however because of the dominance of the configurations asymmetric in rapidity and the presence of at least three particles in the final state, which makes threshold configurations less relevant, in $W+2$-jet production $\mathrm{d}\sigma/\mathrm{d}\Delta y$ and $\mathrm{d}\sigma/\Delta\phi$ take on a completely new light. In addition, we have considered the mean number of jets, which as expected rises approximately linearly with Δy. Finally, we have computed the transverse momentum distribution of the impact factor for $W+1$-jet production. At LO this is bound from below by momentum conservation at the minimum transverse energy of the jet opposite to the $W+1$-jet configuration, but with additional gluon radiation it is allowed to reach zero, where the distribution is finite. The implicit requirement that one of the incoming partons is a quark with a much flatter pdf in the relevant region of the parton momentum fractions means that the BFKL effects stand a much better chance of surviving the inclusion of the pdfs than in the pure dijet case, where the very steeply falling gluon pdf suppresses the BFKL gluon evolution. Combined with the hope that the $W+2$jet setup is less sensitive to pollution from other logarithms this means that this setup might be far better suited for BFKL studies, despite the slight complication of the inclusion of an electroweak particle. In particular we note that all the observables in this study depend only on the QCD partons, and the duty of the W is only to introduce a hard lepton that might help trigger the event, and to require an incoming quark.

Chapter 6

Conclusions

We have formulated a solution to the BFKL evolution equation that consists of an explicit sum over the phase space of “resolved” gluons, while the effects of unresolved and virtual contributions are also taken properly into account. In this way, the implementation of the numerical integration of the resulting solution reproduces the results obtained in the standard analytic approach, where such are available. Furthermore it is possible to introduce the running of the coupling into the BFKL solution.

In the study of dijet production we saw that the BFKL Monte Carlo solution to the BFKL evolution provides first of all an efficient tool in calculating cross sections when complicated cuts are placed on the leading dijets. This was demonstrated in the study of dijets at the Tevatron. Secondly, and much more importantly, the BFKL MC provides a tool for studying in detail the radiation from the BFKL chain. The study of these exclusive states require a very fast and stable implementation of the Monte Carlo integration, which is achieved through the techniques reviewed in Chapter 3. We have studied the number of jets produced in the BFKL evolution, and the amount of energy going into this radiation. We have thereby verified that the contribution from the BFKL radiation to the total centre of mass energy for dijet production is indeed subleading in the sense that the asymptotic behaviour is unchanged. However, we also showed that the energy consumption of the BFKL evolution is sufficient to make an impact at energies reachable by colliders in the foreseeable future. This is partly because the gluon density function of the proton is very steeply decreasing at the values of the parton momentum fractions probed in dijet production. Therefore, the extra energy taken up by the BFKL radiation compared to the pure dijet case is enough to introduce a significant drop in the parton fluxes and a corresponding decrease in the hadronic cross sections. The result is that the partonic prediction of a rise in cross section over the LO result as a function the rapidity span is modified to an almost no–change situation.

We then presented a study of the dijet angular decorrelation, for which the effects of the pdfs cancel to a large extent. This analysis shows clearly how the event configuration returns to the LO setup as the rapidity separation between the leading dijets closes in on the maximum allowed value at a given energy. This suggests that the BFKL resummation at hadron colliders has an area of applicability limited from two sides in the rapidity span. From below since the logarithms resummed have to be large, and from above since there has to bee sufficient energy available to produce the gluon radiation that is being resummed.

We concluded the dijet study by a detailed examination of an analysis of a dijet sample from the Tevatron. Here we showed that the set of experimental cuts applied severely limits the predictive power of the data sample with respect to the extraction of a BFKL intercept.

Finally we considered $W + 2$–jet production at hadron colliders. This process share many properties with dijet production in the sense that when the dijets are required to be produced at large rapidity separations, the process factorises into two impact factors connected by a t–channel gluon exchange. One of the scattering centers will at leading order consist of an incoming quark and an outgoing quark and W. The other impact factor will consist of a incoming and outgoing parton. In the large Δy limit, where Δy is the rapidity difference between the two outgoing partons, the t–channel gluon is susceptible to BFKL evolution. It turns out that in this case the BFKL evolution does indeed lead to an increase of the hadronic cross section over the LO prediction, since the quark pdf varies sufficiently slowly with the parton momentum fraction that the pdf suppression from an increased centre of mass energy due to the BFKL radiation does not cancel the rise in the partonic cross section predicted from the BFKL evolution of the t–channel gluon exchange. Since the normalisation of the cross section might not be stable against higher order corrections, we suggested another BFKL observable, namely the azimuthal angle between the two (leading) jets. This shows considerably larger decorrelation in the case of BFKL evolution than at the leading order.

The Monte Carlo BFKL and the impact factor framework can be applied to many other processes than the two described in this thesis. We are currently investigating the process $gg \to b\bar{b}b\bar{b}$ at hadron colliders, which will dominate the forward b–production channel at the LHC. Furthermore, we are investigating the possibilities of applying the MC BFKL to processes such as $\gamma^* g \to q\bar{q}g$ at ep colliders and $\gamma^*\gamma^* \to q\bar{q}q\bar{q}$ at e^+e^- colliders. All these processes show dominance of the t–channel gluon exchange in the forward channels.

Appendix A

Solving for ω_0

In this appendix we will show how the integral of Eq. (2.66) is performed, since this is central to the reformulation of the fixed coupling BFKL solution. The relevant integral is

$$I(\mathbf{q}_\perp, \mu^2) = \int \frac{\mathrm{d}^2\mathbf{k}_\perp}{k_\perp^2} \left[\Theta(\mu^2 - k_\perp^2) - \frac{q_\perp^2}{\mathbf{k}_\perp^2 + (\mathbf{q}_\perp + \mathbf{k}_\perp)^2} \right]. \tag{A.1}$$

We start by using

$$\mathrm{d}^2\mathbf{k}_\perp = k\,\mathrm{d}k\,\mathrm{d}\theta, \tag{A.2}$$

where $k = |\mathbf{k}_\perp|$. We can now perform the resulting integral over θ

$$\begin{aligned} I(\mathbf{q}, \mu^2) &= \int_0^\infty \frac{\mathrm{d}k}{k} \int_0^{2\pi} \mathrm{d}\theta \left[\Theta(\mu^2 - k^2) + \frac{q^2}{2k^2 + q^2 + 2kq\cos\theta} \right] \\ &= 2\pi \int_0^\infty \frac{\mathrm{d}k}{k} \left[\Theta(\mu^2 - k^2) - q^2 \frac{\sqrt{1 + \frac{4kq}{2k^2 - 2kq + q^2}}}{2k^2 + 2kq + q^2} \right], \end{aligned} \tag{A.3}$$

were we have dropped the $\perp$ index and set $q = |\mathbf{q}|$. The last remaining integral is most easily performed by splitting it into the two integration regions of $k < \mu$ and $k \geq \mu$. One thereby readily (at least by using any of the available algebraic manipulation programmes) obtains

$$I(\mathbf{q}, \mu^2) = \pi \ln\left(\frac{\mu^2}{q^2}\right). \tag{A.4}$$

In the running coupling case, the relevant integral contains an additional logarithm of q^2, but the integral is performed similarly, with just one more split in the integration region at the scale for the freezing of the evolution.

Appendix B

The Only Difficult Integral of the BFKL MC

Of all the integrals arising in the BFKL MC of Eq. (2.67)–(2.68) and Eq. (2.79)–(2.80), only the nested integrals over rapidities is a problem. The integrals over the transverse momenta of the BFKL gluons and the phase space integrals over the impact factors can all be performed efficiently using the importance sampling distribution of Eq. (3.30)–(3.31) with suitable choices of the parameters, which are easily optimised by comparing the resulting $g(x)$ with the distribution of the cross section in any of the variables. The same is true for the integration over the rapidity of the particles emerging from the impact factors. Here, the valid integration region is often so small that a simple flat distribution is often sufficient, although other slightly more optimised distributions have often been chosen for hadronic quantities due to the rapid fall–off in rapidity due to the pdf suppression.

The reason that the nested integrals over rapidities of the BFKL gluons is difficult to optimise is exactly that the rapidities are *not* independent variables. The nesting of the integrals complicates the importance sampling procedure, since the integration limits of every single integration variable varies with the choice of the other integration variables. However, some analytic insight can be gained, which will help in constructing the importance sampling. The nested integrals can be written on the form

$$I_n = \int_0^{\Delta y} \mathrm{d}y_1\, A_1^{y_1} \int_0^{y_1} \mathrm{d}y_2\, A_2^{y_2} \int_0^{y_2} \mathrm{d}y_3\, A_3^{y_3} \cdots \int_0^{y_{n-1}} \mathrm{d}y_n\, A_n^{y_n}, \tag{B.1}$$

where each A_n is given in the constant coupling scenario by

$$A_n = \left[\frac{(\mathbf{q}_{a\perp} + \sum_{j=1}^{n-1} \mathbf{k}_{j\perp})^2}{(\mathbf{q}_{a\perp} + \sum_{j=1}^{n} \mathbf{k}_{j\perp})^2}\right]^{\bar{\alpha}_s}, \tag{B.2}$$

and in the running coupling case by

$$A_n = \left[\frac{\widetilde{\alpha}_s((\mathbf{q}_{a\perp} + \sum_{j=1}^{i} \mathbf{k}_{j\perp})^2)}{\widetilde{\alpha}_s((\mathbf{q}_{a\perp} + \sum_{j=1}^{i-1} \mathbf{k}_{j\perp})^2)}\right]^{C_A/(\pi b)}. \tag{B.3}$$

The difference between Eq. (B.2) and Eq. (B.3) will prove to lead to a significantly different numerical behaviour in the two cases. In both cases, the length of the vector sum will not change much from one emission to the next (especially so when we are considering A_n with n not too small). This is because the BFKL chain is dominated by soft gluon emissions, and each step in the approximately random walk from $\mathbf{q_{a\perp}}$ to $\mathbf{q_{b\perp}}$ is small. This means that the fractions in the A_n are of the order one, although all the physics lies in the deviation from one. It is also seen that whereas the A_n in the constant coupling case Eq. (B.2) will be closer to one than the fraction (since $\bar{\alpha_s} < 1$), the A_n in the running coupling case will tend to be pushed away from one since $C_A/(\pi b) \approx 1.44$. It is interesting to note that if we assume all the A_n are so close to one that we can ignore the dependence of the integrand on any of the y_n, the value of the integral is $(\Delta y)^n/n!$. In fact it is possible to solve the nested integrals analytically. One such closed formula consisting of the sum over just $n+1$ terms is

$$I_n = \sum_{i=0}^{n} B_i^{\Delta y} \prod_{j=0, j\neq i}^{n} \frac{1}{\log(B_i/B_j)} \tag{B.4}$$

where

$$B_k = \prod_{j=1}^{j=k} A_j \tag{B.5}$$

and $B_0 = 1$. This however highlights a problem of all the analytic solutions we have dealt with: They are extremely sensitive to any of the A_i getting close to one (or in this case any product of them coming close to one), which of course is the case where one of the nested integrals become trivial. In fact, it proved almost impossible to get a stable numerically prediction using the above analytic solution (or any of the many variants tried). The analytic solution is of course also not the aim of the method, since it would integrate out part of the gluon phase space and thereby it would not be possibly to reconstruct the total energy and momentum of the BFKL gluons.

Instead it proves useful to rewrite the nested integrals as (taking $n = 3$ as an example)

$$I_3 = \int_0^1 \mathrm{d}z_1 \int_0^1 \mathrm{d}z_2 \int_0^1 \mathrm{d}z_3 \; A_1^{z_1\,\Delta y} A_2^{z_1 z_2\,\Delta y} A_3^{z_1 z_2 z_3\,\Delta y} (\Delta y)^3 z_1^2 z_2. \tag{B.6}$$

This rewriting highlights the different power like behaviour due to the nesting and the exponential behaviour due the A_n terms. For the constant coupling case, since the A_i's are all close to one, the z_i's are now generated according to the distribution z_i^{n-i} (the number n of nested integrals in this case is $n = 3$):

$$\int_0^1 \mathrm{d}z_1 \int_0^1 \mathrm{d}z_2 \int_0^1 \mathrm{d}z_3 A_1^{(\Delta y) z_1} A_2^{(\Delta y) z_1 z_2} A_3^{(\Delta y) z_1 z_2 z_3} (\Delta y)^3 z_1^2 z_2 \tag{B.7}$$

$$=(\Delta y)^3 \int_0^{1/n} \mathrm{d}c_1 \int_0^{1/(n-1)} \mathrm{d}c_2 \int_0^{1/(n-2)} \mathrm{d}c_3$$
$$A_1^{(\Delta y)\sqrt[n]{c_1 n}} A_2^{(\Delta y)\sqrt[n]{c_1 n}\,\sqrt[n-1]{c_2(n-1)}} A_3^{(\Delta y)\sqrt[n]{c_1 n}\,\sqrt[n-1]{c_2(n-1)}\,\sqrt[n-2]{c_3(n-2)}}, \tag{B.8}$$

where we have set $\mathrm{d}c_1 = z_1^{n-1}\mathrm{d}z_1$ etc. This is the basis of the Monte Carlo integration of the nested rapidity integral in the constant coupling case. The rapidities are found using $y_1 = (\Delta y) z_1$, etc. Finally, the contribution for this specific choice of rapidities to the integral is found as

$$(\Delta y)^n \prod_{i=1}^{n} A_i^{(\Delta y)\prod_{j=1}^{i} z_j} \frac{1}{n+1-i}. \tag{B.9}$$

The method above proves to converge very fast for the constant coupling case. However, it also proves next to useless for the running coupling case, since the power behaviour of the z_i in Eq. (B.6) is less dominant (and therefore the importance sampling according to the power behaviour might actually *increase* the variance rater than reducing it). Instead, for the running coupling case we just pick the rapidities uniformly in the allowed intervals, which coincides with the preferred method if all $A_i = 1$. The different importance sampling techniques can in this case easily make up a factor 100 in the necessary running time for a satisfactory result for rapidity spans of more than 4 units of rapidity.

References

[1] R. Barate et al. Measurement of the spectral functions of axial-vector hadronic tau decays and determination of alpha(s)(m(tau)**2). *Eur. Phys. J.*, C4:409, 1998.

[2] R. K. Ellis, W. James Stirling, and B. R. Webber. QCD and collider physics. *Cambridge Monogr. Part. Phys. Nucl. Phys. Cosmol.*, 8:1–435, 1996.

[3] T. Muta. Foundations of Quantum Chromodynamics. second edition. *World Sci. Lect. Notes Phys.*, 57:1–409, 1998.

[4] Michael E. Peskin and D. V. Schroeder. An introduction to quantum field theory. Reading, USA: Addison-Wesley (1995) 842 p.

[5] J. Ambjørn and J.L. Petersen. Quantum field theory. Lecture notes, Niels Bohr Institute, 1994.

[6] K. G. Chetyrkin, B. A. Kniehl, and M. Steinhauser. Strong coupling constant with flavor thresholds at four loops in the MS scheme. *Phys. Rev. Lett.*, 79:2184–2187, 1997.

[7] F. Bloch and A. Nordsieck. Note on the radiation field of the electron. *Phys. Rev.*, 52:54–59, 1937.

[8] Frank G. Krausz. Cancellations of mass singularities in Yang-Mills theories. *Nucl. Phys.*, B126:340, 1977.

[9] F. G. Krausz. Mass singularities in Yang-Mills theories. *Phys. Lett.*, B66:251–254, 1977.

[10] T. Kinoshita. Mass singularities of feynman amplitudes. *J. Math. Phys.*, 3:650–677, 1962.

[11] T. D. Lee and M. Nauenberg. Degenerate systems and mass singularities. *Phys. Rev.*, 133:B1549–B1562, 1964.

[12] Raymond Brock et al. Handbook of perturbative QCD: Version 1.0. *Rev. Mod. Phys.*, 67:157–248, 1995.

[13] B. L. Combridge and C. J. Maxwell. Untangling large p(t) hadronic reactions. *Nucl. Phys.*, B239:429, 1984.

[14] Vittorio Del Duca. An introduction to the perturbative QCD pomeron and to jet physics at large rapidities. 1995.

[15] J. R. Forshaw and D. A. Ross. Quantum chromodynamics and the pomeron. Cambridge, UK: Univ. Pr. (1997) 248 p. (Cambridge lecture notes in physics. 9).

[16] J. A. M. Vermaseren. The symbolic manipulation program FORM. KEK-TH-326.

[17] E. A. Kuraev, L. N. Lipatov, and Victor S. Fadin. Multi - reggeon processes in the Yang-Mills theory. *Sov. Phys. JETP*, 44:443–450, 1976.

[18] E. A. Kuraev, L. N. Lipatov, and V. S. Fadin. The Pomeranchuk singularity in nonabelian gauge theories. *Sov. Phys. JETP*, 45:199–204, 1977.

[19] W. James Stirling. Production of jet pairs at large relative rapidity in hadron-hadron collisions as a probe of the perturbative pomeron. *Nucl. Phys.*, B423:56–79, 1994.

[20] A. H. Mueller and H. Navelet. An inclusive minijet cross-section and the bare Pomeron in QCD. *Nucl. Phys.*, B282:727, 1987.

[21] S. Catani et al. QCD. 2000. hep-ph/0005025.

[22] Marcel Froissart. Asymptotic behavior and subtractions in the mandelstam representation. *Phys. Rev.*, 123:1053–1057, 1961.

[23] Vittorio Del Duca and Carl R. Schmidt. Dijet production at large rapidity intervals. *Phys. Rev.*, D49:4510–4516, 1994.

[24] Lynne H. Orr and W. J. Stirling. Dijet production at hadron hadron colliders in the BFKL approach. *Phys. Rev.*, D56:5875–5884, 1997.

[25] Carl R. Schmidt. A Monte Carlo solution to the BFKL equation. *Phys. Rev. Lett.*, 78:4531–4535, 1997.

[26] Lynne H. Orr and W. James Stirling. The collision energy dependence of dijet cross sections as a probe of BFKL physics. *Phys. Lett.*, B429:135–144, 1998.

[27] Guido Altarelli, Richard D. Ball, and Stefano Forte. Factorization and resummation of small x scaling violations with running coupling. *Nucl. Phys.*, B621:359–387, 2002.

[28] M. Ciafaloni, D. Colferai, G. P. Salam, and A. M. Stasto. Expanding running coupling effects in the hard Pomeron. 2002.

[29] William H. Press, Saul A. Teukolsky, William T. Vetterling, and Brian P. Flannery. *Numerical Recipes in FORTRAN*. Cambridge University Press, 2nd edition, 1992.

[30] F. James. Monte Carlo theory and practice. *Rept. Prog. Phys.*, 43:1145, 1980.

[31] G. Peter Lepage. Vegas: An adaptive multidimensional integration program. CLNS-80/447.

[32] Martin Luscher. A portable high quality random number generator for lattice field theory simulations. *Comput. Phys. Commun.*, 79:100–110, 1994.

[33] F. James. RANLUX: A FORTRAN implementation of the high quality pseudorandum number generator of luscher. *Comp. Phys. Commun.*, 79:111–114, 1994.

[34] Leif Lonnblad. CLHEP: A project for designing a C++ class library for high-energy physics. *Comput. Phys. Commun.*, 84:307–316, 1994.

[35] J. R. Andersen, V. Del Duca, S. Frixione, C. R. Schmidt, and W. James Stirling. Mueller-Navelet jets at hadron colliders. *JHEP*, 02:007, 2001.

[36] Carlo Ewerz and Bryan R. Webber. Jet rates at small x to single-logarithmic accuracy. *JHEP*, 04:022, 1999.

[37] Carlo Ewerz and Bryan R. Webber. Multiplicity of (mini-)jets at small x. *JHEP*, 08:019, 1999.

[38] Vittorio Del Duca and Carl R. Schmidt. BFKL versus $O(\alpha_s^3)$ corrections to large rapidity dijet production. *Phys. Rev.*, D51:2150–2158, 1995.

[39] Alan D. Martin, R. G. Roberts, W. James Stirling, and R. S. Thorne. Parton distributions and the LHC: W and Z production. *Eur. Phys. J.*, C14:133–145, 2000.

[40] Stefano Frixione and Giovanni Ridolfi. Jet photoproduction at HERA. *Nucl. Phys.*, B507:315, 1997.

[41] Vittorio Del Duca and Carl R. Schmidt. Transverse momentum distributions in large-rapidity dijet production at the Tevatron. 1994.

[42] Vittorio Del Duca and Carl R. Schmidt. Azimuthal angle decorrelation in large rapidity dijet production at the Tevatron. *Nucl. Phys. Proc. Suppl.*, 39BC:137–140, 1995.

[43] G. Corcella et al. Herwig 6.4 release note. 2001.

[44] M. Ciafaloni, D. Colferai, G. P. Salam, and A. M. Stasto. Tunneling transition to the Pomeron regime. *Phys. Lett.*, B541:314–326, 2002.

[45] S. Abachi et al. The azimuthal decorrelation of jets widely separated in rapidity. *Phys. Rev. Lett.*, 77:595–600, 1996.

[46] W. T. Giele, E. W. N. Glover, and David A. Kosower. Higher order corrections to jet cross-sections in hadron colliders. *Nucl. Phys.*, B403:633–670, 1993.

[47] W. T. Giele, E. W. N. Glover, and David A. Kosower. The two jet differential cross-section at $O(\alpha_s^3)$ in hadron collisions. *Phys. Rev. Lett.*, 73:2019–2022, 1994.

[48] Yuri L. Dokshitzer. QCD, theoretical issues. 1997.

[49] B. Abbott et al. Probing BFKL dynamics in the dijet cross section at large rapidity intervals in p anti-p collisions at $\sqrt{s} = 1800\text{GeV}$ and 630GeV. *Phys. Rev. Lett.*, 84:5722–5727, 2000.

[50] I. I. Balitsky and L. N. Lipatov. The Pomeranchuk singularity in quantum chromodynamics. *Sov. J. Nucl. Phys.*, 28:822–829, 1978.

[51] S. Frixione. A general approach to jet cross sections in QCD. *Nucl. Phys.*, B507:295–314, 1997.

[52] J. F. Gunion, A. Stange, and S. Willenbrock. Weakly-coupled Higgs bosons. 1995.

[53] R. N. Cahn and Sally Dawson. Production of very massive Higgs bosons. *Phys. Lett.*, B136:196, 1984.

[54] Robert N. Cahn, Stephen D. Ellis, Ronald Kleiss, and W. James Stirling. Transverse momentum signatures for heavy Higgs bosons. *Phys. Rev.*, D35:1626, 1987.

[55] Yuri L. Dokshitzer, S. I. Troian, and Valery A. Khoze. Collective QCD effects in the structure of final multi - hadron states. (in russian). *Sov. J. Nucl. Phys.*, 46:712–719, 1987.

[56] J. D. Bjorken. Rapidity gaps and jets as a new physics signature in very high-energy hadron-hadron collisions. *Phys. Rev.*, D47:101–113, 1993.

[57] Vernon D. Barger, R. J. N. Phillips, and D. Zeppenfeld. Mini - jet veto: A tool for the heavy Higgs search at the lhc. *Phys. Lett.*, B346:106–114, 1995.

[58] J. R. Andersen, V. Del Duca, F. Maltoni, and W. James Stirling. W boson production with associated jets at large rapidities. *JHEP*, 05:048, 2001.

[59] T. Stelzer and W. F. Long. Automatic generation of tree level helicity amplitudes. *Comput. Phys. Commun.*, 81:357–371, 1994.

[60] Alan D. Martin, R. G. Roberts, W. James Stirling, and R. S. Thorne. Parton distributions: A new global analysis. *Eur. Phys. J.*, C4:463–496, 1998.

[61] G. Marchesini and B. R. Webber. Monte carlo simulation of general hard processes with coherent qcd radiation. *Nucl. Phys.*, B310:461, 1988.

[62] I. G. Knowles. Spin correlations in parton - parton scattering. *Nucl. Phys.*, B310:571, 1988.

[63] G. Marchesini et al. Herwig: A monte carlo event generator for simulating hadron emission reactions with interfering gluons. version 5.1 - april 1991. *Comput. Phys. Commun.*, 67:465–508, 1992.